Doctoral Dissertation

Evaluation and Prediction of Interfacial Thermal Resistance between Water and Nanostructure Surfaces using Molecular Dynamics Method and Thermal Circuit Model

Zhiwen Jiang

January 2025

Graduate School of Engineering

Osaka University

Abstract

With the development of microelectronic devices and the miniaturization of energy systems, thermal management at the nanoscale has become increasingly important. For instance, reducing the interfacial thermal resistances (ITRs) can prevent devices from overheating, whereas increasing the ITRs enables microdevices to maintain stable operation under extreme temperature conditions.

The solid-liquid (S-L) ITR is a critical factor influencing nanoscale heat transfer processes. The S-L ITRs of flat surfaces primarily depend on factors such as wettability and liquid pressure in the experimental and molecular dynamics (MD) studies. The S-L ITRs of flat surfaces can be measured using both experimental and MD methods. However, it is important to explore the relationship between the S-L ITRs of flat surfaces and those of nanostructure surfaces, which would facilitate the design of heat transfer in nanostructure surfaces by enabling the evaluation and prediction of the S-L ITRs, thereby reducing the computational and experimental costs of MD simulations and experiments for nanostructure surfaces.

The objectives of the present study are to evaluate the ITRs of nanostructure surfaces using MD simulations, to predict the ITRs of nanostructure surfaces through thermal circuit models (TCMs) in nanoscale heat transfer, and to assess the feasibility of employing the coarse-grained (CG) water model as a replacement for the simple point charge/extension (SPC/E) water model in the fields of ITR evaluation based on MD simulations and TCMs.

To evaluate and predict the S-L ITRs of nanostructure surfaces, the relationship between the S-L ITR and the density depletion length (DDL) on nanostructure surfaces was investigated using the CG and SPC/E models in copper (Cu)-water and Cu-graphene-water systems, employing non-equilibrium molecular dynamics (NEMD) simulations; Six TCMs were proposed to predict the ITRs of nanostructure surfaces. The TCMs A and B were established under the assumption that there was no energy transfer between water and the nanopillar sidewalls; the TCMs C and D assumed that heat transfer between the water and the solid walls occurred under analogous temperatures of the nanopillar sidewalls and groove bottom surfaces; the TCMs E and F were analogous to TCMs C and D, considering the temperature difference of the nanopillar sidewalls from that of the groove bottom surfaces. TCMs A, C, and E utilized the thermal conductivities of solids and liquids calculated from MD simulations, while the other TCMs employed experimental and empirical thermal conductivities.

The findings obtained in this dissertation are summarized as follows. The ITRs between

the groove bottom surface and water near the top nanopillar surface could be correlated with the DDL. The DDL could effectively be related to S-L ITRs, even on nanostructure surfaces, including the Wenzel and Cassie-Baxter states. Regardless of water models, the DDL depended on water pressure, surface wettability, and surface roughness. The TCMs C to F could reasonably predict the ITRs in the Wenzel state on nanostructure surfaces, especially the TCMs E and F show good performance in predicting ITRs of nanostructure surfaces. Considering the energy transfer between the nanopillar sidewalls and water, the TCMs C to F could also approximately predict the ITRs of nanostructure surfaces in the Cassie-Baxter state. Regarding the influence of water molecular models, the CG model could replace the SPC/E water model for the qualitative evaluation of S-L ITRs. The composite surface slightly weakened the accuracy of TCM predictions in the Wenzel and CB states because the graphene coating affected the distribution of the energy exchange ratio between the nanopillar sidewalls and the liquid. The ITR of flat surfaces can be used to evaluate and predict the ITRs of nanostructure surfaces through the proposed TCMs, providing thermal design and safety guidance for heat transfer and heat dissipation at the interfaces between nano and micro-devices, thus saving experimental and computational costs substantially.

Table of contents

Nomenclature

<>	Ensemble average
$A_{g\text{-}g}$	Area of the graphene in the x-y plane
A_{flat}	Area of a flat surface in the x-y plane
A_{ng}	Area of a groove bottom surface in the x-y plane
A_{np}	Area of a top nanopillar surface in the x-y plane
A_1	Local area in TCMs, the component of A_{flat}
A_2	Local area in TCMs, the component of A_{flat}
A_d	Coefficient of an exponential curve
aa	Coefficient of a linear fitting function
bb	Coefficient of a linear fitting function
c_{cg}	Parameter of the CG water model
C_{miss}	Number of missing carbon atoms
C_{tot}	Total number of carbon atoms
C_{long}	Energy-conversion constant
C_{VDOS}^{-1}	Normalization coefficient of the vibrational density of states
damp	Damping factor (custom coefficient)
d_{cg}	Parameter of the CG water model
dfct	Defect concentration
dz	Slab size in the z-direction
DDL	Density depletion length
E^{cold}	Cumulative energy in cold walls
E^{hot}	Cumulative energy in hot walls
E_{ij}^{REBO}	REBO energy
E_i	Total energy of atom i
E_β	Embedded energy
E_{tot}	Total energy
E_{sys}	System energy
E_{bath}	External energy
F	Total force
F_c	A conservative force term
F_f	Frictional resistance or viscous damping
F_τ	Force generated by the random collision
F_{1a}	Force of 1_{st} particle in the x-, y-, or z-direction under pairwise and bonds
F_{2a}	Force of 2_{nd} particle in the x-, y-, or z-direction under pairwise and bonds
F_{3a}	Force of a particle in the x-, y-, or z-direction related to angles
F_{1b}	Force of 1_{st} particle in the different direction of F_{1a} under pairwise and bonds

F_{2b}	Force of 2_{nd} particle in the different direction of F_{2a} under pairwise and bonds
F_{3b}	Force of a particle in the different direction of F_{3a} related to angles
$\vec{F}_i$	Force of particle i with vector
$\vec{F}_{ij}$	Pairwise force of particle i and j with vector
$f_A(r)$	Force interactions of the CG water model
$f_C(r)$	Cutoff function of the CG water model
$f_R(r)$	Repulsive function of the CG water model
H	System Hamiltonian
Int	Positive integer
K	Kinetic energy
$k_{g\text{-}g}$	Thermal conductivity of graphene
k_B	Boltzmann constant
$k_{Cu\text{-}exp}$	Thermal conductivity of Cu by experiments
$k_{Cu\text{-}MD}$	Thermal conductivity of Cu by MD simulations
$k_{liq\text{-}exp}$	Thermal conductivity of water by experiments
$k_{liq\text{-}MD}$	Thermal conductivity of water by MD simulations
L	Liouville operator
L_1	Local size in the x-direction, the component of L
L_2	L- L_1
L_{Cu}	Thickness of the Cu nanopillar
L_{groove}	Width of the groove in the x-direction
L_{NANO}	Thickness of liquid in the groove
L_{cr}	Contact region thickness
$L_{g\text{-}g}$	Thickness of the graphene coating
L_{gro}	$L_{gro}=2L_{groove}$
L_{pillar}	Nanopillar width
L_{th}	Original water thickness in the groove
L_X	Size of a simulation box in the x-direction
L_Y	Size of a simulation box in the y-direction
L_Z	Size of a simulation box in the z-direction
L_{fst}	Cases of fast force
L_{slw}	Cases of slow force
M	Mass
m_{cg}	Parameter of the CG water model
m_i	Mass of a particle i
N	Number of particles, etc.
n_{cg}	Parameter of the CG water model
nd	Coefficient of exponential curves
overlap	Overlap of the vibrational density of states

P	Pressure
P_{tot}	Total water pressure in the x-, y-, or z-direction
p_i	Conjugate momentum
$\dot{p}_i$	First-order partial derivative of p_i
Q	Rate of heat flow
Q_C	Local rate of heat flow in substance C
Q_D	Local rate of heat flow in substance D
Q_{flat}	Rate of heat flow on a flat surface
Q_1	Local rate of heat flow, the component of Q_{flat}
Q_2	Local rate of heat flow, the component of Q_{flat}
Q_n	Rate of heat flow on a nanostructure surface
q	Heat flux
q_n	Heat flux of a nanostructure surface
qc	Charge of a particle
q_i	Cartesian coordinates
$\dot{q}_i$	First-order partial derivative of q_i
R	Thermal resistance
R_{eq-A}	Equivalent thermal resistance of model A
R_{eq-B}	Equivalent thermal resistance of model B
R_{eq-C}	Equivalent thermal resistance of model C
R_{eq-D}	Equivalent thermal resistance of model D
R_{eq-E}	Equivalent thermal resistance of model E
R_{eq-F}	Equivalent thermal resistance of model F
R_{g-g}	Internal thermal resistance of graphene
R_{S-g}	Local thermal resistance between the Cu and graphene
R_{S-liq*}	Representative of the local thermal resistance, such as R_{S-liq1}
R_{S-liq1}	Local thermal resistance between the top nanopillar surface and water
R_{S-liq2}	Local thermal resistance between the groove bottom surface and water
R_{S-liq3}	Local thermal resistance between the nanopillar sidewalls and water
R_{S-liq4}	Same as R_{S-liq3}
R_{S-liq5}	Local thermal resistance between the graphene coating and the water
R_{S-liq6}	Same as R_{S-liq5}
R_{Cu}	Internal thermal resistance of Cu
R_{Cu*}	$R_{Cu*}=0.5R_{Cu}$
R_{liq}	Internal thermal resistance of liquid
R_{liq*}	$R_{liq*}=0.5R_{liq}$
R_{f1}	Local thermal resistance of a flat surface for the area of A_1
R_{f2}	Local thermal resistance of a flat surface for the area of A_2
R_{eq-12}	Equivalent thermal resistance of R_{f1} and R_{f2}

R_1	$R_{S\text{-}liq1}$ and R_{Cu*}
R_2	R_{liq*}
R_3	R_{Cu*}
R_4	$R_{S\text{-}liq2}$ and R_{liq*}
R_B	Parallel thermal resistance composed of $R_{S\text{-}liq3}$ and $R_{S\text{-}liq4}$ in Cu-water systems, and composed of $R_{S\text{-}liq3}$, $R_{S\text{-}liq4}$, $R_{S\text{-}liq5,}$ and $R_{S\text{-}liq6}$ in Cu-graphene-water systems
R_C	Local thermal resistance of the substance C
R_D	Local thermal resistance of the substance D
R_{flat}	Thermal resistance of a flat surface
R_{AS}	Local thermal resistance of the substance A
R_{BS}	Local thermal resistance of the substance B
R_c	Radius of the approximated circle
r_c	Cutoff radius
r_i	Position of a particle i
$\vec{r}_i$	Position of a particle i with vector
r_{1a}	Position of 1_{st} particle in the x-, y-, or z-direction under pairwise and bonds
r_{2a}	Position of 2_{nd} particle in the x-, y-, or z-direction under pairwise and bonds
r_{3a}	Position of a particle in the x-, y-, or z-direction under angles
r_{1b}	Position of 1_{st} particle in the different direction of r_{1a} under pairwise and bonds
r_{2b}	Position of 2_{nd} particle in the different direction of r_{2a} under pairwise and bonds
r_{3b}	Position of a particle in the different direction of r_{3a} under angles
r_{ij}	Distance between atoms i and atoms j
$\vec{r}_{ij}$	Distance with vector between atoms i and atoms j
S_{seg}	Area of the segment of a circle
S_{xx}	Stress in the x-direction
S_{yy}	Stress in the y-direction
S_{zz}	Stress in the z-direction
t	Time
T	Temperature
T_C	Temperature of cold sources
T_H	Temperature of hot sources
T_L	Temperature of liquid near the surface of cold walls on a flat surface
T_{L1}	Water temperature near the top nanopillar surface
T_{L2}	Water temperature near the groove bottom surface
T_S	Temperature of a solid surface on a flat surface
T_{S1}	Solid temperature at the groove bottom surface
ΔT	Temperature difference and temperature jump
ΔT_f	Temperature jump, T_{L2}-T_{S1}

ΔT_{th}	Temperature jump, T_{L1}-T_{S1}
ΔT_{flat}	Temperature jumps between liquid and solid surfaces on a flat surface
ITR	Interfacial thermal resistance
ITR_f	ITR of a nanostructure surface calculated by T_f
ITR_{flat}	ITR on a flat surface
ITR_{MD}	ITR of a nanostructure surface calculated by T_{th}
ITR_{th}	Same as the ITR_{MD}
TR	Internal thermal resistance of the liquid and solid
U	Potential energy
V(t)	Velocity autocorrelation at time t
VDOS	Vibrational density of states
$VDOS_\alpha(t)$	VDOS of graphene
$VDOS_\beta(t)$	VDOS of water
V	Volume
v	Velocity
v_a	Velocity in the x-, y-, or z-direction
v_b	Velocity in the different directions of v_a
v_i	Velocity of a particle i
$\vec{v}_i$	Velocity with a vector of a particle i
vol	Volume in a slab region ($dz \times L_X \times L_Y$)
α	Interaction strength in the Lennard-Jones potential function
β_{cg}	a parameter of the CG water model
Γ	Phase space
δ	Root mean square error
ε	Parameter of Lennard-Jones potential function
ε_i	Parameter of atom i in the Lennard-Jones potential function
ε_j	Parameter of atom j in the Lennard-Jones potential function
ε_{ij}	Parameter between atoms i and j based on the Lorentz-Berthelot combining rule
ϵ	Dielectric constant
θ	Angle of a sector at a circular point
λ_3	Parameter of the CG water model
ρ	Density
ρ_l^b	Bulk densities of the liquids
ρ_s^b	Bulk densities of the solids
$\rho_l(z)$	Densities of the liquid along the z-direction
$\rho_s(z)$	Densities of the solids along the z-direction
ρ_β	Atomic electron density
σ	Parameter of Lennard-Jones potential function
σ_i	Parameter of atom i in the Lennard-Jones potential function

σ_j	Parameter of atom j in the Lennard-Jones potential function
σ_{ij}	Average value of the parameter between σ_i and σ_j
$\Phi_{\alpha\beta}$	Pairwise potential function between the particles α and β
Ψ	Definition of surface roughness
ω	Frequency
Δt	Interval time
γ_{cg}	Parameter of the CG water model
θ_0	Parameter of the CG water model

1. Introduction

1.1 Backgrounds

1.1.1 Scientific and industrial backgrounds

As well known, when two substances of different temperatures interact at interfaces, heat transfer occurs in accordance with the principles of thermodynamics, moving from the region of higher temperature to that of lower temperature. Heat flow is transferred through heat carriers such as phonons and electrons at the interfaces between different materials, causing interfacial thermal resistances (ITRs) due to a discontinuous interface, as shown in Figure 1.1, which concerns the solid-liquid (S-L) interface.

The initial study of Cu and liquid helium II demonstrates the relatively large S-L ITR phenomenon[1]. Kapitza resistance [2] at S-L interfaces between liquid helium and solid was extensively studied and attracted great attention in the 1940s. Kapitza resistance is also referred to as ITR and thermal boundary resistance (TBR). Then, the acoustic mismatch model (AMM) and diffuse mismatch model (DMM) are put forward to explain the ITR phenomenon[3, 4] over half a century. With the miniaturization of microelectronics and the emergence of nanotechnology, the research focus on ITRs has shifted. A large amount of heat flux is generated in microelectronic devices to achieve more powerful performance, and the development of micro energy technologies such as lithium batteries has changed the research on ITRs from the macro scale to the microscale and nanoscale. In industry and technology, the ITR is an essential factor.

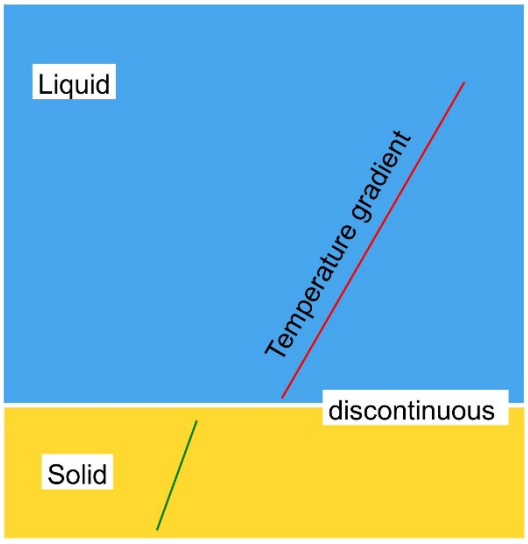

Figure 1.1 A solid-liquid interface based on a flat surface

The industrial demand for artificial intelligence (AI) technology is increasing, especially in powerful computing and deep learning when using a large number of high-performance

chips, which generate a lot of heat during operation. ITR affects the heat dissipation efficiency and it becomes one of the key factors limiting microdevice performance and reliability. Therefore, thermal management at the nanoscale has become a key issue, understanding and predicting ITR have great meaning for the thermal management of electronic devices.

Interfacial thermal resistance (ITR) is always present in microelectronic devices. There are ITRs at the interfaces between electronic devices and heat dissipation devices. For example, the interfaces between the thermal interface materials (TIMs) and the electronic devices, and the interfaces between the heat dissipation device and the electronic devices can generate ITRs. There are usually billions of transistors inside a chip device, and it is necessary to ensure that the heat flux can be effectively dissipated to avoid damaging the devices. In recent years, the semiconductor manufacturing process node has been reduced to 3 nm or less. Due to physical limitations such as quantum tunneling, the architecture of chips has shifted from two-dimensional (2D) to three-dimensional (3D) [5], and the direct liquid cooling technology employs a non-conductive liquid in contact with the heat dissipation surface, which eliminates the harmful effects of solid-solid (S-S) interface resistance and improves the thermal management of chips[6]. Therefore, the maturation and application of nanotechnology have increased the demand for research on ITR.

Micro heat pipes (MHPs) are miniaturized and high-performance heat exchange devices used in many fields of heat dissipation in microelectronic devices, smartphones, and computer processors. Graphene coatings can modify the surface properties such as metals and MHPs, and may have significant implications for the design of surface coatings that are electrically and thermally conductive and water-impermeable, attracting considerable attention to the graphene coating [7]. For example, from a macroscopic perspective, the enhanced thermal performance of MHPs with graphene coatings [8] depends mainly on the ultrafast transport of water through the graphene coating, which affects evaporation and condensation. However, ITRs[9, 10], size effect[9], and graphene coatings [7] can affect the performance of MHPs when the liquid film thickness shifts to the nanoscale.

In fact, ITRs are widespread in the industrial fields, and it is essential to evaluate and predict ITRs for designing heat transfer systems and providing guidance for the safety of microdevices.

1.1.2 Research of S-L ITRs on flat surfaces by experiments and MD simulations

(a) experimental research

Some powerful experimental tools have been developed to measure thermal resistance at the microscale and even at the nanoscale, such as the time-domain thermoreflectance (TDTR) method[11] and the continuous wave frequency domain thermal reflection (CW-FDTR) method [12]. Using the TDTR method to measure energy transfer across the interface of flat surfaces, the ITRs between water and the self-assembled monolayer

(SAM) solid walls at the nanoscale were obtained [13]. The CW-FDTR method can be used to measure the ITRs between liquids, such as water and ethanol; the ITRs between liquid and the sensors consisting of aluminum surfaces matched molecular dynamics (MD) simulation results[12]. In an experimental study [14], a scanning thermal microscope (SThM) probe tip was used to measure and infer the thermal conductivity of the liquid film to be 6.7 nW/K in an area with a diameter of around 90 nm. An experimental study[15] shows that the amount of nanoparticle adhesion is not sufficient to change the macroscopic wettability and S-L ITRs, which indicates that as the nanoparticle-deposited layers increased, the S-L ITRs decreased. Although experimental technology can measure the ITRs at the microscale and nanoscale, it is very difficult to obtain the S-L energy transfer accurately. Therefore, computer simulations are useful methods.

(b) classical MD simulation

The development of fast and efficient high-performance computer (HPC) technology has enabled computer simulation of the atomic and nanoscale heat transfer at S-L and S-S interfaces. In the field of computer simulation, there are many powerful computational methods, such as classical MD and density functional theory (DFT). In computer simulation, DFT is based on the principles of quantum mechanics and can usually accurately describe the interactions between particles, while MD simulation is based on classical Newtonian mechanics with force fields to describe the interactions between particles. Although DFT simulations are more accurate than MD simulations, MD simulations have the advantages of large time and computational scales, and the interactions between particles described by the force fields can also match the experimental results. For example, a coarse-grained (CG) model generated by a machine learning method can simulate the freezing process of millions of water molecules over 230 ns using MD simulations[16].

(c) key factors of ITR in MD research

The non-equilibrium molecular dynamics (NEMD) simulations [17] show that the S-L ITRs on the flat surfaces of Ar (argon)-solid systems cannot be ignored at the nanoscale because the thermal resistances of the liquid are much smaller compared to the S-L ITRs, which are strongly dependent on wettability. Also, the NEMD simulation [18] in the SPC/E-gold system shows that the distance between the gold surface near the SPC/E water molecules and the position of the maximum water density peak is almost constant, which is independent of the bulk water pressure, while there is a dependence between the S-L ITRs and the bulk water pressure. The MD simulations [19] with the liquid as the n-perfluorohexane on a flat surface show that the increased liquid structure adsorption and the decreased S-L ITRs depend on the increasing liquid pressure. The study of single-atom-scale heat flux at the S-L interface using MD simulation[20] shows that the ITR on flat surfaces can be explained by the local quantities of heat flux, which helps to control

heat transfer and thermal resistance at the S-L interface. The results show that the graphene coating on copper (Cu) surfaces can increase heat transfer by 30-40% during water condensation [21], and the graphene coating on the Cu surface increases the S-L ITRs[22]. Therefore, the wettability, liquid pressure, and coating were key factors affecting S-L ITR.

(d) evaluating ITR in MD research

The density depletion length (DDL) is a physical parameter at the nanoscale that can be measured experimentally and reproduced by MD simulations, which includes factors such as wettability and water hydrogen bonds[23]. In MD simulations, the DDL is defined based on the water density approaching the solid surface relative to the normalized distance from the density of the solid surface [24]. The MD study [25] on flat surfaces successfully establishes a relationship between the S-L ITR and DDL in Si-SPC/E water and Si-graphene-SPC/E water systems, showing that when water molecules are arranged in a clustered structure in the vicinity of the S-L interface, a low DDL indicates a close distance between water and solid atoms, which is conducive to the S-L heat transfer. Therefore, exponential curves can be used to uniformly describe the relationship between S-L ITR and DDL on flat surfaces under different wettability conditions.

The above MD studies[17, 18, 22] show that S-L ITRs on flat surfaces are related to key factors such as wettability, liquid pressure, and coatings. Therefore, the DDL can be related to these factors to evaluate and predict S-L ITRs. However, most DDL studies[23, 25] have focused on flat surfaces, and whether DDL can evaluate S-L ITRs of nanostructure surfaces including the Wenzel and Cassie-Baxter (CB) states is worth exploring.

1.1.3 Research of S-L ITRs on nanostructure surfaces by experiments and MD simulations

(a) experimental research

The S-L ITRs of nanostructure surfaces [26] and nanopattern surfaces[27] have been the main focus of the related research at the nanoscale. For example, an experimental report[28] uses the TDTR to measure the thermal boundary conductance (TBC), which is the mathematical reciprocal of the ITR, and TBC at the interface between Si nanostructures and metallic aluminum is increased by about 88% (the ITR is reduced) because nanostructure surfaces enhance interfacial heat transport by increasing the effective contact area. Compared with bare Cu, the nanostructure Cu interface exhibits enhanced boiling performance because the nanostructures easily induce nanobubbles and stabilize nucleation[29]. An experimental study shows that the surface roughness of single-crystal silicon (Si 111) in contact with liquid helium is related to phonon scattering, resulting in temperature-dependent thermal contact resistance[30]. A thin-film

thermocouple (TFT) array experimental device is used to explore the relationship between the nanofin effect (nFE) and thermal resistance during the evaporation of nanoporous materials[31].

(b) ITR in MD research

With modern nanotechnology, it is feasible to experimentally study the S-L ITRs on nanostructure surfaces. However, due to the high cost and challenges associated with achieving energy transfer at the nanoscale, most researches utilize MD simulations to study the S-L ITRs. For example, as the contact area between the nanostructure surfaces and SPC/E water molecules increases, more SPC/E water molecules can be adsorbed on the different nanostructure surfaces of Cu, resulting in an increase in the interaction energy per unit area between the nanostructure surfaces and SPC/E water molecules, thereby reducing the S-L ITR[32]. Another study[33] shows that agglomeration on various nanostructure surfaces during condensation is determined by the synergistic interactions between dropwise development and ordered nucleation. A numerical study of the SPC/E water-solid ITRs [34] indicates that increasing the residence time of the SPC/E water molecules is influenced by the nanostructure sizes and the temperature of the SPC/E water molecules, resulting in a decrease in the S-L ITRs. The research [35] on ITRs in the boiling phenomenon in the TIP4P-Ew water-gold system shows that the S-L ITRs do not depend on the phase change from liquid to boiling, and by increasing the roughness of the nanostructure surfaces, the energy interaction between water and the nanostructure surface is enhanced, thereby reducing the S-L ITRs. A Study on the wetting phenomenon of liquids on nanostructure surfaces using NEMD simulations [36] shows that the total energy per unit volume of liquid molecules near the groove surface is lower than the total energy of the bulk of the liquid film outside the groove. An MD simulation in gas-liquid systems [37] shows that the liquid molecules adsorbed by the nanostructure surface are more than those adsorbed by the flat surface, and with the enhancement of the interaction between solid and liquid, the momentum adjustment coefficient value of the nanostructure surface gradually approaches to that of the flat surface. In summary, nanostructure surface is an effective way to decrease ITR.

(c) wettability on nanostructure surfaces

There are two different wettability states on the rough surface of nanostructure surfaces. One is the Wenzel state[38], where the liquid fills the grooves of the nanostructure surfaces; the other one is the Cassie-Baxter (CB) state[39], where liquid water does not significantly penetrate the grooves of the nanostructure surface, such as in Figure 1.2.

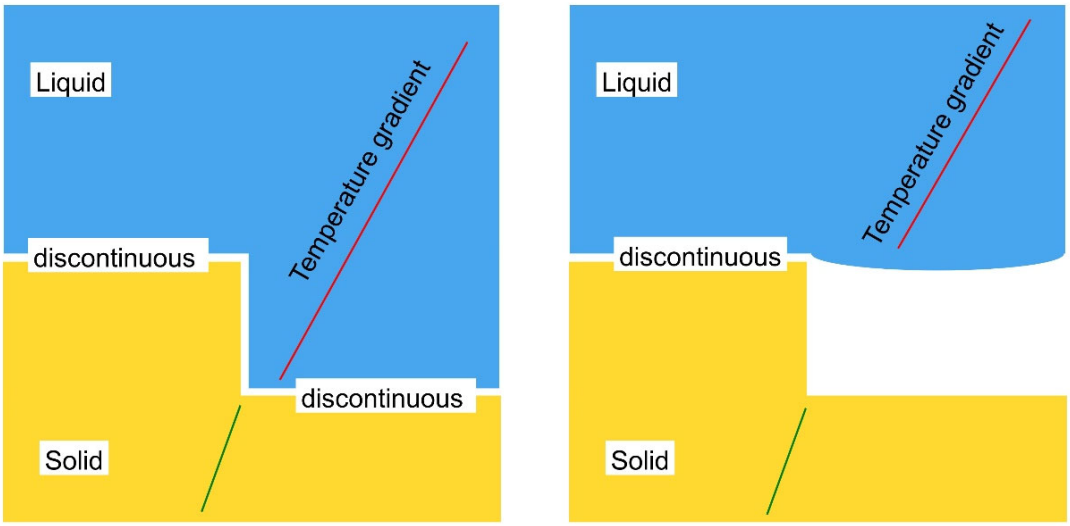

Figure 1.2 Solid-liquid interfaces on nanostructure surfaces in the Wenzel (left) and Cassie-Baxter (right) states.

(d) TCM in MD research

An MD simulation study on flat surfaces [40] shows that in two solid interfaces and confined solid film systems, the thickness of the disordered film plays a crucial role in influencing the extent to which the total thermal resistance (R) from the MD simulation matches the results generated by the TCMs. Parallel TCMs are utilized to assess the impact of graphene orientation on the thermal conductivity of composite materials [41]. On the flat surface of the Cu-Si system, TCMs are very crucial for heat transport at metal/nonmetal interfaces; however, these TCMs overestimate the ITRs due to the simple series of TCMs that ignore the electron-phonon coupling across the interface[42].

In summary, the study of ITRs on nanostructure surfaces primarily focuses on the surface wettability and the adsorption layer of the nanostructure surfaces. However, research on predicting ITRs in different wettability states—from the Wenzel state to the CB state—and the relationship between ITRs on nanostructure surfaces and flat surfaces is still insufficient. The wettability states in Chapters 3 and 4 refer to two typical states, the Cassie-Baxter (CB) state which includes the transition from the Wenzel state to the CB state and the Wenzel state. In Chapters 5 and 6, this transition is defined as the actual CB state due to a change in the heat transfer path. The DDL and TCMs present promising solutions for evaluating and predicting ITRs.

1.2 Significance and Purpose

In nanoscale thermal management, S-L ITR is important in heat transfer. The experimental and MD simulation results indicate that S-L ITRs on flat surfaces primarily depend on some factors such as wettability and liquid pressure. Meanwhile, the nanostructure surfaces affect S-L ITRs substantially, such as by modifying the sizes (roughness) and wettability of nanostructure surfaces, although the experimental reports measuring S-L ITRs remain limited. Therefore, it is worth exploring whether it is possible to connect the S-L ITRs of flat and those of nanostructure surfaces, which is beneficial for designing, evaluating, and predicting the S-L ITRs of nanostructure surfaces, and reducing the MD calculations and experimental costs. Predicting the ITRs of nanostructure surfaces and evaluating the ITRs can assist researchers and engineers in quickly estimating the S-L ITRs of nanostructure surfaces to ensure that the S-L ITRs are within a controllable range, and engineers can provide guidance for the safety of microdevices when designing the heat transfer of nanostructure surfaces.

Previous studies in Section 1.1 have primarily concentrated on the impact of wettability, nanostructure sizes, and surface structural geometry on the S-L ITRs. However, the relationship between nanostructure and flat surfaces remains insufficiently explored. Therefore, the present dissertation employs the DDL to evaluate the S-L ITRs of nanostructure surfaces including Wenzel and CB states, and utilizes the TCMs to predict the S-L ITRs of nanostructure surfaces.

The DDL can be measured and extracted experimentally, and the MD results show that the DDL has been used to evaluate the S-L ITR of flat surfaces with different wettability, and can connect the experimental S-L ITRs with the S-L ITRs calculated by MD simulations at the nanoscale. However, DDL remains unclear when evaluating the S-L ITRs of nanostructure surfaces in the Wenzel and CB states.

Thermal circuit models (TCMs) have been widely utilized in macroscopic fields of thermal engineering, with some applications in MD calculations of thermal conductivity. TCMs effectively describe the process of heat transfer by representing thermal resistances as electric resistances. By drawing an analogy to electric circuits, TCMs can simplify and facilitate the analysis of complex energy transfer processes and can predict thermal conductivity and thermal resistance, thereby providing robust support for thermal design. However, the application of TCMs to predict the ITRs of nanostructure surfaces is insufficient. Therefore, the present dissertation proposes various TCMs to explore the potential heat flow paths.

The water models exhibit different molecular structures, such as the three-site SPC/E and one-site CG models. The three-site SPC/E model comprises a rigid body made up of two hydrogen atoms and one oxygen atom. The one-site CG model in the present research is the same as the ML-BOP model of the previous study [16], combining these three atoms into one site. The three-site SPC/E model can describe the molecular behavior,

demonstrating that the density calculated by MD approaches the experimental density at 300 K and the thermal conductivity of the SPC/E model calculated by MD simulations is reasonable. The CG model has the advantage of large-scale MD calculations. It is also essential to assess the performance of the CG and SPC/E models in evaluating and predicting the ITR from an engineering point of view.

The present dissertation aims to evaluate the ITRs of nanostructure surfaces by MD simulations and to predict the ITRs of nanostructure surfaces using TCMs. Additionally, a key objective is to validate whether the coarse-grained (CG) model can serve as a viable alternative to the SPC/E model.

Copper (Cu) recognized as a good heat conductor, water as a widely used heat transfer medium, and graphene coatings with improving heat transfer, hold significant research value in studying S-L heat transfer processes. For instance, MHPs are typically constructed using a Cu-water system, and the incorporation of graphene coatings on the MHPs can enhance the heat transfer performance; the graphene coating and the Cu nanostructure surfaces can improve heat transfer. Previous studies in Section 1.1 have also investigated the Cu-water and graphene coating-water systems to study heat transfer at the nanoscale. Consequently, Cu, water, and graphene are employed in the present dissertation.

1.3 Outline of this dissertation

The present dissertation is organized into seven main chapters, each briefly summarized below.

Chapter 1. The background information, the previous research work, and the significance and purpose of studying S-L ITRs are provided in Chapter 1. The previous research works include the S-L interface, flat and nanostructure surfaces, wettability, thermal circuit models (TCMs), and single-layer graphene coatings. Additionally, the basic structure and a brief introduction to each subsequent chapter are also presented.

Chapter 2. The present chapter describes the basic foundations and calculation methods used in molecular dynamics (MD) simulations. It covers topics such as the energy of MD simulations, solid and liquid force fields, interaction strength parameters, integration algorithms for MD simulations, contact angle measurements, pressure calculations for water, methods for calculating thermal resistances, TCMs, and calculations of density depletion length.

Chapter 3. The ITRs at S-L interfaces are investigated using the non-equilibrium molecular dynamics (NEMD) method with the CG and SPC/E models. The relationship between DDL and ITRs on flat and nanostructure surfaces is described in Chapter 3. The

different interaction strengths between the solid atoms and water molecules, nanopillar widths, and water pressure as the DDL factors are utilized to assess the ITRs calculated by MD simulations in the Wenzel and Cassie-Baxter states. In addition, two ITR definitions of nanostructure surfaces are considered in Cu-water systems.

Chapter 4. The ITRs at S-L interfaces calculated by the NEMD simulations with the CG and SPC/E models are investigated in the Cu-graphene-water systems. The influence of the graphene coating and water models on the S-L ITRs calculated by MD simulations is considered under various wettability conditions, and the relationship between DDL and ITRs on flat and nanostructure surfaces is also investigated in Chapter 4.

Chapter 5. The ITRs predicted by TCMs are compared with the ITRs calculated by NEMD simulations using the CG and SPC/E models in Cu-water systems. The effects of water pressure, nanopillar widths, the water models, and the contact region thickness in the CB state on the relationship between ITRs predicted by TCMs and those calculated by MD simulations are investigated in Cu-water systems. It should be noted that the ITR of nanostructure surfaces is defined between the water near the top nanopillar surface and the groove bottom surface in Chapter 5.

Chapter 6. The present chapter presents the relationships between the ITRs predicted by TCMs and those calculated by NEMD simulations using the CG and SPC/E models in Cu-graphene-water systems. The effects of the defect concentration of the graphene coating, the water models, and the contact region thicknesses in the CB state on the relationship between the ITRs predicted by TCMs and those calculated by MD simulations are investigated in Cu-graphene-water systems. The ITR definition of nanostructure surfaces was the same as in Chapter 5.

Chapter 7. The conclusions of the dissertation are described in the present chapter.

2. Theory and Methodology

The present chapter mainly introduces the main theories and calculation methods of the molecular dynamics (MD) simulation, which includes energy conservation, the main formulas, the force fields with various parameters, the interfacial thermal resistance (ITR) calculation method, thermal circuit models (TCMs), and density depletion length calculation.

2.1 Energy of MD simulation

In classical MD simulations, the total energy (E) in a system consists of the system energy (E_{sys}) and the external energy (E_{bath}), as shown in Eq. (2.1). The system energy (E_{sys}) refers to the kinetic energy (K) and potential energy (U) of particles without outside exchange, which calculated by Eq. (2.2). The external energy (E_{bath}) is added to the system to obtain the temperature gradient in the present study, such as Langevin thermostat in Section 2.3.

$$E_{tot} = E_{sys} + E_{bath} \tag{2.1}$$

$$E_{sys} = K + U \tag{2.2}$$

Under the thermostat bath, the first term on the right side in Eq. (2.3) is the change in energy within the particles. The second term on the right side in Eq. (2.3) is the energy exchanged by the thermostat bath, which is used to compensate for the change in kinetic energy or potential energy of the system. When the thermostat bath transfers energy to the system, the second term is negative, indicating the rate of heat flow into the system; conversely, the system transfers energy to the thermostat bath. In short, the total energy of the system is conserved, indicating that the term on the left side is zero.

$$\frac{dE_{tot}}{dt} = \frac{dE_{sys}}{dt} + \frac{dE_{bath}}{dt} \tag{2.3}$$

The kinetic energy (K) of the N-particles can be calculated by Eq. (2.4a), where m_i and v_i are the mass and the velocity of the i_{th} particle, respectively. K can be used to calculate the temperature of N-particles in Eq. (2.4b). k_B denotes the Boltzmann constant; N is the number of particles.

$$K = \sum_{i}^{N} \frac{1}{2} m_i v_i^2 \tag{2.4a}$$

$$K = \frac{3}{2} k_B N T \tag{2.4b}$$

U in Eq. (2.2) is the potential energy of the interaction between particles, which is usually determined by the properties of the particles. For example, in the SPC/E water molecules, the potential energy is composed of the van der Waals force and Coulomb force, as shown in Section 2.2.

2.2 Force fields and interaction strengths

The embedded atom method (EAM) [43] represents the force fields of metals and alloys with similar accuracy to the density functional theory (DFT). The general equation (2.5) describes the total energy of atom i as follows:

$$E_i = E_\beta\left(\sum_{j\neq i}\rho_\beta(r_{ij})\right) + \frac{1}{2}\sum_{j\neq i}\Phi_{\alpha\beta}(r_{ij}) \tag{2.5}$$

The symbol E_β represents the embedded energy, which is a function associated with the atomic electron density (ρ_β). r_{ij} denotes the distance between atoms i and atoms j, and the $\Phi_{\alpha\beta}$ is the pairwise potential function. The atom i and atom j can be of type α or β. The Cu atoms form the solid walls, with an atomic mass of 63.55 g/mol.

Reactive empirical bond order (REBO) [44] describes the force field of carbon atoms and is employed in the present study. REBO is widely used to calculate functions of covalent bond potential energies and interatomic forces. In the REBO model, the total potential energy is the sum of the pair interactions in the nearest neighbors, which depends on the distance between atoms and the local atomic environment. The functions of parameterized bonds are used to describe chemical pair bonding interactions. The general equation (2.6) is as follows:

$$E = \sum_i \sum_{j\neq i} E_{ij}^{REBO} \tag{2.6}$$

The present study employs two water models including the three-site SPC/E and one-site CG water models, which have different water molecular structures; the CG model in the present study integrates three sites into one site; an SPC/E water molecule has a three-site rigid body consisting of two hydrogen atoms and one oxygen atom. The water models are usually developed with the purpose of various researches. Although researchers are committed to developing water models that describe more accurate thermal properties, the developed water models are still not perfect. The thermal property of bulk water depends on water models. In comparison with experimental results, the SPC/E and CG models can also reproduce some important thermal properties of bulk water[16, 45–48], such as water density, diffusion coefficient, and heat capacity. The CG model is employed in large-scale MD simulations, such as an MD calculation using two million CG water molecules over 230 ns [16]. The consistency of the heat transfer process at S-L interfaces between the one-site CG and three-site SPC/E models is investigated, as well as the feasibility of using the CG model instead of the SPC/E model in ITR research.

The present study utilizes the three-site SPC/E model [49] with the SHAKE algorithm [50] to maintain the hydrogen-oxygen-hydrogen angle at 109.47° and the oxygen-hydrogen bond distance at 0.1 nm. The long-range Coulomb interaction of the SPC/E model is computed using the particle-particle-mesh (P3M or PPPM) method[51]. The

PPPM method is a Fourier-based Ewald summation technique used to calculate the electrostatic potential energy of N-charged particles in the long-range forces. The PPPM method interpolates particles onto a grid and utilizes the Fast Fourier Transform (FFT) algorithm to solve the grid potential by solving the discrete Poisson equation, aiming to reduce computational expenses. The oxygen atoms in each SPC/E water molecule interact through van der Waals forces (ε = 0.006739 eV and σ = 3.166 Å) and long-range forces, which are calculated by Eq. (2.7), and a hydrogen atom in each SPC/E water molecule interacts with the atoms in other SPC/E molecule only through long-range forces, and hydrogen atoms have no direct interaction with Cu and carbon atoms. The charges (qc_i and qc_j) of the oxygen atom and hydrogen atoms are -0.8476 and 0.4238, respectively. The C_{long} represents an energy-conversion constant, and "ϵ" denotes the dielectric constant in Eq. (2.7). "r_c" denotes the cutoff radius, which has the same meaning in Eq. (2.9).

$$E_{ij} = 4\varepsilon[(\frac{\sigma_{ij}}{r_{ij}})^{12} - (\frac{\sigma_{ij}}{r_{ij}})^{6}] + \frac{C_{long} q c_i q c_j}{\epsilon r_{ij}} \qquad r < r_c \qquad (2.7)$$

The CG model [16] developed on the Tersoff-Brenner theory[52] is also utilized for all cases of the present study, which is calculated by Eq. (2.8). The CG model (also called ML-BOP in the previous study [16]) utilizes machine learning to accurately describe the thermodynamic properties of water and ice at the nanoscale. Figure 2.1 depicts the molecular structures of the SPC/E and CG models. Oxygen atoms, hydrogen atoms, and CG water molecules are represented by light-blue, orange, and light-blue, respectively. The cutoff function ($f_C(r)$), repulsive ($f_R(r)$), and attractive ($f_A(r)$) force interactions are shown in Eq. (2.8). The parameters, such as c_{cg}, d_{cg}, θ_0, n_{cg}, β_{cg}, λ_2, B_{cg}, R_{cg}, D_{cg}, λ_1, and A_{cg}, for the CG model are taken from the previous study [16], as shown in Table 2.1.

$$U_{pair} = f_C(r_{ij})[f_R(r_{ij}) + b_{ij} f_A(r_{ij})]$$

$$f_C(r) = \begin{cases} 1, r < R - D_{cg} \\ \frac{1}{2} - \frac{1}{2}\sin(\frac{\pi(r - R_{cg})}{2D_{cg}}), \; R - D_{cg} < r < R + D_{cg} \\ 0, r > R + D_{cg} \end{cases}$$

$$f_R(r) = A_{cg} e^{-\lambda_1 r}; \; f_A(r) = -B_{cg} e^{-\lambda_2 r} \qquad (2.8)$$

$$b_{ij} = (1 + \beta_{cg}^{n} \xi_{ij}^{n})^{-\frac{1}{2n}}$$

$$\xi_{ij} = \sum_{k \neq i,j} f_C(r_{ik}) g(\theta_{ijk}) \exp[\lambda_3^{m_{cg}} (r_{ij} - r_{ik})^{m_{cg}}]$$

$$g(\theta) = \gamma_{cg}(1 + \frac{{c_{cg}}^2}{{d_{cg}}^2} - \frac{{c_{cg}}^2}{{d_{cg}}^2 + (\cos\theta - \cos\theta_0)^2})$$

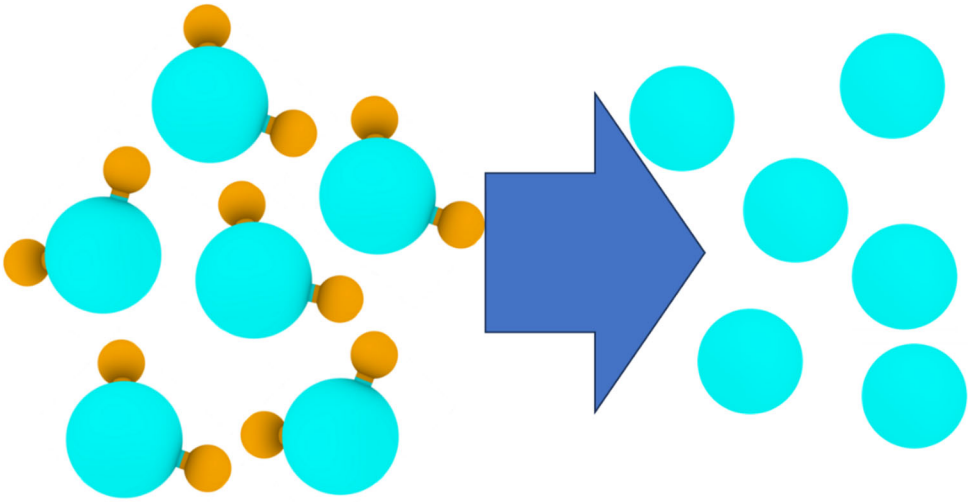

Figure 2.1 The three-site SPC/E and one-site CG water models. The oxygen atom and hydrogen atoms in each SPC/E molecule, and CG water molecules are represented by light-blue, orange, and light-blue, respectively.

Table 2.1 Various parameters of the CG (ML-BOP) model [16].

m_{cg}	1	β_{cg}	0.000001
γ_{cg}	1	λ_2 (Å^{-1})	2.19964
λ_3 (Å^{-1})	0	B_{cg} (eV)	473.621419
c_{cg}	77638.53435	R_{cg} (Å)	3.282761
d_{cg}	16.148387	D_{cg} (Å)	0.270511
θ_0 (rads)	2.06125325	λ_1 (Å^{-1})	2.750522
n_{cg}	0.770018	A_{cg} (eV)	1684.301476

Lennard-Jones (L-J) potential function in Eq. (2.9) is used to describe the interaction between two types of particles, as shown in Figure 2.2, such as water-Cu and water-graphene. The parameters of σ and ε between water molecules (such as oxygen atoms in SPC/E water molecules) and Cu walls are used in Eq. (2.9) based on the Lorentz-Berthelot combining rule, which refers to the previous report [53]. The parameter "α" is a coefficient used to modify the interaction strength between two distinct types of particles, to keep a similar wettability in MD research and experiments, as shown in Figure 2.3. The L-J function (12-6) is well verified to apply for the S-L interactions between water and Cu surfaces [54, 55]. When using the L-J function, the related ITRs in the present study can reproduce those of the previous studies [13, 22, 56] in the MD simulations and experiments. The parameters between Cu and carbon atoms are taken from previous research [53]. To reduce the MD simulation costs, a cutoff (r_c) radius is typically used, beyond which particle interactions are considered to be almost zero and can be ignored.

The interacting particles are within the cutoff radius to form a particle's neighbor list. The r_c of L-J and Coulomb forces in all cases is 0.9 nm.

$$U_{ij} = 4\alpha\varepsilon_{ij}\left\{\left(\frac{\sigma_{ij}}{r_{ij}}\right)^{12} - \left(\frac{\sigma_{ij}}{r_{ij}}\right)^{6}\right\};\ \varepsilon_{ij} = \sqrt{\varepsilon_i \cdot \varepsilon_j};\ \sigma_{ij} = \frac{\sigma_i + \sigma_j}{2} \qquad r < r_c \tag{2.9}$$

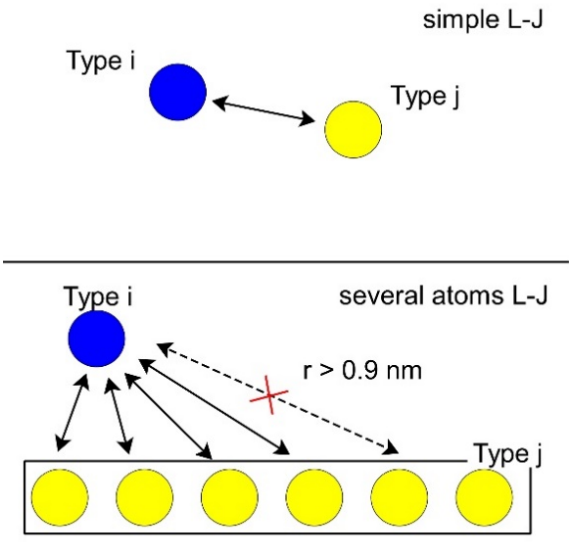

Figure 2.2 The L-J interaction between two different types of particles. The dark blue and yellow are used to represent the particles of types i and j, respectively. The top shows that the L-J interaction between the particles of type i and type j is pairwise. The bottom shows that L-J interactions are ignored when the distance between the particles of type i and j is too far (such as the red cross).

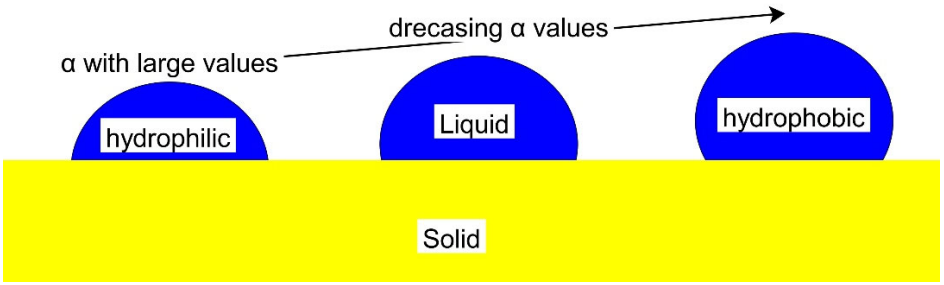

Figure 2.3 Wettability and the parameter "α". The parameter of "α" is often employed to describe various wettability in the MD simulations. For example, the wettability of water on a Cu surface in the present study (hydrophilic state, CA1) is similar to that in the experiment [21].

2.3 Langevin thermostat

The Langevin thermostat is a method used to keep the solid temperature at a constant temperature by either exporting or importing energy, which is calculated by Eq. (2.10). The Langevin thermostat is an infinite heat thermostat that exchanges energy between particles and exports it or adds it to the system energy to monitor energy conservation.

$$\begin{aligned} F &= F_c + F_f + F_\tau \\ F_f &= -\frac{m \cdot v}{damp} \\ F_\tau &\propto \sqrt{-\frac{k_B T \cdot m}{\Delta t \cdot damp}} \end{aligned} \tag{2.10}$$

In Eq. (2.10), F_c represents a conservative force term derived from the interactions between particles. F_f and F_τ represent the forces acting on each atom, where F_f denotes frictional resistance or viscous damping, which is proportional to the velocity of the particles. F_τ refers to the force generated by the random collision between atoms and particles at temperature (T). The temperature (T) denotes the setting temperature, "m" represents the mass of an atom, "damp" denotes the damping factor (custom coefficient), and Δt refers to the interval time.

2.4 Second Newton's law and integration algorithms

Atoms and molecules are assumed to be regarded as classical particles in MD simulations. Therefore, Newton's second law is applicable and it is used to calculate the motion of particles.

$$\vec{F}_i = m_i \frac{d^2 \vec{r}_i}{dt^2} \tag{2.11}$$

In Eq. (2.11), $\vec{r}_i$ and m_i represent the position with vector (→) and the mass of the i_{th} particle, respectively. The equation (2.11) is also applicable to particle systems but only for pairwise calculations. For example, when the j_{th} particle exerts a force on the i_{th} particle, the force equation is modified, as shown in Eq. (2.12).

$$\vec{F}_{ij} = -\frac{\partial U(r_{ij})}{\partial r_{ij}} \frac{\vec{r}_{ij}}{r_{ij}};\ \vec{r}_{ij} = \vec{r}_i - \vec{r}_j \tag{2.12}$$

U denotes a pairwise potential function that depends on the distance (r_{ij}) between particle i_{th} and j_{th} during the interval time Δt.

The reversible reference system propagation algorithm (r-RESPA)[57, 58] is a time-stepping algorithm and is based on the Trotter expansion of the classical Liouville propagator, as shown in Eq. (2.13), where the "L" is the Liouville operator for a system, $\Gamma = \{q_j, p_j\}$ refers to the phase space [57, 58], q_j and p_j are the conjugate momentum and

position, respectively. F_j denotes the force on the j_{th} particle, and the Poisson bracket is denoted by {..., ...}. The "H" corresponds to a Hermitian operator and also refers to the Hamiltonian. The r-RESPA algorithm is designed for the forces under different time scales, using a smaller time step to process rapidly changing forces and a larger time step to process slowly changing forces. For example, in the case of the two-layer nested r-RESPA algorithm, the "L" can be divided into "L_{fst}" and "L_{slw}" in Eq. (2.14), which corresponds to the cases of the fast force and the slow force, respectively. When applying the Trotter-Suzuki formula, Eq. (2.15) is obtained, and "int" denotes a positive integer; in the cases of Chapter 3, Δt is 2.0 fs, and "int" is 4, which indicates that the Δt/int is 0.5 fs for the calculations of bonds and angles.

$$jL = \{\cdots, H\} = \sum_j \left[\dot{q}_j \frac{\partial}{\partial q_j} + F_j \frac{\partial}{p_j}\right];\ \Gamma(\Delta t) = e^{jL\Delta t}\Gamma(0) \tag{2.13}$$

$$L = L_{slw} + L_{fst} \tag{2.14}$$

$$\Gamma(\Delta t) \approx e^{j\cdot 0.5\Delta t}\left(e^{jL_{fst}\frac{\Delta t}{int}}\right)^{int} e^{j\cdot L_{slw}\cdot 0.5\Delta t}\Gamma(0) + O(\Delta t^3) \tag{2.15}$$

The Velocity-Verlet algorithm is calculated by Eq. (2.16). The r-RESPA algorithm is primarily designed to reduce computational costs in MD simulation, while the Velocity-Verlet algorithm is a common and classic approach. Essentially, these algorithms provide solutions for numerical integration.

$$\begin{aligned} \vec{r}_i(t+\Delta t) &= \vec{r}_i(t) + \Delta t\vec{v}_i(t) + \frac{\Delta t^2}{2m_i}\vec{F}_i(t) + O(\Delta t^4) \\ \vec{v}_i(t+\Delta t) &= \vec{v}_i(t) + \frac{\Delta t}{2m_i}(\vec{F}_i(t) + \vec{F}_i(t+\Delta t)) + O(\Delta t^2) \end{aligned} \tag{2.16}$$

In Chapter 3, the interval time step (Δt) with the r-RESPA method for the SPC/E and CG models is 2.0 fs for the interactions such as the interactions between Cu atoms using the EAM potential. In Chapter 4, the Velocity-Verlet algorithm is employed with the interval time timestep of 1.0 fs for all cases.

2.5 Contact angle measurement

In the MD measurement of the contact angle (CA), a simulation box with a narrow size in the y-direction is used in the present study, so that the liquid can form a circular column on a flat surface with the top of the column in the x-z plane, such as in Figure 2.4. The values of CA are calculated using a similar method as the reference [59] in the x-z plane. In Chapter 3, measuring CAs is conducted to simulate hydrophilic (CA1) and hydrophobic states (CA2) by adjusting the interaction strength parameter "α". The calculation scheme for measuring the CAs on Cu surfaces, such as the CA1 case, is shown in Figure 2.4.

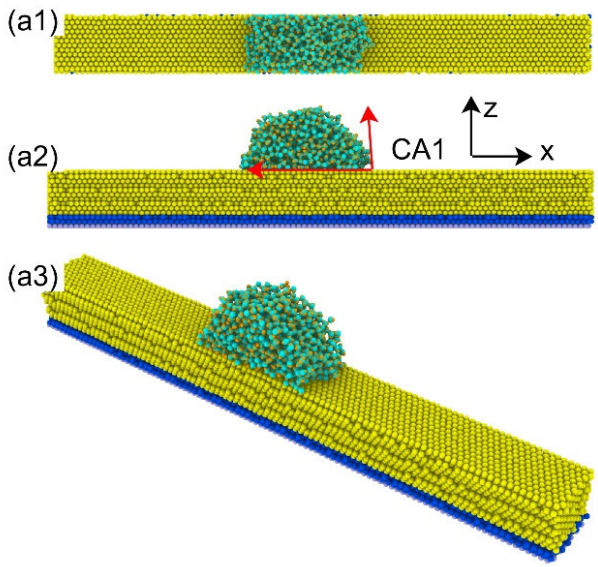

Figure 2.4 The CAs of water columns on Cu surfaces at 300 K. The yellow, dark blue, light-purple, light-blue, and orange correspond to the Cu layers, Langevin layers of Cu atoms, fixed Cu layers, oxygen atoms or CG water molecules, and hydrogen atoms just in the SPC/E model.

Two types of water column CAs are employed: CA1 for a hydrophilic state with a strong interaction strength (around 83.84˚ for the CG water model and 84.75˚ for the SPC/E water model) and CA2 for a hydrophobic state with a weak interaction strength (around 112.14˚ for CG water and 113.83˚ for SPC/E water). The relationship between CAs and the parameter "α" is shown in Figure 2.5. The interaction strength parameters "α" for the interactions between water and Cu are presented in Table 2.2. The calculated contact angle in the CA1 cases in the present dissertation has similarities with the values in a simulation [53] and experimental results [21] on Cu surfaces with the lattice orientation (111).

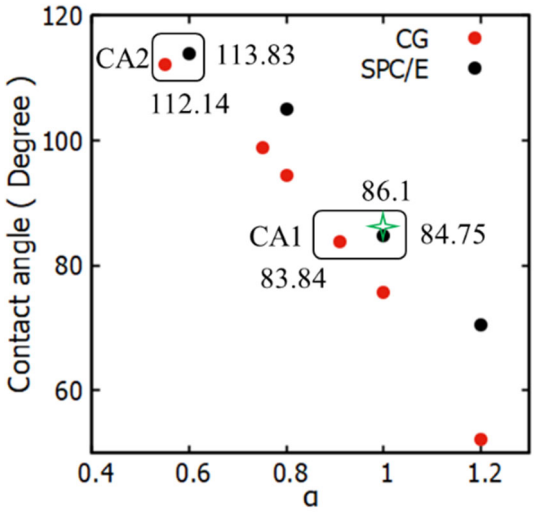

Figure 2.5 Contact angles of the water molecules on flat surfaces (bare Cu surface) at 300 K. The square regions are the CAs that are employed in the present dissertation. The experimental CA value of water on the Cu surface is 86.1˚, as marked by the green star.

The way to measure contact angles in Chapter 4 is the same as that in Chapter 3. There are four types of interaction strengths between liquid and solid (considering Cu and graphene). The first number and second number after "CA", such as CA12, represent the wettability of water on a Cu surface and that on a graphene surface, respectively. The numbers "1" and "2" after "CA" represent the wettability of water on a solid surface as the hydrophilic and hydrophobic state, respectively. For example, CA21 represents that the wettability of water on a Cu surface is in the hydrophobic state and that on a graphene surface is in the hydrophilic state.

Figure 2.6 shows the calculation models for measuring the CAs on the pristine and defective graphene coating. The interaction strength parameters "α" between the CG molecule and carbon, and that between the SPC/E molecule (oxygen) and carbon are shown in Table 2.2. The "a1" to "a4" of Table 2.2 corresponds to "a1" to "a4" in Figure 2.6 (a1 to a4). The parameters of "ε" and "σ" are related to Eq. (2.7) and Eq. (2.9). The calculated CA11 on pristine graphene-Cu surfaces in the present research is similar to the experimental result [21]. The related CA values are influenced by measurement methods and simulation conditions.

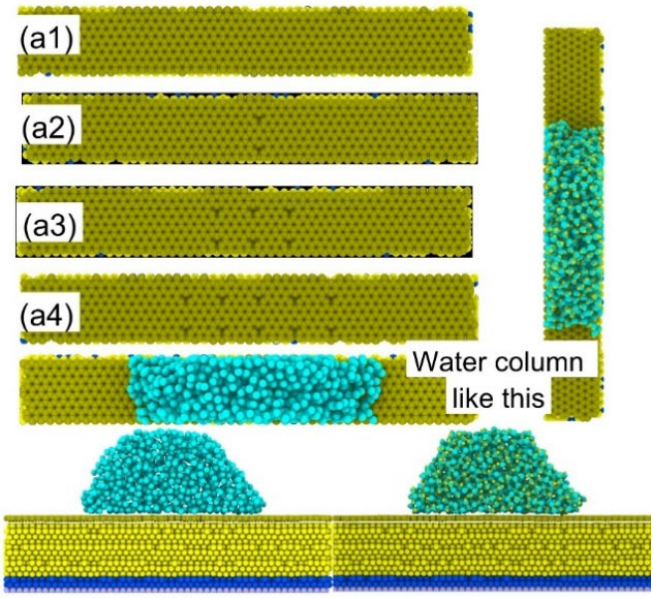

Figure 2.6 The CAs of water columns on pristine and defective graphene-Cu surfaces at 300 K. The grey, yellow, dark blue, light-purple, light-blue, and orange correspond to the graphene, Cu layers, Langevin layers of Cu atoms, fixed Cu layers, Oxygen atoms or CG water molecules, and hydrogen atoms just in the SPC/E model.

Table 2.2 Interactions and CAs of pairs among water, Cu, and graphene.

	α·ε (eV)	σ(Å)	CA	systems
SPC/E-Cu-CA1	0.0115×1.00	2.75	84.6°	Cu-water
SPC/E-Cu-CA2	0.0115×0.60		113.8°	
CG-Cu-CA1	0.0115×0.91		83.6°	
CG-Cu-CA2	0.0115×0.55		112.1°	
SPC/E-CA11-a1	0.00412×1.12	3.19	87.8°	Cu-graphene-water
SPC/E-CA11-a2			89.2°	
SPC/E-CA11-a3			87.1°	
SPC/E-CA11-a4			84.5°	
SPC/E-CA12-a1	0.00412×0.75		112.1°	
SPC/E-CA12-a2			116.4°	
SPC/E-CA12-a3			115.6°	
SPC/E-CA12-a4			113.4°	
SPC/E-CA21-a1	0.00412×1.12		90.2°	
SPC/E-CA21-a2			84.8°	
SPC/E-CA21-a3			90.6°	
SPC/E-CA21-a4			88.8°	
SPC/E-CA22-a1	0.00412×0.75		114.7°	
SPC/E-CA22-a2			116.3°	
SPC/E-CA22-a3			116.0°	
SPC/E-CA22-a4			113.0°	
CG-CA11-a1	0.00412×1.00		87.3°	
CG-CA11-a2			87.3°	
CG-CA11-a3			88.2°	
CG-CA11-a4			88.2°	
CG-CA12-a1	0.00412×0.60		112.3°	
CG-CA12-a2			113.7°	
CG-CA12-a3			112.3°	
CG-CA12-a4			111.1°	
CG-CA21-a1	0.00412×1.00		88.2°	
CG-CA21-a2			86.4°	
CG-CA21-a3			89.1°	
CG-CA21-a4			87.3°	
CG-CA22-a1	0.00412×0.60		114.5°	
CG-CA22-a2			112.3°	
CG-CA22-a3			110.4°	
CG-CA22-a4			115.2°	

The molecular weight of CG and SPC/E water molecules is 18.0153 g/mol. The SPC/E water molecule consists of oxygen with a molecular weight of 15.9994 g/mol and hydrogen with a molecular weight of 1.0008 g/mol. The carbon atom in graphene has molecular weights of 12.0107 g/mol.

2.6 Pressure calculation

The method of stress per atom is useful for calculating water pressure [18] for the CG and SPC/E water molecules in the central region of the simulation system. For example, the position of around 5.7 nm to 6.2 nm in the z-direction is employed in Chapter 3. There are 9 tensors to calculate stress, such as xx, xy, xz, yx, yy, yz, zx, zy, and zz. In Eq. (2.17), "a" and "b" in each atom represent the direction x, y, or z of the tensor, the first term ($-mv_a v_b$) represents the kinetic energy contribution of a particle, such as -$mv_X v_X$. The second, third, and fourth terms are a virial contribution consisting of pairwise, bond, and angle contributions. The fifth term also contributes to pressure calculations of SPC/E water from long-range Coulomb interactions [60]. "r_1" and "r_2" are the positions of particles in the pairwise interaction in the second term (N_p) or those of the related bond in the third term (N_b). The "F_1" and F_2 represent the pairwise interaction forces between two atoms in the second term or the forces between the related bond in the third term. " F_1, F_2, F_3" and "r_1, r_2, r_3" in the fourth term correspond to the forces and positions of an angle such as in the SPC/E model, respectively. "r_{ia}" and "F_{ib}" in the fifth term are related to factors in the contribution of the long-range Coulomb forces. The subscript of "N" indicates the number of the corresponding interactions, such as the bond ("b") and the angle ("a"). "n" is the number of looping over the related neighbors (N) of one particle, bond, or angle.

To convert stress into water pressure, the P_{tot} is employed in Eq. (2.18). The average stress value in the x-direction (S_{XX}), y-direction (S_{YY}), and z-direction (S_{ZZ}) for each particle in the equal volume (vol) is divided by the volume (vol) to obtain the total pressure P_{tot}.

$$S_{ab} = -mv_a v_b - \left(\frac{1}{2}\sum_{n=1}^{N_p}(r_{1a}F_{1b} + r_{2a}F_{2b}) + \frac{1}{2}\sum_{n=1}^{N_b}(r_{1a}F_{1b} + r_{2a}F_{2b}) + \right.$$
$$\left. \frac{1}{3}\sum_{n=1}^{N_a}(r_{1a}F_{1b} + r_{2a}F_{2b} + r_{3a}F_{3b}) + \mathrm{Kspace}(r_{ia}, F_{ib})\right) \quad (2.17)$$

$$P_{tot} = \frac{\overline{(S_{xx} + S_{yy} + S_{zz})}}{vol} \quad (2.18)$$

2.7 Calculation method of thermal resistances on a flat surface

The present section introduces the calculation of thermal resistances, such as the rate of heat flux. In Eq. (2.19), E^{hot} and E^{cold} are the cumulative energy subtracted from the cold heat source and added to the hot heat source, controlled by the Langevin method during the related simulation time (t), respectively. Figure 2.7 shows a case of flat surfaces with initial simulation box sizes. The L_X, L_Y, and L_Z refer to the length of simulation box sizes in the x-direction, the y-direction, and the z-direction, respectively.

$$Q = \frac{E^{hot} - E^{cold}}{2t};\ q = \frac{Q}{A_{flat}} \tag{2.19}$$

The A_{flat} (=$L_X \cdot L_Y$) is the area of the calculation domain in the x-y plane. The heat flow rate (Q) is the average of E^{hot} and E^{cold} per unit of time. The heat flux (q) is equal to the Q divided by A_{flat}.

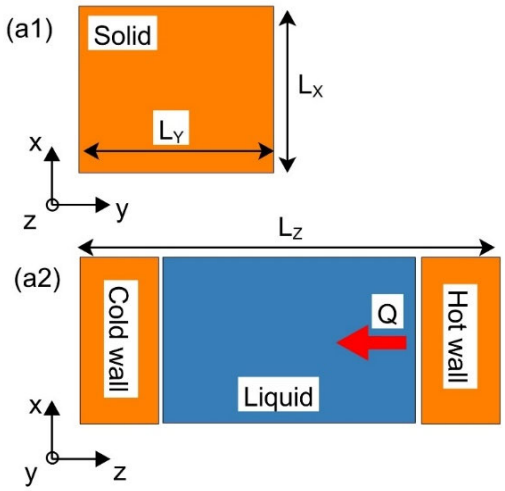

Figure 2.7 A system size of a flat surface. (a1) and (a2) show the sizes (L_X and L_Y) in the x-y plane of the system and the system size (L_Z) along the z-direction, respectively.

The ITR (unit: $m^2 \cdot K/W$) of flat surfaces between the liquid and cold walls is calculated by Eq. (2.20a), where the ΔT represents the temperature jump at the S-L interface of a flat surface. The ITR in the Cu-water system is defined between Cu and water, while that in the Cu-graphene-water system is defined between graphene and water. The internal thermal resistance (TR, unit: $m^2 \cdot K/W$) of the liquid and solid region is calculated using Eq. (2.20b), where ΔT is the temperature difference, such as that of the water. The thermal resistance (R, unit: K/W) between the liquid and cold wall surface is calculated by Eq. (2.21) and it is used to apply to TCMs. It should be noted that the thermal resistances in the present dissertation are distinguished by ITR and R due to different units.

$$ITR = \frac{\Delta T}{q} \tag{2.20a}$$

$$TR = \frac{\Delta T}{q} \tag{2.20b}$$

$$R = \frac{\Delta T}{Q} \tag{2.21}$$

2.8 Thermal circuit models

2.8.1 Simple serial and parallel networks of thermal resistances

Figure 2.8 shows a simple TCM diagram that includes serial and parallel networks. The Kirchhoff circuit law in electrical circuits is a classic solution applied to heat transfer fields in the TCMs. The rate of heat flow (Q) is analogous to electric current, and the temperature difference (T_H minus T_C) is analogous to the voltage difference. From this perspective, the thermal resistance of heat transfer is series and consists of R_{AS} and R_{BS} in Figure 2.8 (AB), which can be calculated by Eq. (2.22).

$$Q = \frac{T_H - T_C}{R} = \frac{T_H - T_C}{R_{AS} + R_{BS}} \tag{2.22}$$

The thermal resistance of heat transfer is parallel, consisting of R_C and R_D, as shown in Figure 2.8 (CD), and can be calculated by Eq. (2.23). The TCMs are usually applied to macroscale cases, such as the fin design[61] in engineering.

$$Q = Q_C + Q_D;\ \frac{1}{R} = \frac{1}{R_C} + \frac{1}{R_D} \tag{2.23}$$

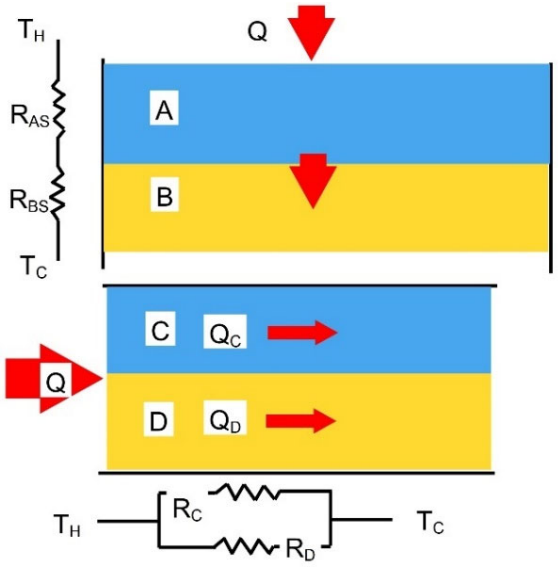

Figure 2.8 Simple serial and parallel thermal resistances using the TCM scheme.

2.8.2 TCMs over S-L interfaces in a Cu-water system

Figure 2.9 (a1) describes the temperature jump at the solid (green)-liquid (red) interface on a flat surface. Figure 2.9 (a2) shows an example of a flat surface divided into two regions (A_1 and A_2) in the x-y plane. Figure 2.9 (a3) illustrates the local thermal resistances on a nanostructure surface.

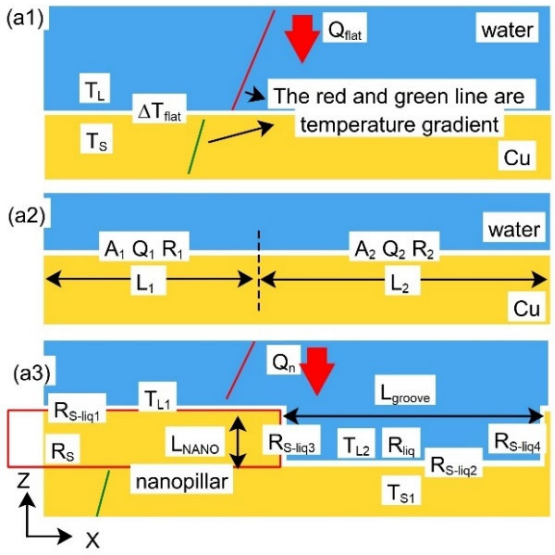

Figure 2.9 Flat and nanostructure surfaces for calculating thermal resistances. Q_{flat} and Q_n refer to the heat flow rate of flat surfaces and that of nanostructure surfaces, respectively.

The T_L and T_S in Figure 2.9 (a1) denote the temperatures of water and the solid surface at the S-L interface, respectively. A fitting curve is obtained by fitting the temperature gradient of the water to obtain the water temperature (T_L) near the solid walls. Another fitting curve is obtained by fitting the temperature gradient of the solid walls to obtain the solid temperature (T_S) at the S-L interface. The temperature jump (ΔT_{flat}) in Eq. (2.24) is calculated by using T_L and T_S. Q_{flat} in Eq. (2.25) denotes the rate of heat flow on a flat surface, and the heat flux (q_{flat}) is equal to the Q_{flat} divided by A_{flat}. The ITR_{flat} in Eq. (2.26) is equal to the R_{flat} multiplied by A_{flat}.

$$\Delta T_{flat} = T_L - T_S \tag{2.24}$$

$$R_{flat} = \frac{\Delta T_{flat}}{Q_{flat}} \tag{2.25}$$

$$ITR_{flat} = R_{flat} \cdot A_{flat} \tag{2.26}$$

The regions A_1 and A_2 in Figure 2.9 (a2) correspond to the heat flow rates (Q_1) with thermal resistance (R_{f1}) and heat flow rates (Q_2) with thermal resistance (R_{f2}), respectively. L_1 and L_2 in the x-direction are related to the length of regions A_1 (=$L_1 \cdot L_Y$) and A_2 (=$L_2 \cdot L_Y$). L_X is the sum of L_1 and L_2 in Eq. (2.27). A_{flat} in Eq. (2.28) was the sum of A_1 and A_2. Q_{flat} in Eq. (2.29) is the sum of Q_1 and Q_2.

$$L_X = L_1 + L_2 \tag{2.27}$$

$$A_{flat} = A_1 + A_2 \quad (2.28)$$

$$Q_{flat} = Q_1 + Q_2 \quad (2.29)$$

The R_{f1} and R_{f2} are calculated by Eq. (2.30). Q_1 and Q_2 in Eq. (2.31) denote the rates of local heat flow. The equivalent thermal resistance ($R_{eq\text{-}12}$) consisting of the thermal resistances (R_{f1} and R_{f2}) is described by Eq. (2.32), and the $R_{eq\text{-}12}$ is still equal to the R_{flat}, where the symbol '‖' denotes the parallel thermal resistance. Therefore, the local thermal resistance can be effectively applied to the thermal resistance at S-L interfaces.

$$R_{f1} = \frac{\Delta T_{flat}}{Q_1}; R_{f2} = \frac{\Delta T_{flat}}{Q_2} \quad (2.30)$$

$$Q_1 = Q_{flat}\frac{A_1}{A_{flat}};\ Q_2 = Q_{flat}\frac{A_2}{A_{flat}} \quad (2.31)$$

$$R_{eq-12} = (R_{f1} \parallel R_{f2}) = \left({R_{f1}}^{-1} + {R_{f2}}^{-1}\right)^{-1} = R_{flat} = \frac{\Delta T_{flat}}{Q} \quad (2.32)$$

Before establishing TCMs, it is still necessary to consider converting the thermal resistance (R) of a flat surface to that of a nanostructure surface. A nanostructure surface consists of a flat surface and a nanopillar in the present study. Figure 2.9 (a3) shows the local R of a nanostructure surface, including the local S-L R, the internal thermal resistance (TR) of the liquid, and the TR of the nanopillar. In Eq. (2.33), Eq. (2.34), and Eq. (2.35), L_{Cu}, L_{groove}, and L_{NANO} represent the thickness of the nanopillar along the z-direction, the width of the groove in the x-direction, and the thickness of penetration water in the groove in the z-direction, respectively. The A_{np} and A_{ng} in Eq. (2.33) refer to the area of the top nanopillar surface and that of the groove bottom surface, respectively. The R_{Cu} and R_{liq} represent the internal thermal resistances of the nanopillar and that of the water in the groove, respectively, and are calculated by Eq. (2.34) and Eq. (2.35) based on the analogy of the classical Fourier law, where the thermal conductivities ($k_{Cu\text{-}MD}$ and $k_{liq\text{-}MD}$) from MD simulations are calculated by classic Fourier's Law on flat surfaces, and those ($k_{Cu\text{-}exp}$ and $k_{liq\text{-}exp}$) of the experimental (empirical) values are also employed as shown in Table 2.3.

$$A_{np}=((L_X - L_{groove}) \cdot L_Y);\ A_{ng}=L_{groove} \cdot L_Y \quad (2.33)$$

$$R_{Cu} = \frac{L_{Cu}}{k_{Cu-MD} \cdot A_{np}};\ R_{liq} = \frac{L_{NANO}}{k_{liq-MD} \cdot A_{ng}} \quad (2.34)$$

$$R_{Cu} = \frac{L_{Cu}}{k_{Cu-exp} \cdot A_{np}};\ R_{liq} = \frac{L_{NANO}}{k_{liq-exp} \cdot A_{ng}} \quad (2.35)$$

$$R_{S-liq*} = \frac{A_{flat}}{A_*}R_{flat} = \frac{L_X}{L_*}R_{flat};\ \text{S refers to Cu, graphene;}\ *\in 1,2,\cdots \quad (2.36)$$

$R_{S\text{-}liq1}$ represents the thermal resistance between the top nanopillar surface and water, and $R_{S\text{-}liq2}$ refers to the thermal resistance between the groove bottom surface and water, which

are calculated by Eq. (2.36). $R_{S\text{-}liq3}$ and $R_{S\text{-}liq4}$ denote the thermal resistance between the nanopillar sidewall surface and water, calculated by Eq. (2.36). L_* and A_* refer to the size in the x direction and the area for local nanostructure surfaces corresponding to the calculation of the local thermal resistance in the present study. In summary, the local thermal resistance ($R_{S\text{-}liq*}$) on a nanostructure surface is equal to the local thermal resistance on a flat surface under a similar area. The detailed values of the $R_{S\text{-}liq1}$ and R_{Cu}, R_{liq}, $R_{S\text{-}liq2}$, $R_{S\text{-}liq3}$, and $R_{S\text{-}liq4}$ are shown in Table S5.1 and Figures S5.1 to S5.12 of the Appendix.

Table 2.3 The thermal conductivity of water and Cu on flat surfaces. The $k_{liq\text{-}MD}$ of water and the $k_{Cu\text{-}MD}$ of Cu are calculated using MD simulations. The $k_{liq\text{-}exp}$ of water and the $k_{Cu\text{-}exp}$ of the bulk Cu are taken from the open database [62] and the previous report[63], respectively. The units of k_{MD} and k_{exp} are W/(m·K).

Items	$k_{Cu\text{-}liq}$	$k_{Cu\text{-}MD}$	$k_{liq\text{-}exp}$	$k_{Cu\text{-}exp}$
CA1-CG-P1	0.43	3.26	0.62	406
CA1-CG-P2	0.44	2.31	0.59	
CA1-CG-P3	0.39	6.16	0.56	
CA2-CG-P1	0.44	3.84	0.63	
CA2-CG-P2	0.42	2.43	0.60	
CA2-CG-P3	0.39	3.15	0.58	
CA1-SPC/E-P1	0.90	2.76	0.63	
CA1-SPC/E-P2	0.84	2.65	0.59	
CA1-SPC/E-P3	0.83	2.62	0.56	
CA2-SPC/E-P1	1.00	2.80	0.64	
CA2-SPC/E-P2	0.83	2.31	0.60	
CA2-SPC/E-P3	0.85	2.88	0.59	

The thermal conductivity of the solid is affected by the thickness at the nanometer scale, but S-L ITRs are almost independent of the solid thickness [64, 65]. The thermal conductivity calculated by MD is reasonable compared to the previous studies[66, 67].
Figure 2.10 shows TCM diagrams on a nanostructure surface. The TCMs in the present study are also developed from Kirchhoff circuit laws. Models A and B are simple TCMs, which assume that heat flow is just along the z-direction and acts on the surfaces in the x-y plane, which also indicates that there is no energy transfer between water and nanopillar sidewalls. Models C and D are developed on the assumption that the temperature of the nanopillar sidewalls and groove bottom surfaces is basically constant. The 2D temperature distribution in Figures S5.17 to S5.22 of the Appendix shows that the temperature of the nanopillar sidewalls is almost similar to that of the groove bottom surface. Models E and F are more complex heat transfers based on the possibility of actual heat transport, indicating that there are different temperatures in the nanopillar sidewalls,

the top nanopillar surface, and the groove bottom surface, which are similar to an unbalanced Wheatstone bridge [68]. In models E and F, the heat transfer between the water and the nanopillar sidewalls, that between the water and the groove bottom surfaces, and that between the top nanopillar surface and water are different. Models A, C, and E employ the thermal conductivities of liquid and solid calculated by MD simulations, and models B, D, and F utilize the experimental (empirical) thermal conductivities of solid and liquid. R_S has the same meaning as R_{Cu} but includes external thermal resistances in Section 2.8.3.

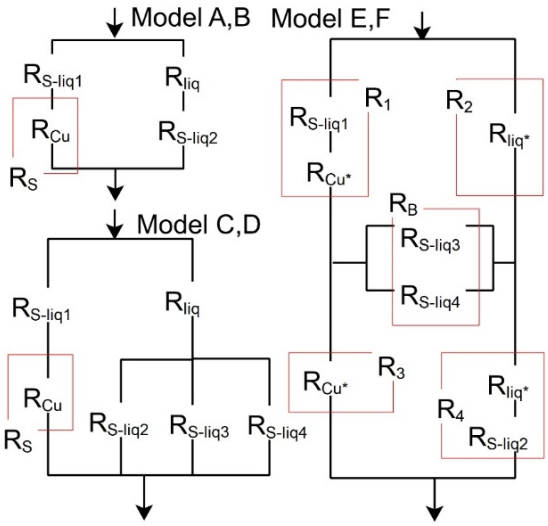

Figure 2.10 TCM schemes on a nanostructure surface.

After establishing the TCMs, it is necessary to calculate the equivalent thermal resistance ($R_{eq\text{-}}$) of each model for obtaining the ITRs. In models A and B, the left and right heat transfer paths are composed of $R_{S\text{-}liq1}$ and R_S, $R_{S\text{-}liq2}$ and R_{liq}, respectively. The equivalent thermal resistances ($R_{eq\text{-}A}$ and $R_{eq\text{-}B}$) of models A and B can be obtained by Eq. (2.37), and it should be emphasized that the symbol '‖' refers to the parallel thermal resistance calculated like Eq. (2.32). $R_{eq\text{-}A,B}$ denotes $R_{eq\text{-}A}$ and $R_{eq\text{-}B}$. The difference between models A and B is that the former uses the thermal conductivity of water and solids calculated by MD simulations, while the latter utilizes the experimental (empirical) thermal conductivity of solids and water.

$$R_{eq-A,B} = \left(R_{S-liq1} + R_S\right) \parallel \left(R_{S-liq2} + R_{liq}\right) \tag{2.37}$$

In models C and D, the left path of heat transfer is composed of $R_{S\text{-}liq1}$ and R_S. The right path of heat transfer includes R_{liq} and the parallel thermal resistance of $R_{S\text{-}liq2}$, $R_{S\text{-}liq3}$, and $R_{S\text{-}liq4}$. The equivalent thermal resistances ($R_{eq\text{-}C}$ and $R_{eq\text{-}D}$) in models C and D can be obtained using Eq. (2.38), where $R_{eq\text{-}C,D}$ refers to $R_{eq\text{-}C}$ and $R_{eq\text{-}D}$. The difference between models C and D is that the former uses the thermal conductivities of solids and water

calculated by MD simulations, while the latter utilizes the experimental and empirical thermal conductivities of solids and water.

$$R_{eq-C,D} = \left(R_{S-liq1} + R_S\right) \parallel \left(R_{S-liq2} \parallel R_{S-liq3} \parallel R_{S-liq4} + R_{liq}\right) \quad (2.38)$$

In models E and F, the paths of heat transfer are composed of R_1, R_2, R_3, R_4, and R_B. $R_{eq-E,F}$ refers to R_{eq-E} and R_{eq-F}. The R_1 is comprised of R_{S-liq1} and R_{Cu*}; R_2 is the same as the R_{liq*} just in Cu-water systems; R_3 is the same as the R_{Cu*} just in Cu-water systems; R_4 is comprised of R_{S-liq2} and R_{liq*}; R_{Cu} (R_{Cu}=2R_{Cu*}) is assumed to be evenly distributed to R_1 and R_3 according to the nanopillar thickness. R_{liq*} (R_{liq}=2R_{liq*}) is also assumed to be evenly distributed to R_2 and R_4 according to the water thickness in the groove. R_B denotes the parallel thermal resistance of R_{S-liq3} and R_{S-liq4}. The equivalent thermal resistances (R_{eq-E} and R_{eq-F}) in models E and F can be calculated by Eq. (2.39) and are the same as a solution for an unbalanced Wheatstone bridge[68]. The main difference between models E and F is that the former uses the thermal conductivity of water and solids calculated by MD simulations, while the latter utilizes the experimental (empirical) thermal conductivity of water and solids.

$$R_{eq-E,F} = (R_1 + R_3) \parallel (R_2 + R_4) \frac{1 + \frac{R_1 \parallel R_3 + R_2 \parallel R_4}{R_B}}{1 + \frac{(R_1 + R_2) \parallel (R_3 + R_4)}{R_B}} \quad (2.39)$$

In the present study, two CB states are defined to predict ITR, including the general and actual CB states. The general CB state indicates that the liquid water almost does not penetrate grooves [39]. The penetration of water in the groove is not ignored in the field of heat transfer as defined by the actual CB state. In the general CB state, the values of R_{S-liq2} in models A to F are cut off, which are almost infinite, indicating that there is no energy transfer on the groove bottom surface and liquid. The A_{flat} multiplied by R_{eq-A} to R_{eq-F} is defined to obtain the ITR_{Model}. The ITR_{Model} corresponds to the equivalent ITRs on a nanostructure surface used for predicting six TCMs.

2.8.3 TCMs on a composite surface

Thermal circuit models (TCMs) of the composite surface are built on those of Cu-water systems. The composite surface has the same meaning as the Cu-graphene-water system in the present dissertation. Figure 2.11 (a1) shows that the Cu surface is covered with the graphene coating, and the temperature jump (ΔT_{flat}) is defined between the water and the graphene coating. T_S and T_L in Figure 2.11 (a1) denote the temperatures of the graphene coating and the liquid close to the graphene coating, respectively. The Q_{flat} refers to the heat flow rate on the composite surface. Q_n denotes the heat flow rate on a nanostructure surface, as shown in Figure 2.11 (a2).

The R_{S-liq1} and R_{S-liq2} describe the local thermal resistances between the graphene and the liquid, and those between the groove bottom surface and the water, respectively. R_{S-liq3}

and $R_{S\text{-}liq4}$ denote the local thermal resistances between the nanopillar sidewall of Cu and the water. $R_{S\text{-}liq5}$ and $R_{S\text{-}liq6}$ refer to the local thermal resistances between the graphene coating in the y-z plane and the water. R_S includes $R_{S\text{-}g}$, $R_{g\text{-}g}$, and R_{Cu}. $R_{g\text{-}g}$ and $R_{S\text{-}g}$ are shown in the next paragraph. The $R_{S\text{-}liq1}$ to $R_{S\text{-}liq6}$ are also calculated by $R_{S\text{-}liq*}$ of Eq. (2.36), and the area of $R_{S\text{-}liq5}$ and $R_{S\text{-}liq6}$ are $L_{g\text{-}g}\cdot L_Y$, where $L_{g\text{-}g}$ is shown in Eq. (2.40a). The values of $R_{S\text{-}liq1}$+R_S, R_{Cu}, R_{liq}, $R_{S\text{-}liq2}$, $R_{S\text{-}liq3}$, $R_{S\text{-}liq4}$, $R_{S\text{-}liq5}$, and $R_{S\text{-}liq6}$ are shown in Tables S6.1 to S6.2 and Figures S6.3 to S6.26 of the Appendix.

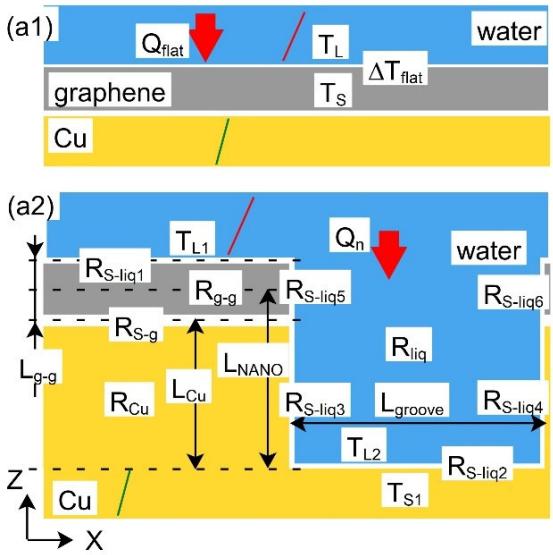

Figure 2.11 The cases of a flat surface and nanostructure surface in the Cu-graphene-water system for calculating thermal resistances.

In Eq. (2.40a), $L_{g\text{-}g}$ and $A_{g\text{-}g}$ are related to the thickness of graphene in the z-direction and the area ($=L_Y\cdot(L_X\text{-}L_{groove})$) of graphene, which are used to calculate $R_{g\text{-}g}$. $R_{S\text{-}g}$ is the local thermal resistance between graphene and the top nanopillar surface, which was calculated using Eq. (2.40b). The R_{flat} of Eq. (2.40b) between graphene and the top nanopillar surface is multiplied by the ratio, which is the area on a flat surface to the related area corresponding to those on a nanostructure surface. $R_{g\text{-}g}$ and $k_{g\text{-}g}$ correspond to internal thermal resistances of graphene and out-of-plane thermal conductivity, respectively.

$$R_{g-g} = \frac{L_{g-g}}{k_{g-g}\cdot A_{g-g}} \tag{2.40a}$$

$$R_{S-g} = \frac{A_{flat}}{A_*}R_{flat} = \frac{L_X}{L_*}R_{flat};\ S \in Cu;\ * \in 1,2,\cdots \tag{2.40b}$$

There are insufficient reports about the out-of-plane internal thermal resistance ($TR_{g\text{-}g}$) and $k_{g\text{-}g}$ for a single graphene layer[69]. The $k_{g\text{-}g}$ for graphite of about 8 $W\cdot m^{-1}\cdot K^{-1}$ [69] is applied to single-layer graphene even if $k_{g\text{-}g}$ for graphite underestimates $k_{g\text{-}g}$ for single-layer graphene due to weak van der Waals forces in the multilayer graphene, and the

internal thermal resistance of graphene ($TR_{g\text{-}g}$) is used to be around 3.98×10^{-11} $m^2\cdot K/W$ in the present study. The definitions of the TCMs on composite surfaces have the same formatting as that in the Cu-water system. Figure 2.12 shows the six TCMs on the composite surfaces. Models A to F were defined in Section 2.8.2, but the heat transfer path of the components differs from those in Cu-water systems, such as $R_{g\text{-}g}$, which is applicable only in Cu-graphene-water systems.

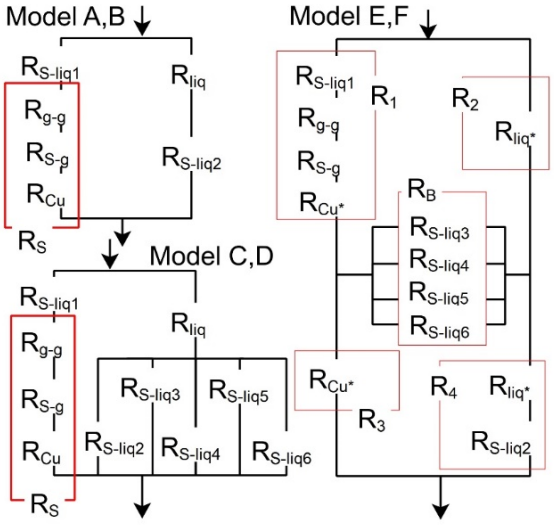

Figure 2.12 TCM schemes on a composite surface

In models A and B, the left paths of heat transfer are composed of $R_{S\text{-}liq1}$ and Rs ($R_{g\text{-}g}$, $R_{S\text{-}g}$, and R_{Cu}); the right paths of heat transfer are composed of $R_{S\text{-}liq2}$ and R_{liq}. The equivalent thermal resistances ($R_{eq\text{-}A}$ and $R_{eq\text{-}B}$) of models A and B can also be calculated by Eq. (2.37). The difference between models A and B is that the former uses the thermal conductivities of water and solids calculated by MD simulations, while the latter utilizes the experimental (empirical) thermal conductivities of water and solids.

In models C and D, it was also observed that the 2D temperature distribution is presented in Figures S6.33 to S6.40 of the Appendix, and the temperature of the nanopillar sidewalls is similar to that of the groove bottom surface. The right path of heat transfer is the same as in models A and B. The left path of heat transfer includes $R_{liq,}$ and the parallel thermal resistance consists of $R_{S\text{-}liq2}$ to $R_{S\text{-}liq6}$. The equivalent thermal resistances ($R_{eq\text{-}C}$ and $R_{eq\text{-}D}$) in models C and D can be calculated through Eq. (2.41). The difference between models C and D is that the former uses the thermal conductivities of water and solids calculated by MD simulations, while the latter utilizes the experimental (or empirical) thermal conductivities of water and solids.

$$R_{eq-C,D} = \left(R_{S-liq1} + R_S\right) \parallel \left(R_{S-liq2} \parallel R_{S-liq3} \parallel R_{S-liq4} \parallel R_{S-liq5} \parallel R_{S-liq6} + R_{liq}\right) \quad (2.41)$$

The heat transfer paths in models E and F are similar to those in Section 2.8.2 but differ from R_1 and R_B in Section 2.8.2. R_1 includes additional thermal resistances of $R_{g\text{-}g}$ and $R_{S\text{-}g}$. R_B includes additional thermal resistances of $R_{S\text{-}liq5}$ and $R_{S\text{-}liq6}$. The equivalent thermal resistances ($R_{eq\text{-}E}$ and $R_{eq\text{-}F}$) in models E and F can also be calculated using Eq. (2.39). The main difference between models E and F is that the former uses the thermal conductivities of the water and solids calculated by MD simulations, while the latter utilizes the experimental (empirical) thermal conductivities of the water and solids. The area (A_{flat}) multiplied by $R_{eq\text{-}A}$ to $R_{eq\text{-}F}$ is defined to obtain the ITR_{Model}, which corresponds to the equivalent ITR on a nanostructure surface used for predicting six TCMs.

2.8.4 ITRs calculated by MD simulations on nanostructure surfaces

There are different definitions of ITRs on nanostructure surfaces [34, 35, 70]. The T_{L1}, T_{L2}, and T_{S1} in Figure 2.9 (a3) and Figure 2.11 (a2) are related to the temperature of the water approaching the top nanopillar surface, the water temperature close to the groove bottom surface and the temperature of the groove bottom surface. A fitting curve of water temperature is obtained by fitting the temperature gradient of the water to calculate the water temperature (T_{L1} and T_{L2}) near the top nanopillar surface and the groove bottom surface. A fitting curve of solid temperature is obtained by fitting the temperature gradient of the solid walls to calculate the solid temperature (T_{S1}) at the groove bottom surface. The temperature jump (ΔT_{th}) in Eq. (2.42) represents the difference between the water temperature (T_{L1}) near the top nanopillar surface in the x-y plane and the solid temperature (T_{S1}). The temperature jump (ΔT_f) in Eq. (2.43) represents the difference between the water temperature (T_{L2}) near the groove bottom surface in the x-y plane and the solid temperature (T_{S1}). The heat flux (q_n) in Eq. (2.44) on a nanostructure surface is equal to the heat flow rate (Q_n) divided by A_{flat}. The ITR_{MD} (ITR_{th}) in Eq. (2.45) is equal to ΔT_{th} divided by q_n and used to compare to that predicted by TCMs. The ITR_f is equal to ΔT_f divided by q_n in Eq. (2.46) and is used to compare to the ITR_{th} in Chapters 3 and 4.

$$\Delta T_{th} = T_{L1} - T_{S1} \quad (2.42)$$

$$\Delta T_f = T_{L2} - T_{S1} \quad (2.43)$$

$$q_n = \frac{Q_n}{A_{Flat}} \quad (2.44)$$

$$ITR_{MD}\ (\ ITR_{th}) = \frac{\Delta T_{th}}{q_n} \quad (2.45)$$

$$ITR_f = \frac{\Delta T_f}{q_n} \quad (2.46)$$

2.9 Calculation of density depletion length

The density depletion length (DDL) refers to the quantification of the liquid depletion layer, which signifies the existence of a liquid layer with diminished density at the S-L interface in both MD simulations and experimental surfaces[23, 24]. The $\rho_s(z)$ and $\rho_l(z)$ represent the densities of the solids and liquid along the z-direction, respectively. dz indicates the slab size in the z-direction while ρ_s^b and ρ_l^b denote the bulk densities of the solids and liquids, as defined in Eq. (2.47). The symbol (∞) refers to half the MD system size along the z-direction in the present study. The DDL unit is "nm" and the slab size (dz) is 0.01 nm. The $\rho_l(z)$ in the case of nanostructure surfaces includes the distance between the nanopillar sidewall and water in the x-y plane.

$$\mathrm{DDL} = \int_0^{\infty} \left[1 - \frac{\rho_s(z)}{\rho_s^b} - \frac{\rho_l(z)}{\rho_l^b}\right] dz \tag{2.47}$$

The essence of DDL is used to compute and measure the distance from the liquid at S-L interfaces to the outermost walls near the water [23, 24] using a normalized method. Consequently, in the present investigation, the simplified calculation of the DDL is used with reference to the previous report [23] by assuming that each slab of the solid walls possesses a uniform density equivalent to the bulk density (ρ_s^b) of the solid walls. Figures 2.13 (a1) and (a2) show the scheme to calculate the DDL on a flat and nanostructure surface, respectively.

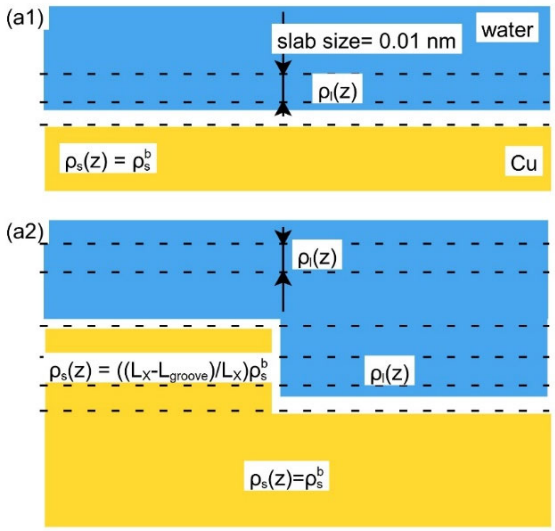

Figure 2.13 The calculation method for the DDL on flat and nanostructure surfaces.

In order to calculate the distance between the solid and liquid interfaces, the position of the solid surface should be determined, and it is assumed that the solid density near the S-L interface is not more than 2.0×10^{-4} g/cm^3 in all cases.

The ρ_s^b and ρ_s of the nanostructure surface are consistent with those of the flat surface.

The $\rho_s(dz)$ of the nanopillar can be calculated using Eq. (2.48).

$$\rho_s(dz) = \frac{L_X - L_{groove}}{L_X} \cdot \rho_s^b \tag{2.48}$$

In the Cu-graphene-water system, the defect concentration (dfct) of the graphene coating in Eq. (2.49) is calculated by using the number of missing carbon atoms in a defective graphene coating divided by the number of carbon atoms in a pristine graphene coating, where C_{tot} and C_{miss} represent the number of carbons in pristine graphene and the number of missing carbons in the defective graphene, respectively. ρ_s of the defective graphene can be calculated using Eq. (2.50)

$$dfct = \frac{C_{miss}}{C_{tot}} \tag{2.49}$$

$$\rho_s(dz) = (1 - dfct) \cdot \rho_s^b \tag{2.50}$$

2.10 Main software packages and post-processing tools

The LAMMPS package[71] is employed for all simulations. Python and Fortran codes are used to extract the original data and generate normalized data. The OVITO package[72] is primarily used to generate graphics for the calculation models. The graphics and figures are generated using the Veusz package.

2.11 Calculation Procedure

In all cases, the first step utilizes 2.0 ns as the computation time to maintain the water and the walls in an equilibrated state at 275 K or 280 K with the temperature controlling and Langevin thermostat, respectively. The second stage during 2.0 ns, is used to build a temperature gradient in the system, which is adjusted by the temperature of the cold wall at 250 K and that of the hot wall at 300 K using the Langevin thermostat; The temperature control of the water is removed simultaneously. The data, such as water temperature and the one-dimensional (1D) water density, are collected for 4.0 ns in the third step.

3 The effect of water pressure and nanopillar widths on ITRs in water-Cu systems

The influence of water models, nanopillar widths, and water pressure on the interfacial thermal resistances (ITRs) at water-Cu interfaces through non-equilibrium molecular dynamics (NEMD) simulations across flat and nanostructure surfaces was investigated and DDL was employed to evaluate S-L ITRs in the present chapter. The effects of these factors on the DDL and S-L ITRs were considered in Chapter 3. The calculation models and numerical details were introduced in Section 3.1. The influences of water pressure on ITRs on flat and nanostructure surfaces are shown in Section 3.2. The effect of nanopillar widths on ITRs on nanostructure surfaces was demonstrated in Section 3.3. The density contour of water molecules was displayed in Section 3.4. The relationship between the DDL and ITRs is shown in Section 3.5.

3.1 Calculation models and numerical details

The initial size of the system box was 4.08 (L_X) × 3.98 (L_Y) × 12.34 (L_Z) nm^3. The water region distance (L) was 6.50 nm along the z-direction between the parallel walls to hold water molecules, as shown in Figure 3.1. The computational model included the CG and SPC/E models with solid walls. The Cu atoms with a lattice constant of 0.255 nm constructed solid walls, the hot and cold walls consisted of 13 layers and the inter-layer thickness was 0.208 nm initially. Each layer in the flat solid walls consisted of 288 Cu atoms. The nanostructure surface consisted of a nanopillar and a flat surface (substrate) in the present dissertation, as shown in Figure 3.1(g). On nanostructure surfaces, nanopillar sizes of 1.91 (L_{pillar}) × 3.98 × 1.59 (L_{NANO}) and 1.40 (L_{pillar}) × 3.98 × 1.59 nm^3 were used in the present chapter, and the nanopillar consisted of 8 Cu layers. Various water pressure conditions were employed on flat surfaces, as shown in Table 3.1, and nanostructure surfaces, as shown in Table S3.2 of the Appendix. One layer of the outermost hot or cold walls far from the water region was unmoved, as shown in the light-purple layers in Figure 3.1. The third and second layers of each outmost wall were used as the hot and cold regions controlled by the Langevin thermostat in order to hold the constant wall temperature, as shown in the red and dark blue layers in Figure 3.1. The water and solid domains along the z-direction were divided into equal-volume regions. The CG and SPC/E water regions were divided into equal slab regions for a temperature distribution of 0.3 nm along the z-axis. The slab regions in the z-direction had a density distribution with the thickness of 0.01 nm (dz) for both water models. The periodic boundary is employed in the x-direction and y-direction for Chapters 3 and 4.

In Table 3.1, "P-MD" represents the water pressure generated by MD simulations, and its unit is MPa. The "P-Exp" refers to the experimental (empirical) water pressure according to the method employed by the research [18] using the software [73] with inputting the

temperature and specific volume of water (based on the thermodynamic properties of water), and its unit is MPa. The "Error (%)" denotes a relative error between the water pressure calculated by MD and the experimental pressure. In the Wenzel state, liquid water filled the groove. The Cassie-Baxter (CB) states in the MD simulations are determined when the following conditions are satisfied: the distance between the position of the liquid and that of the groove bottom surface was assumed to be greater than 0.2 nm, the water density at the position of the liquid was no less than 0.01g/cm^3. In the present chapter, three types of initial velocity distributions were used for the ITR and DDL calculations to generate the error bars in related figures. The related tables and figures in the Appendix were only shown by one of three MD simulations.

Table 3.1 Water models, water pressures, and the number of water molecules under various interaction strengths between water and Cu on flat surfaces. "Number" refers to the number of water molecules. The "P-MD" and "P-Exp" correspond to the water pressure calculated by MD and experimental values, respectively. The R_{flat} and ITR_{flat} are related to thermal resistance and interfacial thermal resistance. The units of R_{flat} and ITR_{flat} are K/W and K·m^2/W, respectively. The "SPC/E" and "CG" represent the SPC/E and CG models for all cases. The "CA" was explained in Section 2.5, CA1 and CA2 are related to the hydrophilic and hydrophobic states.

		Number	P-MD	P-Exp	Error (%)	R_{flat}	ITR_{flat}
CG	CA1-P1	3524	110.13	116.10	-5.15	4.38E+08	7.12E-09
	CA1-P2	3424	47.94	48.35	-0.86	5.25E+08	8.53E-09
	CA1-P3	3340	2.65	--	--	5.97E+08	9.70E-09
	CA2-P1	3524	128.78	136.3	-5.52	8.28E+08	1.35E-08
	CA2-P2	3424	66.69	67.00	-0.46	9.32E+08	1.51E-08
	CA2-P3	3340	21.96	19.02	15.43	1.21E+09	1.97E-08
SPC/E	CA1-P1	3524	116.57	96.54	20.74	3.99E+08	6.98E-09
	CA1-P2	3424	44.86	30.42	47.46	4.63E+08	7.52E-09
	CA1-P3	3372	7.53	--	--	4.70E+08	7.63E-09
	CA2-P1	3524	135.86	117.8	15.33	7.10E+08	1.15E-08
	CA2-P2	3424	60.19	51.21	17.54	8.54E+08	1.39E-08
	CA2-P3	3372	35.81	20.33	76.15	1.04E+09	1.69E-08

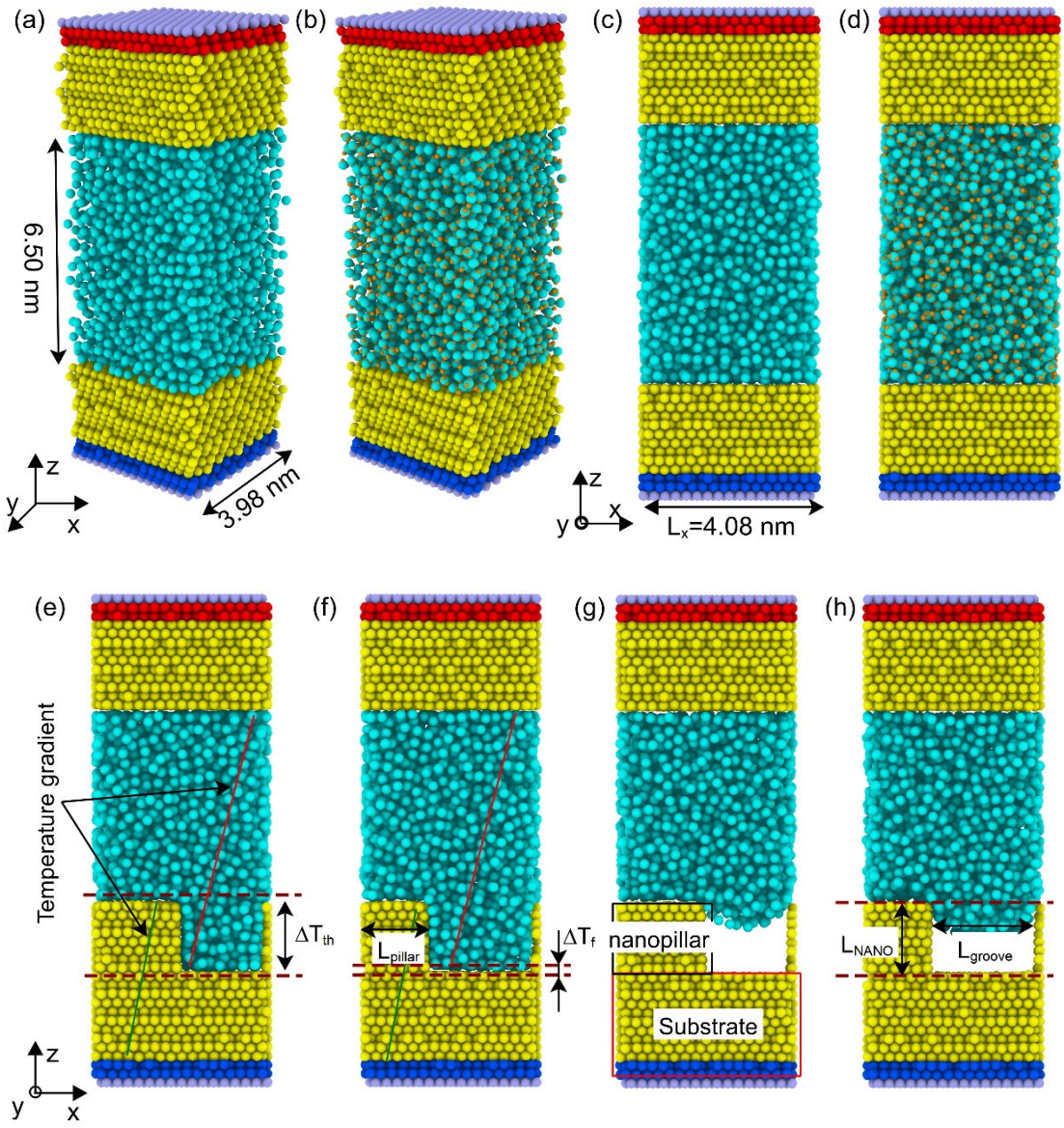

Figure 3.1 Calculation models of various flat and nanostructure surfaces. The dark blue and red atoms represent cold and hot regions controlled by the Langevin thermostat. The fixed walls consisted of light-purple atoms. The nanopillar widths (L_{pillar}) w 1.91 nm and 1.40 nm for nanostructure surfaces in (e) and (f), corresponding to "S19" and "S14". The light-blue particles were the CG water molecules and oxygen (O) atoms of the SPC/E model, and the orange particles were hydrogen (H) atoms. The Wenzel and CB states are shown in (e and f) and (g and h), respectively. The red and blue lines depict the temperature gradients of water and solids, respectively. L_{NANO}, L_{pillar}, and L_{groove} on the nanostructure surfaces represent the nanopillar thickness, the nanopillar width, and the groove width, respectively.

3.2 The effect of water pressure on ITRs

Water pressure was an important factor that changed the S-L ITRs. The previous research[18] has mainly focused on flat surfaces, so the present section investigated the relationship between S-L ITRs with different definitions and water pressure on nanostructure surfaces. In the present section, a flat substrate and rectangular nanopillars, depicted in Figure 3.1(g), were utilized as the nanostructure surface. The temperature jump was observed on both the substrate surfaces and the nanopillars, resulting in varied temperature jumps across different surface regions, which led to the various definitions of ITRs[34, 35] for nanostructure surfaces. The definition of ITRs assumed the equivalence between the Wenzel and CB states. This assumption resulted from the generation of ITRs by heat flow through the S-L interface. In the ideal CB state, most energy was exchanged through the top nanopillar surface, and there was almost no energy transfer between the nanopillar sidewalls and the water. In the present section, there are two different definitions of ITRs, outlined in Eq. (2.45) and Eq. (2.46), using temperature jumps (ΔT_{th} and ΔT_f) as illustrated in Figure 3.1(e) and (f). The red and blue curves in Figure 3.2 illustrated a nearly linear decrease in the interfacial thermal resistance (ITR_{flat}) across flat surfaces, irrespective of the interaction strengths. The ITR[56] of 7.33×10^{-9} $K\cdot m^2/W$ on a flat surface was similar to that of the SPC/E-CA1-P3 of 7.63×10^{-9} $K\cdot m^2/W$ under the same temperature of the cold and hot walls. The ITR[22] of 1.07×10^{-8} $K\cdot m^2/W$ on a flat surface was similar to that of the SPC/E-CA2-P3 of 1.69×10^{-8} $K\cdot m^2/W$ under similar wettability.

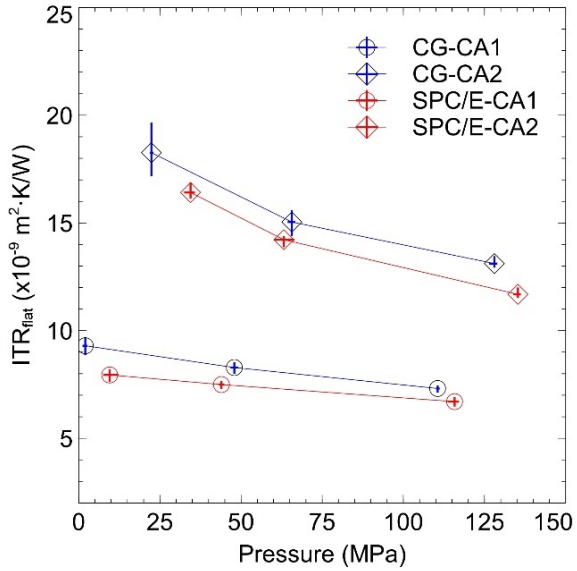

Figure 3.2 Relationship between ITRs and water pressure on flat surfaces. Red and blue represent the SPC/E and CG models, respectively. Dots and diamonds represent hydrophilic (CA1) and hydrophobic (CA2) states.

It was observed that the water pressure of the CG model was almost consistent with that of experimental data of water [73], specifically within the water in the liquid state at approximately 275 K, as detailed in Table 3.1. The ITR_{flat} of the CG model was slightly higher than that of the SPC/E model. This deviation could be attributed to the maximum peak of the CG water density in the vicinity of a solid surface, which was smaller than that of the water density of the SPC/E model, as shown in Figure 3.3.

Figures 3.3(a) and (b) present 1D density profiles of the SPC/E and CG water molecules along the z-direction (axis), illustrating the adsorption layers near flat surfaces in the CA1 and CA2 cases. The water density profiles are very important in identifying the water adsorption state pertinent to ITRs at the S-L interface. The first maximum peak of the water density of the CG model was lower than that of the SPC/E model in a similar case. At 6.0 nm of the simulation system along the z-direction, the average densities under similar water pressures, even using the CG and SPC/E models, corresponded closely to the density of the CG and SPC/E water molecules at about 280 K, as mentioned in previous research[16, 74]. The observed decrease in the first maximum peak of the SPC/E and CG water density stemmed from the change in wettability from the CA1 to the CA2 cases. In addition, the second peak of the CG water density shifted toward the cold wall, relative to the SPC/E model. The increase in water pressure increased the density of both the first and second peaks of water, thus increasing the density of water approaching the solid surface. Under similar conditions of wettability and water pressure, the changes in the water adsorption layers were evident, according to the 1D density profile, to weaken the resemblance between the two water models. These changes affected the peak of the water density and its corresponding position, thereby influencing the ITR deviation between the CG and SPC/E models, possibly related to the density of the CG and SPC/E water molecules on flat surfaces.

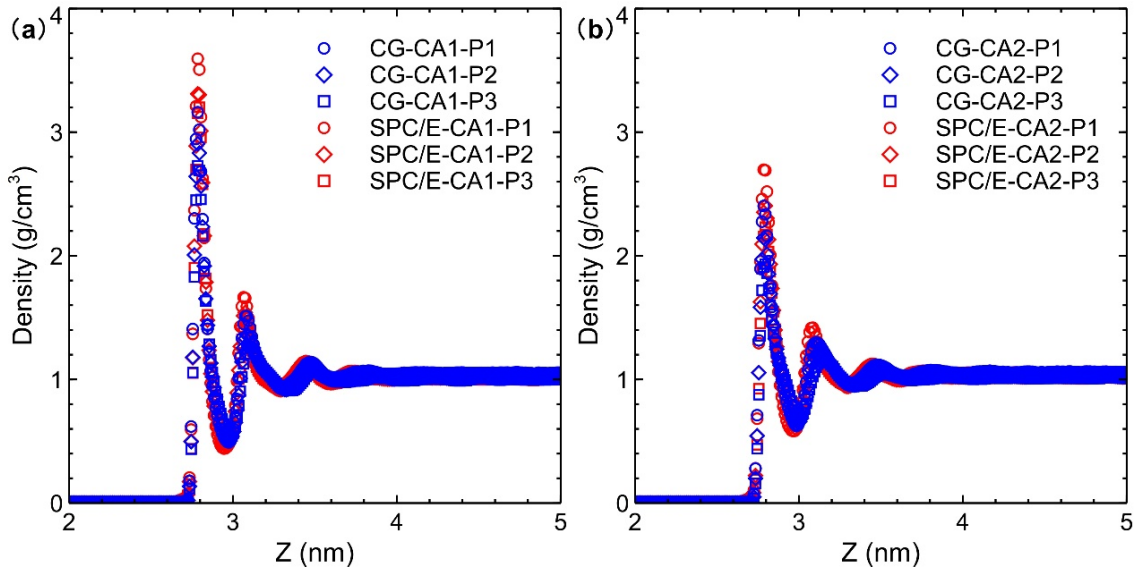

Figure 3.3 One-dimensional (1D) water density on flat surfaces. Red and blue represent the SPC/E and CG models. Dots, diamonds, and squares represent water pressure from P1 to P3; the related pressure of water is shown in Table 3.1.

Figure 3.4 illustrates the water models and the interaction strengths between water and solid walls that affected the relationship between ITRs and water pressure on nanostructure surfaces of the S19 cases. The ITR_{th} and ITR_f were determined using Eq. (2.45) and Eq. (2.46), with the results of the ITR_f and ITR_{th} depicted in Figures 3.4(a) and (b). In the presence of the CB states on nanostructure surfaces, heat transfer occurred predominantly on the top nanopillar surface along the z-direction rather than through the nanopillar sidewalls in the y-z plane. Regardless of the CA1 and CA2 cases, the ITR_f and ITR_{th} in the cases of the SPC/E and CG models exhibited an increase with decreasing pressure of the SPC/E and CG water molecules, as illustrated in Figures 3.4(a) and (b). The ITR_f of the CG model almost matched that of the SPC/E model under similar water pressure conditions, as shown in Figure 3.4(a). The ITR_{th} exhibited a slight inconsistency between the CG and SPC/E models, as shown in Figure 3.4(b). Despite the minimal variation in ITR_f concerning the water models, the dependence of ITR_{th} on the choice between SPC/E and CG models mirrored observations on flat surfaces. In the CB state, at low water pressures, ITR_{th} was observed to exceed ITR_f under different water model conditions, but there were fewer differences in the trends between ITR_{th} and ITR_f. These disparities changed due to the S-L interface and temperature jump phenomena. The scarcity of water molecules in the groove of the nanostructure surfaces contributed to a significant increase in the ITR_{th} in the CB state.

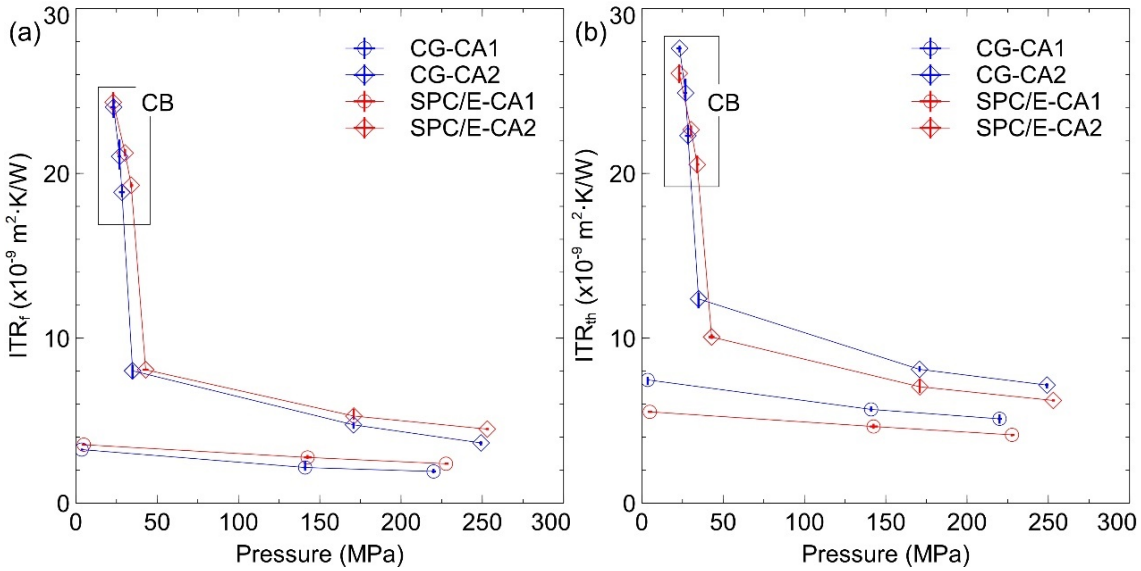

Figure 3.4 Relationship between ITRs and water pressure in the cases of S19 on nanostructure surfaces. (a) shows the ITR_f and pressure of the water molecules. (b) shows the ITR_{th} and water pressure. Red and blue represent the SPC/E and CG models. Dots and diamonds represent hydrophilic (CA1) and hydrophobic (CA2) states.

3.3 The effect of nanopillar widths on ITRs

The sizes of the nanostructures were the main factor affecting the S-L ITR, so it was necessary to verify and investigate the effect of the nanostructure size on the S-L ITR. Figure 3.5 depicts the relationship between surface roughness (Ψ) and interfacial thermal resistances (ITRs). Utilizing the definition of surface roughness (Ψ) given in Eq. (3.1) has enhanced the understanding of the nanostructure geometry that affects the S-L ITRs. L_{pillar} was related to the nanopillar width.

$$\Psi = \frac{{L_{pillar}}^2}{(L_{pillar} + L_{groove})^2} \tag{3.1}$$

On nanostructure surfaces, ITR_f initially experienced a sharp decline, followed by a gradual decrease with increasing groove width, similar to the previous findings[35] (reproduced using "Ref.Ψ1" in Figure 3.5) utilizing the TIP4P/Ew-Gold system, as shown in Figure 3.5(a). In comparison, ITR_{th} and ITR_f are shown in Figures 3.5(a) and (b). The tendency of ITR_{th} in Figure 3.5(b) was almost consistent with the previous research [26] (reproduced using "Ref.Ψ2" in Figure 3.5) in the Platinum (Pt)-Ar system. In addition, the ITR of the CG models consistently almost exhibited higher values than those of the SPC/E models under the condition of the identical roughness Ψ, which was consistent with observations from flat surfaces. Under low pressure, when the CB state was observed, both ITR_f and ITR_{th} escalated four to ten times compared to the Wenzel state, irrespective

of Ψ and water models. In short, the width of the nanopillar had almost no effect on the different definitions of the ITRs.

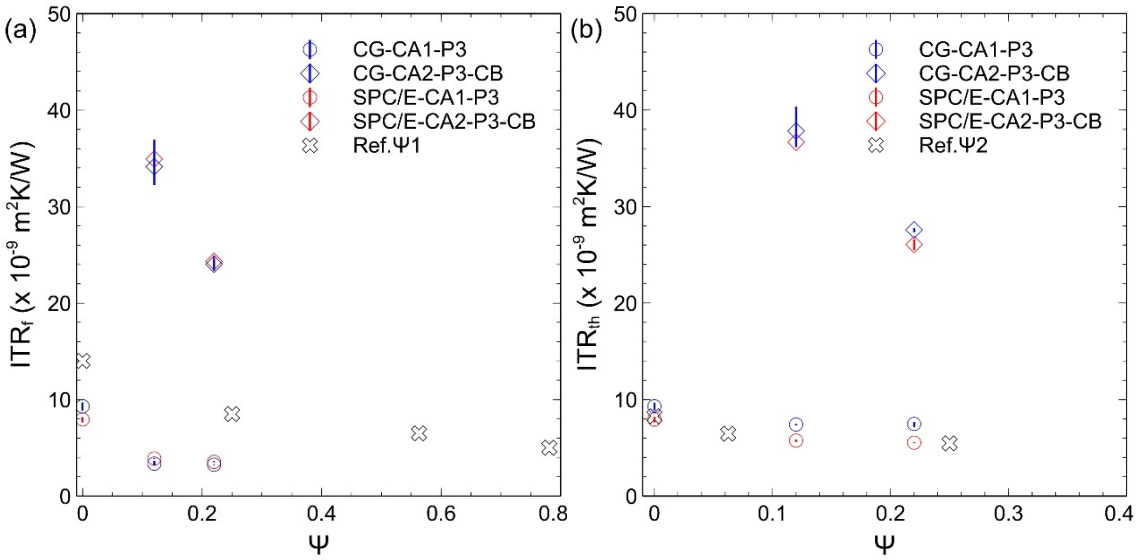

Figure 3.5 Relationship between surface roughness (Ψ) and ITRs on nanostructure surfaces. (a) show the relationship between ITR_f and Ψ. (b) show the relationship between ITR_{th} and Ψ. Red and blue represent the SPC/E and CG models, respectively. The dots and diamonds correspond to the hydrophilic (CA1) and CB states, respectively.

3.4 Two-dimensional (2D) density contour of water on nanostructure surfaces

The 2D density contour of the water molecules aided in understanding the relationship between water pressure and the nanopillars under the CG and SPC/E models for the relationships between the liquid adsorption layer and the ITRs. Figures 3.6 to 3.9 show the 2D density distribution of the CG and SPC/E water molecules near the solid surfaces in the CA1 and CA2 cases under varying pressure conditions. The number of CG and SPC/E water molecules was adjusted to maintain the approximate water pressure for both water models, and the number of water molecules and water pressure are given in Table S3.2 of the Appendix. Figures 3.6 to 3.9 exhibit a similar pattern of 2D density distribution of the SPC/E and CG water molecules under the nanopillar widths of S19 and S14. Under the high pressure conditions of the SPC/E and CG water, the water density tended to concentrate on the top nanopillar surfaces and the groove bottom surfaces in the x-y plane, especially in the CA2 cases. Figures 3.6 to 3.9 (a and c) show a non-uniform density distribution on the groove bottom surface, contrasting with the relatively uniform density observed on the top nanopillar surface. Meanwhile, the presence of uniform and dense density of the water on the top nanopillar surface in Figures 3.6(a) and (b) to Figures

3.9(a) and (b) were attributed to the stronger adsorption capacity of the top nanopillar surface compared to the groove bottom surface. Although the SPC/E water density exhibited slightly more pronounced characteristics than that of the CG model under approximate conditions, these findings aligned with the results on the flat surfaces obtained from the 1D density profile in Figure 3.3. In addition, the different types of FCC crystal surfaces[59] could contribute to the different water densities on the nanopillar sidewalls and the groove bottom surface (FCC 111).

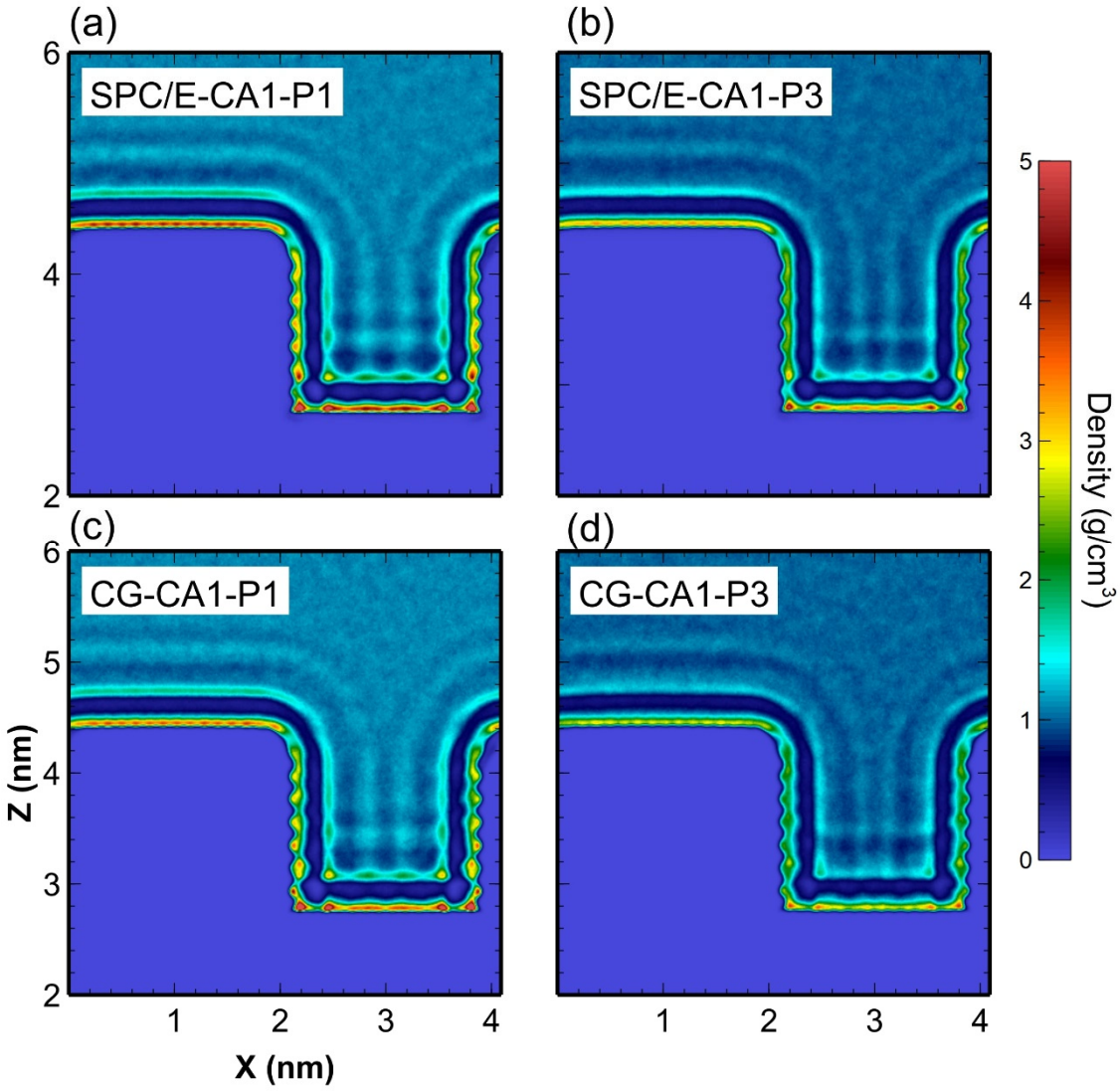

Figure 3.6 Two-dimensional (2D) water density on nanostructure surfaces in the CA1 cases under different pressures, water models, and nanopillar widths of S19.

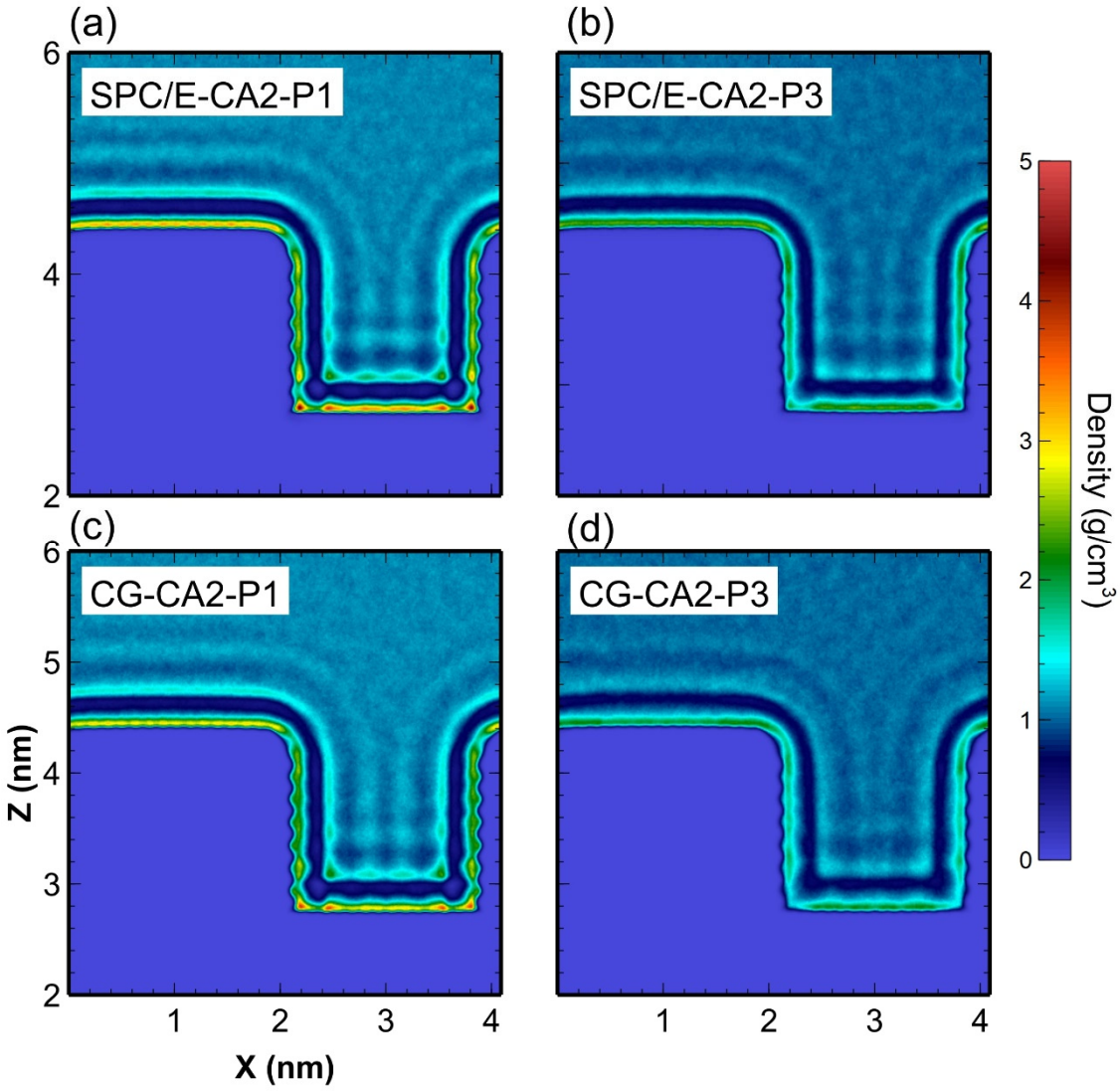

Figure 3.7 Two-dimensional (2D) water density on nanostructure surfaces in the CA2 cases under different pressures, water models, and nanopillar widths of S19.

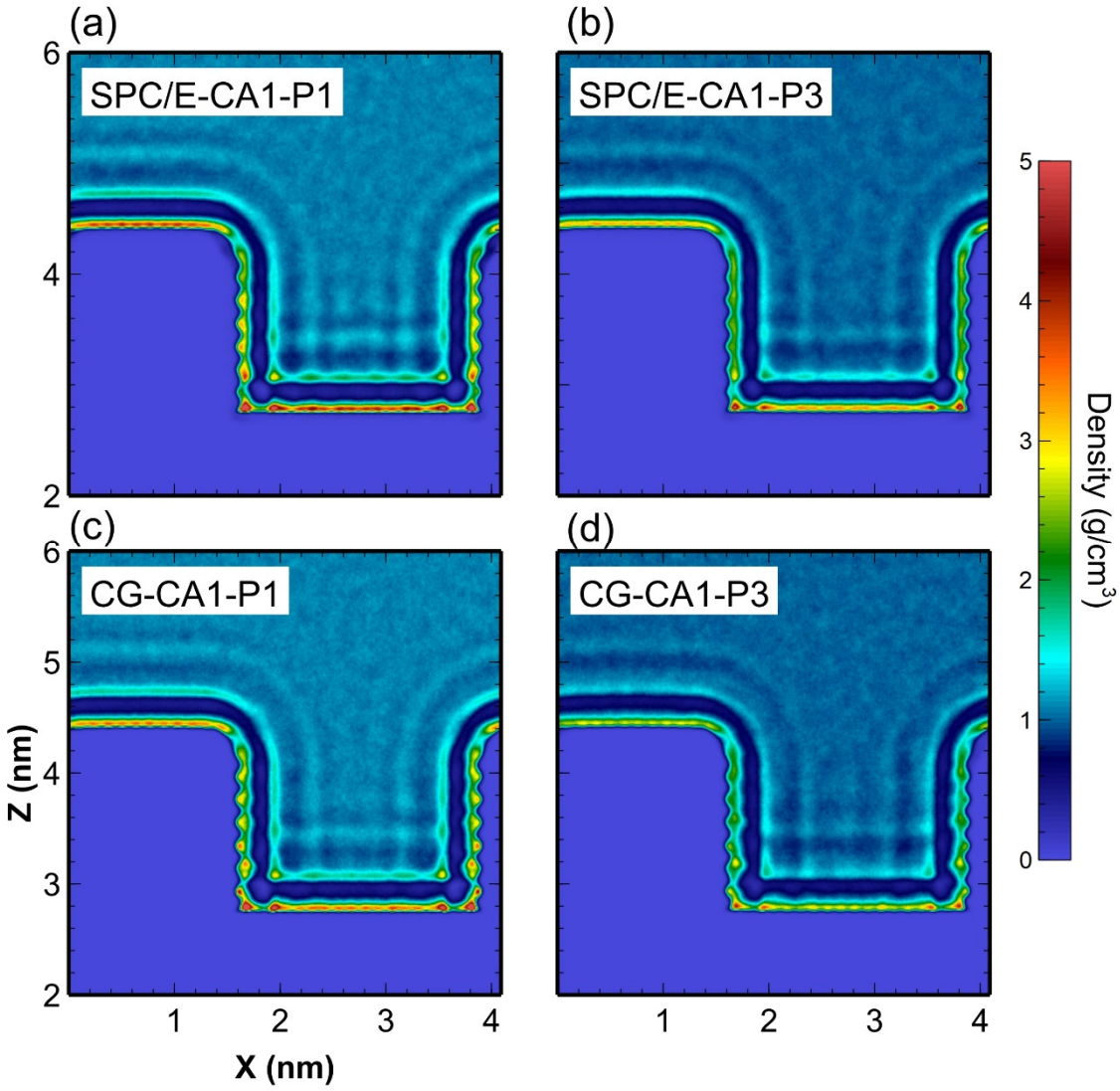

Figure 3.8 2D water density on nanostructure surfaces in the CA1 cases under different pressures, water models, and nanopillar widths of S14.

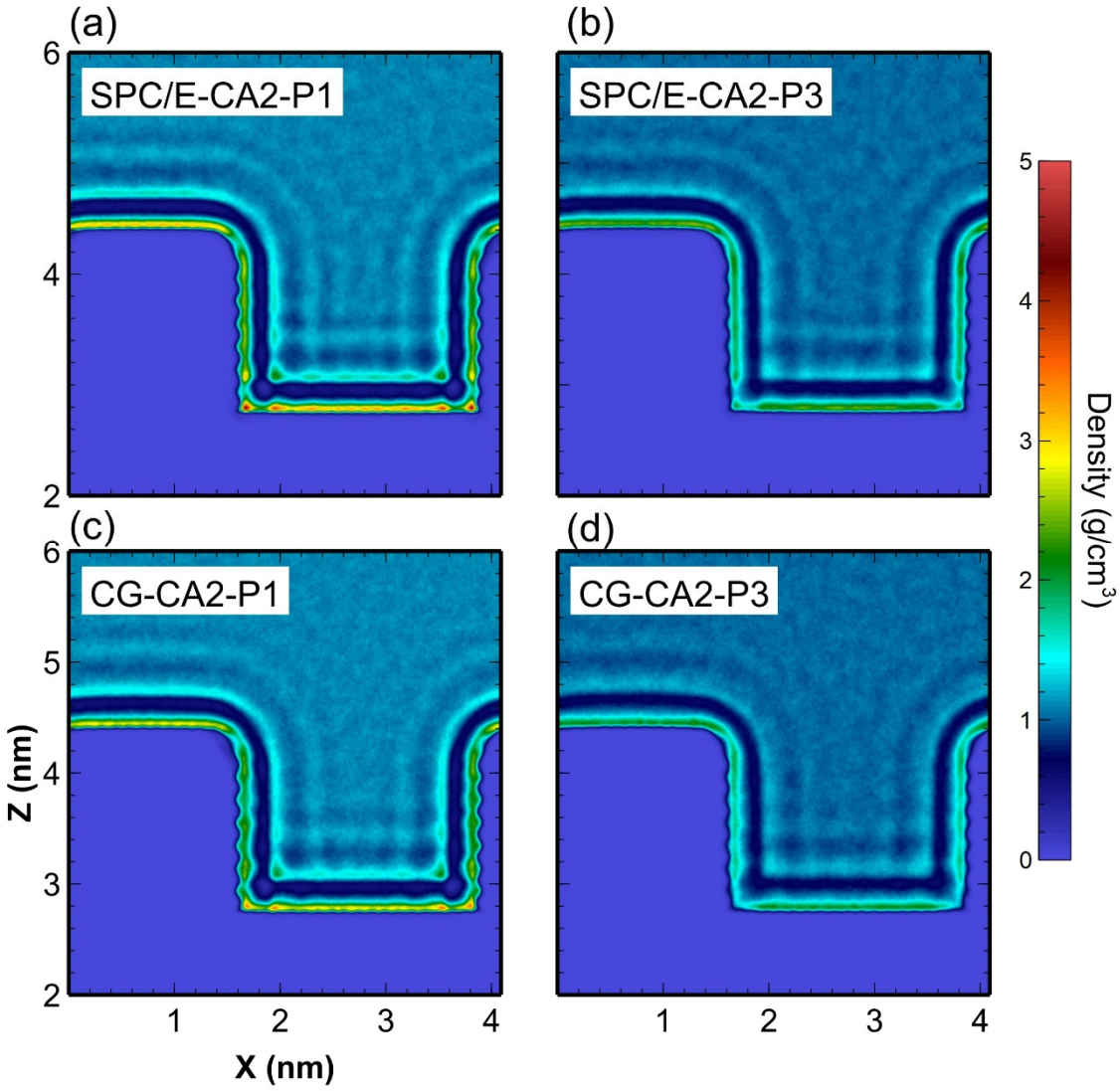

Figure 3.9 Two-dimensional (2D) water density on nanostructure surfaces in the CA2 cases under different pressures, water models, and nanopillar widths of S14.

3.5 Relationship between DDL and ITRs

The density depletion length (DDL) was a way to evaluate S-L ITR on flat and nanostructure surfaces. The DDL-ITR relationship of a flat surface was first investigated under the different water pressures. Figure 3.10 illustrates the relationship on flat surfaces between the DDL calculated using Eq. (2.47) and the S-L ITRs. In Figure 3.10, the exponential curves of "SPC/E-flat" and "CG-flat" depict the relationship between DDL and S-L ITRs under various interaction strengths for flat surfaces. It was observed that as the DDL increased, the S-L ITRs increased, and the tendency was strongly related to Eq. (3.2) with the coefficient of determination (CoD≥0.97 in most cases). In Eq. (3.2), the coefficients of the exponential function referred to the "A_d" and "nd", and the units of "A_d" and "nd" were "$m^2 \cdot K/W$" and "nm^{-1}", as shown in Table 3.2.

$$ITR = A_d \cdot e^{nd \cdot DDL} \quad (3.2)$$

The exponential trend is a good way to describe the relationship between DDL and S-L ITR, indicating it is applicable to flat and nanostructured surfaces, based on the previous study [25] and the coefficient of determination is shown in the present section. In Figures S3.14 and S3.15 of the Appendix, more data points are used to show that an exponential curve is a good representation of the DDL-ITR relationship. The relationships of the DDL and S-L ITRs were dependent on the CG and SPC/E models. The ITRs of the CG model tended to be higher than those of the SPC/E model under similar conditions. The O-H vector angles of SPC/E water molecules were directional[75], and hydrogen atoms might be close to the solid surface at the S-L interface, thereby reducing the DDL. It is worth mentioning that the report with the purple curve, reproduced using "Ref.DDL" in Figure 3.10, which was based on the SPC/E-Si simulations[25], might slightly differ from the present work due to solid variations.

Table 3.2 The coefficients of "A_d" and "nd" in Eq. (3.2).

	exponential curves	A_d (10^{-9} K·m^2/W)	nd (nm^{-1})	CoD
Flat surfaces	SPC/E-flat	1.22	23.24	0.99
	CG-flat	2.17	22.15	0.99
ITR_f	SPC/E-Wenzel	0.38	14.94	0.96
	SPC/E-CB	6.37	1.77	0.98
	CG-Wenzel	0.12	17.52	0.97
	CG-CB	6.23	1.78	0.98
ITR_{th}	SPC/E-Wenzel	1.10	10.63	0.94
	SPC/E-CB	6.94	1.74	0.99
	CG-Wenzel	1.00	10.31	0.97
	CG-CB	8.45	1.56	0.98

As the previously reported the relationship between DDL and ITRs was limited to flat

surfaces, the present study explored and discussed this relationship in the context of nanostructure surfaces.

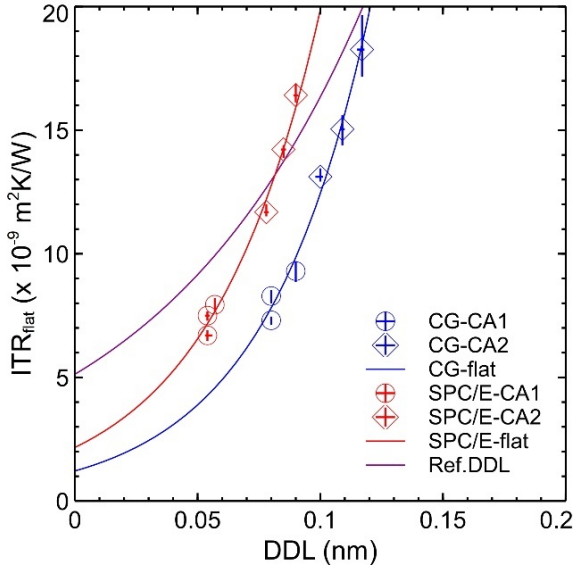

Figure 3.10 The relationships between S-L ITR$_{flat}$ and DDL using the CG and SPC/E models on flat surfaces. The red and blue exponential curves correspond to the SPC/E and CG models, respectively. The MD report [25] of DDL and ITR$_{flat}$ shows a purple curve (depicted as "Ref.DDL"). The circles and diamonds refer to the hydrophilic (CA1) and hydrophobic (CA2) states, respectively.

On the nanostructure surfaces, the relationships between S-L ITRs and DDL could be described by Eq. (3.2). The exponential curves of "SPC/E-Wenzel" and "CG-Wenzel" represent the Wenzel states under various roughness and water pressure, as depicted in Figures 3.11(a) and (b). The exponential curves of DDL-ITR on the nanostructure surfaces were significantly different from those on flat surfaces, indicating that nanostructure surfaces influenced the relationship between DDL and ITR.

In Figure 3.11(b), the ITR$_{th}$ illustrates that the exponential curves of the CG and SPC/E models were closely aligned, in contrast to the variation seen in the ITR$_f$ in Figure 3.11(a). This difference was due to the presence of liquid water filling the groove, which led to the observation of the Wenzel state when the DDL values ranged from approximately 0 to 0.25 nm. Conversely, when the DDL ranged from about 0.6 to 1.0 nm, the groove remained unfilled with liquid water, resulting in the CB state. The trend of ITR$_f$ observed in Figure 3.11(a) resembled that on flat surfaces, with the magnitude of ITRs in the cases of the CG model slightly surpassing that in the SPC/E model when DDL ranges from 0 to 0.25 nm. However, for the SPC/E model, indicated by the red circle shapes of the "SPC/E-CA1" in Figures 3.11(a) and (b), the ITRs in the CA1 cases demonstrated a slightly poor fit to the exponential curves. It might be that SPC/E water molecules were in the hydrophilic states, so the exponential curves could roughly describe the

relationships between S-L ITRs and DDL under different pressures.

It remained unclear whether the DDL could be applied to ITRs with different definitions. Interestingly, ITR_f and ITR_{th} exhibited slight sensitivity to the CG and SPC/E models used when the DDL ranged from about 0.6 to 1.0 nm. The intersection of the fitting curves in Figures 3.11(a) and (b) represents the critical point that was inferred to be associated with the transition from the Wenzel to the CB state. The Wenzel and CB states could be judged by 2D density distribution, such as the Wenzel state in Section 3.4. Consequently, the DDL served as a descriptor of the wettability state and facilitated approximate prediction of ITRs.

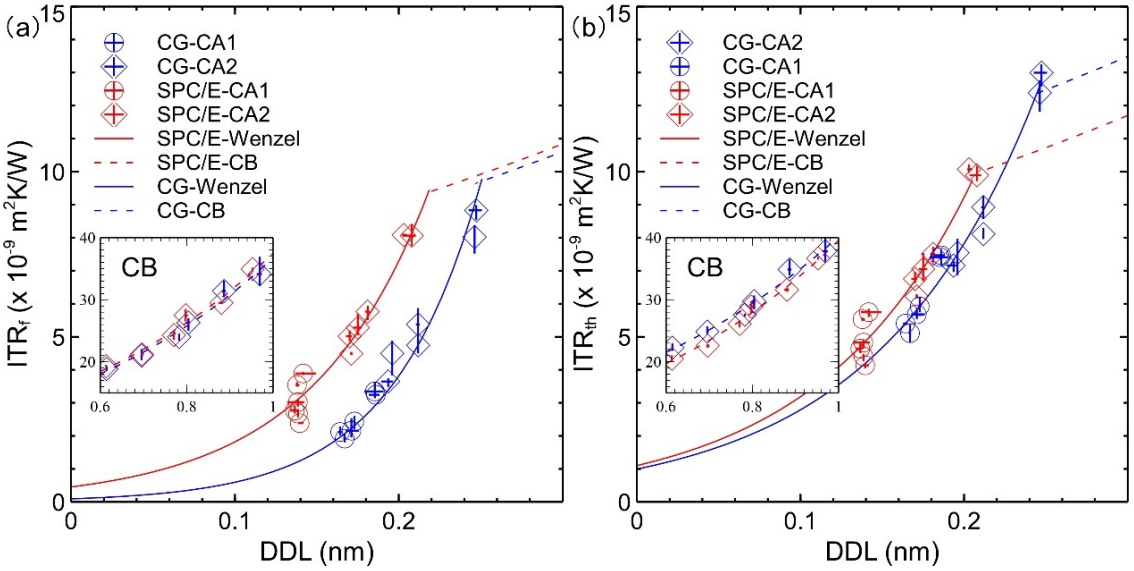

Figure 3.11 The relationships between ITR and DDL using the CG (blue) and SPC/E (red) models on nanostructure surfaces. ITR_f and ITR_{th} are shown in (a) and (b). The relationships between DDL and ITRs in the CB states are shown in the small plots. The solid and dashed exponential curves represent the Wenzel states and CB states, respectively. The circles and diamonds represent the hydrophilic (CA1) and hydrophobic (CA2) states, respectively.

4 The effect of defective graphene coating on ITRs in water-graphene-Cu systems

In the present chapter, the influences of the defective surface on the relationship between DDL and S-L ITRs were investigated by NEMD simulations in the water-graphene-Cu system. To evaluate the effect of the defective surface on the S-L ITR, the computational models and numerical details were introduced in Section 4.1. The effect of defect concentration on the S-L ITR using the SPC/E and CG models is shown in Section 4.2. The relationships between ITR and DDL on flat and nanostructure surfaces were presented in Section 4.3.

4.1 Calculation models and numerical details

The CG and SPC/E models with graphene-Cu surfaces were used on flat and nanostructure surfaces in the present chapter. The initial size of the system box was 4.08 (L_X) × 3.98(L_Y) × 12.34(L_Z) nm^3, and it was the same as in Chapter 3. The distance in the z direction was 6.50 nm between the top and bottom walls to hold the graphene coating and water molecules, as shown in Figure 4.1(a). Each Cu wall consisted of 13 layers with a thickness of 2.51 nm on a flat surface and was coated with a single-layer graphene. The lattice constants [22, 53] of the Cu and graphene were 0.255 nm. A nanostructure surface consisted of a Cu nanopillar and a single-layer graphene coating, as shown in Figure 4.1(e). The Cu nanopillar width and height were 1.91 nm and 1.61nm, respectively. The nanopillar was composed of 7 Cu layers. The initial distance between graphene and Cu surfaces was around 0.3 nm on flat and nanostructure surfaces. The water pressure ranged from 1 to 50 MPa in the present chapter, and the details of the water pressure are given in Table S4.1 of the Appendix. The periodic boundary was employed in the x- and y-directions as in Chapter 3.

The defect concentration of the graphene coating was given by using the number of missing carbon atoms in a defective graphene coating divided by the number of carbon atoms in a pristine graphene coating, as shown in Eq. (2.49). The pristine graphene coating has 576 and 288 atoms on a flat and nanostructure surface, respectively. The pristine (SV0.0) and defective graphene on flat and nanostructure surfaces are shown in Figure 4.2, and the structure of the pristine graphene was similar to the previous reports[22, 76]. Figures 4.2 (a) to (c) show the calculation models on flat surfaces of pristine graphene (SV0.0), 2.1% of defective graphene (SV2.1), and 2.8% of defective graphene (SV2.8), respectively. Figures 4.2 (d) to (f) show the calculation models on nanostructure surfaces of pristine graphene (SV0.0), 2.1% of defective graphene (SV2.1), and 2.8% of defective graphene (SV2.8), respectively. The lattice orientation of Cu was FCC (111) in the z-direction. The single vacancy (SV) of defective graphene surfaces is employed in Chapter 4. A single vacancy in graphene refers to a type of defect where one

carbon atom is missing from the neighboring perfect hexagonal lattice of carbon atoms. In the present study, the defect size, similar to a hole diameter, caused by missing carbon atoms is constant.

The color layers and related functions in Figure 4.1 were the same as in Chapter 3, and the grey corresponds to the graphene coating or carbon atoms. The CG and SPC/E water regions were divided into equal slab regions for a temperature distribution of 0.3 nm along the z-axis. The slab regions in the z-direction had a density distribution with the thickness of 0.01 nm (dz) for both water models. In the present chapter, three types of initial velocity distributions were used for the ITR and DDL calculations in each case to generate the error bars in related figures. The related tables and figures in the Appendix were shown by only one of three MD simulations.

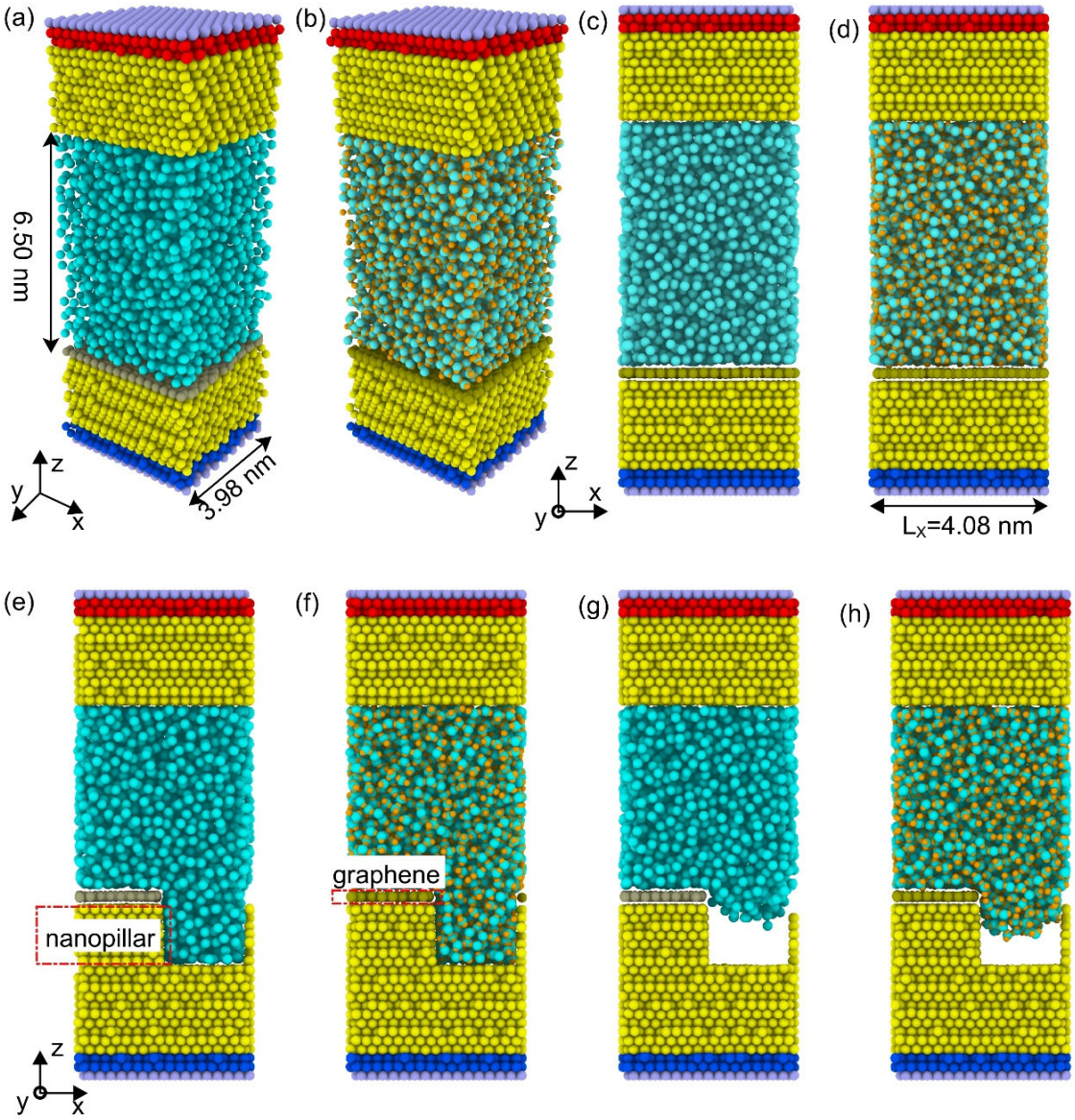

Figure 4.1 Calculation models of Cu-graphene-water systems. (a) and (c) show that single-layer graphene is coated on the entire Cu bottom surfaces using the CG model; (b) and (d) show that single-layer graphene covers the entire Cu bottom surfaces using the SPC/E model. The dark blue and red atoms were cold and hot regions controlled by the Langevin thermostat. The fixed walls consisted of light-purple atoms. The nanopillar width was 1.91 nm for nanostructure surfaces such as in (e). The light-blue particles were CG water molecules in CG water cases and oxygen atoms in the SPC/E model. The orange particles were hydrogen atoms just in the SPC/E model. The grey particles denote the graphene coating. The Wenzel and CB states are shown in (e, f) and (g, h), respectively.

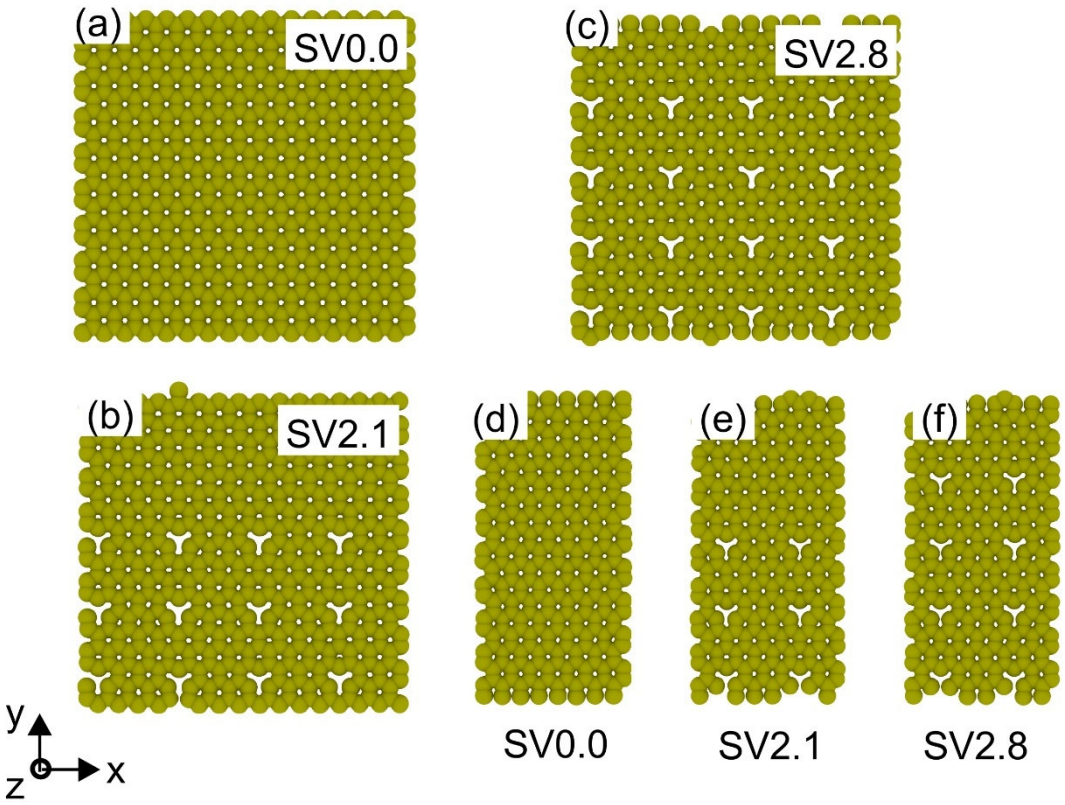

Figure 4.2 A single layer of pristine and defective graphene. (a) to (c) correspond to the pristine and defective graphene coating on flat surfaces, and (d) to (f) correspond to the pristine and defective graphene coating on nanostructure surfaces. The pristine graphene, 2.1% defective graphene, and 2.8% defective graphene on flat and nanostructure surfaces correspond to the SV0.0, SV2.1, and SV2.8, respectively.

4.2 The effect of defective surfaces on water density and ITRs on flat surfaces

4.2.1 The effect of defective surfaces on water density

To investigate the effect of graphene defect concentration on ITRs, it was necessary to observe the adsorption of water molecules on the graphene coating. Figures 4.3(a) to (d) show the 1D water density on the different wettability surfaces.

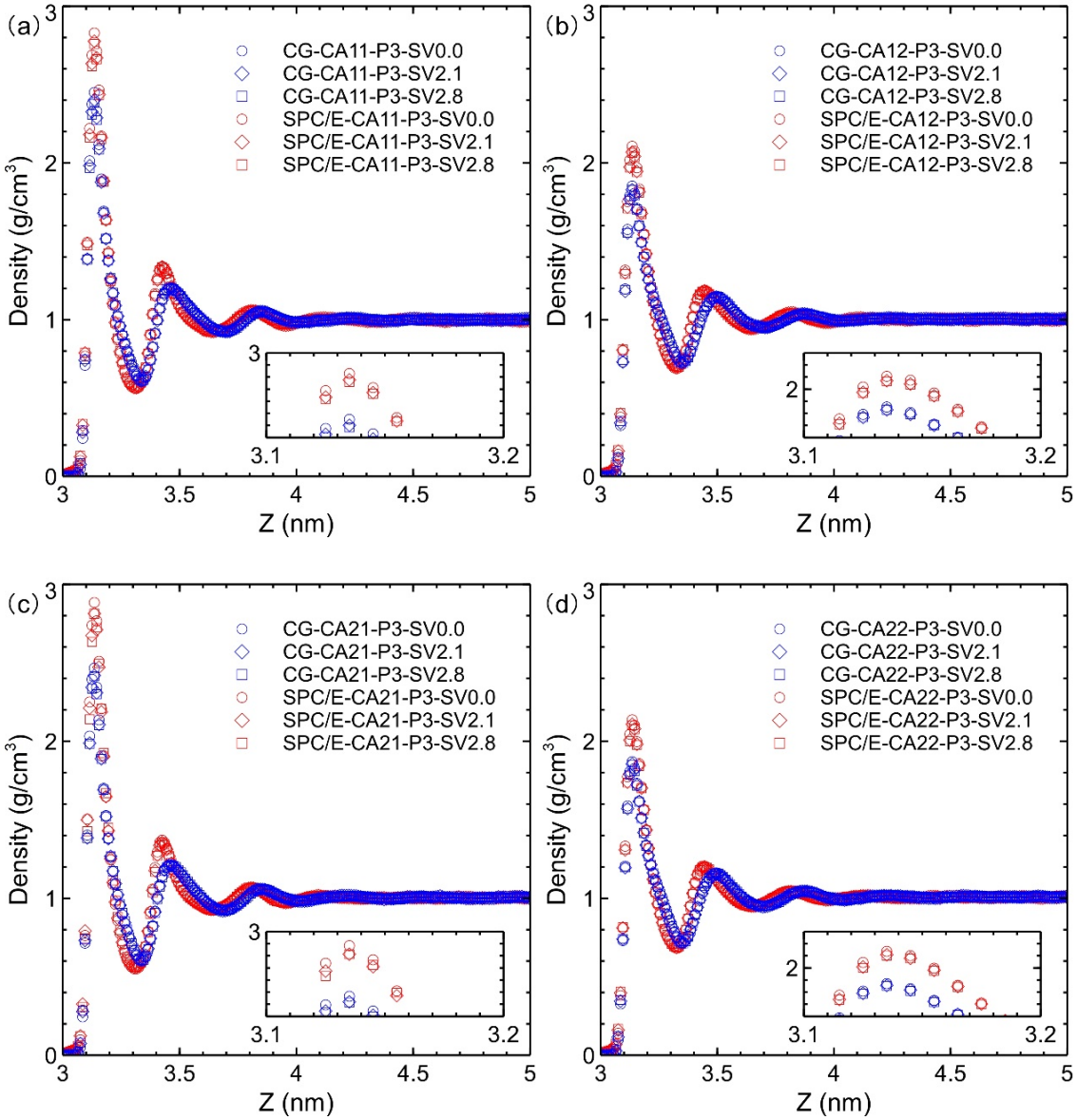

Figure 4.3 1D density profile of water molecules on flat surfaces. The blue and red correspond to the CG and SPC/E models, respectively. The dot, diamond, and square correspond to the cases SV0.0, SV2.1, and SV2.8, respectively. (a) to (d) refer to the cases CA11, CA12, CA21, and CA22.

The calculation results of the CG and SPC/E models in the present chapter were shown in blue and red, respectively. The CA11, CA12, CA21, and CA22 cases describe different wettability of liquid on a solid surface (Cu and graphene) and the meanings of CA11, CA12, CA21, and CA22 are explained in Section 2.4. By observing the one-dimensional (1D) density profile of the CG and SPC/E water molecules in Figure 4.3, the maximum peak of the CG and SPC/E water density increased as the defect concentration decreased. The defect concentration did not greatly change the water density in the hydrophilic and hydrophobic states, and the decreasing trend was not very obvious. Overall, as the defect concentration decreased, the maximum water density on periodically defective graphene preferred to increase gradually regardless of water models. The defect concentration in graphene had a very slight impact on the water adsorption under the present conditions. It was surmised that the missing carbon atoms formed a small defect region, forming the CB state for the small defect, which typically decreased the water adsorption on the graphene coating.

4.2.2 The effect of defective surfaces on ITRs

In the present section, the effect of defect surfaces on ITRs between graphene and water was investigated, using the vibrational density of states (VDOS) method. Figure 4.4 shows the relationship between defect concentration and ITRs on flat surfaces. The ITRs were calculated between graphene and water in the present calculation models. The defect concentration cases included SV0.0, SV2.1, and SV2.8. Figures 4.4 (a) and (b) show ITR on the graphene surface under the water pressure of P3 in the CA11, CA12, CA21, and CA22 cases of Section 2.4. The ITR reported in the Cu-graphene (SV0.0)-water system [22] was around 2.39×10^{-8} K·m^2/W in the hydrophilic state, which was similar to that of 2.45×10^{-8} K·m^2/W in the present case of the SPC/E-CA21. The ITRs of the CG model were slightly higher than those of the SPC/E model, which was like in Chapter 3, because the maximum peaks of the SPC/E water density were slightly higher than those of the CG water density. The ITRs decreased slightly with increasing defect concentration. The increase in defect concentration implied a decrease in the number of C atoms in the graphene coating, and the effect of graphene decreased for the energy transfer between the liquid and the Cu surface. Assuming that the defect concentration was infinite, the liquid and Cu directly exchanged energy. From the results of Chapter 3, the S-L ITR could be greatly reduced. It was speculated that defective graphene could improve the phonon channel. Therefore, the relationship between ITR and defect concentration was usually related to the overlap of VDOS and the results are shown in Figures 4.5 to 4.7. The differences in the water models were also related to the "GCu-distance", and the definition of the "GCu-distance" was the distance between the graphene and Cu surfaces with all wettability states (such as CA11 cases) in Figure 4.4 (c). The defect concentration increased with the "GCu-distance" because the increased loss of graphene atoms resulted in a reduction in the adsorption of the graphene coating on the Cu walls. In particular, the

"GCu-distance" of the CG model was slightly larger than that of the SPC/E model, which might also be the direct factor that caused the ITRs of the CG model to be larger than that of the SPC/E model, indicating the reduced "GCu-distance" enhanced the heat transfer between the SPC/E water and Cu. In Figures 4.4 (a) and (b), the ITRs of the SPC/E and CG model under the weak wettability of Cu tended to be slightly larger than that of the strong wettability of Cu surfaces because the wettability depended on the outermost surfaces in contact with water, such as graphene.

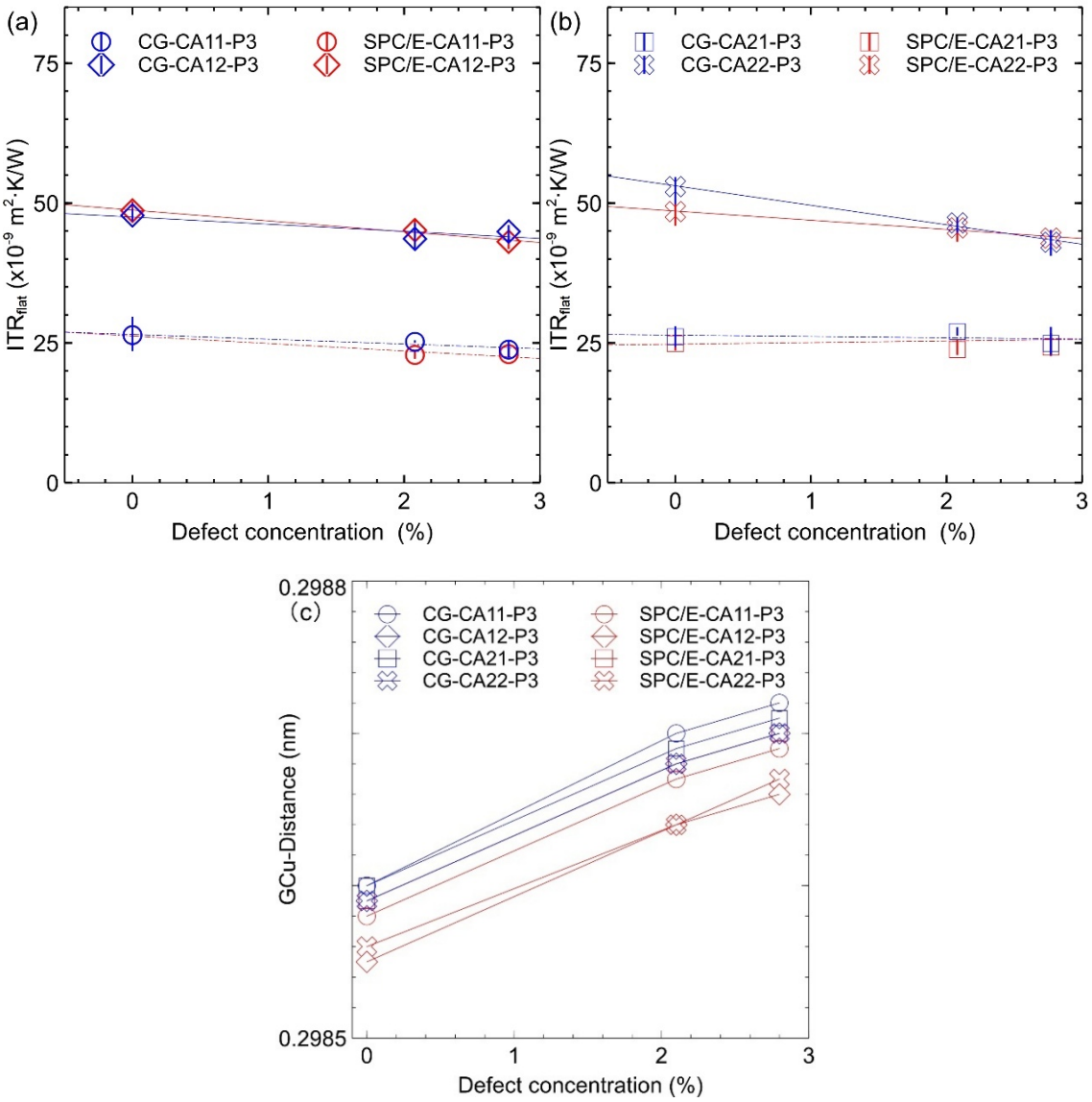

Figure 4.4 The effect of defect concentration and graphene-Cu distances on ITRs on flat surfaces. The blue and red were related to the CG and SPC/E models. (a) and (b) correspond to the CA11 (CA12), and CA21 (CA22) cases. Dot, diamond, square, and cross correspond to the CA11, CA12, CA21, and CA22 cases, respectively. The lines in (a) and (b) do not strictly fit the data points, which just shows the tendency for the ITRs to decrease according to the increase of defect concentration.

Figures 4.4(a) and (b) exhibited that the ITRs almost decreased with the increase of the defect concentration. This phenomenon was usually related to the overlap of the VDOS, which was similar to the results of previous reports [77, 78]. To evaluate the heat transfer between water molecules and the graphene coating, the VDOS was calculated by the velocity autocorrelation function (VACF, $V(t\text{-}t_0)$) of solids and water using the Fourier transform, as shown in Eq. (4.1a). The $V(t\text{-}t_0)$ in Eq. (4.1a) and Eq. (4.1b) was calculated by the velocity ($\vec{v}$) of the solids and water, such as the velocity ($\vec{v}$) of the Cu. $\vec{v}(t_0)$ and $\vec{v}(t\text{-}t_0)$ are the velocity vectors of the particle at time t_0 and $t\text{-}t_0$, respectively. <> is an ensemble average, which represents the statistical average over the time ($t\text{-}t_0$). To normalize the VDOS of the solid and water in Figures 4.5 and 4.6, the VDOS[79] was calculated using the normalization coefficient (${C_{VDOS}}^{-1}$) in Eq. (4.1c). The unit of "ω" is THz.

$$VDOS(\omega) = \int_{t_0}^{+\infty} V(t - t_0)\, e^{i\omega t} dt \tag{4.1a}$$

$$V(t - t_0) = < \vec{v}(t - t_0)\vec{v}(t_0) > \tag{4.1b}$$

$${C_{VDOS}}^{-1} . \int_{t_0}^{+\infty} V(t - t_0) d\omega = 1 \tag{4.1c}$$

Figures 4.5 and 4.6 describe the frequency and VDOS of the solids and water including the CG (in 4.5) and SPC/E (in 4.6) models. The small figures in Figures 4.5 and 4.6 describe the frequency and VDOS of the solid and water. The VDOS frequency range was from 0 to 60 THz. The curves of black, green, and blue refer to the defect concentrations of SV0.0, SV2.1, and SV2.8 at different wettability states (CA11, CA12, CA21, and CA22). The water layer thickness along the z-direction was about 1.4 nm for plotting the water VDOS and frequency. The Cu VDOS related to the VDOS peak remained almost constant for all the cases around 0–10 THz [53, 76, 80]. The VDOS frequency of the CG and SPC/E models was concentrated at 0–10 THz and 0-30 THz, which was similar to the research on the CG water and SPC/E models [81]. The graphene VDOS frequency at 0–30 THz and 40–55 THz was similar to some reports [53, 82, 83]. The overlap of VDOS between graphene and water was calculated using Eq. (4.2). α and β were related to graphene and water, respectively.

$$overlap(\omega) = \frac{\int_0^{+\infty} VDOS_\alpha(t) VDOS_\beta(t) d\omega}{\int_0^{+\infty} VDOS_\alpha(t) d\omega \int_0^{+\infty} VDOS_\beta(t) d\omega} \tag{4.2}$$

In Figures 4.5 and 4.6, the VDOS peaks D and G of defective graphene could be observed at 42 THz and around 49 THz. The VDOS G peak on the pristine graphene coating did not occur due to the pristine graphene being adsorbed by Cu surfaces to acquire a steady graphene coating [22, 25], and the VDOS G peak moved[53, 83, 84] to around 42 THz.

When the defective surfaces were coated on Cu surfaces, the VDOS G peak formed due to some graphene atoms unmatched to Cu surfaces. The experimental study of Raman spectroscopy on defective graphene [85] demonstrated a peak D with strong intensity and a peak G; meanwhile, the VDOS peak in the present cases also appeared at similar frequencies.

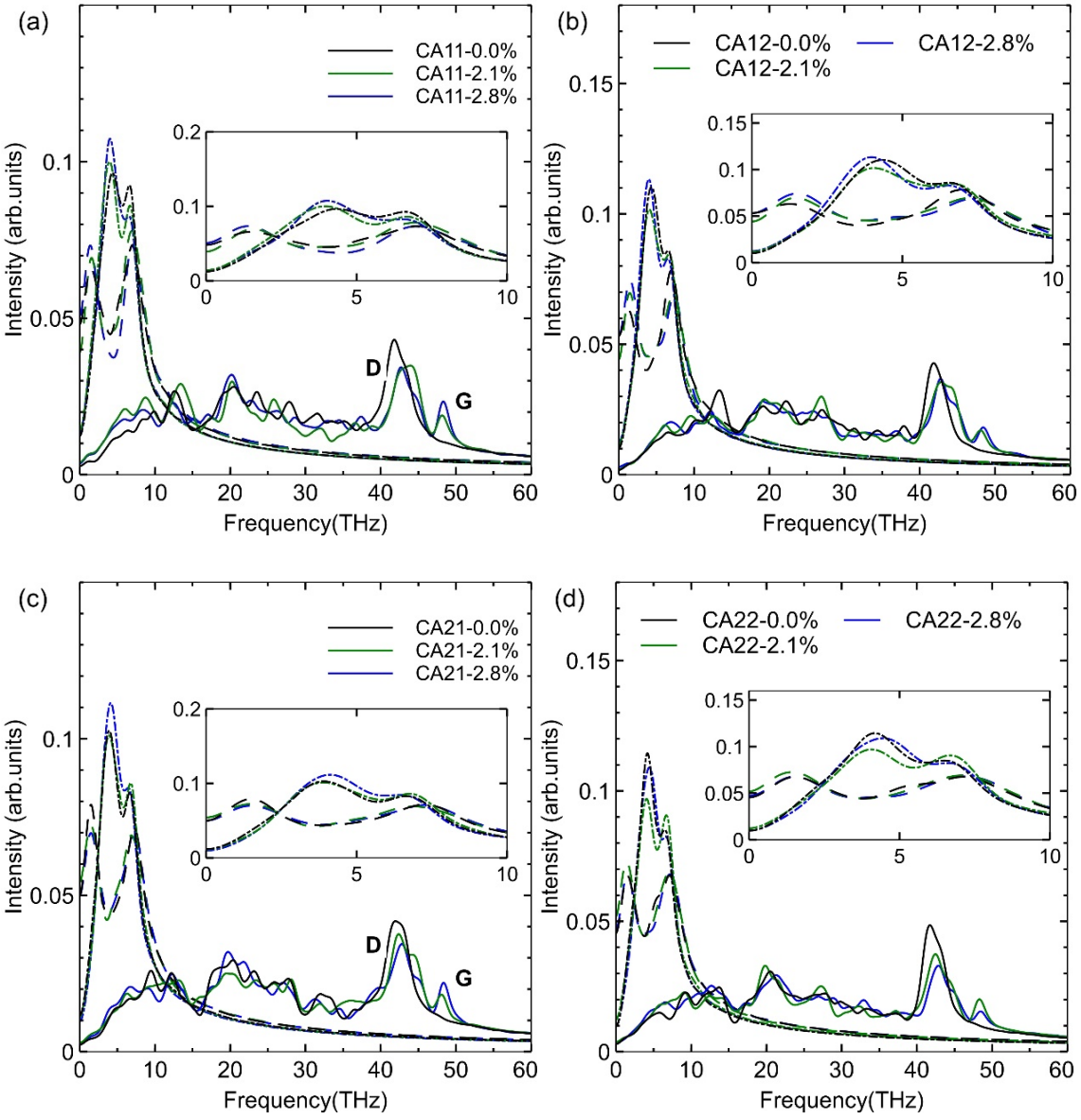

Figure 4.5 The effects of VDOS on ITRs using the CG model at various defect concentrations. The curves in black, green, and blue correspond to the defect concentrations of 0.0%, 2.1%, and 2.8%, respectively. The dashed-dotted, dashed, and solid curves in (a) to (d) after smoothing the VDOS curves are related to the water, the Cu surface near the graphene coating, and the graphene coating, respectively. The small figures in (a) to (d) describe the VDOS of the water (dashed-dotted) and Cu surfaces (dashed).

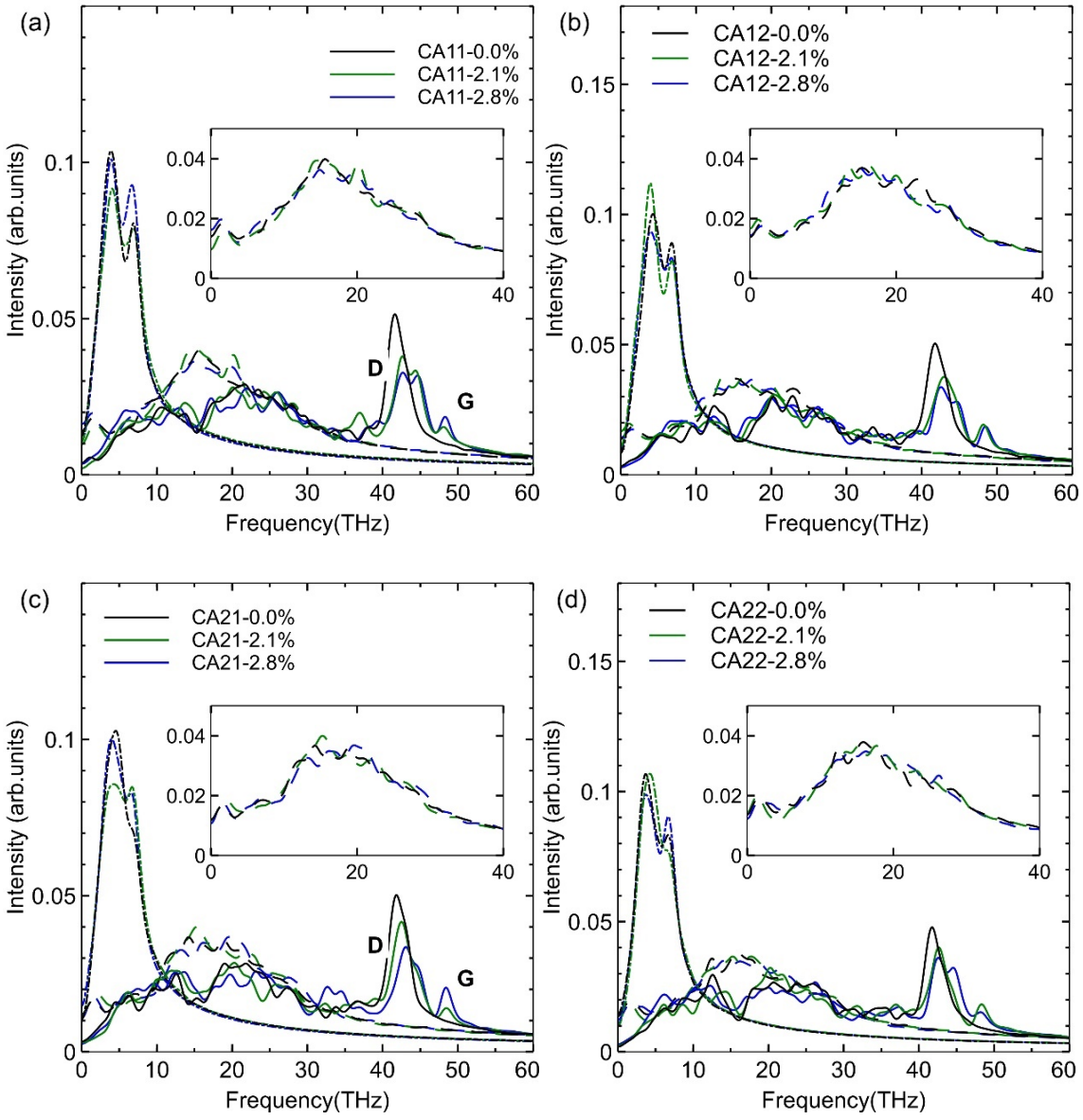

Figure 4.6 Effects of VDOS on ITRs using the SPC/E model at various defect concentrations.

The VDOS D peak was caused by structural disorder and phonon scattering [85, 86], as well as forced matching. However, the VDOS of peaks D and G peaks had a minor influence on the overlap colocation region and could not strongly affect the S-L ITRs. The VDOS intensity and frequency of the CG models were different from those of the SPC/E models, which might affect the values of the VDOS overlap, the relationships between the VDOS overlap and ITRs are shown in Figure 4.7.

In the acoustic mismatch model (AMM), the acoustic mismatch between the water and the graphene coating was usually described by the overlap of VDOS [77, 78]. The ITRs on all wettability surfaces using the CG model almost increased as the overlap of VDOS

decreased, similar to some reported trends [87]; however, the VDOS overlap using the SPC/E model could not clearly describe this like the CG model. An MD study[79] also showed that VDOS overlap and ITR mismatch might occur due to the weak interaction strength between water and the solid surface. Therefore, DDL could be considered to evaluate ITRs, as shown in Section 4.4.

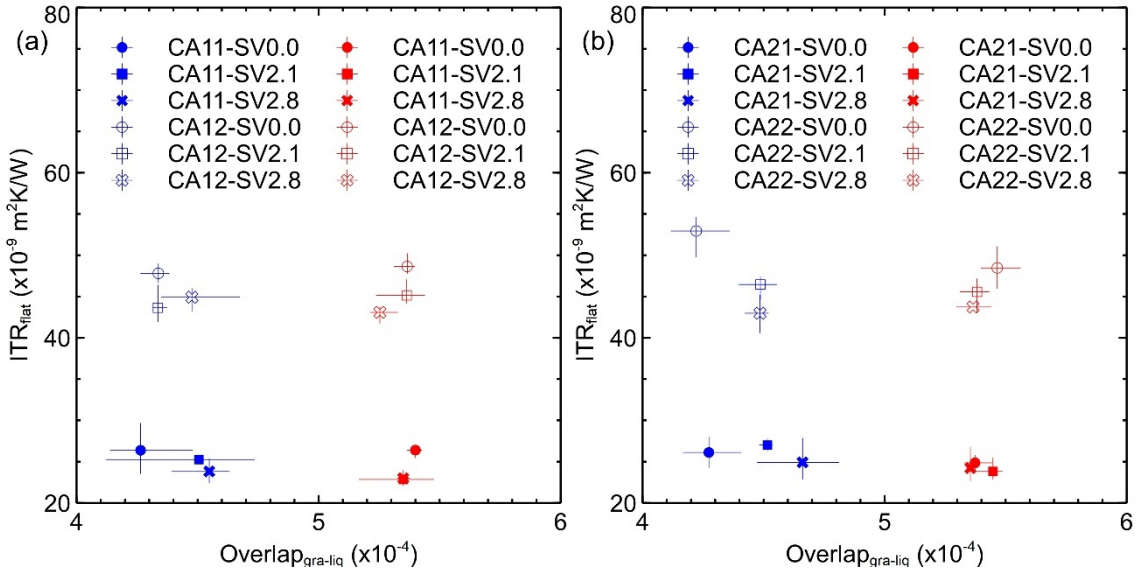

Figure 4.7 Effects of VDOS overlaps on the ITRs of the flat surfaces using the CG and SPC/E models. The red and blue correspond to the CG and SPC/E models, respectively. The solid and hollow in (a) and (b) correspond to CA11 with CA12 cases, and CA21 with CA22 cases, respectively.

4.3 The effect of defective surfaces on ITRs on nanostructure surfaces

It should be noted that the ITR definition of the nanostructure surface was previously explained in Section 2.8.4. Figures 4.8 (a) and (b) correspond to the wettability surfaces of CA11 and CA12. Figures 4.8 (a) and (b) did not clearly show the decreasing trend of ITR_f and ITR_{th} as the graphene defect concentration decreased, which might be related to the definition of ITR. The ITR_f occurred at the groove bottom surface, and the graphene was located at the top nanopillar surface to reduce the impact on the S-L ITRs. The ITR_{th} was defined between the groove bottom surface and the liquid near the graphene in the x-y plane, as shown in Figure 4.1(e), but the groove was filled with water, which indicated a larger amount of heat transferred from the liquid to the solid surface; therefore, the defective graphene did not have enough influence on the ITR_{th}. In short, the nanostructure surface with defective graphene in the Wenzel state could not effectively affect the ITRs. Based on the cases in the Wenzel state, it was speculated that defective graphene in the

CB state might affect the ITRs.

The CB state, which was carried out in MD simulations in the CA21 and CA22 cases by adjusting the number of water molecules, was also defined in Chapter 2. In Figure 4.9, it was observed that the ITR_{th} and ITR_f in the CG and SPC/E models slightly decreased with the increase in defect concentration under the wettability surfaces of CA21 and CA22. Only a limited number of water molecules contacted the Cu nanopillar sidewalls in the CB state, and most of the heat transfer between the solid and the liquid occurred on the graphene coating, which was close to the case of the flat surfaces.

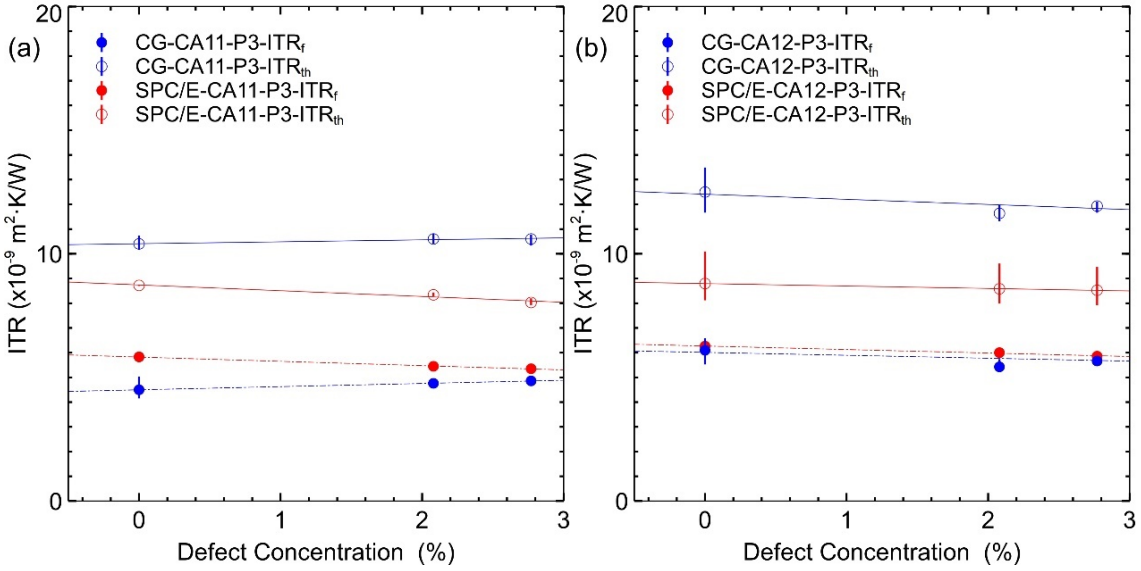

Figure 4.8 The relationship between defect concentration and ITRs on nanostructure surfaces in the Wenzel states. The blue and red correspond to the CG model and SPC/E models, respectively. The (a) and (b) correspond to the cases CA11 and CA12, respectively. The solid and hollow shapes were related to the cases ITR_f and ITR_{th}. The lines do not strictly fit the data points, which just shows the tendency for the ITRs to decrease according to the increase of defect concentration.

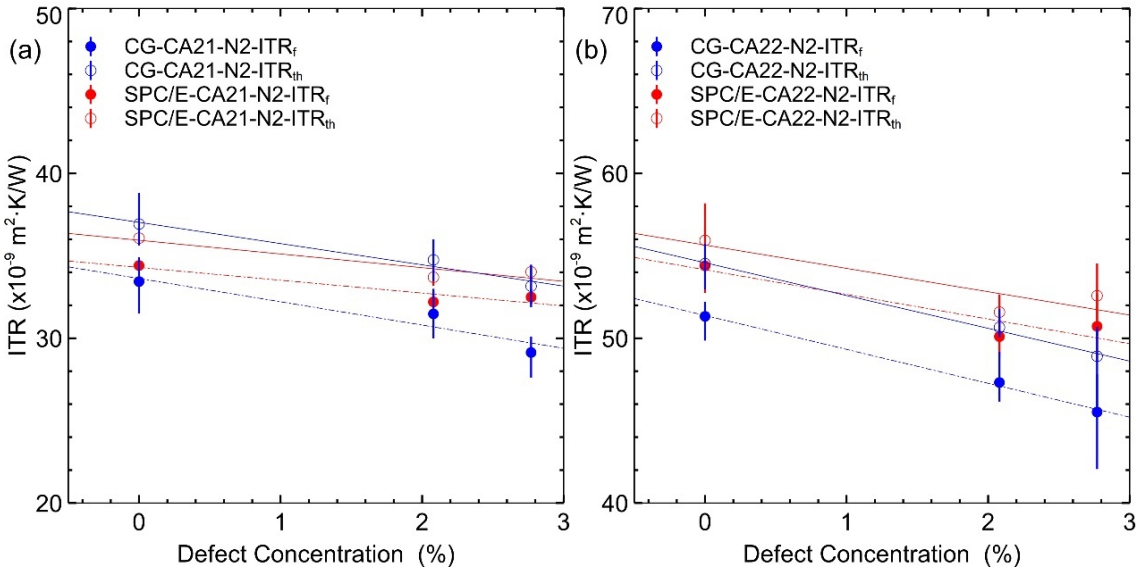

Figure 4.9 The relationship between defect concentration and ITRs on nanostructure surfaces in the CB states. The blue and red correspond to the CG and SPC/E models, respectively. The (a) and (b) correspond to the CA21 and CA22 cases, respectively. The solid and hollow shapes were related to the cases ITR_f and ITR_{th}. The lines do not strictly fit the data points, which just shows the tendency for the ITRs to decrease according to the increase of defect concentration.

4.4 Two-dimensional (2D) density contour of water on defective surfaces

The 2D density contour of water helps to understand the relationship between the defective surface and the liquid adsorption layers in the case of the CG and SPC/E models. Figures 4.10 and 4.11 show the two-dimensional local density contours related to the SPC/E model in (4.10), the CG model in (4.11), graphene, and Cu. The CA11, CA12, CA21, and CA22 cases in Figures 4.10 and 4.11 were defined in Chapter 2. Since the interaction strength in the CA12 and CA22 cases was lower than that in the CA11 and CA21 cases, water density distribution near the graphene coating was lower. When the defect concentration was 0.0%, the water density was uniformly concentrated on the graphene coating. On the defective graphene coating, there was a slightly less pronounced CG and SPC/E water density, and the uniform CG and SPC/E water density corresponding to the defective graphene was lower than that of the pristine graphene coating. From the results of 2D water density, as the graphene defect concentration increased, the density distribution of the CG and SPC/E water molecules on graphene became less significant. The 2D density of the CG water molecules was lower than that of the SPC/E model, which corresponded to the maximum peak of the 1D density profiles

between the CG and SPC/E models. In summary, the water molecules could not stay in the defective surface and the uneven density distribution of the CG and SPC/E water molecules was caused by the defect concentration between graphene and water.

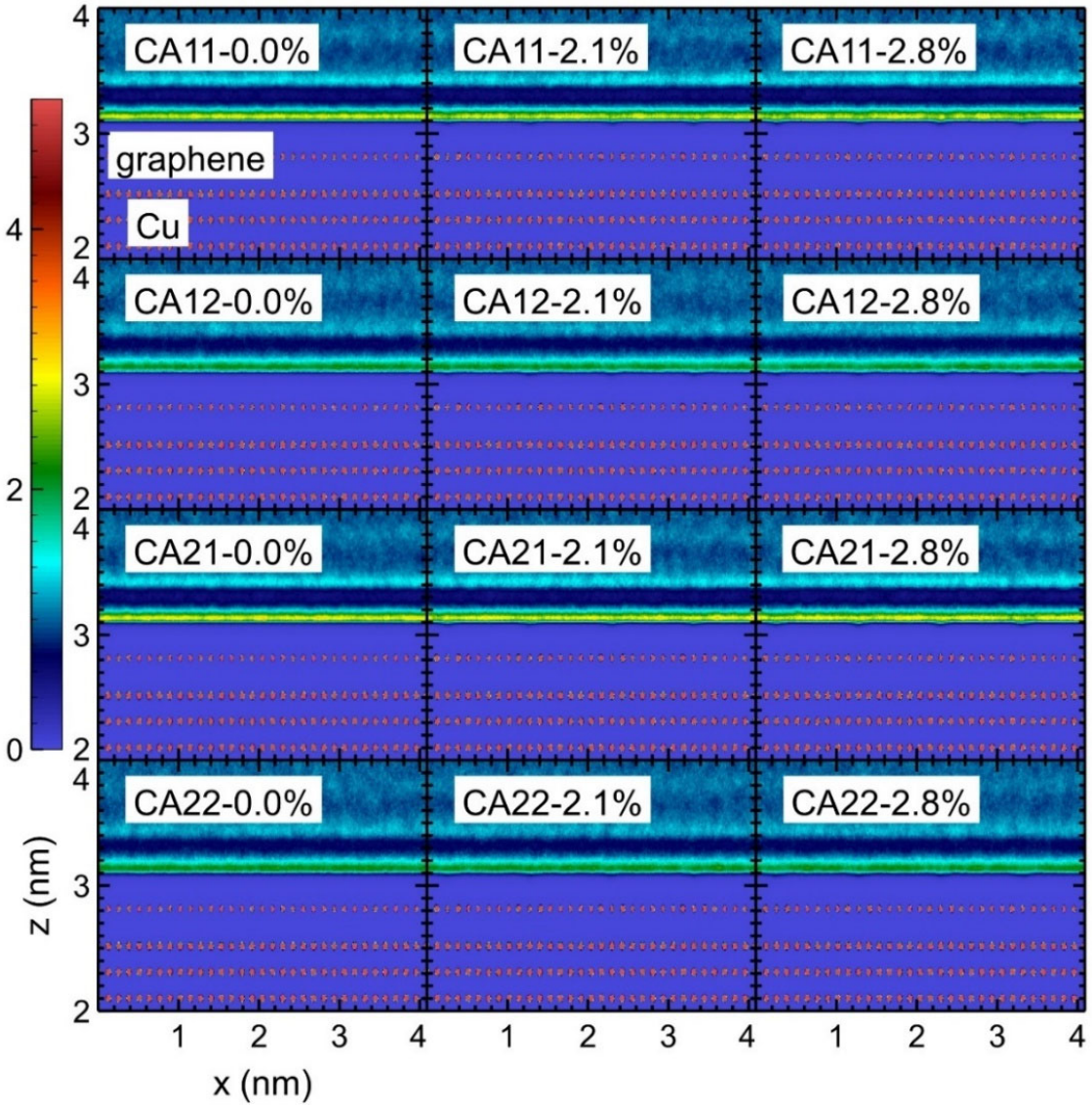

Figure 4.10 Density of two-dimensional (2D) water on the graphene surface in the case of the SPC/E model.

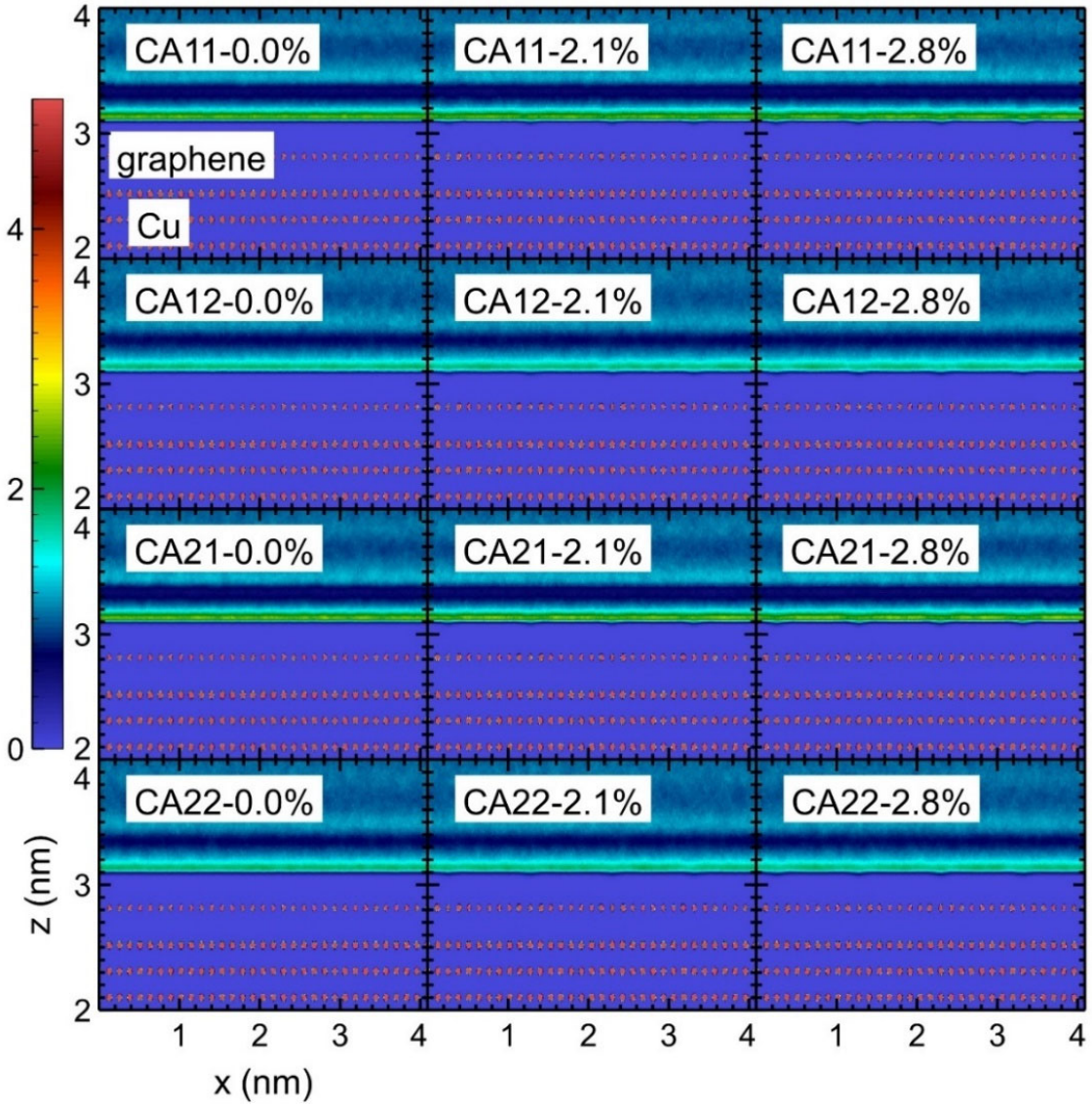

Figure 4.11 Density of two-dimensional (2D) water on the graphene surface in the case of the CG model.

4.5 Relationship between DDL and ITRs

4.5.1 Relationship between DDL and ITRs on flat surfaces

The density depletion length (DDL) contributed to understanding and evaluating the ITRs at the S-L interfaces; in general, the larger the DDL, the greater the ITR[25]. Each exponential curve of the DDL-ITR included various water wettability states and was calculated using Eq. (3.2). Figure 4.12 shows the relationships between DDL and ITR on a flat surface. The DDL value of around 0.142 nm in the case CA11-SPC/E-P3 was similar to the DDL values of around 0.151 nm, which were calculated in the SPC/E water-Si (111) coated with single-layer graphene under approximate wettability conditions at the contact angle of around 90 degrees [25].

Compared with the Cu-water system in Chapter 3, the average values of the DDL increased by about 0.03 nm, which obviously represented an increase in the S-L interface by the graphene coating. The exponential curves of the DDL-ITR were lower than that of the case in Chapter 3, which indicated that if the ITR had the same value, the DDL on the graphene coating was larger than that in Chapter 3, regardless of water models. The interaction between the graphene coating and water was different from that between Cu and water. The DDL of the present section was greater than that in Chapter 3 due to the different S-L interactions; the ITR of the present section was larger than that in Chapter 3 because the graphene coating weakened the phonon channel to increase the ITR. Since the ITR strongly depended on the solid surface, the ITR on the graphene coating surface was different from the ITR on the Cu surface. In short, these differences caused the exponential curve in the present chapter inconsistent with that in Chapter 3.

The DDL-ITR was not significantly affected by the defect surfaces, and the case of defect concentrations was also included in the DDL calculation, as shown in Section 2.9; in most cases, the DDL values remained almost constant even when the defect concentration increased; the S-L interface between water and defect surfaces did not change because the single vacancy in the graphene coating could not accommodate the water molecules. The red exponential curves of the SPC/E model were higher than those of the CG model, which was similar to the results of Chapter 3; the main reason was that the DDL in the cases of the SPC/E model was smaller than that in the cases of the CG model under approximate conditions. For all data points containing various wettability and graphene defect concentrations, the growth trends between ITRs and DDL roughly followed exponential trends, which remained feasible for predicting ITRs. The details of the fitting coefficient are given in Table 4.1.

Table 4.1 The coefficients of the exponential curve on flat surfaces.

Exponential curves	A_d (10^{-9} K·m^2/W)	nd (nm^{-1})	CoD
CG	0.56	22.5	0.92
SPC/E	1.14	21.4	0.96

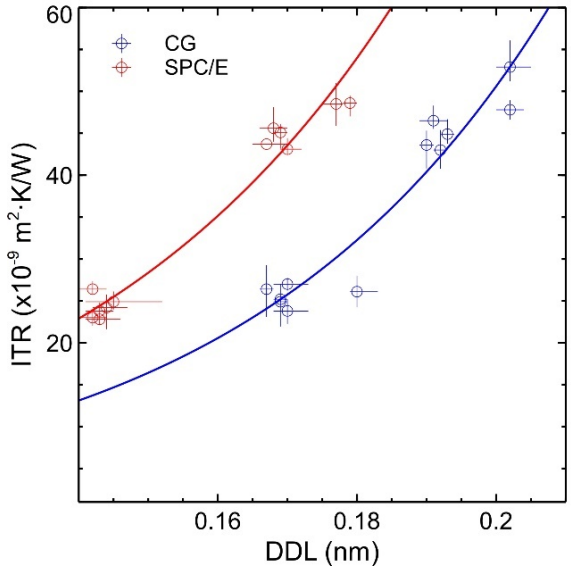

Figure 4.12 The DDL and ITR on flat surfaces. The red and blue correspond to the SPC/E and CG models, respectively.

4.5.2 Relationship between DDL and ITRs on nanostructure surfaces

In order to study the effect of defect concentration on the relationship between DDL and ITR of the nanostructure surfaces, Figure 4.13 shows the relationships of the nanostructure surfaces between the S-L ITR and DDL in the Wenzel and CB states. Figures 4.13 (a) and (b) correspond to the ITR_f and ITR_{th}, respectively. The circles of the SPC/E (as depicted in red) and CG (as depicted in blue) models correspond to the Wenzel states, including the cases CA11 and CA12 with the defective graphene coatings. The crosses and diamonds correspond to the cases CA21 and CA22 in the CB states. The solid, dashed, and dashed-dotted correspond to the ITR_f and ITR_{th} of the exponential curves and contained various wettability states and the defective graphene coating.

In the Wenzel state, the data points of DDL and ITR were very close to the exponential curve of Chapter 3. A single-layer graphene coating that only covered the top nanopillar surface was different from the flat surface of the present chapter, which led to a small increase in DDL compared with Chapter 3; the groove of the nanostructure mainly facilitated energy transfer between Cu and water, as in Chapter 3, which might cause the data points of ITR and DDL to be close to the exponential curve of Chapter 3 and not strictly follow that. In the CB state, energy transfer on the nanostructure surface was mainly between the top nanopillar surface and water, and the top nanopillar surface of Chapter 3 was the Cu surface. The DDL almost depended on the groove of the

nanostructure surface, similar to Chapter 3. Therefore, the ITR of the present chapter increased larger than that of Chapter 3, which made the DDL-ITR curves of the present chapter slightly larger than those of Chapter 3.

The fitting coefficient of the SPC/E and CG models in the Wenzel state was just above 0.70. The details of the fitting coefficient are given in Table 4.2. The relationship in the Wenzel state between DDL and ITRs could be roughly related to the exponential growth trend, which indicated that DDL could roughly evaluate the ITRs. However, the relationship was not confirmed strictly because the defect concentration did not significantly increase or decrease DDL and ITRs.

Table 4.2 The coefficients of the exponential curve on nanostructure surfaces

Exponential curves	A_d (10^{-9} K·m^2/W)	nd (nm^{-1})	CoD
CG-CA11(CA21)-ITR$_f$	0.43	11.2	0.71
CG-CA11(CA21)-ITR$_{th}$	2.13	7.45	0.73
CG-CA21-ITR$_f$	12.1	1.14	0.62
CG-CA21-ITR$_{th}$	13.9	1.11	0.69
CG-CA22-ITR$_f$	13.0	1.55	0.87
CG-CA22-ITR$_{th}$	16.0	1.39	0.87
SPC/E-CA11(CA21)-ITR$_f$	1.84	6.31	0.73
SPC/E-CA11(CA21)-ITR$_{th}$	2.94	6.01	0.74
SPC/E-CA21-ITR$_f$	10.16	1.43	0.93
SPC/E-CA21-ITR$_{th}$	11.38	1.35	0.92
SPC/E-CA22-ITR$_f$	9.67	2.03	0.94
SPC/E-CA22-ITR$_{th}$	10.84	1.93	0.94

The dashed and dashed-dotted exponential curves of the SPC/E and CG models were distinguished by the cases CA21 and CA22 in the CB state. The fitting coefficient between DDL and ITRs using the SPC/E and CG models in the CA21 and CA22 cases ranged from 0.62 to 0.94 because the DDL did not change much and there were only two types of the number of water molecules (water pressure). In the SPC/E water models, the additional reason was that the ITRs also did not change much, which increased the fitting coefficient of the SPC/E model. Compared with the DDL-ITR$_f$ and DDL-ITR$_{th}$ in Chapter 3, there seemed to be also an exponential intersection between the Wenzel and CB states under the defective graphene coating. The values of DDL and ITR in each case were similar in the Wenzel state. In addition, the different wettability in the CB states split the exponential curve of the DDL-ITRs into two. In Figure 4.13, the relationship of DDL-ITR in the SPC/E and CG models roughly was examined to the exponential curve on the graphene coating because DDL did not change so much in the cases of various graphene surfaces. It could be inferred that the different wettability was primarily responsible for the tearing exponential curves on the nanostructure surface in the CB state.

The ITRs in the CA21 cases were less than those in the CA22 cases because the

wettability became weaker. The DDL in the CB state strongly depended on the distance between the position of the liquid in the groove and the groove bottom surface, and this distance was included in the definition of the actual CB state in Chapter 2. In the CB state, different wettability mainly changed the distance between the solid and liquid. The distance between the position of the liquid in the groove and the groove bottom surface did not change too much, as shown in Figure 6.4. Different wettability with the same number of water molecules almost maintained a similar thickness of the penetration liquid, which indicated wettability could not change DDL in the CB state so much. Therefore, different wettability resulted in two exponential curves in the CB state. In short, the exponential curves of the CB state between DDL and ITR are almost determined by the wettability.

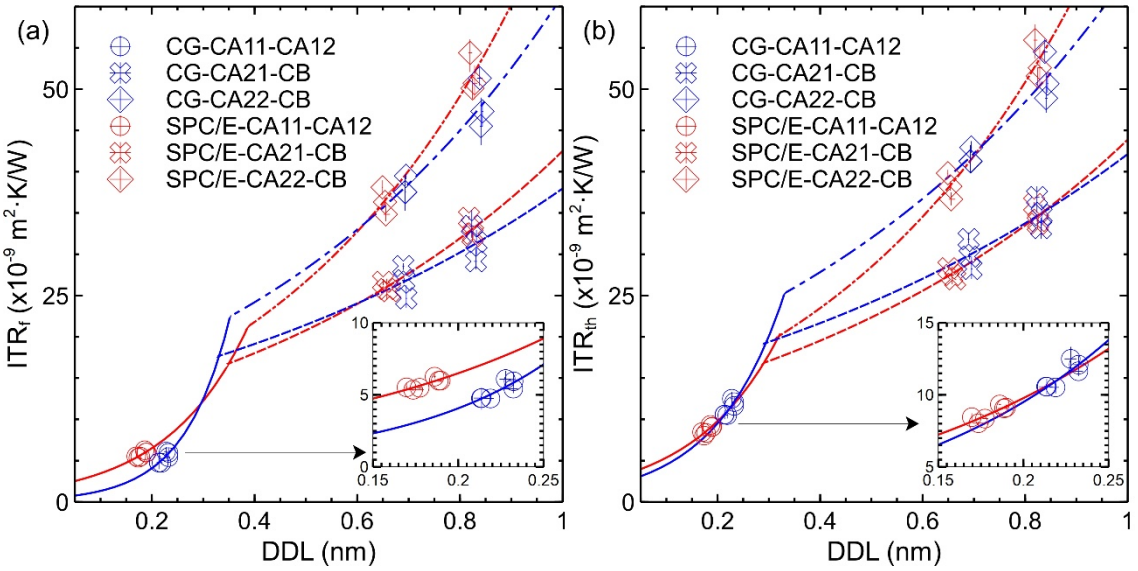

Figure 4.13 The DDL and ITR for different wettability states and defect concentrations. The red and blue correspond to the SPC/E and CG models, respectively. The circles, crosses, and diamonds correspond to the Wenzel state, the cases CA21 of the CB state, and the cases CA22 of the CB state, respectively. (a) and (b) referred to the ITR_f and ITR_{th} of nanostructure surfaces. The number of water molecules in the CB state was related to the cases of N1 and N2.

5 Application of TCMs in water-Cu systems

In Chapter 5, the influences of nanopillar width and water pressure on the relationship between the ITRs calculated by MD simulations and those predicted by thermal circuit models (TCMs) were investigated in the water-Cu systems. The computational models and numerical details are introduced in Section 5.1. The effects of water pressure on the relationship between ITRs calculated by MD simulations and those predicted by TCMs are shown in Section 5.2. The effects of nanopillar widths on the relationship between ITRs calculated by MD simulations and those predicted by TCMs are described in Section 5.3.

5.1 Calculation models and numerical details

In the present chapter, the thermal resistances (R) of flat surfaces and six TCMs were used to predict the ITR_{MD} of a nanostructure surface calculated by MD simulations. The calculation method of ITR_{MD} and the values of ITR_{MD} were described in Chapter 2 and presented in Chapter 3, respectively. ITR_{Model} was calculated based on six TCMs, which were explained in Section 2.8.2. It should be emphasized that there was a difference between thermal resistance (R) and ITRs. The main difference between R and ITR was that the unit of R is K/W, and the unit of the ITR is $K \cdot m^2/W$; the details of those differences have been shown in Section 2.8. The related tables and figures in the Appendix were shown by only one of three MD simulations. The root mean square error (δ, RMSE) is usually used to evaluate the difference between the predicted and observed values[88], as shown in Eq. (5.1).

$$\delta(*) = \sqrt{\frac{\sum_{i=1}^{N}(ITR_{MD,i} - ITR_{Model,i})^2}{N}};\ *\in A \text{ to } F \tag{5.1}$$

The unit of δ is 10^{-9} $K \cdot m^2/W$, and the predicted and observed values were related to ITR_{Model} and ITR_{MD} in the present chapter, respectively. The smaller the RMSE, the more accurate the predicted model. For example, δ(A) represents the RMSE value of model A in the present study. The "N" denotes the number of conditions in the case of model * in Eq. (5.1).

5.2 The effect of water pressure on the relationship between ITR_{MD} and ITR_{Model}

5.2.1 The effect of water pressure on ITR_{flat} calculated by MD

Water pressure was a very important factor affecting the ITR, which was considered in the present section. The S-L thermal resistance (R_{flat}) determined by MD simulations has

a correlation with water pressure [18]. Figure 5.1 illustrates the relationship between R_{flat} at the S-L interfaces and water pressure on flat surfaces under hydrophilic (CA1) and hydrophobic (CA2) conditions using the CG and SPC/E models. As the water pressure increased, the S-L R_{flat} decreased almost linearly, regardless of the water models and surface wettability; this phenomenon occurred because higher water pressure resulted in a denser packing of water molecules on the solid surfaces, which significantly enhanced the S-L coupling, thus facilitating heat transfer. The increased water pressure also provided more phonon transmission channels, which further enhanced the phonon transport between the solid and liquid, thereby reducing the thermal resistance [18]. The ITRs of the CG and SPC/E models were higher in the CA2 cases compared to the CA1 cases. In addition, the ITRs in the cases of the CG model were slightly higher than those in the cases of the SPC/E model in the CA1 cases, according to Chapter 3, probably because the maximum peak of the water density of the CG model was lower than that of the water density of the SPC/E model. In order to describe the relationship between S-L R and water pressure, a linear relationship was used approximately. The relationships depicted in the fitting lines of Figure 5.1 were utilized to derive $R_{S\text{-}liq^*}$ in the thermal circuit models (TCMs) by incorporating water pressure as a variable. The detailed values of water pressure and the number of water molecules on flat surfaces are given in Table S3.1 of the Appendix.

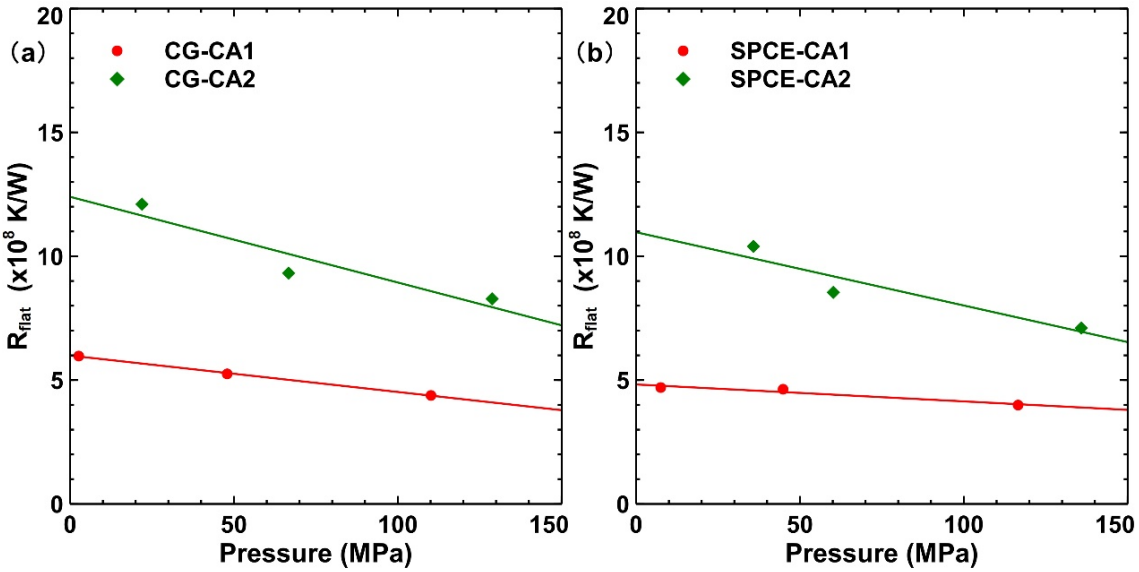

Figure 5.1 Relationship between S-L R_{flat} and water pressure (Pressure) in Cu-water systems. An approximate line was used to describe the relationship between R and water pressure. The green and red correspond to the fitting lines between R_{flat} and water pressure in the CA1 and CA2 cases, respectively. The coefficients of the green and red fitting functions in (a) and (b) are given in Table 5.1. The value of water pressure was similar to the previous report [18].

Table 5.1 The coefficients of green and red fitting functions (y=aa·x+bb) in Figure 5.1.

Lines	aa	bb	CoD
CG-red	-0.0147	5.99	0.99
CG-green	-0.0346	12.4	0.88
SPC/E-red	-0.0068	4.82	0.93
SPC/E-green	-0.0296	10.97	0.88

5.2.2 TCMs in the Wenzel state

To better understand the performance of TCMs, the case of the Wenzel state was first considered in the present section. In Figures 5.2 to 5.4 and 5.7, the dots, diamonds, and squares correspond to various water pressures of P1, P2, and P3; the blue and red represent the CG and SPC/E models for all cases; the pressure conditions decreased on the nanostructure surfaces in the order of P1, P2, and P3, and the number of the CG and SPC/E water molecules are given in Table S3.2 of the Appendix.

In the present chapter, the general CB state implied that the liquid water molecules did not penetrate into the grooves on the rough surface at all [39]. The CB state in the MD simulations referred to the cases where the liquid water did not fully penetrate to the bottom of the groove along the z-direction. The CB states were determined in MD simulations based on the distance between the position where water density drops below 0.01 g/cm³ and the groove bottom surface, which exceeded 0.2 nm; when the water molecules within the groove met these criteria, the CB state was considered the actual CB state, which differed from the general CB state. In the general CB state, no liquid water was present in the groove, and the present assumption was applied to the TCMs. Consequently, in the general CB states, the L_{NANO} in R_{liq} was assigned very small values to effectively sever the heat path on the right side of the TCMs diagrams shown in Figure 2.10, and R_{liq} was considered to be nearly infinite.

Models A to F were developed based on the data of water pressures ranging from P1 to P3, including scenarios with varying nanopillar widths in both the Wenzel and CB states. It was important to note that the pressure conditions decrease sequentially from P1 to P2 and P3.

Figure 5.2 presents a comparison between the ITR_{Model} predictions from the TCMs and the ITR_{MD} values derived from MD simulations in the Wenzel and actual CB states using models A and B. The ITRs predicted by the TCMs deviated significantly from the black line across the water models when considering the general CB states, with all δ values in Figures 5.2 to 5.4 exceeding 12.0. To validate the accuracy of the TCMs, the δ values were firstly discussed only in the Wenzel state (ITRs<25 $K \cdot m^2/W$).

The δ(A)-P1 to δ(A)-P3 values of the CG model in the Wenzel state from P1 to P3, including the nanopillar widths of S19 and S14 for all cases in Section 5.2, were 1.70, 4.21, and 6.52, respectively, as shown in Figure 5.2(a). The corresponding δ(B)-P1 to δ(B)-P3 values were 0.98, 3.34, and 5.67, as shown in Figure 5.2 (b). For the SPC/E

model, the δ(A)-P1 to δ(A)-P3 values in the Wenzel state from P1 to P3 were 1.88, 3.72, and 5.60, respectively, as shown in Figure 5.2 (a), and the δ(B)-P1 to δ(B)-P3 values were 1.96, 3.77, and 5.77, as shown in Figure 5.2 (b). The water pressure dependence was incorporated into the TCMs, as explained in the discussion of Figure 5.1. Therefore, the δ(A) and δ(B) values based on the CG and SPC/E models were also influenced by water pressure. Lower water pressure resulted in lower TCM accuracy because the $R_{S\text{-}liq*}$ in ITR_{Model} was dependent on water pressure, and models A and B assumed that heat flow was transported exclusively along the z-direction. The ITR_{Model} values predicted by models A and B were similar to those of ITRs on flat surfaces under comparable water pressures, with the rate of ITRs decreasing with decreasing water pressure. The values of the δ(A) and δ(B) exhibited under the influences of water pressure, and there was no major difference between the SPC/E and CG models when models A and B were used to predict the ITRs.

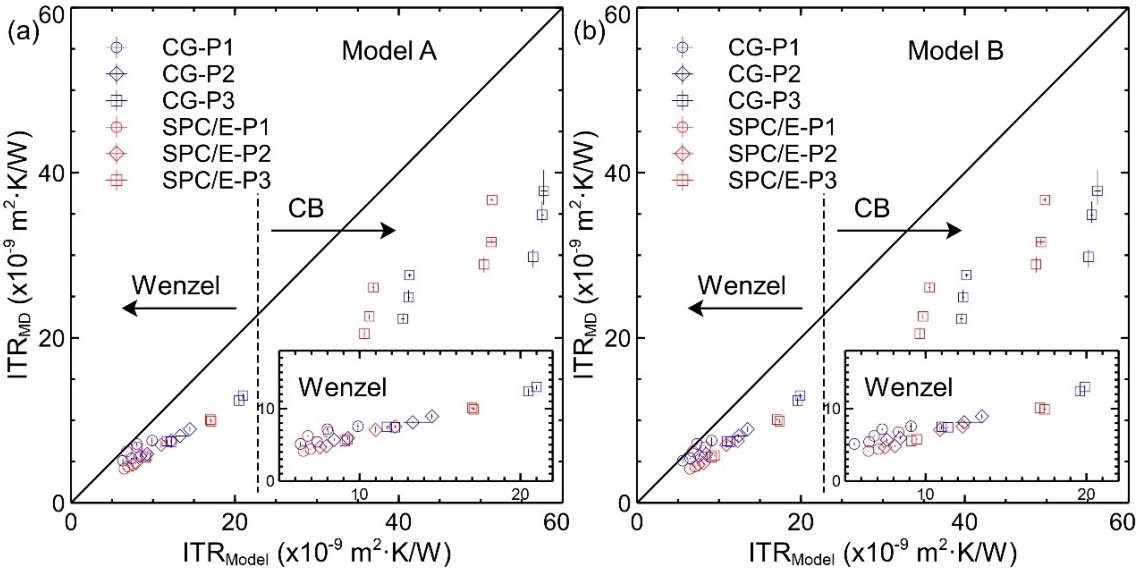

Figure 5.2 Influence of water pressure on the relationships between ITR_{MD} and ITR_{Model} in the Wenzel and general CB states. (a) and (b) refer to models A and B. The dots, diamonds, and squares represent various water pressures of P1, P2, and P3 for all cases. The blue and red correspond to the CG and SPC/E models for all cases.

Meanwhile, there was no significant difference between models A and B. The detailed values of local thermal resistances are shown in Table S5.1 and Figures S5.1 to S5.12 in the Appendix. For example, for all cases in the CG model, the range of R_{Cu} and $R_{S\text{-}liq1}$ in the present chapter was from 0.13×10^9 K/W to 0.00054×10^9 K/W and from 3.45×10^9 K/W to 0.58×10^9 K/W, respectively; for all cases in the SPC/E model, the range of R_{Cu} and $R_{S\text{-}liq1}$ in the present chapter was from 0.13×10^9 K/W to 0.00054×10^9 K/W and from 3.07×10^9 K/W to 0.07×10^9 K/W, respectively. The thermal resistance value of Cu (R_{Cu}) was a small proportion of $R_{S\text{-}liq1}$, so whether it was the thermal conductivity in the experiments or that

calculated by MD, the role of R_{Cu} in TCM was limited. The thermal resistance of water (R_{liq}) was slightly different from the thermal conductivity in the experiments and that calculated by MD, but this difference was still not dominant in the TCM result. For example, for all cases in the CG model, the R_{liq} proportion of R in the right path of heat transfer was below 17%, and for all cases in the SPC/E model, the difference between R_{liq} calculated by the thermal conductivity of MD and that of the experimental thermal conductivity was below 12% of R in the right path of heat transfer. Therefore, models A and B show similar prediction values.

It was assumed that the heat flow in models A and B only passed through the top nanopillar surface and the groove bottom surface. The rate of heat flow in the right path of heat transfer calculated by MD was always larger than that derived by TCMs, as shown in Figures S5.23 (a) and (b) of the Appendix, indicating the heat flow rate in TCM could not match that in MD simulations, therefore, models A and B could not accurately predict the ITR calculated by MD simulations. As explained before, models A and B did not take into account the heat flow on the nanopillar sidewalls. Meanwhile, in the cases of the heat flow in models A and B, the Q calculated by MD simulations in the CB state was roughly close to that derived from TCMs, although the ITRs predicted by the TCMs still had a large deviation from the ITRs calculated by MD simulations. Therefore, the energy transfer on the nanopillar sidewalls was an important factor in the reasonable construction of TCM.

Models C and D were built on the assumption of similar temperatures in the nanopillar sidewalls and the groove bottom surface, which could be confirmed in the 2D temperature distribution of water and solids, as shown in Figures S5.17 to S5.22 of the Appendix. The δ(C)-P1 to δ(C)-P3 values of the CG model in the Wenzel state from P1 to P3, including the nanopillar widths of S19 and S14 for all cases in Section 5.2, were 0.48, 1.16, and 1.26, respectively, as shown in Figure 5.3(a). The corresponding δ(D)-P1 to δ(D)-P3 values were 0.97, 0.18, and 0.37, as shown in Figure 5.3(b). For the SPC/E model, the δ(C)-P1 to δ(C)-P3 values in the Wenzel state from P1 to P3 were 1.00, 0.56, and 0.65, as shown in Figure 5.3(a), while the δ(D)-P1 to δ(D)-P3 values were 0.85, 0.99, and 1.24, as shown in Figure 5.3(b). The δ(C) values of the CG model and the δ(D) values of the SPC/E model followed a trend similar to that of models A and B. However, this similarity might be coincidental because the δ(D) values for the CG model and the δ(C) values for the SPC/E models exhibited an opposite trend. A possible explanation for this, similar to models A and B, was that water pressure and heat transfer directly influenced the outermost solid surface in the x-y plane. In contrast, for models C and D, water pressure and heat flow also impacted the nanopillar sidewalls. Models C and D were less dependent on water pressure, as the heat transfer path at the S-L interface was fully considered, as shown in Figure 2.10. As a result, the predictive accuracy of models C and D was improved compared to models A and B. There was also no significant difference in the Wenzel state between models C and D because of the same reason as models A and

B. The detailed values of local thermal resistances are shown in Table S5.1 and Figures S5.1 to S5.12 in the Appendix.

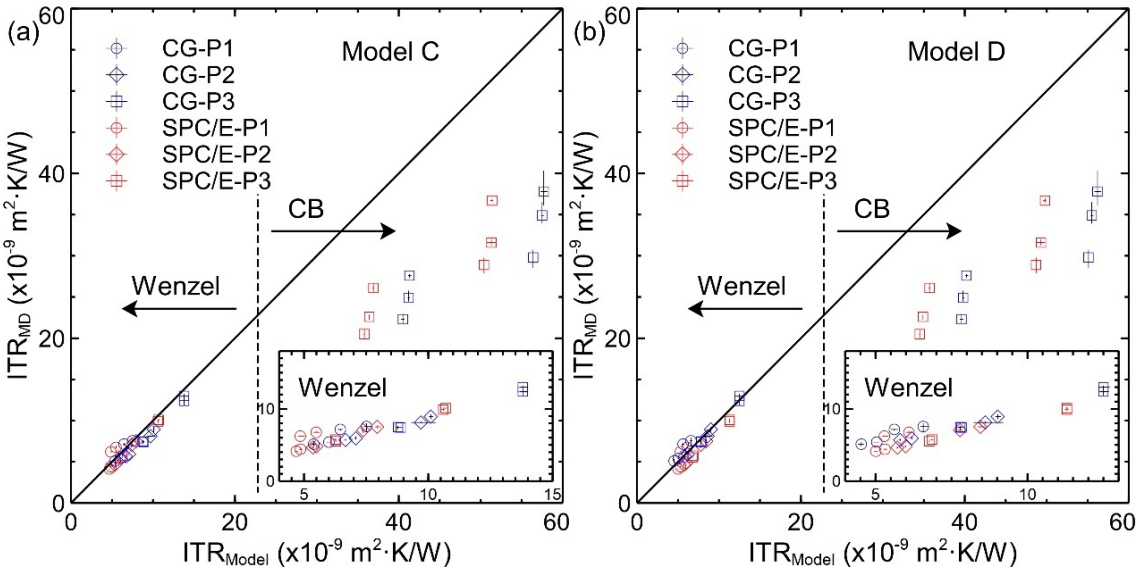

Figure 5.3 Influence of water pressure on the relationships between ITR_{MD} and ITR_{Model} in the Wenzel and general CB states. (a) and (b) refer to models C and D.

For the CG model, the δ(E)-P1 to δ(E)-P3 values in the Wenzel state from P1 to P3, including the nanopillar widths of S19 and S14 for all cases in Section 5.2, were 0.89, 0.32, and 0.28, respectively, as shown in Figure 5.4(a). The corresponding δ(F)-P1 to δ(F)-P3 values were 1.67, 0.74, and 1.03, as shown in Figure 5.4(b). For the SPC/E model, the δ(E)-P1 to δ(E)-P3 values in the Wenzel state from P1 to P3 were 1.14, 0.24, and 0.24, respectively, as shown in Figure 5.4(a), while the δ(F)-P1 to δ(F)-P3 values were 1.10, 0.22, and 0.28, as illustrated in Figure 5.4(b). Most of the δ(E) and δ(F) values exhibited small deviations, especially at relatively low water pressures.

Models E and F were based on the different temperatures in the top nanopillar surface, the nanopillar sidewalls, and the groove bottom surface. In models E and F, the heat flow was in several parallel processes, involving energy transfer between the top nanopillar surface in the x-y plane and water, that between the nanopillar sidewalls in the y-z plane and water, and that between the groove bottom surface in the x-y plane and water. These heat transfer processes almost followed the principle of a Wheatstone unbalanced bridge, approximating the actual heat transfer process on nanostructure surfaces. Consequently, models E and F indicated a good prediction accuracy compared to the other models.

The detailed values of local thermal resistances are shown in Table S5.1 and Figures S5.1 to S5.12 of the Appendix. The R_{Cu} and R_{liq} are divided into smaller values, like R_{Cu*} and R_{liq*}. For example, for all cases in the CG model, the range of R_{Cu} and $R_{S\text{-}liq1}$ in the present chapter was from 0.06×10^9 K/W to 0.00027×10^9 K/W and from 1.73×10^9 K/W to 0.29×10^9 K/W, respectively; for all cases in the SPC/E model, the range of R_{Cu} and $R_{S\text{-}liq1}$ in

the present chapter was from 0.06×10^9 K/W to 0.00027×10^9 K/W and from 1.54×10^9 K/W to 0.35×10^9 K/W, respectively. Therefore, the TCM model constructed using the thermal conductivities of the solids and water from MD simulations and experiments could not significantly affect the ITR_{Model}, and the R_{Cu} and R_{liq} had limited effect on the TCM prediction, so the prediction values in model E were similar to those in model F.

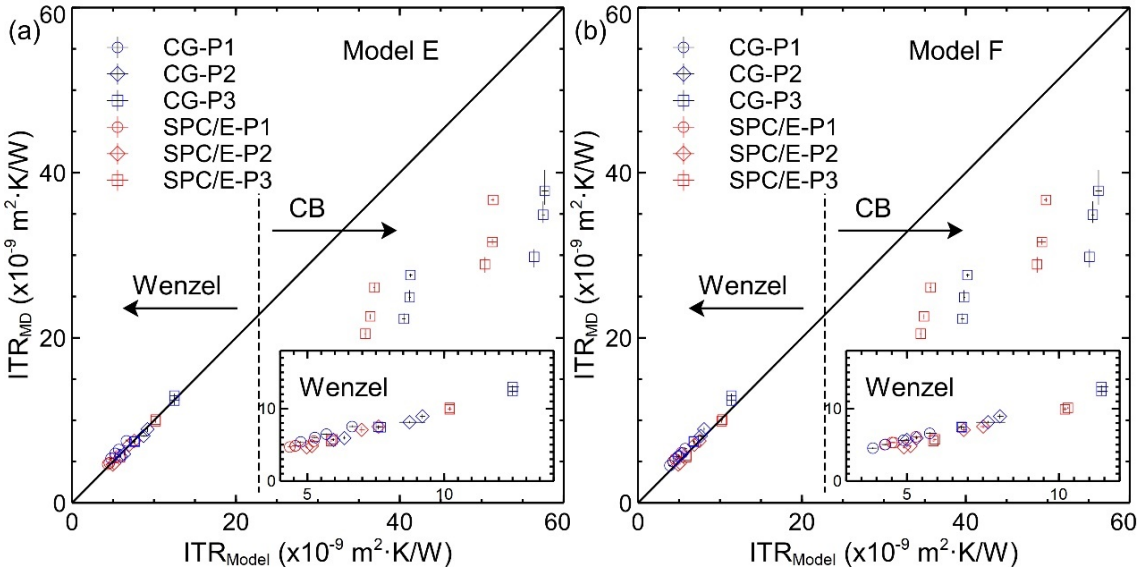

Figure 5.4 Influence of water pressure on the relationships between ITR_{MD} and ITR_{Model} in the Wenzel and general CB states. (a) and (b) refer to the models E and F.

5.2.3 TCMs under a correction of contact region thickness

To improve the performance of TCM in the CB state based on the previous section, it was necessary to add a correction about the contact region thickness. Figures 5.2 to 5.4 demonstrate that the data points in the general CB states under the pressure condition of P3 deviated significantly from the black straight line. When considering the Wenzel and general CB states, the δ values exceeded 12.0 within the water pressure range (10 to 40 MPa) because models C to F resembled models A and B in that all heat transfer paths from water to the solid bottom became identical once R_{liq} approached infinity. Models C to F did not accurately predict heat transfer paths in the general CB states. Consequently, it was essential to consider heat transfer from the nanopillar sidewalls, even in the CB state, which was the actual CB state.

Figure 5.5 depicts the 1D density profile of the SPC/E and CG water molecules in the actual CB states along the z-direction. It was observed that the maximum peak of the SPC/E water density was larger than that of the CG water density. A possible reason for this was that the SPC/E model might not accurately represent the water density around 250 K, showing values higher than the experimental data, while the CG model aligned more closely with the experimental values [16]. Water molecules did not fill the groove due to the weak van der Waals forces between water and Cu. The penetration thickness

of water molecules in the groove, as shown in Figure 5.5, depended primarily on the water pressure, which was adjusted by the number of water molecules in the Cu-water systems. Increasing the number of water molecules to increase the water pressure resulted in more water molecules penetrating the grooves.

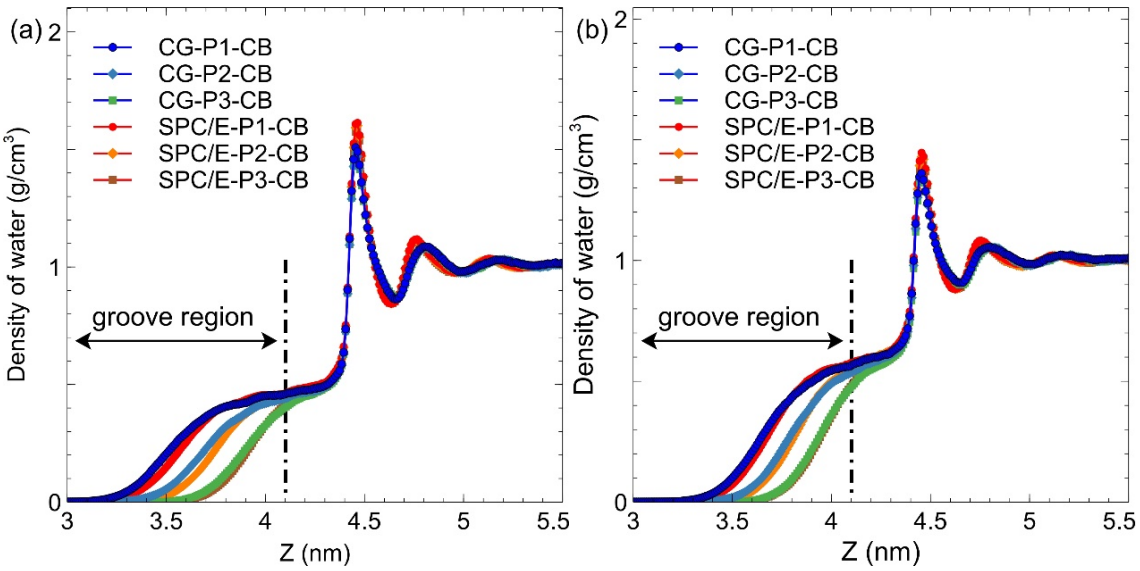

Figure 5.5 1D density profile of the CG and SPC/E water molecules along the z-direction in the actual CB states. The dots, diamonds, and squares correspond to the different water pressures of P1, P2, and P3. The nanopillar widths of 1.91 nm and 1.40 nm were related to S19 in (a) and S14 in (b), respectively. The water pressure ranged from 10 to 40 MPa (P3 to P1).

In order to describe the contact region between the nanopillar sidewalls and water molecules approximately, a scheme for calculating the contact region thickness was proposed in the present study, as shown in Figure 5.6.

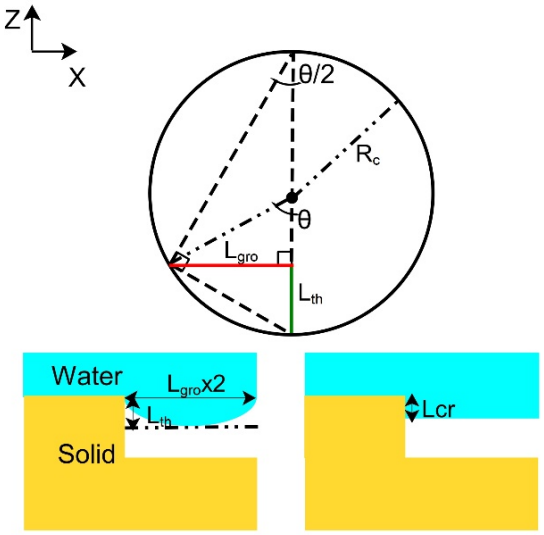

Figure 5.6 Calculation method of the contact region thickness in Cu-water systems. The L_{gro}, R_c, and L_{cr} represent the half of the L_{groove}, the radius of the approximated circle, and the contact region thickness in the z-direction, where the unit of θ is radians.

Considering the 1D density profiles of water within the groove in the actual CB states, the contact region thickness (L_{cr}) was defined and calculated using the following equations:

$$\frac{2R_c - L_{th}}{L_{gro}} = \frac{L_{gro}}{L_{th}} \tag{5.2}$$

$$\theta = 2 \cdot \arctan\frac{L_{gro}}{2R_c - L_{th}} \tag{5.3}$$

$$S_{seg} = \theta {R_c}^2 - \frac{2L_{gro} \cdot (R_c - L_{th})}{2} \tag{5.4}$$

$$L_{cr} = \frac{S_{seg}}{2L_{gro}}; 2L_{gro} = L_{groove} \tag{5.5}$$

The original water thickness (L_{th}) was determined by subtracting the maximum position where the water density was not greater than 0.01 g/cm³ from the position of the top nanopillar surface along the z-direction. The calculations in Eq. (5.2) were based on the principle of triangle similarity, which included a small right triangle formed by red and green lines, as well as adjacent right triangles, the angle (θ) of a sector at a circular point, and the area (S_{seg}) of a segment of a circle were calculated by Eq. (5.3) and Eq. (5.4), respectively, as illustrated in Figure 5.6. It was assumed that the contact region thickness (L_{cr}), calculated using Eq. (5.5), corresponded to the height at which the area (S_{seg}) of the segment of a circle was converted into a rectangular area with the same groove width. The related values of L_{th} and L_{cr} are given in Table 5.2. It was assumed that the heat flow

was from the water to the nanopillar sidewalls through the contact region thickness (L_{cr}) in the actual CB states. Therefore, the TCMs could be directly applied to the actual CB states by replacing L_{NANO} with L_{cr} in Eq. (2.34) and Eq. (2.35) for R_{liq}, and by replacing L^* with L_{cr} in Eq. (2.36) for $R_{S\text{-}liq3}$ and $R_{S\text{-}liq4}$.

Table 5.2 The original water thickness (L_{th}) and contact region thickness (L_{cr}) in Cu-water systems. The L_{th} and L_{cr} in Cu-water systems were based on the 1D density of the water profile and calculated by Eq. (5.2) to Eq. (5.5), respectively.

Cases	L_{th}	L_{cr}	Cases	L_{th}	L_{cr}
CG-S19-P1-CB	0.92	0.70	SPC/E-S19-P1-CB	0.88	0.65
CG-S19-P2-CB	0.74	0.54	SPC/E-S19-P2-CB	0.68	0.48
CG-S19-P3-CB	0.52	0.37	SPC/E-S19-P3-CB	0.50	0.34
CG-S14-P1-CB	0.80	0.57	SPC/E-S14-P1-CB	0.77	0.54
CG-S14-P2-CB	0.65	0.46	SPC/E-S14-P2-CB	0.62	0.43
CG-S14-P3-CB	0.47	0.32	SPC/E-S14-P3-CB	0.48	0.32

For models C to F, the contact region thickness within the groove using MD simulations in the actual CB state under an approximate water pressure range (40 to 10 MPa) was depicted in Figure 5.7. The values of δ(C)-P3 to δ(F)-P3 for the CG model were 1.09, 0.70, 0.84, and 0.94, respectively. For the SPC/E model, the values of δ(C)-P3 to δ(F)-P3 were 0.94, 1.26, 0.88, and 1.03, respectively. Compared with the general CB states, which neglected the contact region thickness in the groove, the values of δ(C)-P3 to δ(F)-P3 were significantly reduced, indicating that the energy transfer between water and the nanopillar sidewalls played a crucial role in the heat transfer process in the actual CB states. Figure S5.13 in the Appendix shows the definition of the heat flow rate of the "bottom", "sidewalls", and the "top", which were calculated by MD simulations. In the actual CB states, the energy proportion was consistent with the general perception, the top nanopillar surface carried most of the S-L energy transfer process; there was almost no energy transfer ("bottom", close to zero) between the groove bottom surface and the water; the energy transfer between the nanopillar sidewalls and water accounts for about 30% or lower in Figure S5.16. Only considering the models A to F of energy transfer on the top nanopillar surface in Figures 5.2 to 5.4, there was a large deviation. Therefore, the present study just emphasized that the energy transfer through the nanopillar sidewalls and water was very important when predicting ITRs calculated by TCMs. The energy proportions of each case calculated by MD simulations were also shown in Figures S5.14 to S5.16 of the Appendix. The lower water pressure reduced the number of water molecules in the groove, and the δ in the actual CB states increased, as highlighted by the red square region in Figure 5.7(a) because a smaller contact region thickness decreased the contribution of S-L $R_{S\text{-}liq3}$ and $R_{S\text{-}liq4}$. Instead, the $R_{S\text{-}liq3}$ and $R_{S\text{-}liq4}$ of the S-L vapor interfaces might replace the S-L $R_{S\text{-}liq3}$ and $R_{S\text{-}liq4}$ in the TCMs. In the CB state, the trends

in the magnitude of R values for the solids and liquids were similar to those in the Wenzel state. The R values in all TCMs were shown in Table S5.1 and Figures S5.1 to S5.12 of the Appendix.

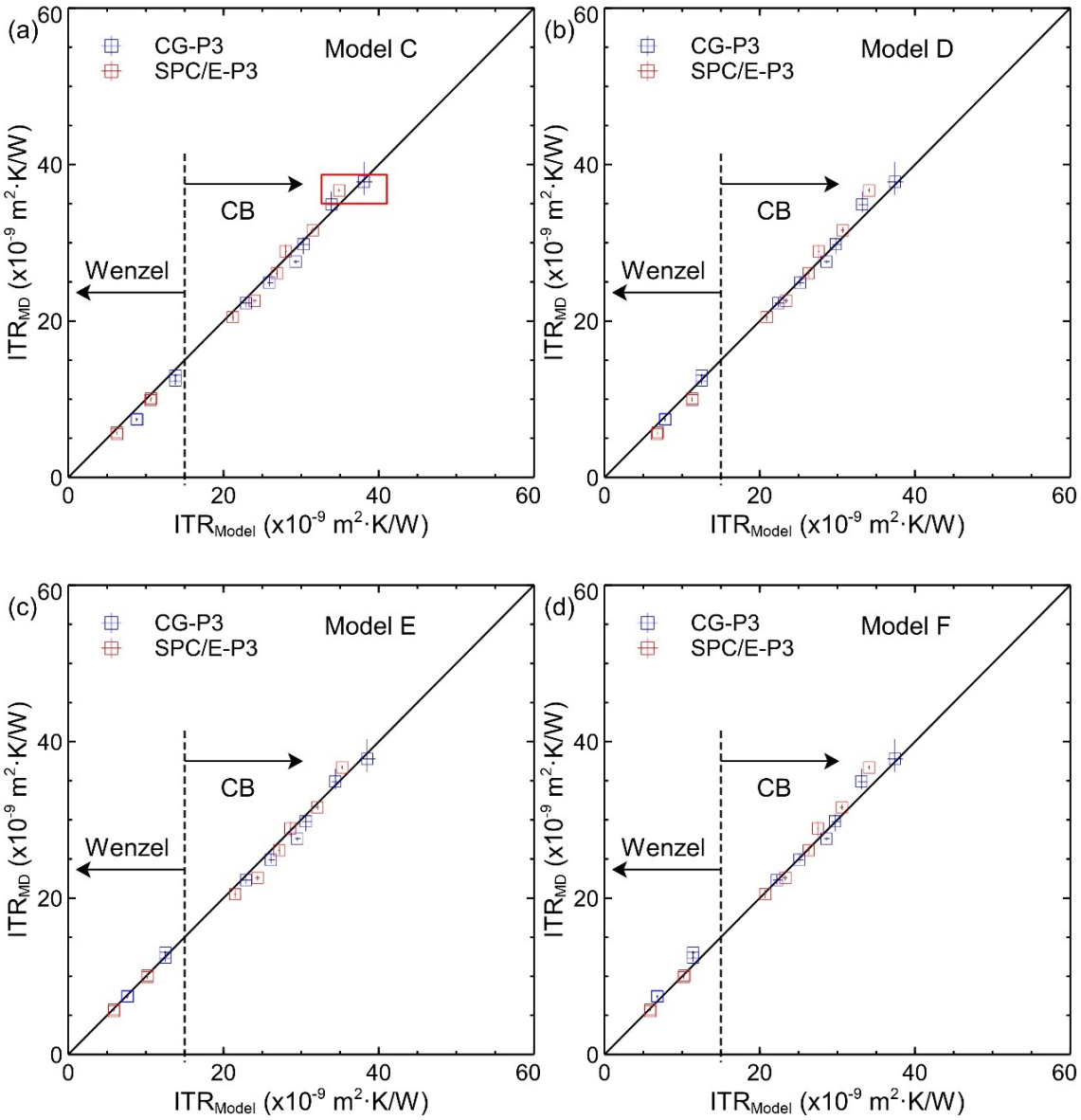

Figure 5.7 Relationship between ITR_{Model} and ITR_{MD} in the Wenzel and actual CB states under a correction of contact region thickness. The water pressure ranged from 10 to 40 MPa (P3 to P1).

Compared to models A and B, Figures S5.23(c) and (d) of the Appendix show that the rate of heat flow in the right and left paths of heat transfer calculated by MD simulations was close to that derived by TCMs due to the heat flux on the nanopillar sidewalls. Therefore, models C and D could be used to predict the ITRs of nanostructure surfaces calculated by MD simulations. In models E and F, the Q calculated by MD simulations

agreed well with the Q derived by the TCMs compared to models A to D. Firstly, it was necessary to consider the energy transfer between the nanopillar sidewalls and the liquid. Secondly, the differences in surface temperatures should be considered to predict ITRs via TCMs correctly. From another perspective, there was no significant change in Figures S5.23(c) to (f) of the Appendix in the Q derived by TCMs, and that calculated by MD simulations, when using the experimental thermal conductivity and thermal conductivity calculated by MD simulations. The thermal conductivity from the experiments and thermal conductivity calculated by MD simulations had limited effects on TCMs.

In summary, the energy transfer between the nanopillar sidewalls and the liquid was very essential. The description of appropriate heat transfer paths and heat flux distribution were the key factors for the prediction of ITRs via TCMs. The above two points were the reasons why TCMs could reasonably and approximately predict the ITRs of the nanostructure surface.

5.3 The effect of nanopillar widths on the relationship between ITR_{Model} and ITR_{MD}

5.3.1 TCMs in the Wenzel state

Studying the nanopillar widths in the Wenzel state was helpful in observing the performance of the TCM. Figures 5.8 to 5.10 show the influence of nanopillar widths on the relationship between ITR_{MD} and ITR_{Model} in the Wenzel and general CB states, assuming that the liquid molecules do not penetrate the grooves at all. The blue and red markers represent the CG and SPC/E models under various water pressures, with the dots (S19) and diamonds (S14) corresponding to the nanopillar widths of 1.91 nm and 1.40 nm, respectively.

In the Wenzel and general CB states, all δ values for the nanopillar widths of S19 and S14 in Figures 5.8 to 5.10 exceeded 8.0. To verify the accuracy of the TCMs, the δ values were firstly discussed in the Wenzel state (ITRs <25 $K \cdot m^2/W$).

Figures 5.8 (a) and (b) correspond to the relationship between ITR_{Model} and ITR_{MD} in models A and B, respectively. The δ(A)-S19 and δ(A)-S14 values for the CG model in Wenzel states were 4.38 and 4.78, respectively. The δ(B)-S19 and δ(B)-S14 values for the CG model in Wenzel states were 3.71 and 3.97, respectively. In the cases of the SPC/E model, the δ(A)-S19 and δ(A)-S14 values in Wenzel states were 3.89 and 4.17, respectively, and the δ(B)-S19 and δ(B)-S14 values were 3.90 and 4.36, respectively. The δ(A) values were almost identical to the δ(B) values for both CG and SPC/E models in the Wenzel states, indicating that the nanopillar widths had little effect on δ(A) and δ(B). The reasons for the large deviations and similar values between the models were discussed in Section 5.2.

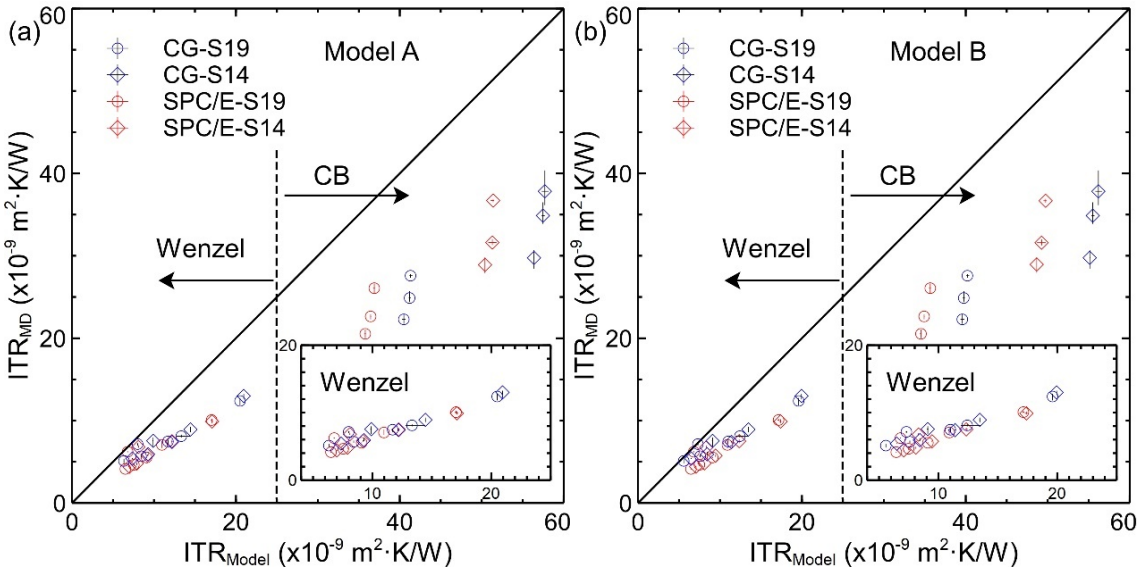

Figure 5.8 Relationship between ITR_{Model} and ITR_{MD} by models A (a) and B (b) in the Wenzel and general CB states. The blue and red represent the CG and SPC/E models under various water pressures. The dots (S19) and diamonds (S14) correspond to the nanopillar widths of 1.91 nm and 1.40 nm, respectively.

Figure 5.9 shows the relationship between ITR_{Model} and ITR_{MD}, which includes model C in (a) and model D in (b). The δ(C) values for the CG model related to S19 and S14 in the Wenzel states were 1.06 and 0.99, respectively, while the δ(D) values were 0.69 and 0.51, respectively. For the SPC/E model related to S19 and S14 in the Wenzel states, the δ(C) values were 0.79 and 0.73, respectively, and the δ(D) values of S19 and S14 were 1.03 and 1.05, respectively. In the Wenzel state, models C and D were improved compared to models A and B. The reasons for the improvement of models C and D with similar values were discussed in the previous section. The small nanopillar width could slightly reduce the deviation between ITR_{MD} and ITR_{Model}, which was explained in the next paragraph.

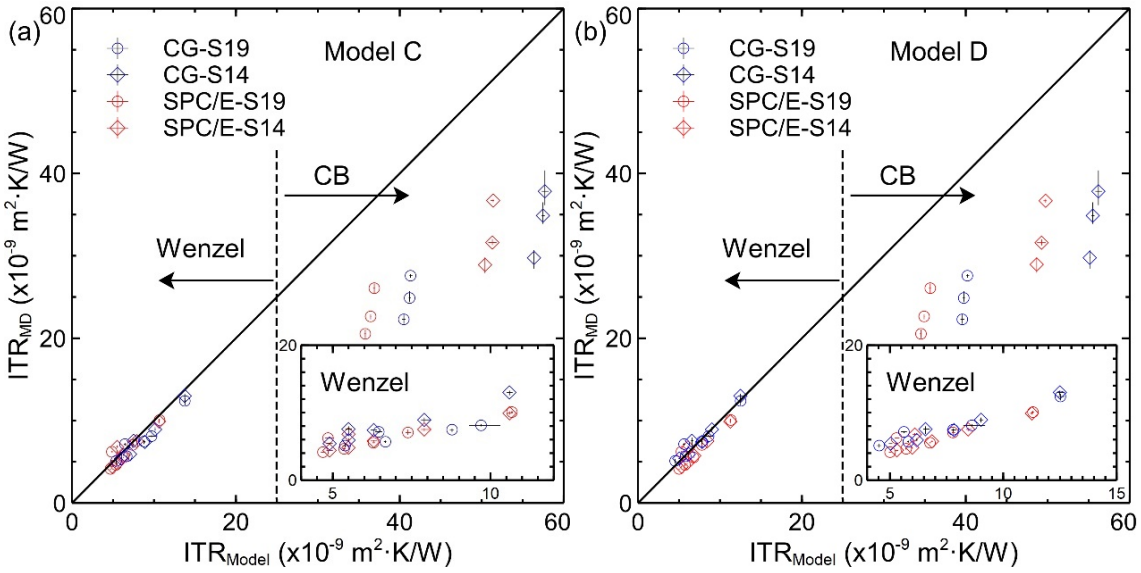

Figure 5.9 Relationship between ITR_{Model} and ITR_{MD} in the general CB and Wenzel states by models C (a) and D (b).

In Figure 5.10, the δ(E) values for the CG model related to S19 and S14 in the Wenzel states were 0.64 and 0.48, respectively, while the δ(F) values were 1.23 and 1.18, respectively. The δ(E) values in the Wenzel states using the SPC/E model were 0.72 for S19 and 0.65 for S14, and the corresponding δ(F) values were 0.71 for S19 and 0.63 for S14. In models C to F, smaller nanopillar widths could slightly reduce δ (*), indicating that the grooves of the nanostructure surfaces produced by small nanopillar widths could accommodate more water molecules, thereby strengthening the right side of the heat path in the TCM diagrams. When the nanopillar size approached zero, the TCMs of a nanostructure surface could be converted to predict the thermal resistances of a flat surface, and the ITR_{Model} aligned with the ITR_{flat} under approximate water pressures.

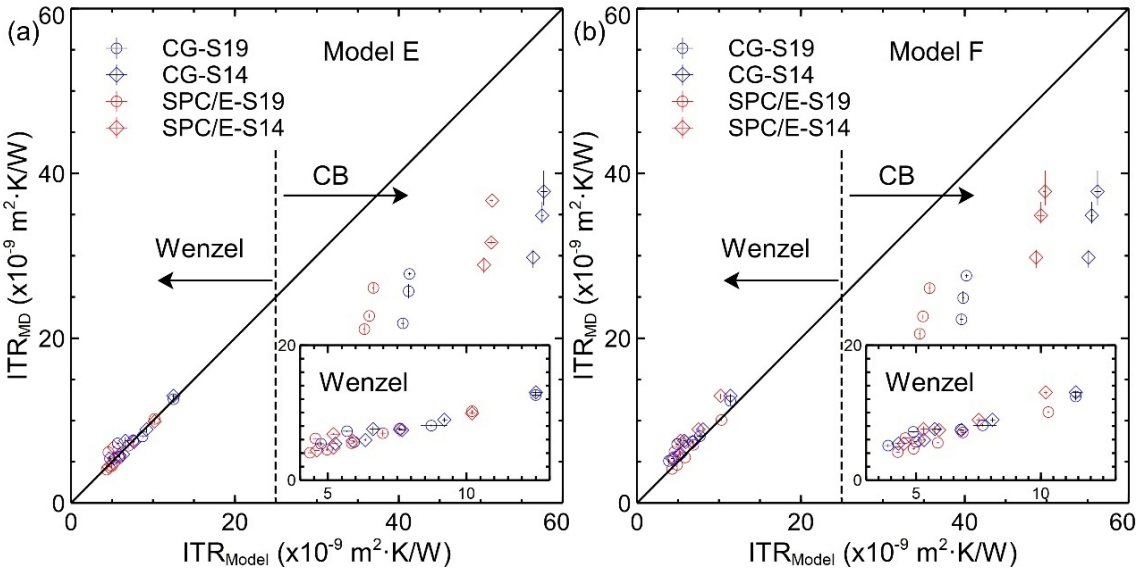

Figure 5.10 Relationship between ITR_{Model} and ITR_{MD} in models E (a) and F (b).

5.3.2 TCMs under a correction of contact region thickness

When considering the Wenzel states and the contact region thickness (L_{cr}) in the actual CB states, as shown in Figure 5.11, the δ(C)-S19 to δ(F)-S19 values for the CG model were 1.14, 0.69, 0.99, and 1.08, respectively, and the δ(C)-S14 to δ(F)-S14 values for the CG model were 0.89, 0.72, 0.54, and 1.15, respectively. In the cases of the SPC/E model, the δ(C)-S19 to δ(F)-S19 values were 0.90, 0.99, 0.91, and 0.79, respectively, and the δ(C)-S14 to δ(F)-S14 values were 0.90, 1.32, 0.73, and 1.16, respectively. The δ(C) to δ(F) values for both water models were significantly reduced compared to those without the correction of contact region thickness. To approximately predict the ITRs in the actual CB state of a nanostructure surface using TCMs, it was essential to consider the heat transfer under a correction of contact region thickness on nanostructure surfaces, regardless of the nanopillar widths. The correction ensured a more approximate representation of the heat transfer process in the actual CB states as described in Section 2.8.2.

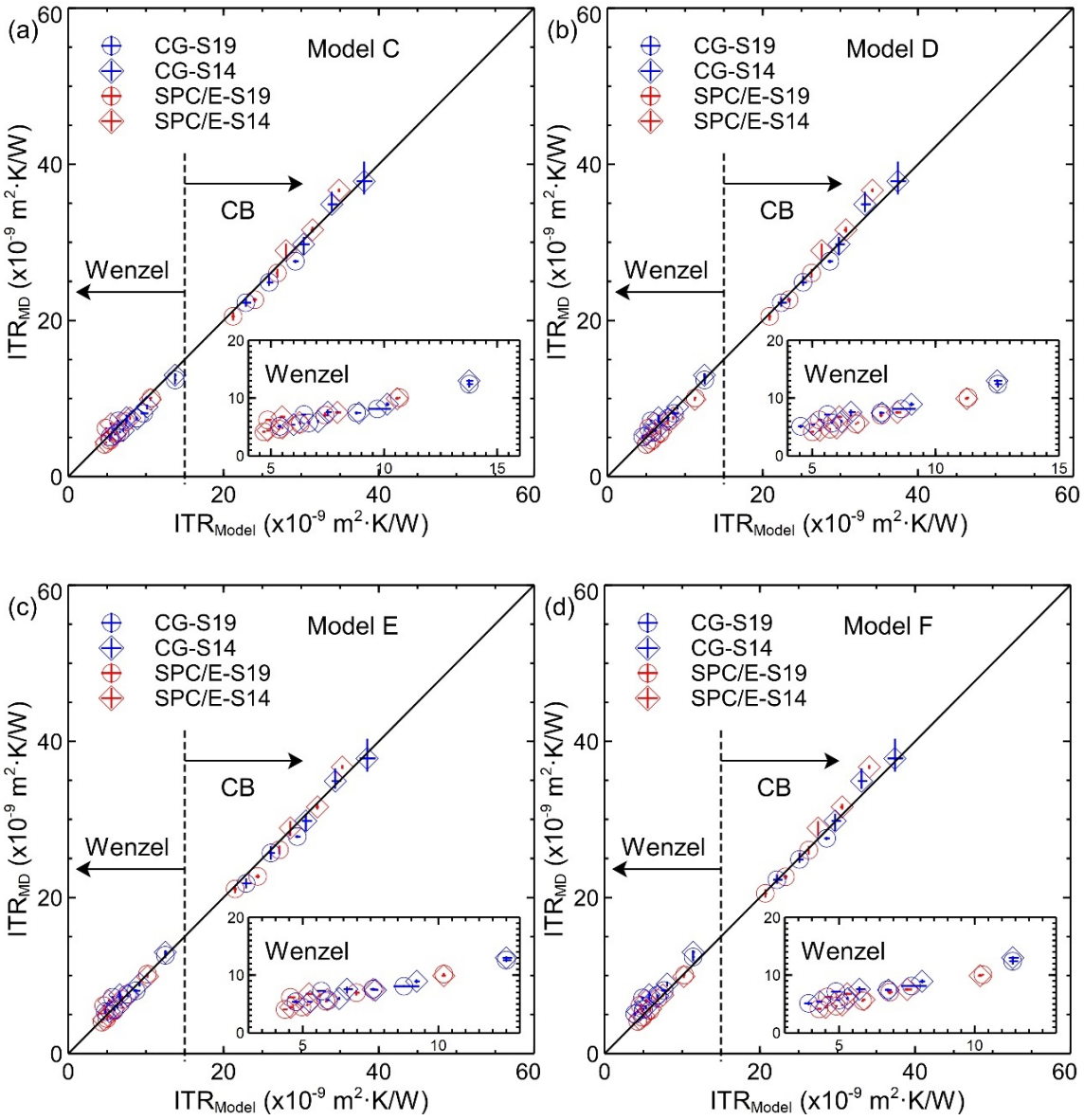

Figure 5.11 Relationship between ITR_{Model} and ITR_{MD} in the actual CB and Wenzel states under a correction of contact region thickness (L_{cr}).

6 Application of TCMs in water-graphene-Cu systems

The present chapter was used to verify the generalizability of thermal circuit models (TCMs) by investigating the water models and defective surfaces on the relationships between interfacial thermal resistances (ITRs) calculated by MD simulations and those predicted by TCMs in water-graphene-Cu systems. The calculation models and numerical details are introduced in Section 6.1. The effects of water models on the relationship between the ITRs calculated by MD simulations and those predicted by the TCMs are shown in Section 6.2, where the TCMs are explained in Section 2.8. The effects of the defective surfaces on the relationship between the ITRs calculated by MD simulations and those predicted by TCMs are described in Section 6.3.

6.1 Calculation models and numerical details

In the present chapter, the thermal resistance (R) of flat surfaces and six TCMs were used to predict the interfacial thermal resistances (ITRs) of a nanostructure surface. ITR_{MD} and TCMs were based on Chapter 4 with more water pressure cases, as given in Tables S4.1 to S4.4. Some components of TCMs in the present chapter were also based on Chapter 3 because there were some interactions between water and Cu, such as $R_{S\text{-}liq3}$. The ITR_{Model} was calculated by six TCMs of the Cu surfaces coated with the graphene. The related tables and figures in the Appendix were shown by only one of three MD simulations. The root mean square error (δ, RMSE) was shown in Section 5.1.

6.2 The effect of water models on the relationship between ITR_{MD} and ITR_{Model}

6.2.1 The effect of water pressure on ITR_{flat} calculated by MD

The present section has the same purpose as Section 5.2.1 because the ITR was dependent on the water pressure. Figure 6.1 shows the relationship between R_{flat} and water pressure on Cu coated with pristine graphene; the R_{flat} was defined between graphene and water. Figures 6.1 (a) and (b) correspond to the CG and SPC/E models. Green, red, blue, and black curves correspond to the cases in the CA11, CA12, CA21, and CA22 cases, respectively. The composite surface was referred to as the water-graphene-Cu system in the present study. The fitting line in the CA11 and CA21 cases was different from that in the CA12 and CA22 cases because the wettability between water and the pristine graphene coating was different, and the S-L interaction strengths determined the contact angles and wettability. The values of R_{flat} on the composite surfaces and water pressure are given in Table 6.2. Therefore, the fitting lines of the CA11 and CA21 were lower than those of the CA12 and CA22. The water pressure, R_{flat}, and fitting coefficients on the

defective graphene coating are shown in the following Figure S6.1.

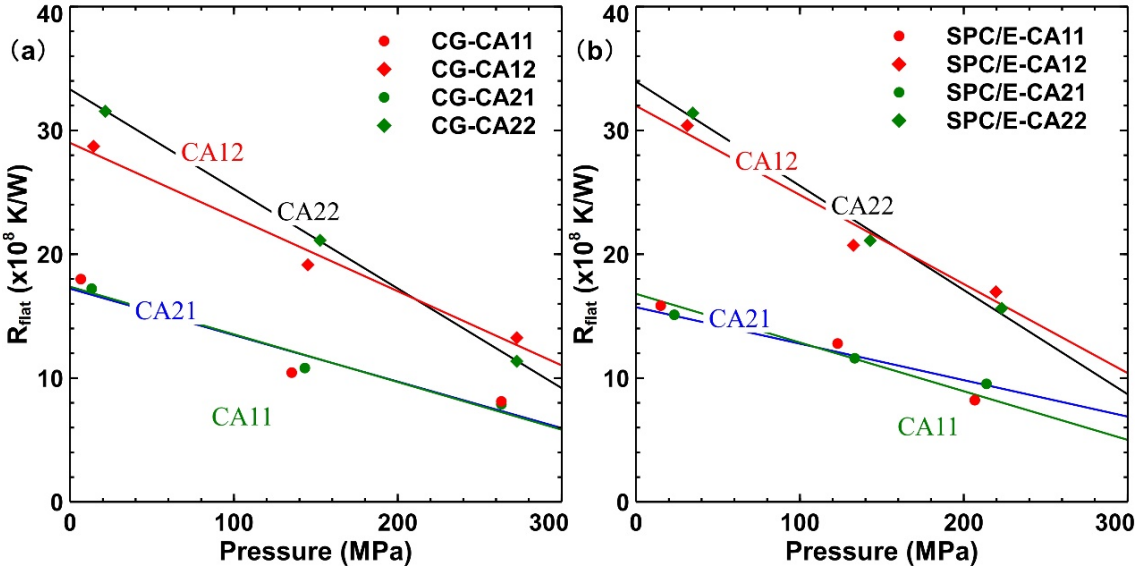

Figure 6.1 The relationships between R_{flat} and water pressure on flat surfaces in the Cu-graphene-water systems. The R_{flat} denotes the thermal resistance between the graphene coating and water on flat surfaces in the Cu-graphene-water systems. An approximate linear line was used to describe the relationship between R and water pressure. The coefficients of the fitting lines are given in Table 6.1. The red, black, green, and blue curves correspond to the related label; for example, the label "CA12" referred to the red fitting lines, including the data points in the CA12 cases. The water pressure values were similar to the previous report [18].

Table 6.1. The coefficients of the fitting lines in Figure 6.1, y=aa·x+bb. The "CoD" referred to the coefficient of determination.

Cases	aa	bb	CoD	Cases	aa	bb	CoD
CG-CA11	-0.039	17.4	0.92	SPC/E-CA11	-0.039	16.8	0.97
CG-CA12	-0.060	29.0	0.98	SPC/E-CA12	-0.072	32.0	0.96
CG-CA21	-0.036	17.1	0.96	SPC/E-CA21	-0.029	15.7	0.99
CG-CA22	-0.077	33.1	0.99	SPC/E-CA22	-0.084	33.9	0.99

Table 6.2. The details of the calculation results in the cases of the CG and SPC/E models on flat surfaces (Cu-graphene-water). The "Number" is the number of the SPC/E and CG water molecules. "P-MD" refers to the water pressure calculated by MD simulations. The "R_{flat}" and ITR_{flat} refer to the thermal resistance and ITR, and the units of R_{flat} and ITR_{flat} are K/W and $K \cdot m^2/W$, respectively. The "CG" and "SPC/E" represent the cases of CG and SPC/E models for all cases.

Items	Number	P-MD(MPa)	R_{flat} (K/W)	ITR_{flat} ($K \cdot m^2/W$)
CA11-CG-P3	3154	6.57	1.80E+09	2.92E-08
CA12-CG-P3		14.36	2.87E+09	4.66E-08
CA21-CG-P3	3150	13.22	1.72E+09	2.80E-08
CA22-CG-P3		21.54	3.15E+09	5.12E-08
CA11-CG-P2	3354	135.27	1.04E+09	1.70E-08
CA12-CG-P2		145.12	1.91E+09	3.11E-08
CA21-CG-P2		143.29	1.08E+09	1.76E-08
CA22-CG-P2		152.55	2.11E+09	3.43E-08
CA11-CG-P1	3500	263.22	8.12E+08	1.32E-08
CA12-CG-P1		272.62	1.33E+09	2.15E-08
CA21-CG-P1		271.78	7.88E+08	1.27E-08
CA22-CG-P1		282.35	1.14E+09	2.12E-08
CA11-SPC/E-P3	3170	15.03	1.59E+09	2.58E-08
CA12-SPC/E-P3		31.23	3.04E+09	4.94E-08
CA21-SPC/E-N2		23.34	1.51E+09	2.45E-08
CA22-SPC/E-P3		34.60	3.14E+09	5.10E-08
CA11-SPC/E-P2	3320	122.99	1.28E+09	2.08E-08
CA12-SPC/E-P2		132.64	2.07E+09	3.37E-08
CA21-SPC/E-P2		133.46	1.16E+09	1.88E-08
CA22-SPC/E-P2		142.87	2.11E+09	3.43E-08
CA11-SPC/E-P1	3420	206.73	8.22E+08	1.33E-08
CA12-SPC/E-P1		219.63	1.70E+09	2.76E-08
CA21-SPC/E-P1		213.86	9.53E+08	1.55E-08
CA22-SPC/E-P1		223.15	1.56E+09	2.54E-08

6.2.2 TCMs in the Wenzel state

The composite surfaces were employed to verify the heat transfer process based on TCMs and to test the generalizability of TCMs on nanostructure surfaces. Figure 6.2 illustrates the effect of water models on the relationships between ITR_{MD} and ITR_{Model} on the Cu surfaces coated with the pristine graphene, and the correction for the contact region thickness of the groove was not considered.

The data points in the present section included various water pressures in the Wenzel and

CB states. In addition, the TCMs diagram for the composite surfaces is presented in Figure 2.12. The differences in TCM schemes between the Cu-water and Cu-graphene-water simulations were discussed in Section 2.8, including variations in the thermal resistance contributions and the unique interfacial properties of the graphene layer, which influenced the overall heat transfer mechanism.

The δ(A) to δ(F) values of the CG and SPC/E models in the Wenzel and general CB states were above 22, as shown in Figure 6.2. To verify the accuracy of the TCMs for the composite surfaces, the δ values exclusively in the Wenzel state (ITRs<25 $K \cdot m^2/W$) were firstly discussed. By focusing on the Wenzel state, it was better to understand the limitations and potential of the TCMs when applied to Cu-graphene-water composite surfaces. The δ(A) to δ(F) values only in the Wenzel states for the CG and SPC/E models are given in Table 6.3.

Table 6.3 The δ(A) to δ(F) values in the Wenzel state

	δ(A)	δ(B)	δ(C)	δ(D)	δ(E)	δ(F)
CG	6.91	5.29	1.62	0.72	1.12	2.29
SPC/E	5.49	6.37	0.53	0.99	1.36	0.92

The prediction accuracy of models A to F using the CG model was similar to that of the SPC/E model. Models C to F outperformed models A and B. Compared with the Cu-water system, TCM prediction deviations using the CG and SPC/E models were slightly larger than those discussed in Section 5.3 because most heat transfer on flat surfaces was assumed to be between graphene in the x-y plane and liquid to calculate $R_{S\text{-}liq5}$ and $R_{S\text{-}liq6}$, but most heat transfer on the nanostructure surfaces was between graphene in the y-z plane and liquid. The results show that the TCMs for the Cu-water system could be applied to the TCMs on composite surfaces, indicating a certain level of similarity in the energy transport mechanisms between the nanostructure surfaces in Chapter 5 and those in the present chapter. The generalizability of the TCMs on the composite surface systems was verified by approximately predicting the ITRs in the Wenzel state.

There was also a slight difference between models A and B, between models C and D, and between models E and F. For all cases of the CG and SPC/E model in Cu-graphene-water systems, the difference in models A to D between R_{Cu} calculated by the thermal conductivity of MD and that calculated by the experimental thermal conductivity was below 3% of the R in the left path of heat transfer; the most of difference between R_{liq} calculated by the thermal conductivity of MD and that calculated by the experimental thermal conductivity was less than 15% of the R in the right path of heat transfer. In models E and F, there was a similar reason as in Chapter 5, and the R_{liq} and R_{Cu} were divided into smaller values. It was found that the TCMs constructed using the thermal conductivities calculated by MD simulations and experimental thermal conductivities of solid and water could not significantly affect the prediction values. The detailed values of local thermal resistances are shown in Tables S6.1 to S6.2 and Figures S6.3 to S6.26 of

the Appendix.

In models A and B, the rate of heat flow in the right path of heat transfer calculated by MD simulations was always larger than that derived by TCMs, as shown in Figures S6.41 (a) and (b) of the Appendix, there was a similar reason as in Section 5.2.2 to explain that the models A and B could not predict the ITR_{MD}.

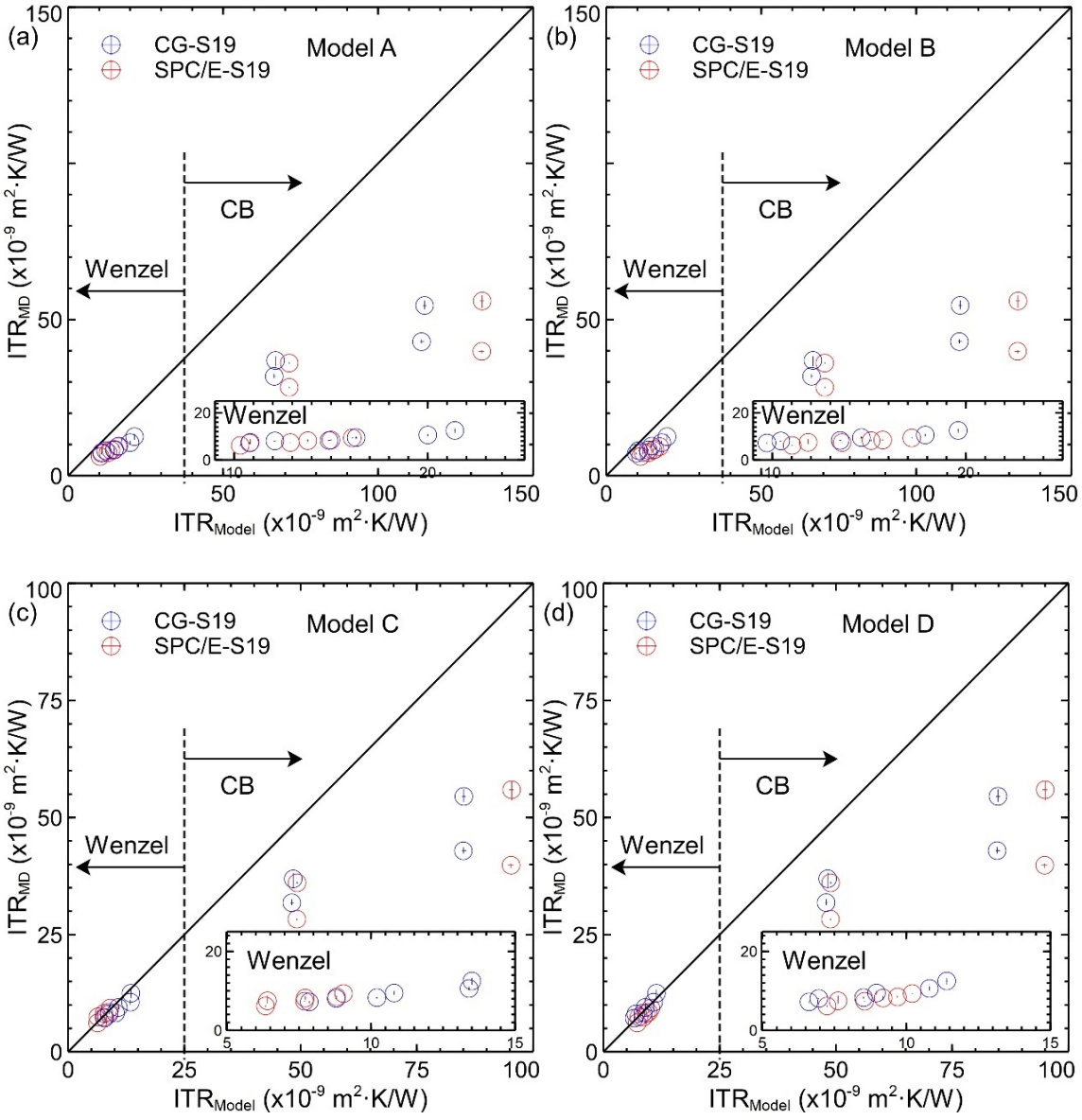

Figure 6.2 Effect of water models on the relationship between ITR_{MD} and ITR_{Model} in the Wenzel and general CB states.

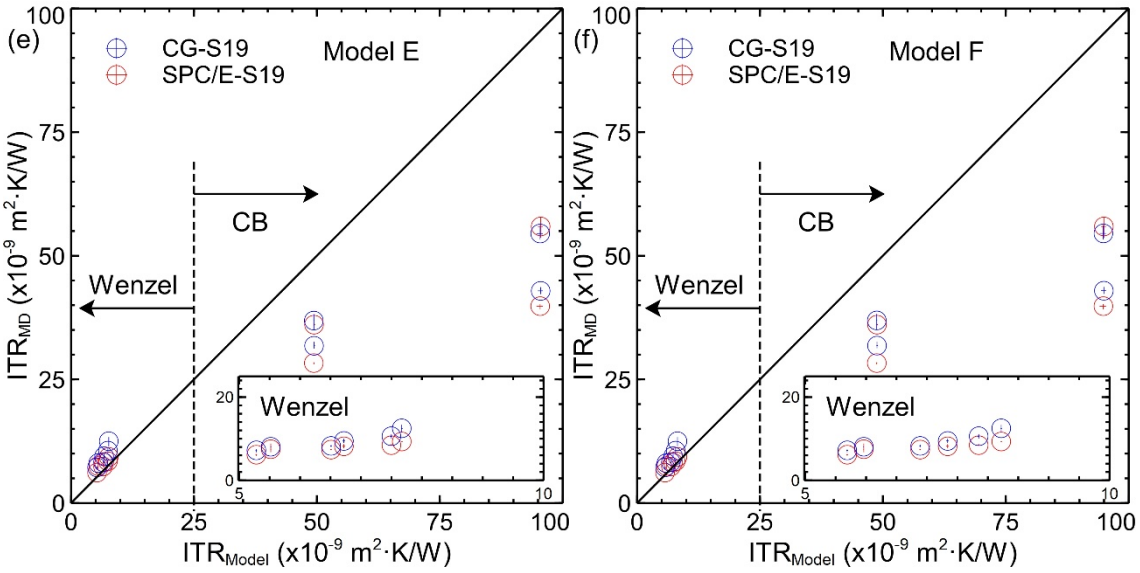

Figure 6.2 (continued) Effect of water models on the relationship between ITR_{MD} and ITR_{Model} in the Wenzel and general CB states.

6.2.3 TCMs under a correction of contact region thickness

It should be considered that the contact region thickness was used to improve the TCM in the CB state, the same as in Section 5.2.3. The water density distribution in the actual CB state on nanostructure composite surfaces was depicted in Figures 6.3 and 6.4. The CG and the SPC/E water molecules within the groove significantly exhibit the penetration thickness, as shown in Figure 6.3. The 2D contour of the Cu-graphene-water and the Cu-water systems were presented in Figures 6.4 and 6.5, respectively, which were used to confirm the difference in the penetration thickness of water within the groove on nanostructure surfaces. The N1 and N2 cases were used to distinguish by the number of the SPC/E and CG water molecules, and the information is given in Table 6.4. It was necessary to explain that employing the number of the SPC/E and CG water molecules in the CB state for the purpose of distinguishing the various cases in the CB state is attributable to the pinning effect. The pinning effect was defined as the moving of the liquid droplet overcoming the resistance against the solid surface[89]. The water density distribution at the corner was obviously different from the 2D density contours in the Cu-water system of Chapter 3. In Figure 6.4 with the water molecule of N2, the penetration thickness of water on the composite surface was similar to that in the case of P3 in the Cu-water systems. On the composite surface with the water molecule of N1, the density of water molecules was influenced by the graphene coating and slightly surrounded the edge of graphene, and in the limited penetration thickness of water, the distribution of water molecules near the Cu sidewalls was similar to that in the Cu-water systems. It was speculated that overcoming the pinning effect required different water pressures as the

liquid moved over uneven and different wettability surfaces, allowing the liquid to penetrate the grooves.

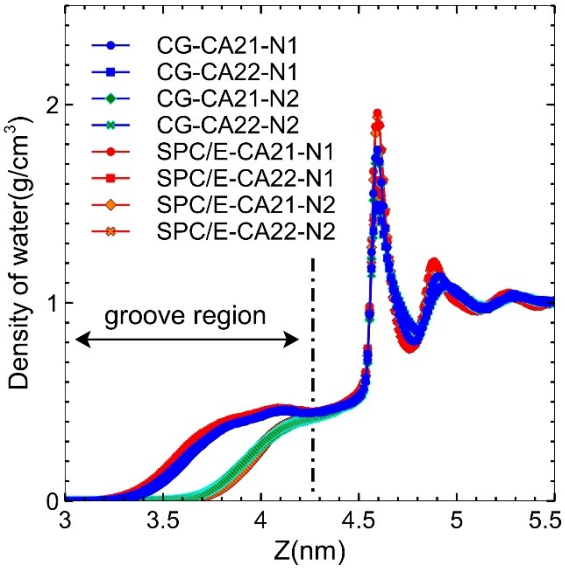

Figure 6.3 1D density profile of the SPC/E and CG water molecules along the z-direction in the actual CB states on the composite surfaces. The red and blue curves correspond to the SPC/E and CG models, respectively. The dots, squares, diamonds, and crosses correspond to various wettability states and the number of water molecules.

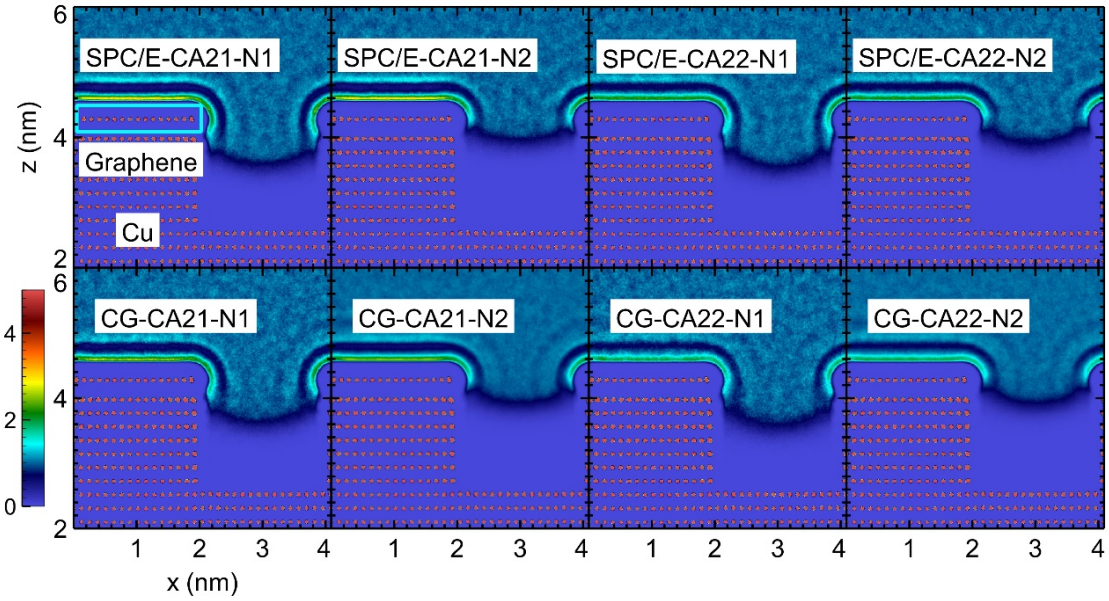

Figure 6.4 2D density contour of the water molecules and solids along the z-direction in the actual CB states on the composite surfaces. The unit of the scalar bar is g/cm^3.

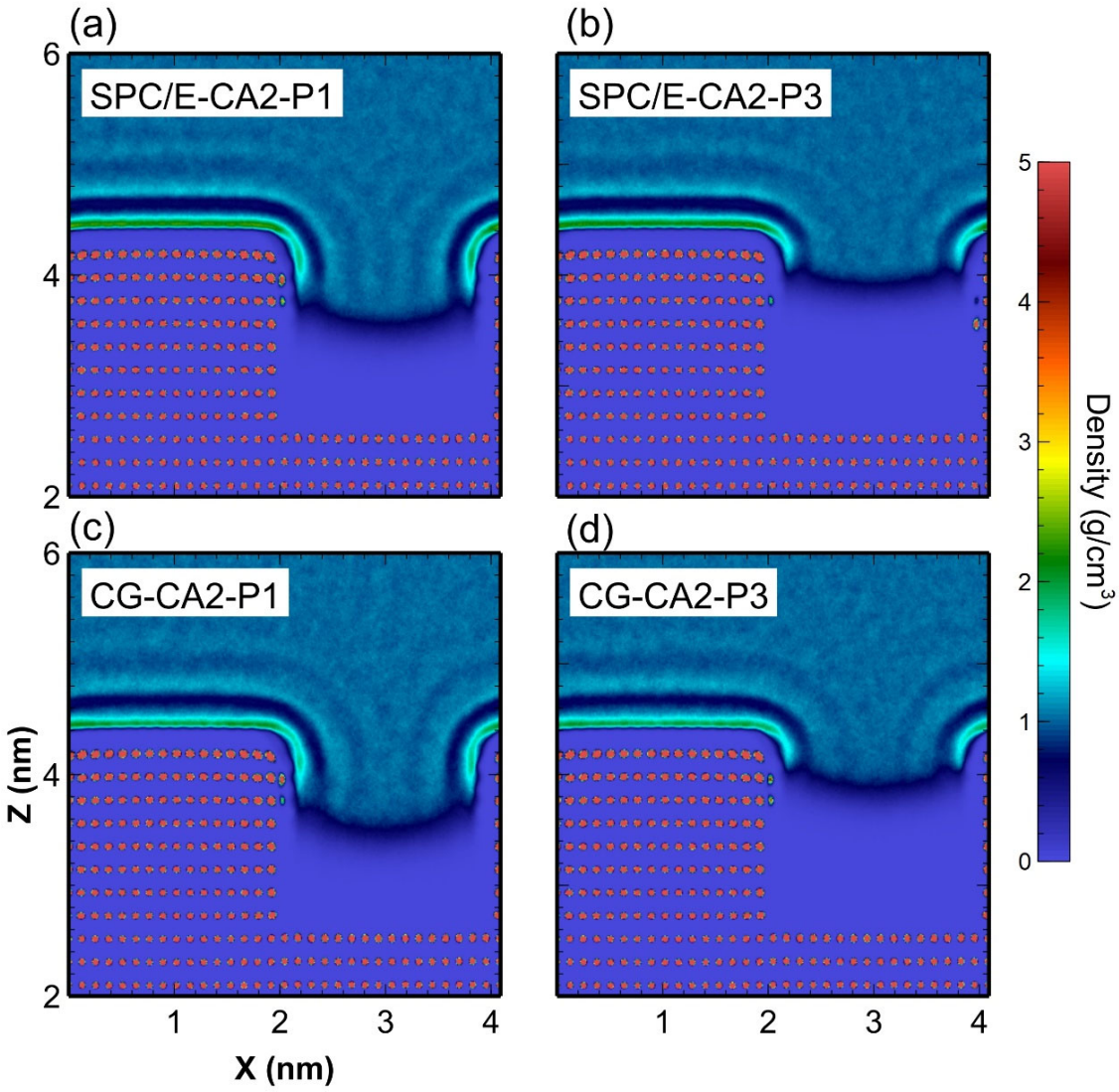

Figure 6.5 2D density contour of the SPC/E and CG water molecules along the z-direction in the actual CB states in Cu-water systems.

Table 6.4 The details of the calculation conditions in the CG and SPC/E models on nanostructure surfaces in Cu-pristine graphene-water systems. The ITR_{MD} unit is ($K \cdot m^2/W$).

	Cases	states	N	P-MD(MPa)	ITR_{MD}
CG-	CA11-P3	Wenzel	2816	2.19	1.06E-08
	CA12-P3		2816	7.08	1.27E-08
	CA11-P2		3000	126.19	8.49E-09
	CA12-P2		3000	129.71	9.04E-09
	CA11-P1		3120	234.03	7.43E-09
	CA12-P1		3120	238.17	8.16E-09
	CA21-N2	CB	2500	25.91	3.75E-08
	CA22-N2		2500	31.92	5.42E-08
	CA21-N1		2580	32.00	3.26E-08
	CA22-N1		2580	32.30	4.23E-08
SPC/E-	CA11-P3	Wenzel	2860	10.94	8.72E-09
	CA12-P3		2860	13.43	9.36E-09
	CA11-P2		2970	97.44	7.37E-09
	CA12-P2		2970	98.67	8.70E-09
	CA11-P1		3115	237.76	5.91E-09
	CA12-P1		3115	238.83	8.84E-09
	CA21-N1	CB	2600	31.51	2.84E-08
	CA22-N1		2600	37.71	3.92E-08
	CA21-N2		2500	27.00	3.59E-08
	CA22-N2		2500	36.33	5.63E-08

Figure 6.6 shows the relationship between ITR_{Model} and ITR_{MD}, which incorporated the correction for the contact region thickness (L_{cr}) of the groove in the Wenzel and actual CB states. The δ(C) to δ(F) values for the CG and SPC/E models in the Wenzel and actual CB states are given in Table 6.5.

Table 6.5 The δ(C) to δ(F) values for the CG and SPC/E models

	Model C	Model D	Model E	Model F
CG	2.96	2.99	3.11	3.69
SPC/E	2.62	2.67	2.86	2.95

The δ(C) to δ(F) values of the CG and SPC/E models indicated a significant reduction compared to those (around 22 $K \cdot m^2/W$) without the correction for the contact region thickness. Compared to the Cu-water systems, the δ(C) to δ(F) values on the composite surfaces increased slightly, which might be attributed to the inconsistency of the thermal resistance of the graphene coating along the x-direction compared to the x-y plane.

In Figure 6.6, most of the δ(C) to δ(F) values in the case of the SPC/E model were slightly smaller than those in the case of the CG model. The edges of graphene in the Wenzel and CB states possibly influenced the transport of water molecules and contact region thickness, resulting in heat transfer of models C to F depending on the water models.
The application of TCMs has highlighted the importance of considering the contact region thickness for the approximate prediction of ITRs. Although the deviation in the ITRs predicted by TCMs in the actual CB state in the Cu-graphene-water system slightly increased, the energy transfer between the nanopillar sidewall and the water still dominated.

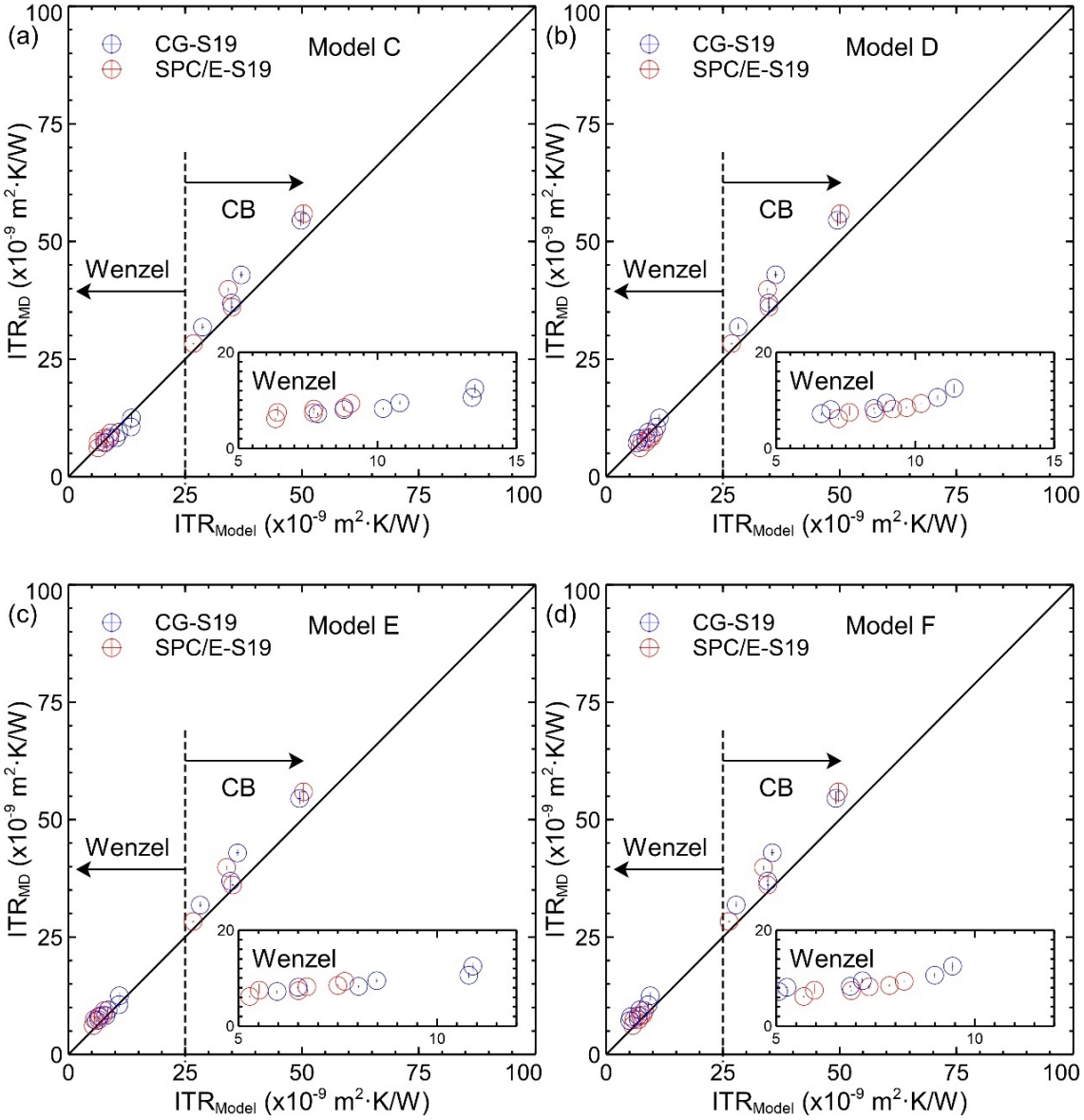

Figure 6.6 Effect of water models on the relationship between ITR_{Model} and ITR_{MD} in the Wenzel and actual CB states using contact region thickness (L_{cr}).

It was observed in the actual CB states that ITR_{MD} was slightly larger than the ITR_{Model} in Figure 6.6, the prediction of TCM in the CB state depended on the energy transfer between water and the nanopillar sidewalls, involving the energy transfer between liquid and graphene in the y-z plane and that between liquid and Cu. The energy transfer in the $R_{S\text{-}liq3}$ path was different from the $R_{S\text{-}liq5}$ path (see Figure 2.12) according to Figure S5.16 in the CA2 cases and Figures S6.27 to S6.32 in the CA22 cases, the energy transfer ratio of "sidewalls" in the Cu-graphene-water systems was larger than that in the Cu-water systems under similar contact region thickness. Therefore, it was important to reasonably distribute the contact region thickness because the energy transfer between the liquid and graphene in the y-z plane is different from those between liquid and Cu sidewalls. According to the 2D distribution of the water density, a limited number of water molecules contacted the Cu walls, compared to the graphene coating. The energy transfer between Cu and liquid could be inferred to be less than expected, which led to the phenomenon that the ITR_{MD} was slightly larger than the ITR_{Model} in the CB state.
From a heat transfer point of view, compared to Figure S5.23, the Q calculated by MD simulations and that derived by TCMs in Figures S6.41(c) to (f) of the Appendix had a larger deviation in models C to F compared to Chapter 5, indicating the energy transfer derived by TCMs could not smoothly match that calculated by MD simulations, because the interaction between the water models and the graphene coating introduced additional complexity due to the different thermal behavior of graphene in different orientations and interactions with water molecules and the pinning effect, which affected the accuracy of TCMs in composite surfaces. There was no significant change in Figures S6.41(c) to (f) of the Appendix in the Q derived by TCMs and Q calculated by MD simulations when using the experimental thermal conductivity and thermal conductivity calculated by MD simulations, which was similar to Chapter 5. In summary, the energy transfer between the nanopillar sidewalls and the liquid was essential and it is necessary to consider the appropriate paths and distribution of heat transfer to estimate ITRs via TCMs.

6.3 The effect of defective surfaces on the relationship between ITR_{MD} and ITR_{Model}

6.3.1 TCMs in the Wenzel state

Similar to Section 6.2.2, the calculation results of the defective graphene surface in the Wenzel state were used to verify the generality of the TCMs. The values of the δ(A) and δ(B) in the CG and SPC/E model ranged from 5.0 to 7.0. The reasons why models A and B could not accurately predict ITRs were discussed in Section 6.2. Figures 6.7(a) and (b) show that ITRs predicted by the TCMs were larger than those calculated by MD simulations. Under larger defect concentrations, models A and B tended to slightly reduce the prediction error, probably because the influence of the graphene coating on the ITRs

calculated by MD simulations and predicted by the TCMs decreased with increasing defect concentration. For example, if the defect concentration was 100%, the system changed from a system with graphene coverage to a bare copper system, and the δ(A) and δ(B) of the Cu-graphene-water system were close to those of the Cu-water system. However, since water filled the grooves in the Wenzel state, the contribution of graphene to the ITRs could not dominate. In the Wenzel state, the δ(C) to δ(F) values of the CG model were less than 2.4, and those of the SPC/E model were less than 1.6, which indicated that models C to F could predict the ITRs. The values of δ(C) to δ(F) of the CG and SPC/E models were close to those of the Cu-water systems. Although the prediction errors of models C to F almost tended to decrease with the increase of defect concentration, it was still not very obvious, and a possible reason was that the numerical difference between defect concentrations was not very large. The δ(A) to δ(F) values between the ITRs calculated by MD and those predicted by TCMs are given in Table 6.6.

Table 6.6 The δ(C) to δ(F) values under the different defect concentrations

	CG			SPC/E		
	SV0.0	SV2.1	SV2.8	SV0.0	SV2.1	SV2.8
δ(A)	6.91	6.56	6.39	5.49	5.33	5.32
δ(B)	5.32	5.21	5.05	6.37	5.94	6.06
δ(C)	1.62	1.35	1.24	0.53	0.67	0.51
δ(D)	0.72	0.64	0.73	0.99	0.98	0.91
δ(E)	1.12	0.97	1.17	1.36	1.32	1.30
δ(F)	2.29	2.06	2.22	1.44	0.92	0.97

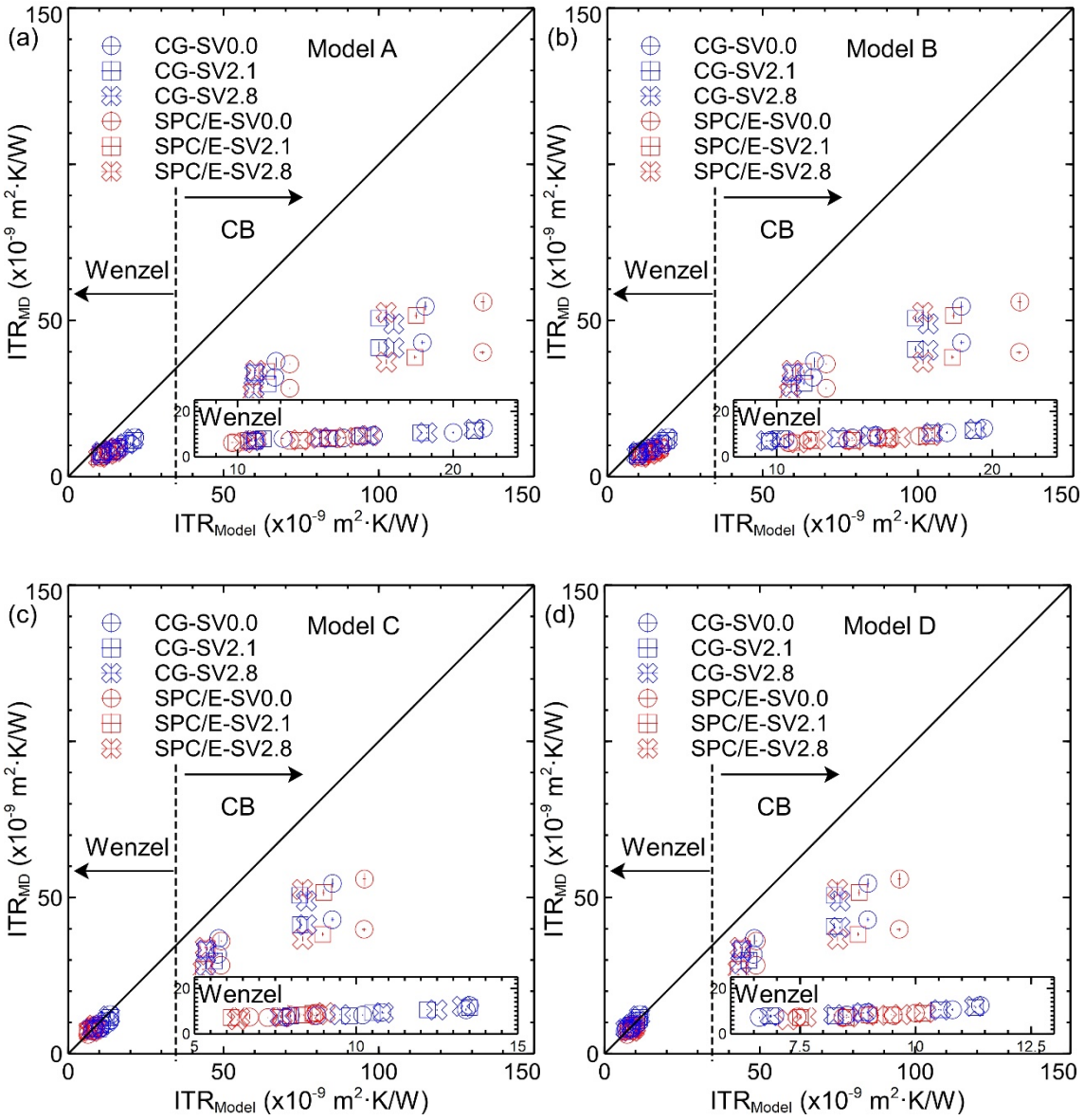

Figure 6.7 Effect of defective surfaces on the relationship between ITR_{Model} and ITR_{MD} in the Wenzel and general CB states.

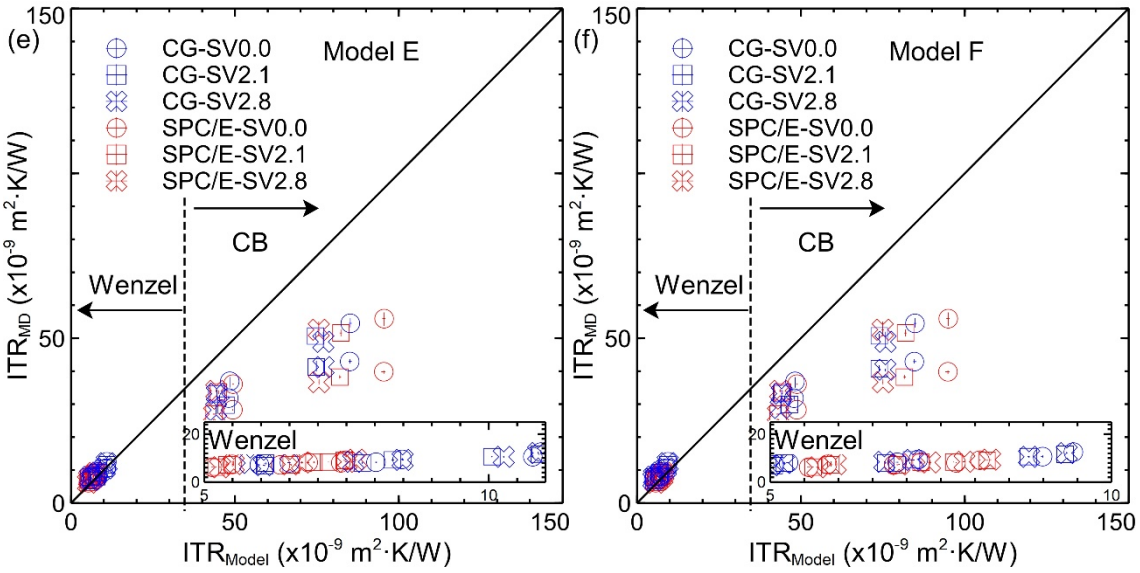

Figure 6.7 (continued) Effect of defective surfaces on the relationship between ITR_{Model} and ITR_{MD} in the Wenzel and general CB states.

6.3.2 TCMs under a correction of contact region thickness

For the cases of defective graphene surfaces, it was still required a correction of contact region thickness to verify the generality of TCMs in the actual CB state. Figure 6.8 shows the relationships between the ITRs calculated by MD simulations and those predicted by TCMs after a correction for the contact region thickness. Compared with the uncorrected values of the δ(C) to δ(F), which were more than around 30 $K \cdot m^2/W$, the values of δ(C) to δ(F) were greatly reduced, which indicated that the energy transfer between the liquid and the nanopillar sidewalls should be considered when using TCM to predict the ITRs containing the CB state in Chapter 5 and section 6.2. The δ(C) to δ(F) values between the ITRs calculated by MD simulations and those predicted by TCMs are given in Table 6.7. The δ(C) to δ(F) values of the CG model were similar to Section 6.3.1 and tended to decrease with increasing defect concentration. However, the SPC/E model shows an increasing trend of δ(C) to δ(F) with increasing defect concentration, which was the opposite trend of the CG model. Considering that the δ(C) to δ(F) values of the SPC/E model in the Wenzel state slightly tended to decrease with increasing defect concentration, the main factor causing the increase could be in the CB state. Compared with the Cu-water system, the values of δ(C) to δ(F) slightly increased due to the influence of the graphene edge and the pinning effect on the TCMs, similar to section 6.2. It was observed in Figure 6.8 that ITR_{MD} was slightly larger than ITR_{Model}, the reason has been explained in Section 6.2.3.

Table 6.7. The δ(C) to δ(F) values between the ITRs calculated by MD simulations and those predicted by TCMs under a correction of contact region thickness.

	CG			SPC/E		
	SV0.0	SV2.1	SV2.8	SV0.0	SV2.1	SV2.8
δ(C)	2.96	2.83	2.23	2.62	2.72	3.10
δ(D)	2.99	2.94	2.17	2.67	2.68	3.10
δ(E)	3.11	2.89	2.25	2.86	2.90	3.23
δ(F)	3.69	3.53	2.92	2.95	2.97	3.34

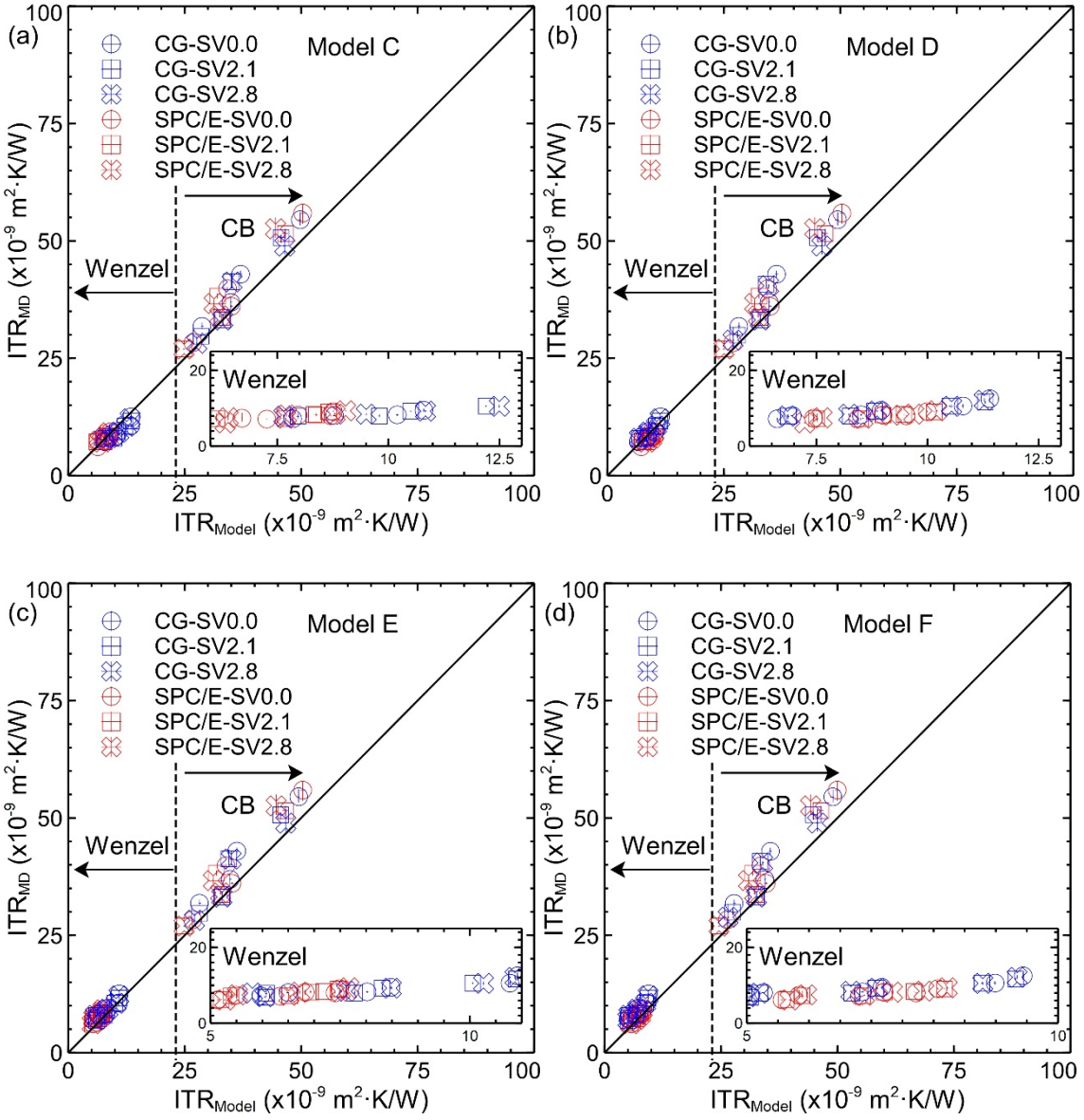

Figure 6.8 Effect of water models on the relationship between ITR_{Model} and ITR_{MD} in the Wenzel and actual CB states using contact region thickness (L_{cr}).

7 Conclusions

7.1 Summary and Conclusions

With the development of microelectronic devices and energy miniaturization, the estimation of the solid-liquid (S-L) interfacial thermal resistance (ITR) of a nanostructure surface is indispensable in nanoscale thermal management. Cu as a common thermal conductive carrier and graphene coating as an improvement in heat transfer have high research value in studying S-L heat transfer processes. For example, micro heat pipes (MHPs) are usually composed of a Cu-water system, and the graphene coating[8] could improve the heat transfer performance of micro heat pipes; the Cu nanostructure surfaces could enhance the boiling heat transfer [32]. The present dissertation aimed to evaluate and predict the S-L ITR to design the heat transfer of nanostructure surfaces by the possibility of evaluating and predicting the ITRs in thermal management. It was examined that the exponential trend between the density depletion length (DDL) and the ITRs could be applied to the Wenzel and Cassie-Baxter (CB) states in MD simulations, and six thermal circuit models (TCMs) were proposed to predict the ITRs of nanostructure surfaces. The summary and main conclusions of the present dissertation are as follows:

In Chapter 1, the background information of the present dissertation is introduced. The literature survey included the development history of ITRs in research and industry, such as Kapitza research and MHPs. The former research results of S-L ITRs on flat surfaces were explained, mainly focusing on MD simulations; S-L ITRs mainly depended on the wettability, liquid adsorption layer, and water pressure. The geometry and nanostructure wettability (the Wenzel and CB states) became important factors affecting the ITRs on nanostructure surfaces. After the literature survey, it was found that: (i) DDL had the potential to evaluate S-L ITRs and it was worth studying in the case of nanostructure surfaces; (ii) so far, there were insufficient reports about predicting the ITRs of nanostructure surfaces by TCMs; (iii) it was still needed to be explored whether the CG model with the potential for large-scale calculations could replace the SPC/E model in the above aspects.

In Chapter 2, the theoretical basis and calculation methods were introduced. The classical theory including the energy of MD simulations, and some physical quantities such as temperature were introduced in the present chapter. The force fields of atoms and molecules were shown via the mathematical forms describing the potential energy of particles in MD simulation, such as the REBO potential function of graphene and the EAM potential function of Cu. The calculation methods of contact angles that were related to the wettability, and the calculation methods of water pressure and DDL were shown in Chapter 2. Finally, the six TCMs and the solutions of equivalent thermal

resistance in TCMs were proposed. Models A and B were established under the condition that there was no energy transfer between water and nanopillar sidewalls. Models C and D assumed that heat transfer between water and solid occurred at similar temperatures of the nanopillar sidewalls and groove bottom surfaces. Models E and F were similar to models C and D, but the temperature of nanopillar sidewalls was different from the groove bottom surfaces. Models A, C, and E employed the thermal conductivities of solid and water calculated by MD simulations, and other TCMs used the experimental thermal conductivities.

In Chapter 3, two exponential curves were employed to describe the relationships between DDL and ITRs on nanostructure surfaces under different water pressures in Cu-water systems. The effects of the water models, water pressure, and nanopillar width on the relationship between the DDL and the ITRs were investigated using NEMD simulations on various flat and nanostructure surfaces by changing the S-L interaction strength, the number of water molecules, the surface geometry in Cu-water systems.
Using the SPC/E and CG models, the temperature jumps at the S-L interface were almost independent of the water pressure. The exponential curve was a good way to describe the relationships between S-L ITRs and DDL on flat surfaces. The discontinuous exponential curves could be related to the relationships between DDL and S-L ITRs on the nanostructure surface in the Wenzel and Cassie-Baxter states. Although there were deviations in the ITR values calculated using the CG and SPC/E models, the S-L ITRs defined between the groove bottom surfaces and the water near the top nanopillar surface, the relationships between DDL and S-L ITRs using the CG and SPC/E models were strongly related to overall exponential curves.

The CG model could replace the SPC/E model for the S-L ITR simulations. The intersection of the exponential curves of the nanostructure surfaces could be related to the transition between the Wenzel and Cassie-Baxter states. Meanwhile, regardless of water models, the DDL almost depended on water pressure, surface wettability, and surface roughness. The S-L ITRs increased with the decrement in water pressure; the S-L ITRs using the CG model were slightly higher than those of the SPC/E models under most different pressure conditions. There was a similar deviation of S-L ITRs, defined between the water near the top nanopillar surface and groove bottom surface, between CG and SPC/E models on nanostructure surfaces in the Wenzel state.

In Chapter 4, the exponential growth trends of DDL were examined to evaluate S-L ITRs on flat surfaces in the case of the graphene coating. On nanostructure surfaces, the exponential curves were also examined for the relationships between ITR and DDL. The effects of the water models and defect surfaces on the relationship between the DDL and S-L ITRs were investigated using NEMD simulations on flat and nanostructure surfaces by changing the S-L interaction strength and the defective graphene coating. The

exponential curves between DDL and S-L ITR on flat surfaces with changing defect concentrations and the wettability surfaces of Cu and graphene were slightly different from those in Chapter 3. The DDL on flat surfaces could roughly evaluate the S-L ITR under approximate water pressure. On the nanostructure surface, the relationship between DDL and S-L ITR was also examined, similar to Chapter 3.

In Chapter 5, the TCM predictions of models C to F made agreements with ITRs calculated by MD simulations in Cu-water systems. The TCM predictions were not strongly dependent on the nanopillar widths and water models. In the Wenzel state, the ITRs calculated by MD simulations were usually smaller than the ITRs predicted by simple TCMs of models A and B. In the Wenzel state, the ITRs calculated by MD simulations could well match the ITRs predicted by the proposed TCM built on models C to F, and the heat path of proposed TCMs on models E and F performed very well when predicting the ITRs. The TCMs built on models C to F could also predict the ITRs of nanostructure surfaces in the Wenzel and CB states under a correction of contact region thickness. The CG model could replace the SPC/E water model for ITR calculation.

In Chapter 6, the composite surface slightly weakened the accuracy of the TCM predictions in the Wenzel and CB states because the graphene coating affected the distribution of energy exchange proportion between the nanopillar sidewalls and liquid. In Cu coated with single-layer pristine and defective graphene, the ITRs predicted by the simple TCMs on models A and B were larger than those calculated by MD simulations, and the proposed TCMs based on models C to F were able to predict the ITRs of composite surfaces in the Wenzel state, which showed no significant difference with Chapter 5. While the TCM predictions slightly depended on the water models and defective surfaces, the δ values of all models slightly increased compared with those without coatings. The reason for the decrease in the accuracy of the TCM was that the energy transfer between the solid and the liquid was a little poorly matched with that calculated by MD simulations. In the Wenzel state, the graphene coating slightly affected the TCM prediction because the energy exchange in the groove was still dominated by the Cu-water interactions. In the CB state, the edge of the graphene coating affected the distribution of energy exchange proportions, resulting in lower predicted values than the calculated values.

7.2 Current problems and future challenges

The present dissertation aimed to evaluate and predict S-L ITRs of nanostructure surfaces. The relationship between ITRs and DDL could be used for nanostructure surfaces including the CB state. The TCMs that consider the energy transfer between the nanopillar sidewalls and water even in the CB state could be used to predict ITRs of nanostructure

surfaces. In general thermal management, the present dissertation could provide support for designing nanostructure surfaces and evaluating ITRs.

In Chapter 5, the prediction accuracy decreased slightly as the decrement in water pressure in the CB state. The heat transfer could occur if the water molecule in the gas state replaced the liquid water with the solid wall. The heat transfer process of solid-liquid mixing gas was more complicated than that of the S-L heat transfer process. The reliability of TCM requires further verification. In Chapter 6, the prediction accuracy in the CB state was slightly affected by the graphene coating, which depends on the contact region thickness, so further research is needed to focus on the contact region thickness on the composite surface.

The contact region thickness in the CB state in Chapters 5 and 6 still requires MD calculations, so it is desirable to calculate and derive the contact region thickness based on surface tension, Laplace pressure, and geometric factors.

Considering practical applications in engineering, the evaluation of the DDL and the prediction of TCMs still need further verification under the MD simulations considering the electrical double layer. The verification of how the liquid molecular size influences the prediction of S-L ITRs on nanostructure surfaces using TCMs should be investigated further.

References

[1] Keesom, W. H.; Keesom, A. P. (1936). On the heat conductivity of liquid helium, *Physica*, Vol. 3, No. 5, 359–360. https://doi.org/10.1016/S0031-8914(36)80312-7

[2] Kapitza, P. L. (1971). The study of heat transfer in Helium II, *Helium 4*, 114–153. https://doi.org/10.1016/b978-0-08-015816-7.50014-6

[3] Pollack Gerald L. (1969). Kapitza resistance, *Reviews of Modern Physics*, Vol. 41, No. 1, 48–81. https://doi.org/10.1103/RevModPhys.41.48

[4] Swartz, E. T.; Pohl, R. O. (1989). Thermal boundary resistance, *Reviews of Modern Physics*, Vol. 61, No. 3, 605–668. https://doi.org/10.1103/RevModPhys.61.605

[5] Waldrop, M. M. (2016). The chips are down for Moore's law, *Nature*, Vol. 530, No. 7589, 145–147. https://doi.org/10.1038/530144a

[6] Bar-Cohen, A.; Arik, M.; Ohadi, M. (2006). Direct liquid cooling of high flux micro and nano electronic components, *Proceedings of the IEEE*, Vol. 94, No. 8, 1549–1570. https://doi.org/10.1109/JPROC.2006.879791

[7] Balandin, A. A.; Ghosh, S.; Bao, W.; Calizo, I.; Teweldebrhan, D.; Miao, F.; Lau, C. N. (2008). Superior thermal conductivity of single-layer graphene, *Nano Letters*, Vol. 8, No. 3, 902–907. https://doi.org/10.1021/nl0731872

[8] Gan, J. S.; Yu, H.; Tan, M. K.; Soh, A. K.; Wu, H. A.; Hung, Y. M. (2020). Performance enhancement of graphene-coated micro heat pipes for light-emitting diode cooling, *International Journal of Heat and Mass Transfer*, Vol. 154, 119687. https://doi.org/10.1016/j.ijheatmasstransfer.2020.119687

[9] Wang, C. S.; Chen, J. S.; Shiomi, J.; Maruyama, S. (2007). A study on the thermal resistance over solid-liquid-vapor interfaces in a finite-space by a molecular dynamics method, *International Journal of Thermal Sciences*, Vol. 46, No. 12, 1203–1210. https://doi.org/10.1016/j.ijthermalsci.2007.01.009

[10] Khrustalev, D.; Faghri, A. (1995). Heat transfer during evaporation on capillary-grooved structures of heat pipes, *Journal of Heat Transfer*, Vol. 117, No. 3, 740–747. https://doi.org/10.1115/1.2822638

[11] Cahill, D. G. (2004). Analysis of heat flow in layered structures for time-domain thermoreflectance, *Review of Scientific Instruments*, Vol. 75, No. 12, 5119–5122. https://doi.org/10.1063/1.1819431

[12] Meng, G.; Chen, J.; Bao, W.; Wang, Z. (2023). Characterization of thermal boundary resistance at solid–liquid interface based on continuous wave frequency domain thermal reflection method, *Heat and Mass Transfer*, Vol. 59, 203–213. https://doi.org/10.1007/s00231-022-03243-w

[13] Ge, Z.; Cahill, D. G.; Braun, P. V. (2006). Thermal conductance of hydrophilic and hydrophobic interfaces, *Physical Review Letters*, Vol. 96, No. 18, 186101. https://doi.org/10.1103/PhysRevLett.96.186101

[14] Shi, L.; Majumdar, A. (2002). Thermal transport mechanisms at nanoscale point

contacts, *Journal of Heat Transfer*, Vol. 124, No. 2, 329–337. https://doi.org/10.1115/1.1447939

[15] Ueki, Y.; Oyabu, T.; Shibahara, M. (2020). Experimental study of influence of nanoparticles adhesion and sedimentation layer on solid-liquid interfacial thermal resistance, *International Communications in Heat and Mass Transfer*, Vol. 117, 104807. https://doi.org/10.1016/j.icheatmasstransfer.2020.104807

[16] Chan, H.; Cherukara, M. J.; Narayanan, B.; Loeffler, T. D.; Benmore, C.; Gray, S. K.; Sankaranarayanan, S. K. R. S. (2019). Machine learning coarse grained models for water, *Nature Communications*, Vol. 10, No. 1, 379. https://doi.org/10.1038/s41467-018-08222-6

[17] Maruyama, S.; Kimura, T. (1999). A study on thermal resistance over a solid-liquid interface by the molecular dynamics method, *Thermal Science & Engineering*, Vol. 7, No. 1, 63–68

[18] Pham, A.; Barisik, M.; Kim, B. (2013). Pressure dependence of Kapitza resistance at gold/water and silicon/water interfaces, *The Journal of Chemical Physics*, Vol. 139, No. 24, 244702. https://doi.org/10.1063/1.4851395

[19] Han, H.; Mérabia, S.; Müller-Plathe, F. (2017). Thermal transport at solid-liquid interfaces: high pressure facilitates heat flow through nonlocal liquid structuring, *Journal of Physical Chemistry Letters*, Vol. 8, No. 9, 1946–1951. https://doi.org/10.1021/acs.jpclett.7b00227

[20] Fujiwara, K.; Shibahara, M. (2019). Detection of heat flux at single-atom scale in a liquid-solid interfacial region based on classical molecular dynamics, *Applied Physics Letters*, Vol. 114, No. 1, 011601. https://doi.org/10.1063/1.5062589

[21] Rafiee, J.; Mi, X.; Gullapalli, H.; Thomas, A. V.; Yavari, F.; Shi, Y.; Ajayan, P. M.; Koratkar, N. A. (2012). Wetting transparency of graphene, *Nature Materials*, Vol. 11, No. 3, 217–222. https://doi.org/10.1038/nmat3228

[22] Pham, A. T.; Barisik, M.; Kim, B. H. (2016). Interfacial thermal resistance between the graphene-coated copper and liquid water, *International Journal of Heat and Mass Transfer*, Vol. 97, 422–431. https://doi.org/10.1016/j.ijheatmasstransfer.2016.02.040

[23] Maccarini, M.; Steitz, R.; Himmelhaus, M.; Fick, J.; Tatur, S.; Wolff, M.; Grunze, M.; Janeček, J.; Netz, R. R. (2007). Density depletion at solid-liquid interfaces: A neutron reflectivity study, *Langmuir*, Vol. 23, No. 2, 598–608. https://doi.org/10.1021/la061943y

[24] Mamatkulov, S. I.; Khabibullaev, P. K.; Netz, R. R. (2004). Water at hydrophobic substrates: Curvature, pressure, and temperature effects, *Langmuir*, Vol. 20, No. 11, 4756–4763. https://doi.org/10.1021/la036036x

[25] Ramos-Alvarado, B.; Kumar, S.; Peterson, G. P. (2016). Solid-liquid thermal transport and its relationship with wettability and the interfacial liquid structure, *Journal of Physical Chemistry Letters*, Vol. 7, No. 17, 3497–3501.

https://doi.org/10.1021/acs.jpclett.6b01605

[26] Shibahara, M.; Takeuchi, K. (2011). A molecular dynamics study on the effects of nanostructural clearances on thermal resistance at a Lennard-Jones liquid-solid interface, *Journal of Thermal Science and Technology*, Vol. 6, No. 1, 9–20. https://doi.org/10.1299/jtst.6.9

[27] Issa, K. M.; Mohamad, A. A. (2012). Lowering liquid-solid interfacial thermal resistance with nanopatterned surfaces, *Physical Review E*, Vol. 85, No. 3, 031602. https://doi.org/10.1103/PhysRevE.85.031602

[28] Lee, E.; Zhang, T.; Yoo, T.; Guo, Z.; Luo, T. (2016). Nanostructures significantly enhance thermal transport across solid interfaces, *ACS Applied Materials and Interfaces*, Vol. 8, No. 51, 35505–35512. https://doi.org/10.1021/acsami.6b12947

[29] Li, C.; Wang, Z.; Wang, P. I.; Peles, Y.; Koratkar, N.; Peterson, G. P. (2008). Nanostructured copper interfaces for enhanced boiling, *Small*, Vol. 4, No. 8, 1084–1088. https://doi.org/10.1002/smll.200700991

[30] Amrit, J. (2010). Impact of surface roughness temperature dependency on the thermal contact resistance between Si(111) and liquid ^{4}He, *Physical Review B*, Vol. 81, No. 5, 054303. https://doi.org/10.1103/PhysRevB.81.054303

[31] Shafer, J.; Lee, J.; Thyagarajan, A.; Banerjee, D. (2022). Experimental study of the nano-fin effect (nFE) during thin film evaporation from nanopores in anodic aluminum oxide (AAO) membrane substrates integrated with nano-thermocouple / thin film thermocouple (TFT) array, *ASME International Mechanical Engineering Congress and Exposition, Proceedings (IMECE)* (Vol. 8), V008T11A017. https://doi.org/10.1115/IMECE2022-96168

[32] Liu, H.; Ahmad, S.; Chen, J.; Zhao, J. (2020). Molecular dynamics study of the nanoscale boiling heat transfer process on nanostructured surfaces, *International Communications in Heat and Mass Transfer*, Vol. 119, 104963. https://doi.org/10.1016/j.icheatmasstransfer.2020.104963

[33] Gao, S.; Liu, W.; Liu, Z. (2019). Tuning nanostructured surfaces with hybrid wettability areas to enhance condensation, *Nanoscale*, Vol. 11, No. 2, 459–466. https://doi.org/10.1039/c8nr05772a

[34] Shibahara, M.; Takeuchi, K. (2008). A molecular dynamics study on the effects of nanostructural clearances on thermal resistance at a liquid water-solid interface, *Nanoscale and Microscale Thermophysical Engineering*, Vol. 12, No. 4, 311–319. https://doi.org/10.1080/15567260802591977

[35] Hu, H.; Sun, Y. (2012). Effect of nanopatterns on Kapitza resistance at a water-gold interface during boiling: A molecular dynamics study, *Journal of Applied Physics*, Vol. 112, No. 5, 053508. https://doi.org/10.1063/1.4749393

[36] Fujiwara, K.; Shibahara, M. (2015). A molecular dynamics study on wetting phenomena at a solid surface with a nanometer-scale slit pore, *Journal of Nanoscience and Nanotechnology*, Vol. 15, No. 4, 3143–3146.

https://doi.org/10.1166/jnn.2015.9655

[37] Suwa, T.; Ueki, Y.; Shibahara, M. (2018). Molecular dynamics study on effects of nanostructures on adsorption onto solid surface, *Computers and Fluids*, Vol. 164, 12–17. https://doi.org/10.1016/j.compfluid.2016.09.020

[38] Wenzel, R. N. (1936). Resistance of solid surfaces to wetting by water, *Industrial and Engineering Chemistry*, Vol. 28, No. 8, 988–994. https://doi.org/10.1021/ie50320a024

[39] Cassie, A. B. D.; Baxter, S. (1944). Wettability of porous surfaces, *Transactions of the Faraday Society*, Vol. 40, 546–551. https://doi.org/10.1039/tf9444000546

[40] Shao, C.; Bao, H. (2015). A molecular dynamics investigation of heat transfer across a disordered thin film, *International Journal of Heat and Mass Transfer*, Vol. 85, 33–40. https://doi.org/10.1016/j.ijheatmasstransfer.2015.01.094

[41] Chen, S.; Liu, Q.; Gorbatikh, L.; Seveno, D. (2021). Does thermal percolation exist in graphene-reinforced polymer composites? A molecular dynamics answer, *Journal of Physical Chemistry C*, Vol. 125, No. 1, 1018–1028. https://doi.org/10.1021/acs.jpcc.0c09249

[42] Lu, Z.; Wang, Y.; Ruan, X. (2016). Metal/dielectric thermal interfacial transport considering cross-interface electron-phonon coupling: Theory, two-temperature molecular dynamics, and thermal circuit, *Physical Review B*, Vol. 93, No. 6, 064302. https://doi.org/10.1103/PhysRevB.93.064302

[43] Daw, M. S.; Foiles, S. M.; Baskes, M. I. (1993). The embedded-atom method: a review of theory and applications, *Materials Science Reports*, Vol. 9, Nos. 7–8, 251–310. https://doi.org/10.1016/0920-2307(93)90001-U

[44] Brenner, D. W.; Shenderova, O. A.; Harrison, J. A.; Stuart, S. J.; Ni, B.; Sinnott, S. B. (2002). A second-generation reactive empirical bond order (REBO) potential energy expression for hydrocarbons, *Journal of Physics Condensed Matter*, Vol. 14, No. 4, 783–802. https://doi.org/10.1088/0953-8984/14/4/312

[45] Pi, H. L.; Aragones, J. L.; Vega, C.; Noya, E. G.; Abascal, J. L. F.; Gonzalez, M. A.; McBride, C. (2009). Anomalies in water as obtained from computer simulations of the TIP4P/2005 model: Density maxima, and density, isothermal compressibility and heat capacity minima, *Molecular Physics*, Vol. 107, Nos. 4–6, 365–374. https://doi.org/10.1080/00268970902784926

[46] Alkhwaji, A.; Elbahloul, S.; Abdullah, M. Z.; Bakar, K. F. B. A. (2021). Selected water thermal properties from molecular dynamics for engineering purposes, *Journal of Molecular Liquids*, Vol. 324, 114703. https://doi.org/10.1016/j.molliq.2020.114703

[47] Lee, S. H. (2014). Temperature dependence of the thermal conductivity of water: A molecular dynamics simulation study using the SPC/E model, *Molecular Physics*, Vol. 112, No. 16, 2155–2159. https://doi.org/10.1080/00268976.2014.891769

[48] Meyer, N.; Piquet, V.; Wax, J. F.; Xu, H.; Millot, C. (2019). Rotational and translational dynamics of the SPC/E water model, *Journal of Molecular Liquids*, Vol. 275, 895–908. https://doi.org/10.1016/j.molliq.2018.08.024

[49] Berendsen, H. J. C.; Grigera, J. R.; Straatsma, T. P. (1987). The missing term in effective pair potentials, *Journal of Physical Chemistry*, Vol. 91, No. 24, 6269–6271. https://doi.org/10.1021/j100308a038

[50] Ryckaert, J. P.; Ciccotti, G.; Berendsen, H. J. C. (1977). Numerical integration of the cartesian equations of motion of a system with constraints: molecular dynamics of n-alkanes, *Journal of Computational Physics*, Vol. 23, No. 3, 327–341. https://doi.org/10.1016/0021-9991(77)90098-5

[51] Hockney, R. W.; Eastwood, J. W. (1988). *Computer Simulation Using Particles*, *Computer Simulation Using Particles*, CRC Press, Boca Raton. https://doi.org/10.1201/9780367806934

[52] Tersoff, J. (1988). New empirical approach for the structure and energy of covalent systems, *Physical Review B*, Vol. 37, No. 12, 6991. https://doi.org/10.1103/PhysRevB.37.6991

[53] Vo, T. Q.; Kim, B. (2016). Transport phenomena of water in molecular fluidic channels, *Scientific Reports*, Vol. 6, 33881. https://doi.org/10.1038/srep33881

[54] Alexeev, D.; Chen, J.; Walther, J. H.; Giapis, K. P.; Angelikopoulos, P.; Koumoutsakos, P. (2015). Kapitza resistance between few-layer graphene and water: liquid layering effects, *Nano Letters*, Vol. 15, No. 9, 5744–5749. https://doi.org/10.1021/acs.nanolett.5b03024

[55] Situ, W.; Zambrano, H. A.; Walther, J. H. (2022). The effect of air solubility on the Kapitza resistance of the copper-water interface, *Journal of Molecular Liquids*, Vol. 366, 120049. https://doi.org/10.1016/j.molliq.2022.120049

[56] Vera, J.; Bayazitoglu, Y. (2015). Temperature and heat flux dependence of thermal resistance of water/metal nanoparticle interfaces at sub-boiling temperatures, *International Journal of Heat and Mass Transfer*, Vol. 86, 433–442. https://doi.org/10.1016/j.ijheatmasstransfer.2015.02.033

[57] Tuckerman, M.; Berne, B. J.; Martyna, G. J. (1992). Reversible multiple time scale molecular dynamics, *The Journal of Chemical Physics*, Vol. 97, No. 3, 1990–2001. https://doi.org/10.1063/1.463137

[58] Han, G.; Deng, Y.; Glimm, J.; Martyna, G. (2007). Error and timing analysis of multiple time-step integration methods for molecular dynamics, *Computer Physics Communications*, Vol. 176, No. 4, 271–291. https://doi.org/10.1016/j.cpc.2006.10.005

[59] Ozcelik, H. G.; Ozdemir, A. C.; Kim, B.; Barisik, M. (2020). Wetting of single crystalline and amorphous silicon surfaces: effective range of intermolecular forces for wetting, *Molecular Simulation*, Vol. 46, No. 3, 224–234. https://doi.org/10.1080/08927022.2019.1690145

[60] Sirk, T. W.; Moore, S.; Brown, E. F. (2013). Characteristics of thermal conductivity in classical water models, *Journal of Chemical Physics*, Vol. 138, No. 6, 064505. https://doi.org/10.1063/1.4789961

[61] Fu, H.; Chen, J.; Wang, H.; Liu, Z.; Sorensen, H.; Bahman, A. S. (2023). 3-D-lumped thermal network models for the reliability analysis of fan-cooled plate-fin heatsink, *IEEE Journal of Emerging and Selected Topics in Power Electronics*, Vol. 11, No. 3, 3480–3491. https://doi.org/10.1109/JESTPE.2023.3237717

[62] Fluid Property Calculator. from https://irc.wisc.edu/properties/

[63] Nath, P.; Chopra, K. L. (1974). Thermal conductivity of copper films, *Thin Solid Films*, Vol. 20, No. 1, 53–62. https://doi.org/10.1016/0040-6090(74)90033-9

[64] Haitao, W.; Yibin, X.; Shimono, M.; Tanaka, Y.; Yamazaki, M. (2007). Molecular dynamics simulation of thermal conductivity of silicon thin film, *Materials Transactions*, Vol. 48, No. 9, 2419–2421. https://doi.org/10.2320/matertrans.MAW200710

[65] Gonçalves, W.; Isaiev, M.; Lacroix, D.; Gomès, S.; Termentzidis, K. (2022). Interfacial thermal resistance between nanoconfined water and silicon: Impact of temperature and silicon phase, *Surfaces and Interfaces*, Vol. 33, 102188. https://doi.org/10.1016/j.surfin.2022.102188

[66] Feng, B.; Li, Z.; Zhang, X. (2009). Role of phonon in the thermal and electrical transports in metallic nanofilms, *Journal of Applied Physics*, Vol. 105, No. 10. https://doi.org/10.1063/1.3129707

[67] Sæther, S.; Erichsen, M. F.; Xiao, S.; Zhang, Z.; Lervik, A.; He, J. (2022). Phonon thermal transport in copper: The effect of size, crystal orientation, and grain boundaries, *AIP Advances*, Vol. 12, No. 6. https://doi.org/10.1063/5.0094170

[68] Vorpérian, V. (2002). *Fast Analytical Techniques for Electrical and Electronic Circuits*, *Fast Analytical Techniques for Electrical and Electronic Circuits*, Cambridge University Press. https://doi.org/10.1017/cbo9780511613791

[69] Fugallo, G.; Cepellotti, A.; Paulatto, L.; Lazzeri, M.; Marzari, N.; Mauri, F. (2014). Thermal conductivity of graphene and graphite: Collective excitations and mean free paths, *Nano Letters*, Vol. 14, No. 11, 6109–6114. https://doi.org/10.1021/nl502059f

[70] Surblys, D.; Kawagoe, Y.; Shibahara, M.; Ohara, T. (2019). Molecular dynamics investigation of surface roughness scale effect on interfacial thermal conductance at solid-liquid interfaces, *Journal of Chemical Physics*, Vol. 150, No. 11, 114705. https://doi.org/10.1063/1.5081103

[71] Plimpton, S. (1995). Fast parallel algorithms for short-range molecular dynamics, *Journal of Computational Physics*, Vol. 117, No. 1, 1–19. https://doi.org/10.1006/jcph.1995.1039

[72] Stukowski, A. (2010). Visualization and analysis of atomistic simulation data with OVITO-the Open Visualization Tool, *Modelling and Simulation in Materials*

Science and Engineering, Vol. 18, No. 1, 015012. https://doi.org/10.1088/0965-0393/18/1/015012

[73] R. E. Sonntag and C. Borgnakke. (2002). Table of thermodynamics and transport properties: computer-aided thermodynamics tables software provided by fundamentals of thermodynamics, NewYork

[74] Teplukhin, A. V. (2019). Thermodynamic and structural characteristics of SPC/E water at 290 K and under high pressure, *Journal of Structural Chemistry*, Vol. 60, No. 10, 1590–1598. https://doi.org/10.1134/S0022476619100044

[75] Antony, A. C.; Liang, T.; Akhade, S. A.; Janik, M. J.; Phillpot, S. R.; Sinnott, S. B. (2016). Effect of surface chemistry on water interaction with Cu(111), *Langmuir*, Vol. 32, No. 32, 8061–8070. https://doi.org/10.1021/acs.langmuir.6b01974

[76] Tang, Y. Z.; Zhang, X. G.; Lin, Y.; Xue, J.; He, Y.; Ma, L. X. (2019). Molecular dynamics simulation of nanofilm boiling on graphene-coated surface, *Advanced Theory and Simulations*, Vol. 2, No. 8, 1900065. https://doi.org/10.1002/adts.201900065

[77] Cao, B. Y.; Zou, J. H.; Hu, G. J.; Cao, G. X. (2018). Enhanced thermal transport across multilayer graphene and water by interlayer functionalization, *Applied Physics Letters*, Vol. 112, No. 4, 041603. https://doi.org/10.1063/1.5018749

[78] Zhang, X.; Chen, H.; Qiao, D.; Yang, M. (2023). Effects of structure defects on thermal transport at the graphene–water interface, *Advanced Materials Interfaces*, Vol. 10, No. 14, 2202518. https://doi.org/10.1002/admi.202202518

[79] Matsubara, H.; Surblys, D.; Bao, Y.; Ohara, T. (2022). Molecular dynamics study on vibration-mode matching in surfactant-mediated thermal transport at solid–liquid interfaces, *Journal of Molecular Liquids*, Vol. 347, 118363. https://doi.org/10.1016/j.molliq.2021.118363

[80] Hung, S. W.; Hu, S.; Shiomi, J. (2019). Spectral control of thermal boundary conductance between copper and carbon crystals by self-assembled monolayers, *ACS Applied Electronic Materials*, Vol. 1, No. 12, 2594–2601. https://doi.org/10.1021/acsaelm.9b00587

[81] Ardham, V. R.; Leroy, F. (2017). Communication: Is a coarse-grained model for water sufficient to compute Kapitza conductance on non-polar surfaces?, *Journal of Chemical Physics*, Vol. 147, No. 15, 151102. https://doi.org/10.1063/1.5003199

[82] El-Machachi, Z.; Wilson, M.; Deringer, V. L. (2022). Exploring the configurational space of amorphous graphene with machine-learned atomic energies, *Chemical Science*, Vol. 13, No. 46, 13720–13731. https://doi.org/10.1039/d2sc04326b

[83] Hu, M.; Zhang, X.; Poulikakos, D. (2013). Anomalous thermal response of silicene to uniaxial stretching, *Physical Review B*, Vol. 87, No. 19, 195417. https://doi.org/10.1103/PhysRevB.87.195417

[84] Androulidakis, C.; Koukaras, E. N.; Parthenios, J.; Kalosakas, G.; Papagelis, K.; Galiotis, C. (2015). Graphene flakes under controlled biaxial deformation,

Scientific Reports, Vol. 5, 18219. https://doi.org/10.1038/srep18219

[85] Pollard, A. J.; Brennan, B.; Stec, H.; Tyler, B. J.; Seah, M. P.; Gilmore, I. S.; Roy, D. (2014). Quantitative characterization of defect size in graphene using Raman spectroscopy, *Applied Physics Letters*, Vol. 105, No. 25, 253107. https://doi.org/10.1063/1.4905128

[86] Eckmann, A.; Felten, A.; Mishchenko, A.; Britnell, L.; Krupke, R.; Novoselov, K. S.; Casiraghi, C. (2012). Probing the nature of defects in graphene by Raman spectroscopy, *Nano Letters*, Vol. 12, No. 8, 3925–3930. https://doi.org/10.1021/nl300901a

[87] Olarte-Plata, J. D.; Bresme, F. (2022). The impact of the thermostats on the non-equilibrium computer simulations of the interfacial thermal conductance, *Molecular Simulation*, Vol. 48, No. 1, 87–98. https://doi.org/10.1080/08927022.2021.1959033

[88] Mikami, N.; Ueki, Y.; Shibahara, M.; Aizawa, K.; Ara, K. (2023). State sensing of bubble jet flow based on acoustic recognition and deep learning, *International Journal of Multiphase Flow*, Vol. 159, 104340. https://doi.org/10.1016/j.ijmultiphaseflow.2022.104340

[89] Kurogi, K.; Yan, H.; Tsujii, K. (2008). Importance of pinning effect of wetting in super water-repellent surfaces, *Colloids and Surfaces A: Physicochemical and Engineering Aspects*, Vol. 317, Nos. 1–3, 592–597. https://doi.org/10.1016/j.colsurfa.2007.11.048

[90] Yenigun, O.; Barisik, M. (2019). Electric field controlled heat transfer through silicon and nano-confined water, *Nanoscale and Microscale Thermophysical Engineering*, Vol. 23, No. 4, 304–316. https://doi.org/10.1080/15567265.2019.1628136

[91] Alosious, S.; Kannam, S. K.; Sathian, S. P.; Todd, B. D. (2020). Kapitza resistance at water-graphene interfaces, *The Journal of Chemical Physics*, Vol. 152, No. 22, 224703. https://doi.org/10.1063/5.0009001

Acknowledgements

Completing my degree has been one of the most significant journeys of my life. Along the way, I am deeply aware that it would not have been possible without the support and help of many people. Here, I would like to extend my heartfelt gratitude to them.

First and foremost, I would like to thank my supervisor, Professor Masahiko Shibahara. Under your meticulous guidance, I have learned how to explore the unknown and persevere on the path of scientific research. Your rigorous academic attitude and broad academic vision have profoundly influenced me and inspired me to pursue excellence in research.

I am also deeply grateful to my thesis committee members: Professor Fumiteru Akamatsu, Professor Shohji Tsushima, and Associate Professor Kunio Fujiwara, for their valuable comments and suggestions.

I also acknowledge my fellow lab members in the Shibahara-Fujiwara Laboratory. Associate Professor Y. Ueki, Ms. H. Okuda, and the students, who kindly supported my research.

I have done this work with the help of my friends. I would like to thank Mr. X. Zhang and Dr. J. Guo for supporting this work.

Special thanks to my family, especially my brother, Mr. Zhiwu Jiang, thank you for supporting me in the background and always providing warm encouragement. Your understanding and love have been the greatest source of strength for me.

All related contents such as Figures are granted and reprinted by permission of Begell House, Informa UK Limited, trading as Taylor & Taylor & Francis Group, and Elsevier Masson SAS. The granted articles are shown in the List of Publications.

List of Publications

Journal papers

- Z. Jiang and M. Shibahara, "Application of a thermal circuit model for the prediction of interfacial thermal resistance between water and a nanostructure surface using molecular dynamics simulations", International Journal of Thermal Science, 208, (2025), 109441. Copyright © 2024 Elsevier Masson SAS. https://doi.org/10.1016/j.ijthermalsci.2024.109441.

- Z. Jiang and M. Shibahara, "Molecular dynamics investigation of the effects of thin periodic defective graphene on the interfacial thermal resistance at liquid-solid interfaces", Numerical Heat Transfer, Part A: Applications, (2024), 1–14 Copyright © 2024 reprinted by permission of Informa UK Limited, trading as Taylor & Taylor & Francis Group, http://www.tandfonline.com. https://doi.org/10.1080/10407782.2023.2300355.

- Z. Jiang and M. Shibahara, "Molecular dynamics study on the relationship between density depletion length and interfacial thermal resistance at nanostructured surfaces", Heat Transfer Research, 54, (2023), 77–92. https://doi.org/10.1615/HeatTransRes.2022044125.

Oral and Poster presentations at the conference

- Z. Jiang and M. Shibahara, "Molecular dynamics study on influences of water models on thermal resistance at the solid-water interface", The 8th Asian Symposium on Computational Heat Transfer and Fluid Flow, ASCHT2021-298, Qingdao, China, September 2021 (poster).

Awards

- Best poster award, The 8th Asian Symposium on Computational Heat Transfer and Fluid Flow, ASCHT2021-298, Qingdao, China, September 2021.

Appendix

Appendix Chapter 2

Table S2.1 The thermal conductivity employed using the MD simulations and experiments under the water pressure of 0 MPa to 30 MPa in the Cu-graphene-water systems.

$k_{Cu\text{-}exp}$ and $k_{liq\text{-}exp}$ are based on the report [63] and open database[62] for all cases.

	Items	$k_{liq\text{-}MD}$	$k_{Cu\text{-}MD}$	$k_{liq\text{-}exp}$	$k_{Cu\text{-}exp}$
CG	CA11-SV0.0	0.35	4.31	0.58	406
	CA11-SV2.1	0.41	2.96	0.59	
	CA11-SV2.8	0.39	2.88	0.58	
	CA12-SV0.0	0.41	3.12	0.60	
	CA12-SV2.1	0.39	3.15	0.59	
	CA12-SV2.8	0.41	2.28	0.60	
	CA21-SV0.0	0.42	8.74	0.58	
	CA21-SV2.1	0.42	4.25	0.58	
	CA21-SV2.8	0.37	8.16	0.58	
	CA22-SV0.0	0.40	6.96	0.59	
	CA22-SV2.1	0.39	3.55	0.59	
	CA22-SV2.8	0.47	2.29	0.59	
SPC/E	CA11-SV0.0	0.76	4.22	0.60	
	CA11-SV2.1	0.83	4.28	0.60	
	CA11-SV2.8	0.74	4.63	0.59	
	CA12-SV0.0	0.83	5.54	0.62	
	CA12-SV2.1	0.91	4.52	0.61	
	CA12-SV2.8	0.85	5.17	0.62	
	CA21-SV0.0	0.79	3.98	0.59	
	CA21-SV2.1	0.87	4.15	0.62	
	CA21-SV2.8	0.89	3.91	0.59	
	CA22-SV0.0	0.73	4.44	0.60	
	CA22-SV2.1	0.97	6.04	0.60	
	CA22-SV2.8	0.83	4.15	0.61	

Table S2.2 The thermal conductivity employed using the MD simulations and experiments under the water pressure of 100 MPa to 200 MPa in the Cu-graphene-water systems.

	Items	$k_{liq\text{-}MD}$	$k_{Cu\text{-}MD}$	$k_{liq\text{-}exp}$	$k_{Cu\text{-}exp}$
CG	CA11-SV0.0	0.44	5.20	0.65	406
	CA11-SV2.1	0.45	5.66	0.65	
	CA11-SV2.8	0.47	4.87	0.65	
	CA12-SV0.0	0.45	3.83	0.65	
	CA12-SV2.1	0.46	3.43	0.66	
	CA12-SV2.8	0.43	3.63	0.65	
	CA21-SV0.0	0.43	3.07	0.65	
	CA21-SV2.1	0.45	6.46	0.64	
	CA21-SV2.8	0.45	4.96	0.65	
	CA22-SV0.0	0.49	3.81	0.65	
	CA22-SV2.1	0.52	5.71	0.65	
	CA22-SV2.8	0.47	10.94	0.66	
SPC/E	CA11-SV0.0	0.84	5.79	0.65	
	CA11-SV2.1	0.83	4.78	0.65	
	CA11-SV2.8	0.95	3.36	0.64	
	CA12-SV0.0	0.99	2.88	0.65	
	CA12-SV2.1	0.78	8.85	0.66	
	CA12-SV2.8	0.87	3.18	0.65	
	CA21-SV0.0	0.84	6.77	0.65	
	CA21-SV2.1	0.89	4.52	0.64	
	CA21-SV2.8	0.78	5.46	0.64	
	CA22-SV0.0	0.85	6.26	0.65	
	CA22-SV2.1	0.81	4.38	0.65	
	CA22-SV2.8	0.83	3.49	0.65	

Table S2.3 The thermal conductivity employed using the MD simulations and experiments under the water pressure in excess of 200 MPa in the Cu-graphene-water systems.

	Items	$k_{liq\text{-}MD}$	$k_{Cu\text{-}MD}$	$k_{liq\text{-}exp}$	$k_{Cu\text{-}exp}$
CG	CA11-SV0.0	0.50	5.35	0.69	406
	CA11-SV2.1	0.49	5.01	0.69	
	CA11-SV2.8	0.49	3.61	0.69	
	CA12-SV0.0	0.46	5.97	0.70	
	CA12-SV2.1	0.53	3.68	0.69	
	CA12-SV2.8	0.57	6.06	0.69	
	CA21-SV0.0	0.48	4.90	0.69	
	CA21-SV2.1	0.44	6.06	0.69	
	CA21-SV2.8	0.48	3.73	0.68	
	CA22-SV0.0	0.56	4.76	0.69	
	CA22-SV2.1	0.55	3.82	0.69	
	CA22-SV2.8	0.58	5.19	0.69	
SPC/E	CA11-SV0.0	0.92	5.65	0.67	
	CA11-SV2.1	1.00	3.40	0.67	
	CA11-SV2.8	1.00	3.41	0.67	
	CA12-SV0.0	1.01	2.63	0.68	
	CA12-SV2.1	1.09	2.22	0.68	
	CA12-SV2.8	0.86	8.41	0.69	
	CA21-SV0.0	0.90	3.33	0.67	
	CA21-SV2.1	0.92	4.40	0.67	
	CA21-SV2.8	1.00	3.54	0.67	
	CA22-SV0.0	0.92	4.31	0.68	
	CA22-SV2.1	0.98	3.80	0.68	
	CA22-SV2.8	0.97	4.72	0.68	

Appendix Chapter 3

S3.1 The effect of slab sizes and interval time on ITRs using the SPC/E model

The influence of slab sizes (dz) and the interval time "dt" on the S-L temperature jump and ITR_{flat} on flat surfaces is shown in Figure S3.0. The temperature fluctuation of water was conducted using MD simulations. When the interval time was 2.0 fs, and the slab size was 0.3 nm or 0.5 nm, the temperature fluctuation occurred near the cold surface. This temperature fluctuation was jointly affected by the slab sizes and "dt". Under the same interval time, the larger the slab size, the more stable it was because the larger slab region contained enough water molecules, which expanded the average temperature sample of water molecules, making the temperature gradient of water smooth. This phenomenon was similar to the previous report[18, 54, 90, 91] because the temperature fluctuation close to solid surfaces was mainly caused by the van der Waals force between solid and liquid[18]. Under the same slab size, the reduction of "dt" might not decrease the temperature fluctuation because water molecules could still be in a situation of high-speed rotation and movement. Under similar cases, the increase in temperature difference at an interval time of 1.0 fs and with an interval time of 2.0 fs was about 1 K to -0.2 K. The different interval time (dt) did not greatly impact the temperature difference. The present study was closely related to ITRs and needed to consider the effect of "dt" and slab sizes on the ITRs of flat surfaces calculated by MD, as shown in Figure S3.0. Figures S3.0 (a to c) and (d to f) on flat surfaces correspond to the cases of CA1-(P1 to P3) and CA2-(P1 to P3), respectively. The details of water pressure on flat surfaces are given in Table 3.1. Under the same "dt" condition, the ITR_{flat} decreased slightly depending on the increase in slab size. When calculating the temperature gradient using the least squares method to calculate the SPC/E water sample, the increase in slab size eliminated the higher temperature fluctuations of water near the cold surface. Under the same slab size, the ITRs did not strongly depend on "dt", including temperature jumping of nanostructure surfaces using the SPC/E model, which is shown in Figures S3.1 to S3.8, and the bars of the ITRs related to the slab sizes and interval time on nanostructure surfaces are shown in Figures S3.12 and S3.13. In short, the influence of slab sizes and "dt" on temperature jumps and ITRs on flat and nanostructure surfaces was limited. Therefore, the slab size of 0.3 nm was employed in the present dissertation, and "dt" was shown in Section 2.4.

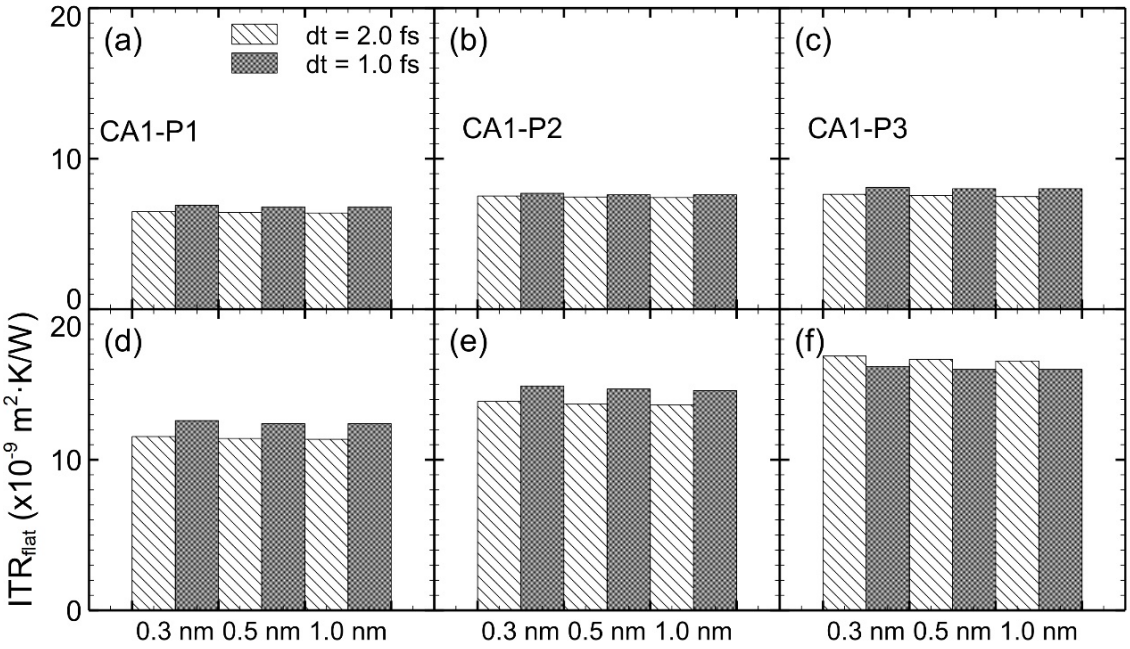

Figure S3.0 The influences of slab sizes and interval time on ITR_{flat} using the SPC/E model on flat surfaces. The light and dark bars describe the calculation results for the interval time of 2.0 fs and the interval time of 1.0 fs, respectively. The light color bar and the adjacent dark color bar form one of three groups. The groups from left, middle, and right correspond to the slab size of 0.3 nm, the slab size of 0.5 nm, and the slab size of 1.0 nm, respectively. (a) to (c) related to the water pressure of P1 to P3 in the CA1 cases, respectively. (e) to (f) related to the water pressure of P1 to P3 in the CA2 cases, respectively.

Figures S3.1 to S3.11 Temperature gradient in Cu-water systems

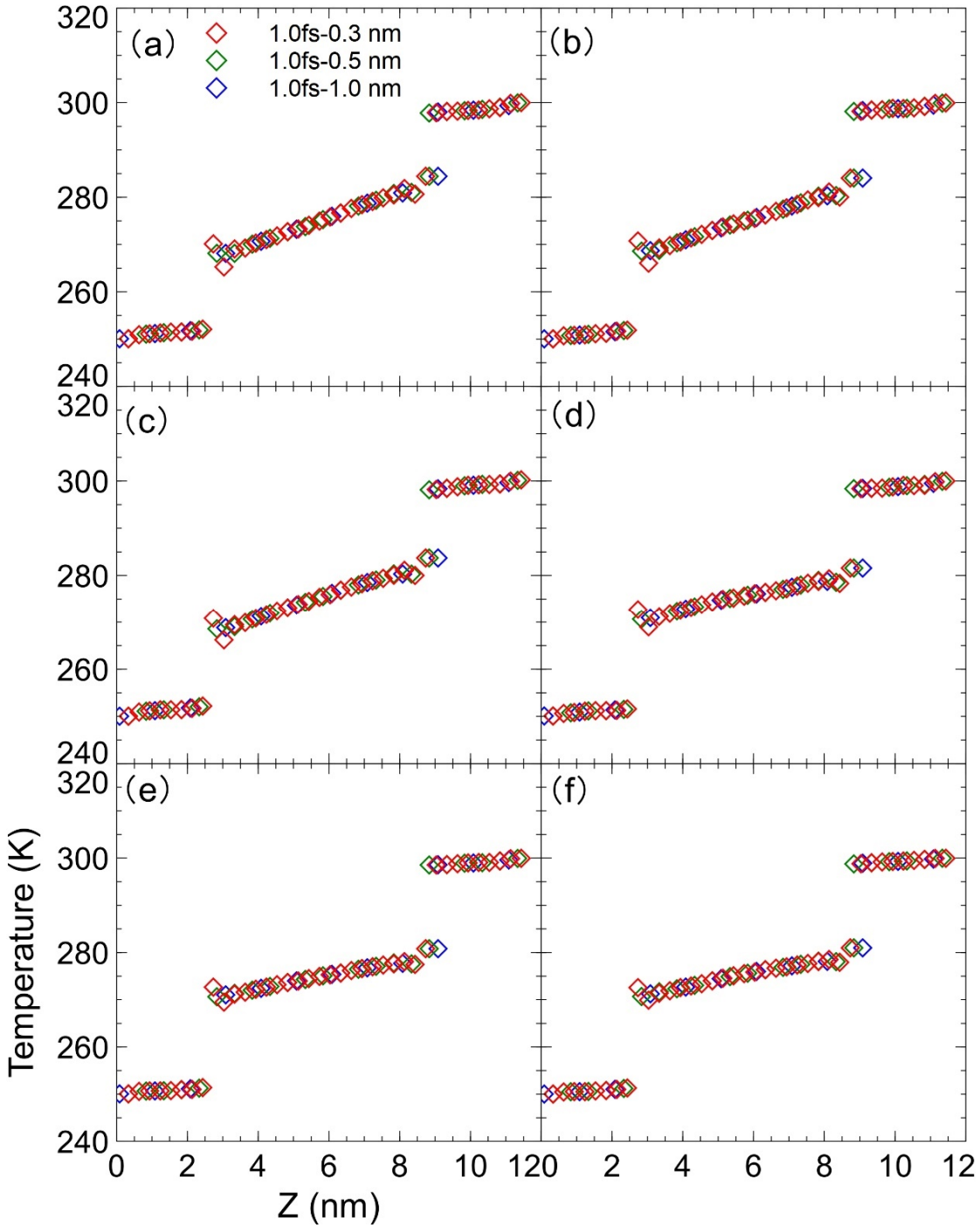

Figure S3.1 The effect of the slab sizes on temperature jumping between Cu and SPC/E water on flat surfaces with the dt of 1.0 fs. Red, green, and blue correspond to the slab sizes of 0.3 nm, 0.5 nm, and 1.0 nm, respectively. (a) to (c) related to the water pressure of P1 to P3 in the CA1 cases, respectively. (d) to (f) related to the water pressure of P1 to P3 in the CA2 cases, respectively.

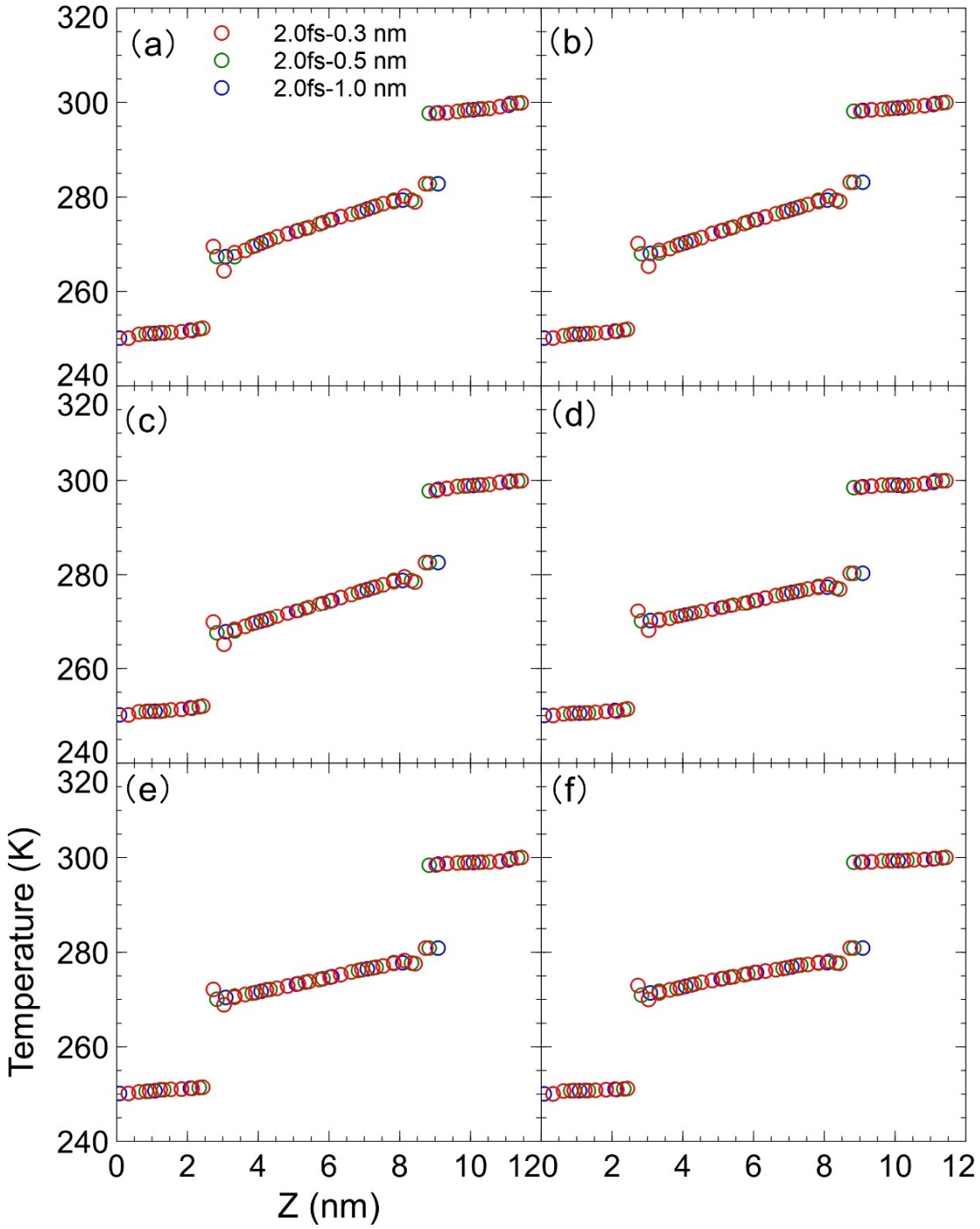

Figure S3.2 The effect of the slab sizes on temperature jumping between Cu and SPC/E water on flat surfaces with the dt (r-RESPA) of 2.0 fs. Red, green, and blue correspond to the slab sizes of 0.3 nm, 0.5 nm, and 1.0 nm, respectively. (a) to (c) related to the water pressure of P1 to P3 in the CA1 cases, respectively. (d) to (f) related to the water pressure of P1 to P3 in the CA2 cases, respectively.

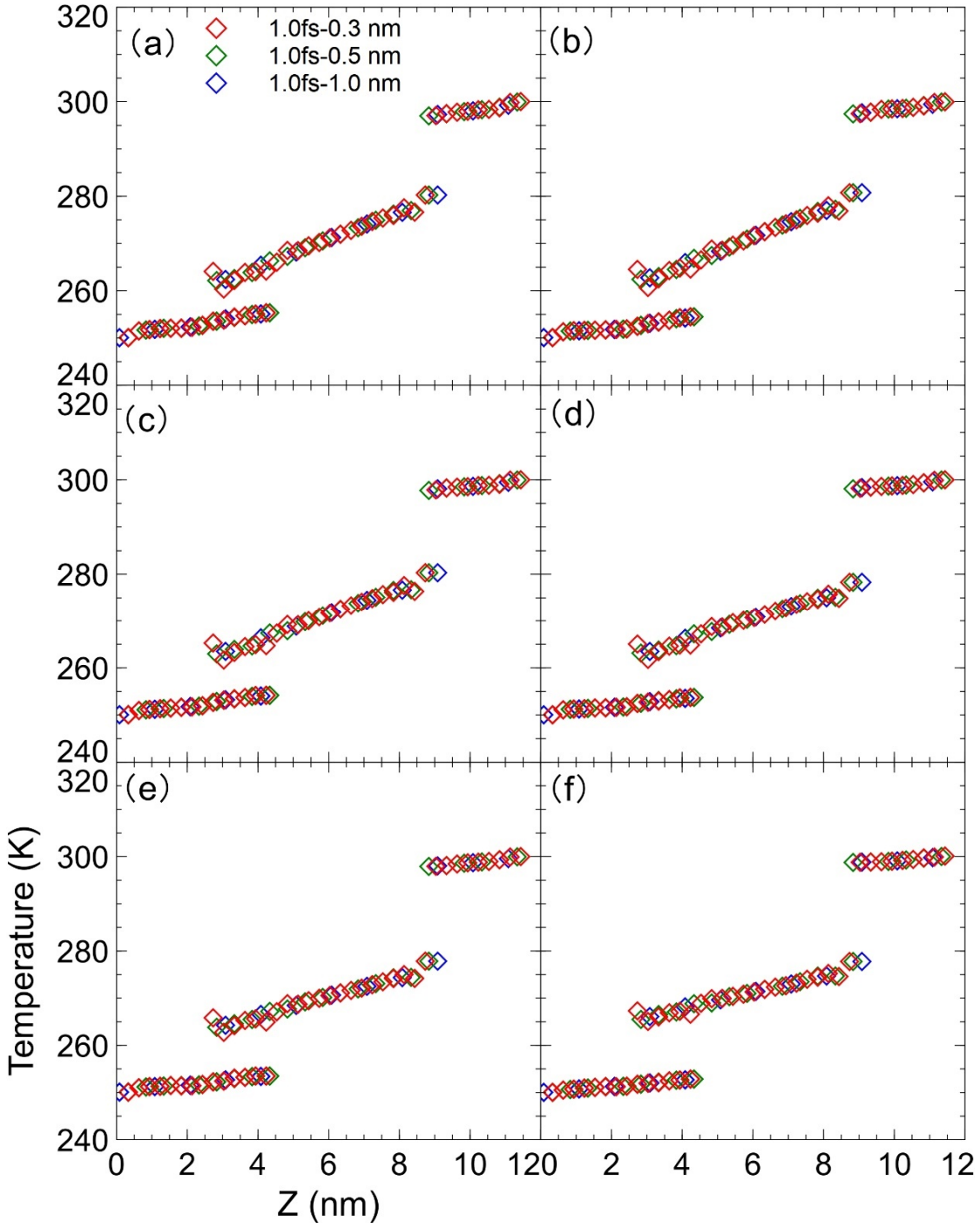

Figure S3.3 The effect of the slab sizes on temperature jumping between Cu and SPC/E water on nanostructure surfaces in the Wenzel states with the dt of 1.0 fs and the nanopillar width of S19. Red, green, and blue correspond to the slab sizes of 0.3 nm, 0.5 nm, and 1.0 nm, respectively. (a) to (c) related to the water pressure of P1 to P3 in the CA1 cases, respectively. (d) to (f) related to the water pressure of P1 to P3 in the CA2 cases, respectively.

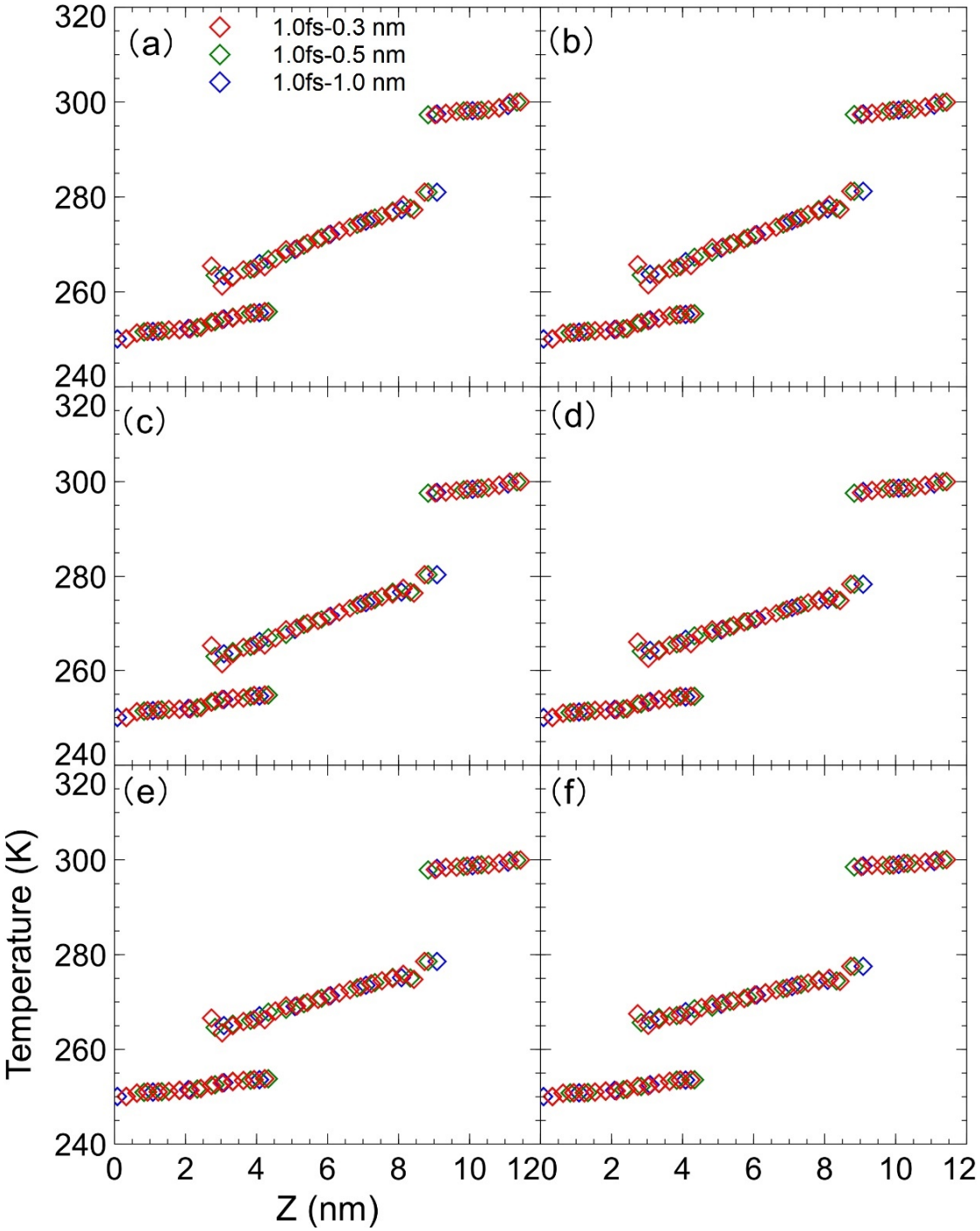

Figure S3.4 The effect of the slab sizes on temperature jumping between Cu and SPC/E water on nanostructure surfaces in the Wenzel states with the dt of 1.0 fs and the nanopillar width of S14. Red, green, and blue correspond to the slab sizes of 0.3 nm, 0.5 nm, and 1.0 nm, respectively. (a) to (c) related to the water pressure of P1 to P3 in the CA1 cases, respectively. (d) to (f) related to the water pressure of P1 to P3 in the CA2 cases, respectively.

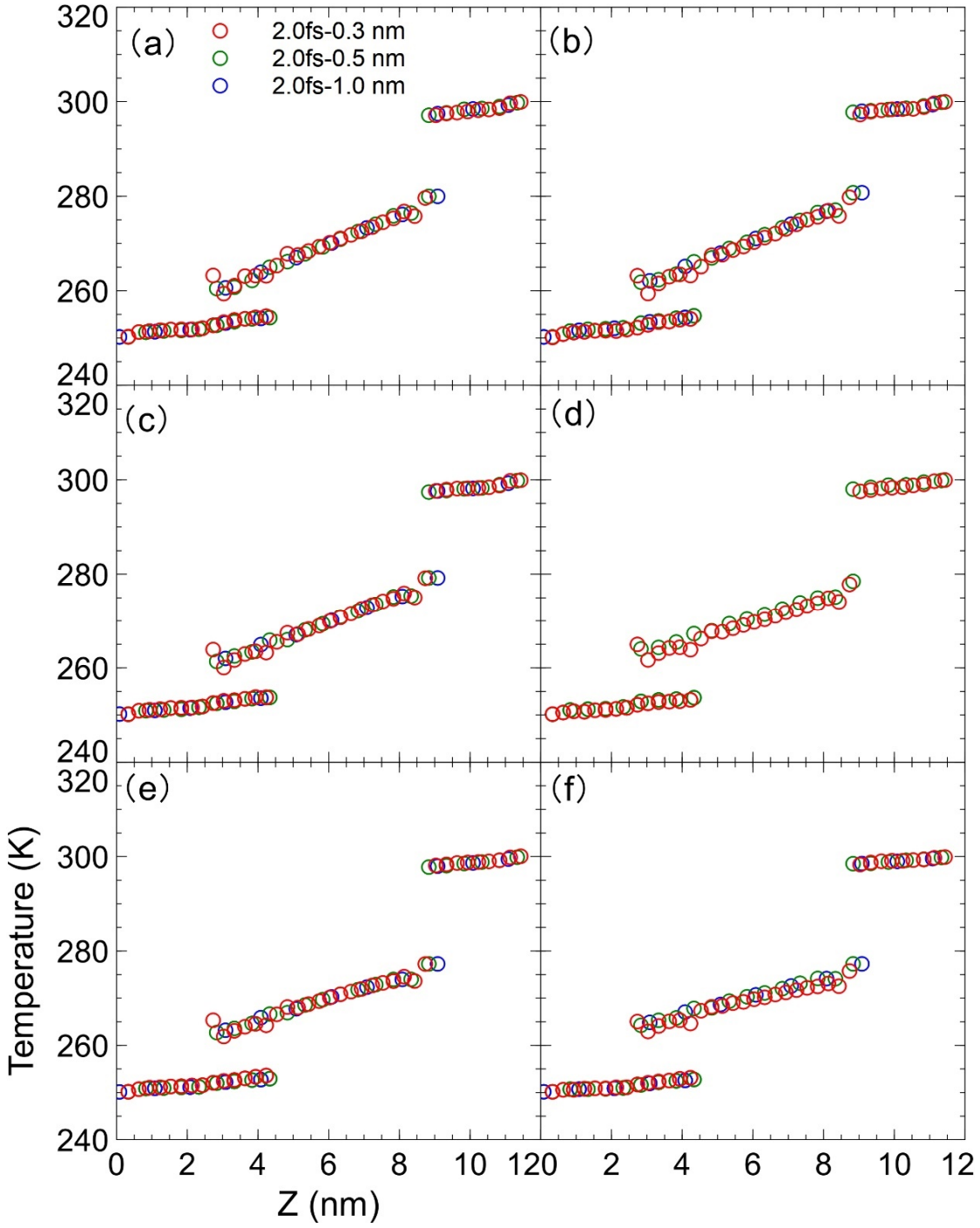

Figure S3.5 The effect of the slab sizes on temperature jumping between Cu and SPC/E water on nanostructure surfaces in the Wenzel states with the dt (r-RESPA) of 2.0 fs and the nanopillar width of S19. Red, green, and blue correspond to the slab sizes of 0.3 nm, 0.5 nm, and 1.0 nm, respectively. (a) to (c) related to P1 to P3 in the CA1 cases, and (d) to (f) related to P1 to P3 in the CA2 cases, respectively.

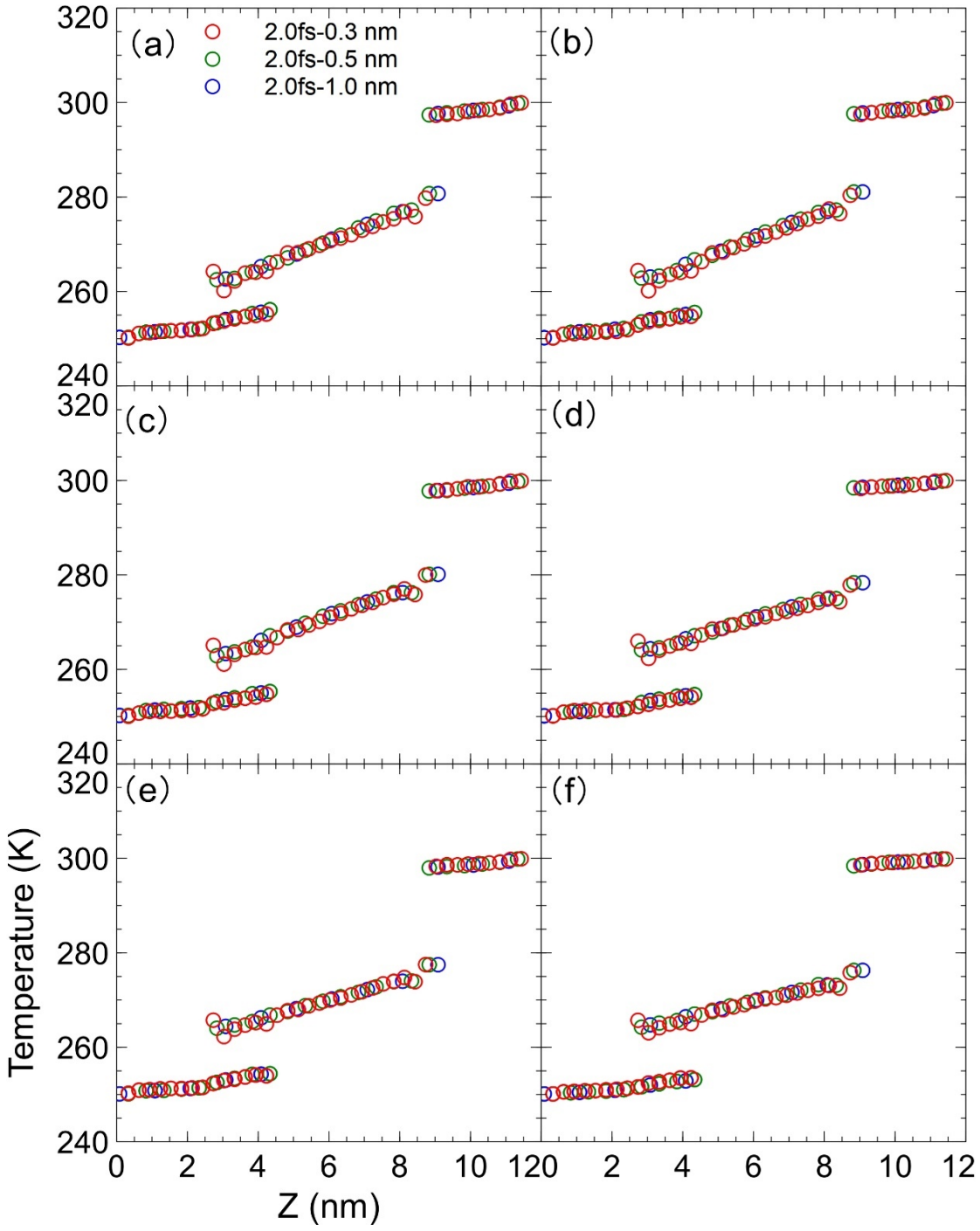

Figure S3.6 The effect of the slab sizes on temperature jumping between Cu and SPC/E water on nanostructure surfaces in the Wenzel states with the dt (r-RESPA) of 2.0 fs and the nanopillar width of S14. Red, green, and blue correspond to the slab sizes of 0.3 nm, 0.5 nm, and 1.0 nm, respectively. (a) to (c) related to P1 to P3 in the CA1 cases, and (d) to (f) related to P1 to P3 in the CA2 cases, respectively.

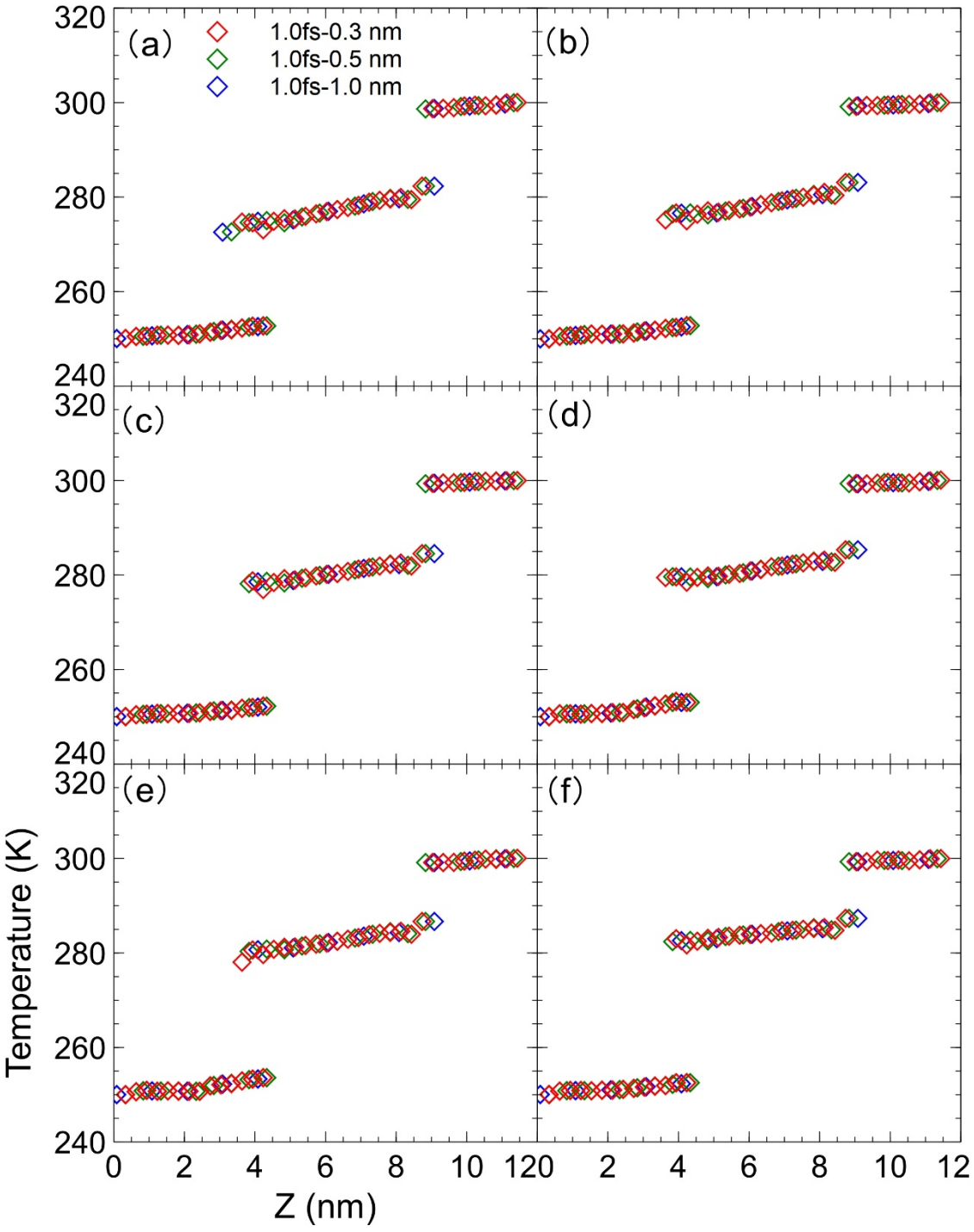

Figure S3.7 The effect of the slab sizes on temperature jumping between Cu and SPC/E water on nanostructure surfaces in the Cassie-Baxter states with the dt of 1.0 fs. Red, green, and blue correspond to the slab sizes of 0.3 nm, 0.5 nm, and 1.0 nm, respectively. (a) to (c) related to the water pressure of P1 to P3 with the nanopillar width of S19, respectively. (d) to (f) related to the water pressure of P1 to P3 with the nanopillar width of S14, respectively.

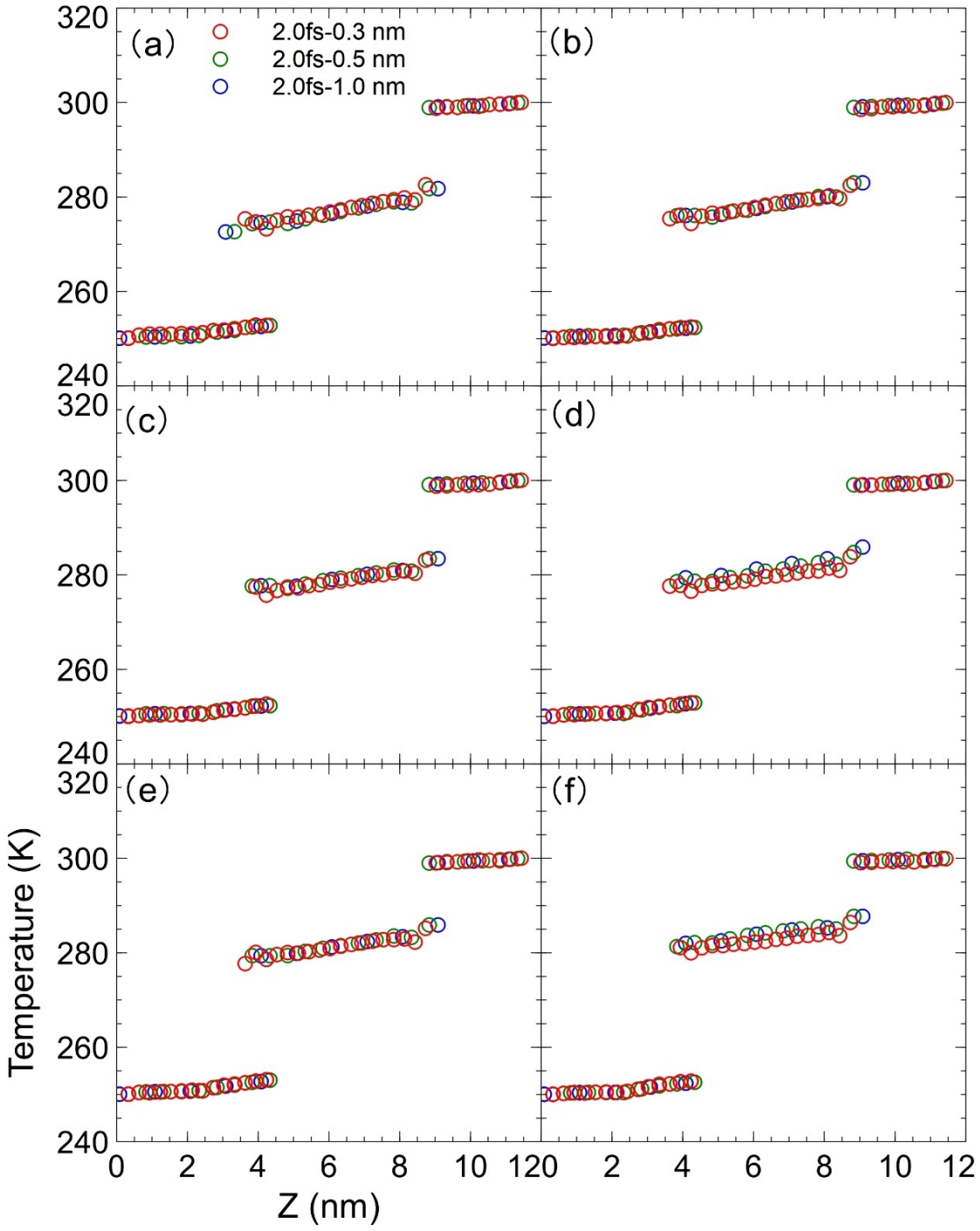

Figure S3.8 The effect of the slab sizes on temperature jumping between Cu and SPC/E water on nanostructure surfaces in the Cassie-Baxter states with the dt (r-RESPA) of 2.0 fs. Red, green, and blue correspond to the slab sizes of 0.3 nm, 0.5 nm, and 1.0 nm, respectively. (a) to (c) related to the water pressure of P1 to P3 with the nanopillar width of S19, respectively. (d) to (f) related to the water pressure of P1 to P3 with the nanopillar width of S14, respectively.

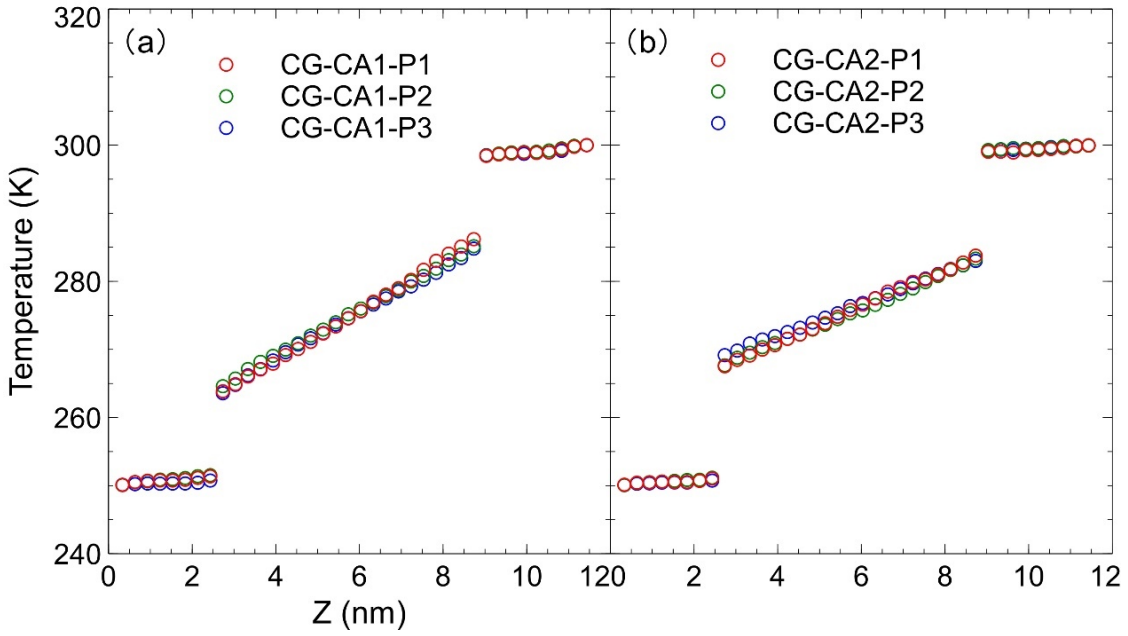

Figure S3.9 The temperature jumps between Cu and CG water on flat surfaces with the dt (r-RESPA) of 2.0 fs and slab size of 0.3 nm. Red, green, and blue correspond to the water pressure of P1, P2, and P3, respectively. The CA1 and CA2 cases were related to (a) and (b), respectively. (a) to (b) were employed in Chapter 3.

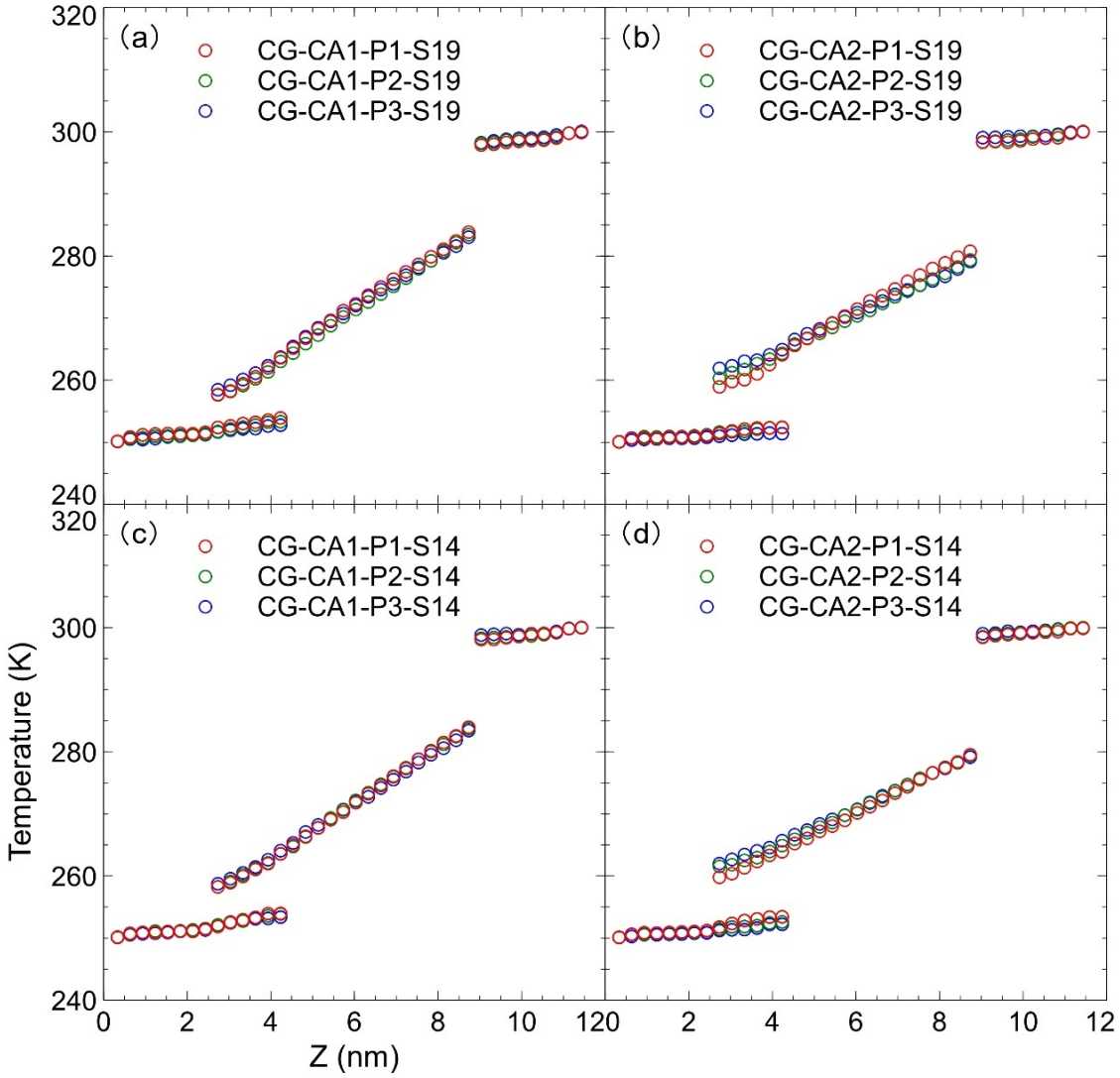

Figure S3.10 The temperature jumping between Cu and CG water on nanostructure surfaces in the Wenzel states with dt (r-RESPA) of 2.0 fs and a slab size of 0.3 nm. Red, green, and blue correspond to the water pressure of P1, P2, and P3, respectively. (a) and (b) were related to the nanopillar width of S19, respectively. (c) and (d) were related to the nanopillar width of S14, respectively. (a) to (d) were employed in Chapter 3.

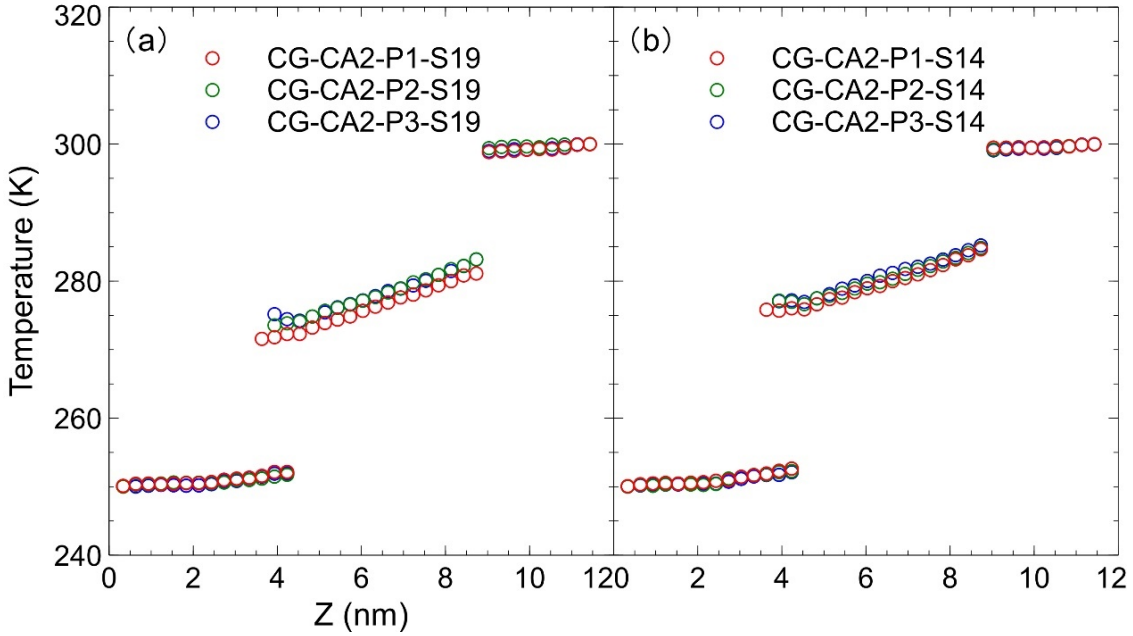

Figure S3.11 The temperature jumping between Cu and CG water on nanostructure surfaces in the Cassie-Baxter states with dt (r-RESPA) of 2.0 fs and a slab size of 0.3 nm. Red, green, and blue correspond to the water pressure of P1, P2, and P3, respectively. (a) and (b) related to the nanopillar width of S19 and S14, respectively. (a) and (b) were employed in Chapter 3.

Figures S3.12 to S3.13 The effect of the slab sizes and interval time on ITR using the SPC/E

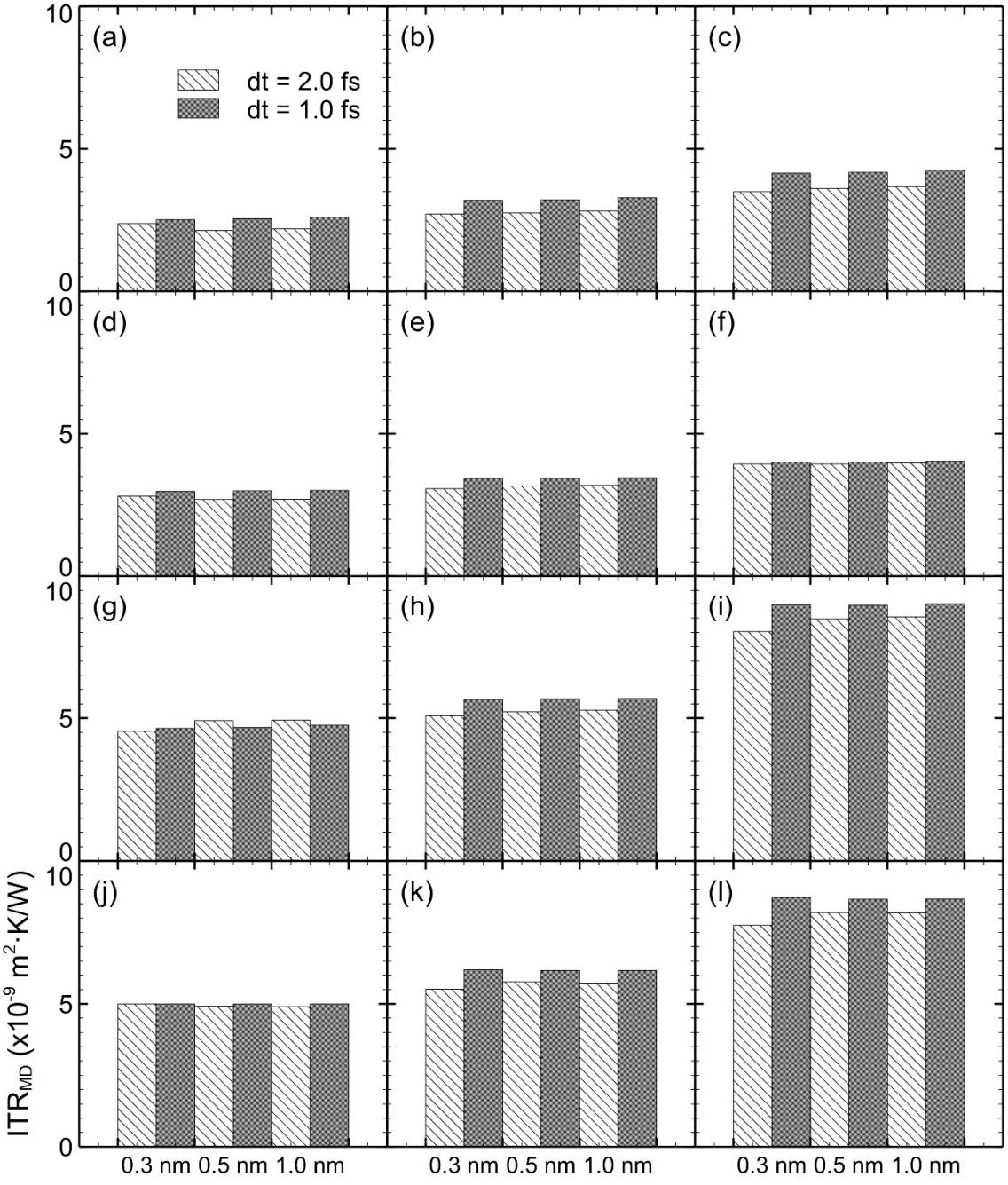

Figure S3.12 The effect of the slab sizes and interval time on ITR_{MD} using the SPC/E model on nanostructure surfaces in the Wenzel states. (a to c), (d to f), (g to i), and (j to l) correspond in the Wenzel states to the cases of CA1-(P1 to P3)-S19, those of CA1-(P1 to P3)-S14, those of CA2-(P1 to P3)-S19, and those of CA2-(P1 to P3)-S14, respectively.

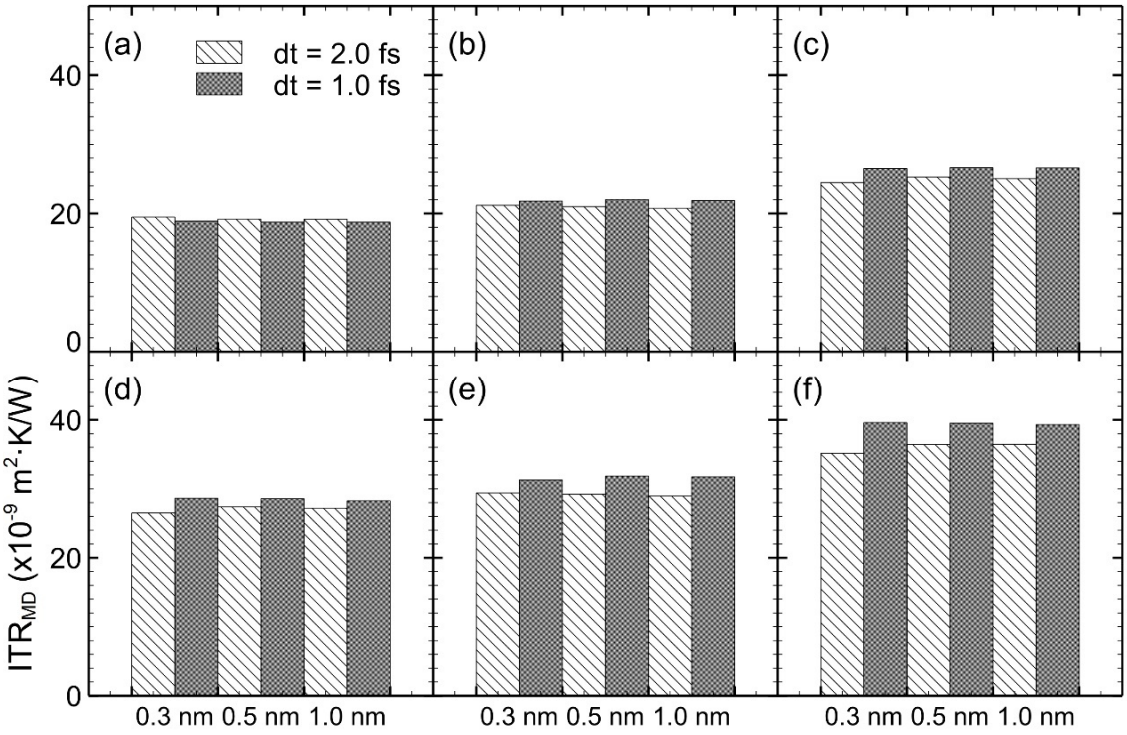

Figure S3.13 The effects of the slab sizes and interval time on ITR using the SPC/E model on nanostructure surfaces in the CB states. (a to c) and (d to f) correspond to the cases of CA2-(P1 to P3)-S19 and those of CA2-(P1 to P3)-S14, respectively.

Table S3.1 The details of the cases of the CG and SPC/E models on flat surfaces (Cu-water systems).

The unit of water pressure (P-MD) calculated by MD simulations is MPa. The units of R_{flat} and ITR_{flat} are K/W and $K \cdot m^2/W$, respectively. The "N" is the number of water molecules. The DDL refers to the density depletion length with the unit of nm. P1 to P3 were used to distinguish different water pressures.

	Items	N	P-MD(MPa)	DDL	R_{flat}	ITR_{flat}
CG	CA1-P1	3524	110.13	0.078	4.38E+08	7.12E-09
	CA1-P2	3424	47.94	0.082	5.25E+08	8.53E-09
	CA1-P3	3340	2.65	0.087	5.97E+08	9.70E-09
	CA2-P1	3524	128.78	0.098	8.28E+08	1.35E-08
	CA2-P2	3424	66.69	0.108	9.32E+08	1.51E-08
	CA2-P3	3340	21.96	0.118	1.21E+09	1.97E-08
SPC/E	CA1-P1	3524	116.57	0.055	3.99E+08	6.48E-09
	CA1-P2	3424	44.86	0.056	4.63E+08	7.52E-09
	CA1-P3	3372	7.53	0.058	4.70E+08	7.63E-09
	CA2-P1	3524	135.86	0.077	7.10E+08	1.15E-08
	CA2-P2	3424	60.19	0.086	8.54E+08	1.39E-08
	CA2-P3	3372	35.81	0.091	1.04E+09	1.69E-08

Table S3.2 The details of the cases of the CG and SPC/E models on nanostructure surfaces in the Cu-water system under a slab size of 0.3 nm.

The units of ITR_{th} and ITR_f are $K \cdot m^2/W$. The nanopillar widths were "S19" and "S14". The "CB" refers to the CB state.

	Items	State	N	P-MD	DDL	ITR_{th}	ITR_f
CG	CA1-S19-P1	Wenzel	3154	221.87	0.168	5.38E-09	1.80E-09
	CA1-S19-P2		3065	141.41	0.170	5.65E-09	1.98E-09
	CA1-S19-P3		2864	4.46	0.188	7.60E-09	3.28E-09
	CA1-S14-P1		3253	196.50	0.166	5.41E-09	2.01E-09
	CA1-S14-P2		3161	122.38	0.173	5.74E-09	2.20E-09
	CA1-S14-P3		2978	4.65	0.186	7.48E-09	3.26E-09
	CA2-S19-P1		3244	249.59	0.195	7.24E-09	3.48E-09
	CA2-S19-P2		3154	171.53	0.212	8.07E-09	4.83E-09
	CA2-S19-P3		3065	35.45	0.247	1.26E-08	8.38E-09
	CA2-S14-P1		3345	223.28	0.196	6.87E-09	3.84E-09
	CA2-S14-P2		3253	149.03	0.212	9.26E-09	5.87E-09
	CA2-S14-P3		3161	35.54	0.249	1.26E-08	8.55E-09
	CA2-S19-P1	CB	2650	30.26	0.613	2.18E-08	1.86E-08
	CA2-S19-P2		2600	25.76	0.693	2.57E-08	2.21E-08
	CA2-S19-P3		2550	24.34	0.785	2.78E-08	2.45E-08
	CA2-S14-P1		2650	21.41	0.808	3.01E-08	2.69E-08
	CA2-S14-P2		2600	17.70	0.882	3.39E-08	3.04E-08
	CA2-S14-P3		2550	15.18	0.972	3.62E-08	3.22E-08

Table S3.2 (continued) The details of the cases of the CG and SPC/E models on nanostructure surfaces in the Cu-water system under a slab size of 0.3 nm.

	Items	State	N	P-MD	DDL	ITR_{th}	ITR_f
SPC/E	CA1-S19-P1	Wenzel	3154	226.79	0.138	4.05E-09	2.37E-09
	CA1-S19-P2		3065	140.32	0.134	4.50E-09	2.71E-09
	CA1-S19-P3		2897	3.74	0.137	5.47E-09	3.49E-09
	CA1-S14-P1		3253	202.92	0.139	4.48E-09	2.81E-09
	CA1-S14-P2		3161	120.92	0.132	4.93E-09	3.07E-09
	CA1-S14-P3		3014	8.11	0.137	5.85E-09	3.94E-09
	CA2-S19-P1		3154	252.14	0.171	6.16E-09	4.54E-09
	CA2-S19-P2		3065	170.44	0.177	6.95E-09	5.08E-09
	CA2-S19-P3		2897	43.09	0.202	1.02E-08	8.03E-09
	CA2-S14-P1		3253	228.77	0.171	6.66E-09	4.99E-09
	CA2-S14-P2		3161	149.60	0.183	7.25E-09	5.51E-09
	CA2-S14-P3		3014	44.58	0.203	9.71E-09	7.75E-09
	CA2-S19-P1	CB	2650	33.34	0.613	2.11E-08	1.95E-08
	CA2-S19-P2		2600	29.85	0.695	2.27E-08	2.12E-08
	CA2-S19-P3		2550	22.26	0.769	2.61E-08	2.45E-08
	CA2-S14-P1		2650	22.73	0.795	2.79E-08	2.65E-08
	CA2-S14-P2		2600	18.25	0.874	3.13E-08	2.94E-08
	CA2-S14-P3		2550	14.09	0.951	3.69E-08	3.52E-08

Figures S3.14 to S3.15 Relationship between DDL and ITR using the CG model with CA3 cases.

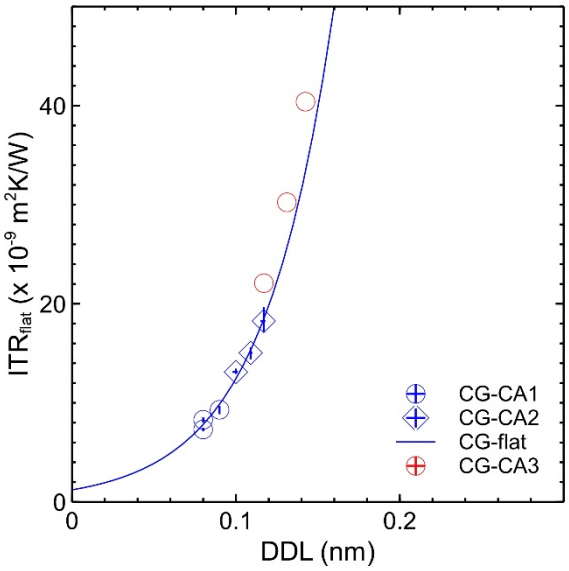

Figure S3.14 Relationship between DDL and ITR on flat surfaces using the CG model with the CA3 cases. The CA3 cases have more weak wettability compared to the CA2 cases. The exponential curve can appropriately express the relationship between DDL and ITR.

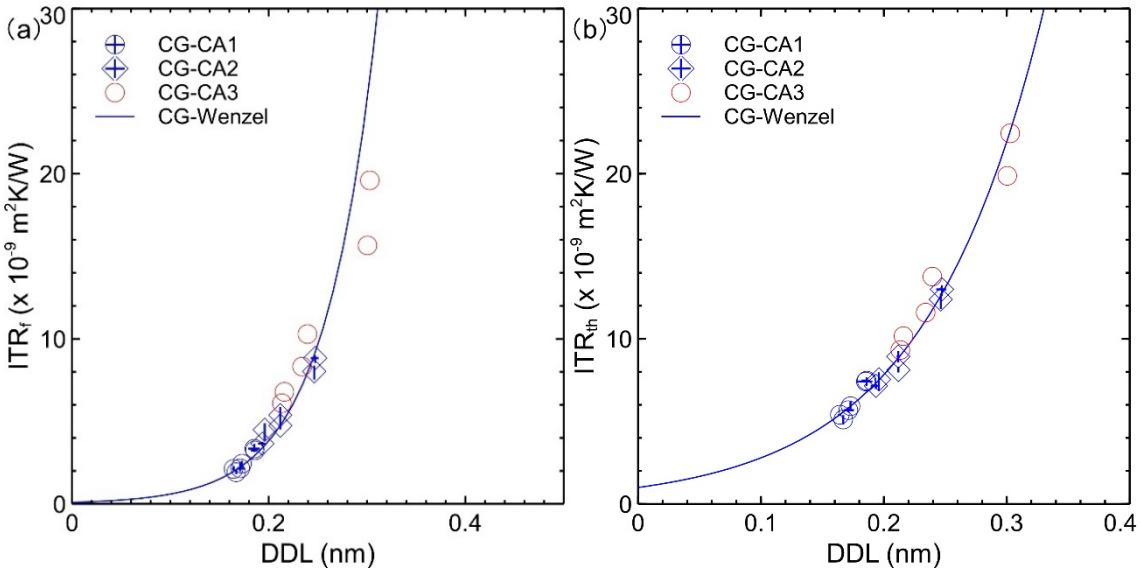

Figure S3.15 Relationship between DDL and ITR on nanostructure surfaces using the CG model with the CA3 cases in the Wenzel state. The CA3 cases have more weak wettability compared to the CA2 cases. The exponential curve can appropriately express the relationship between DDL and ITR.

Appendix Chapter 4

Table S4.1 The details of the cases of CG and SPC/E models on flat surfaces in Cu-graphene-water systems under water pressure of 1 to 50 MPa

	Items	N	P-MD	DDL	ITR_{flat}
CG	CA11-SV0.0	3154	6.57	0.167	2.92E-08
	CA11-SV2.1		6.48	0.169	2.50E-08
	CA11-SV2.8		5.98	0.169	2.40E-08
	CA12-SV0.0		14.36	0.203	4.66E-08
	CA12-SV2.1		14.75	0.189	4.47E-08
	CA12-SV2.8		14.86	0.194	4.67E-08
	CA21-SV0.0	3150	13.22	0.179	2.80E-08
	CA21-SV2.1		14.57	0.169	2.78E-08
	CA21-SV2.8		13.59	0.169	2.70E-08
	CA22-SV0.0		21.54	0.204	5.12E-08
	CA22-SV2.1		21.98	0.193	4.55E-08
	CA22-SV2.8		22.04	0.192	4.54E-08
SPC/E	CA11-SV0.0	3170	15.03	0.144	2.58E-08
	CA11-SV2.1		13.75	0.146	2.35E-08
	CA11-SV2.8		13.83	0.143	2.31E-08
	CA12-SV0.0		31.23	0.179	4.94E-08
	CA12-SV2.1		27.63	0.170	4.61E-08
	CA12-SV2.8		30.15	0.172	4.24E-08
	CA21-SV0.0		23.34	0.142	2.45E-08
	CA21-SV2.1		27.22	0.143	2.21E-08
	CA21-SV2.8		21.23	0.142	2.58E-08
	CA22-SV0.0		34.60	0.179	5.10E-08
	CA22-SV2.1		33.27	0.168	4.81E-08
	CA22-SV2.8		37.21	0.170	4.38E-08

Table S4.2 The details of the cases of CG and SPC/E models on flat surfaces in Cu-graphene-water systems under water pressure of 90 to 200 MPa.

	Items	N	P-MD	DDL	ITR_{flat}
CG	CA11-SV0.0	3354	135.27	0.167	1.70E-08
	CA11-SV2.1		135.97	0.159	1.84E-08
	CA11-SV2.8		135.03	0.158	1.97E-08
	CA12-SV0.0		145.12	0.180	3.11E-08
	CA12-SV2.1		144.73	0.170	2.88E-08
	CA12-SV2.8		143.33	0.171	2.83E-08
	CA21-SV0.0		143.29	0.168	1.76E-08
	CA21-SV2.1		143.14	0.157	1.91E-08
	CA21-SV2.8		143.52	0.157	1.84E-08
	CA22-SV0.0		152.55	0.181	3.43E-08
	CA22-SV2.1		151.34	0.171	2.96E-08
	CA22-SV2.8		151.24	0.171	2.76E-08
SPC/E	CA11-SV0.0	3320	122.99	0.147	2.08E-08
	CA11-SV2.1		124.85	0.135	1.77E-08
	CA11-SV2.8		122.55	0.136	1.73E-08
	CA12-SV0.0		132.64	0.164	3.37E-08
	CA12-SV2.1		135.69	0.150	3.19E-08
	CA12-SV2.8		133.03	0.150	2.71E-08
	CA21-SV0.0		133.46	0.147	1.88E-08
	CA21-SV2.1		130.56	0.138	1.95E-08
	CA21-SV2.8		130.80	0.138	1.73E-08
	CA22-SV0.0		142.87	0.163	3.43E-08
	CA22-SV2.1		141.56	0.153	3.01E-08
	CA22-SV2.8		138.97	0.157	2.98E-08

Table S4.3 The details of the cases of CG and SPC/E models on flat surfaces in Cu-graphene-water systems under water pressure of 200 to 300 MPa.

	Items	N	P-MD	DDL	ITR_{flat}
CG	CA11-SV0.0	3500	263.22	0.157	1.32E-08
	CA11-SV2.1		263.90	0.147	1.38E-08
	CA11-SV2.8		264.67	0.147	1.27E-08
	CA12-SV0.0		272.62	0.168	2.15E-08
	CA12-SV2.1		272.76	0.157	2.05E-08
	CA12-SV2.8		271.59	0.155	1.83E-08
	CA21-SV0.0		271.78	0.159	1.27E-08
	CA21-SV2.1		273.05	0.149	1.25E-08
	CA21-SV2.8		269.14	0.149	1.31E-08
	CA22-SV0.0		282.35	0.167	2.12E-08
	CA22-SV2.1		281.63	0.157	1.93E-08
	CA22-SV2.8		279.16	0.160	1.80E-08
SPC/E	CA11-SV0.0	3420	206.73	0.144	1.33E-08
	CA11-SV2.1		206.13	0.134	1.46E-08
	CA11-SV2.8		205.47	0.134	1.41E-08
	CA12-SV0.0		219.63	0.157	2.76E-08
	CA12-SV2.1		219.76	0.148	2.19E-08
	CA12-SV2.8		219.40	0.147	2.31E-08
	CA21-SV0.0		213.86	0.146	1.55E-08
	CA21-SV2.1		213.43	0.134	1.45E-08
	CA21-SV2.8		214.74	0.137	1.48E-08
	CA22-SV0.0		223.15	0.158	2.54E-08
	CA22-SV2.1		223.90	0.146	2.32E-08
	CA22-SV2.8		219.99	0.145	2.27E-08

Table S4.4 The details of the cases of CG and SPC/E models on nanostructure surfaces in Cu-graphene-water systems

The "N1" and "N2" are the number of the CG and SPC/E water molecules in the CB states, respectively.

	Items	states	N	P-MD	DDL	ITR_f	ITR_{th}
CG	CA11-SV0.0	P3 Wenzel	2816	2.19	0.217	4.85E-09	1.06E-09
	CA11-SV2.1			2.82	0.214	4.69E-09	1.04E-09
	CA11-SV2.8			2.98	0.215	4.88E-09	1.09E-09
	CA12-SV0.0			7.08	0.228	6.01E-09	1.27E-08
	CA12-SV2.1			6.86	0.235	5.63E-09	1.17E-08
	CA12-SV2.8			6.80	0.229	5.70E-09	1.17E-08
	CA21-SV0.0	CB N2	2500	25.91	0.822	3.30E-08	3.75E-08
	CA21-SV2.1			27.73	0.835	3.00E-08	3.35E-08
	CA21-SV2.8			26.01	0.827	2.82E-08	3.19E-08
	CA22-SV0.0			31.92	0.844	5.07E-08	5.42E-08
	CA22-SV2.1			30.90	0.843	4.54E-08	4.96E-08
	CA22-SV2.8			30.74	0.844	4.32E-08	4.71E-08
	CA21-SV0.0	CB N1	2580	32.00	0.691	2.87E-08	3.26E-08
	CA21-SV2.1			28.68	0.694	2.70E-08	3.02E-08
	CA21-SV2.8			28.47	0.698	2.63E-08	2.97E-08
	CA22-SV0.0			32.30	0.694	3.96E-08	4.23E-08
	CA22-SV2.1			28.28	0.695	3.96E-08	4.32E-08
	CA22-SV2.8			30.68	0.694	3.95E-08	4.31E-08
	CA11-SV0.0	P2 Wenzel	3000	126.19	0.200	3.56E-09	8.49E-09
	CA11-SV2.1			125.72	0.202	2.75E-09	7.81E-09
	CA11-SV2.8			126.67	0.204	3.78E-09	8.53E-09
	CA12-SV0.0			129.71	0.204	3.83E-09	9.04E-09
	CA12-SV2.1			130.20	0.206	3.93E-09	9.27E-09
	CA12-SV2.8			131.23	0.213	3.97E-09	9.25E-09
	CA11-SV0.0	P1 Wenzel	3120	234.03	0.184	3.02E-09	7.43E-08
	CA11-SV2.1			233.01	0.188	2.73E-09	6.84E-08
	CA11-SV2.8			234.08	0.190	2.77E-09	7.00E-08
	CA12-SV0.0			238.17	0.184	3.29E-09	8.16E-08
	CA12-SV2.1			237.33	0.194	2.68E-09	7.17E-08
	CA12-SV2.8			237.36	0.195	3.13E-09	7.37E-08

Table S4.4 (continued) The details of the cases of CG and SPC/E models on nanostructure surfaces in Cu-graphene-water systems

	Items		N	P-MD	DDL	ITR_f	ITR_{th}
SPC/E	CA11-SV0.0	P3 Wenzel	2860	10.94	0.169	5.82E-09	8.72E-09
	CA11-SV2.1			13.90	0.176	5.49E-09	8.40E-09
	CA11-SV2.8			12.28	0.180	5.40E-09	8.13E-09
	CA12-SV0.0			13.43	0.186	6.22E-09	9.36E-09
	CA12-SV2.1			18.44	0.190	5.98E-09	9.05E-09
	CA12-SV2.8			17.32	0.191	5.87E-09	9.02E-09
	CA21-SV0.0	CB N1	2600	31.51	0.651	2.70E-08	2.84E-08
	CA21-SV2.1			32.05	0.661	2.45E-08	2.64E-08
	CA21-SV2.8			33.41	0.662	2.54E-08	2.69E-08
	CA22-SV0.0			37.71	0.650	3.72E-08	3.92E-08
	CA22-SV2.1			36.76	0.654	3.68E-08	3.88E-08
	CA22-SV2.8			35.23	0.651	3.40E-08	3.59E-08
	CA21-SV0.0	CB N2	2500	27.00	0.818	3.42E-08	3.59E-08
	CA21-SV2.1			27.08	0.826	3.16E-08	3.31E-08
	CA21-SV2.8			23.61	0.827	3.26E-08	3.38E-08
	CA22-SV0.0			36.33	0.816	5.51E-08	5.63E-08
	CA22-SV2.1			35.90	0.825	4.88E-08	5.05E-08
	CA22-SV2.8			36.90	0.834	5.29E-08	5.50E-08
	CA11-SV0.0	P2 Wenzel	2970	97.44	0.164	4.51E-09	7.37E-09
	CA11-SV2.1			97.46	0.168	4.57E-09	7.31E-09
	CA11-SV2.8			96.88	0.169	4.61E-09	7.21E-09
	CA12-SV0.0			98.67	0.175	5.41E-09	8.70E-09
	CA12-SV2.1			101.18	0.174	5.58E-09	8.70E-09
	CA12-SV2.8			100.80	0.179	5.48E-09	8.81E-09
	CA11-SV0.0	P1 Wenzel	3115	237.76	0.162	3.43E-09	5.91E-09
	CA11-SV2.1			234.61	0.162	3.71E-09	6.25E-09
	CA11-SV2.8			239.20	0.165	3.67E-09	6.14E-09
	CA12-SV0.0			238.83	0.166	5.48E-09	8.84E-09
	CA12-SV2.1			239.95	0.167	5.37E-09	8.57E-09
	CA12-SV2.8			238.82	0.171	5.58E-09	8.81E-09

Appendix Chapter 5

Table S5.1 The detailed thermal resistance of CG models in Cu-water systems.

The $R_{S\text{-}liq3,4}$ was referred to as $R_{S\text{-}liq3}$ and $R_{S\text{-}liq4}$. The R_S, R_{liq}, $R_{S\text{-}liq1}$, $R_{S\text{-}liq2}$, $R_{S\text{-}liq3}$, and $R_{S\text{-}liq4}$ have the same meanings in Section 2.8.2. "Unlimited" means the values were very high. R_S and R_{liq} are calculated by the thermal conductivities of MD simulations.

	Items	State	R_S	R_{liq}	$R_{S\text{-}liq1}$	$R_{S\text{-}liq2}$	$R_{S\text{-}liq3,4}$
CG	CA1-S19-P1	Wenzel	6.68E+07	4.52E+08	5.81E+08	5.13E+08	6.70E+08
	CA1-S19-P2		9.45E+07	4.36E+08	8.34E+08	7.36E+08	9.61E+08
	CA1-S19-P3		3.54E+07	4.95E+08	1.26E+09	1.12E+09	1.46E+09
	CA1-S14-P1		9.11E+07	3.66E+08	9.01E+08	4.72E+08	7.63E+08
	CA1-S14-P2		1.29E+08	3.53E+08	1.22E+09	6.38E+08	1.03E+09
	CA1-S14-P3		4.83E+07	4.01E+08	1.72E+09	9.02E+08	1.46E+09
	CA2-S19-P1		5.68E+07	4.35E+08	8.03E+08	7.09E+08	9.26E+08
	CA2-S19-P2		8.96E+07	4.58E+08	1.38E+09	1.22E+09	1.59E+09
	CA2-S19-P3		6.92E+07	4.88E+08	2.38E+09	2.10E+09	2.75E+09
	CA2-S14-P1		7.74E+07	3.52E+08	1.36E+09	7.12E+08	1.15E+09
	CA2-S14-P2		1.22E+08	3.71E+08	2.11E+09	1.10E+09	1.78E+09
	CA2-S14-P3		9.44E+07	3.95E+08	3.25E+09	1.70E+09	2.75E+09
	CA2-S19-P1	CB	5.68E+07	1.83E+08	2.42E+09	Unlimited	6.63E+09
	CA2-S19-P2		8.96E+07	1.49E+08	2.46E+09		8.69E+09
	CA2-S19-P3		6.92E+07	1.08E+08	2.47E+09		1.29E+10
	CA2-S14-P1		7.74E+07	1.22E+08	3.39E+09		8.30E+09
	CA2-S14-P2		1.22E+08	1.02E+08	3.43E+09		1.05E+10
	CA2-S14-P3		9.44E+07	7.73E+07	3.45E+09		1.49E+10

Table S5.1 (continued) The detailed thermal resistance of the SPC/E models in Cu-water systems. The $R_{S\text{-}liq3,4}$ was referred to as $R_{S\text{-}liq3}$ and $R_{S\text{-}liq4}$. The R_S, R_{liq}, $R_{S\text{-}liq1}$, $R_{S\text{-}liq2}$, $R_{S\text{-}liq3}$, and $R_{S\text{-}liq4}$ have the same meanings in Section 2.8.2. "Unlimited" means the values were very high. R_S and R_{liq} are calculated by the thermal conductivities of MD simulations.

	Items	State	R_S	R_{liq}	$R_{S\text{-}liq1}$	$R_{S\text{-}liq2}$	$R_{S\text{-}liq3,4}$
SPC/E	CA1-S19-P1	Wenzel	7.90E+07	2.14E+08	6.98E+08	6.16E+08	8.05E+08
	CA1-S19-P2		8.23E+07	2.29E+08	8.24E+08	7.27E+08	9.50E+08
	CA1-S19-P3		8.32E+07	2.33E+08	1.02E+09	9.03E+08	1.18E+09
	CA1-S14-P1		1.08E+08	1.74E+08	1.00E+09	5.24E+08	8.45E+08
	CA1-S14-P2		1.12E+08	1.85E+08	1.16E+09	6.09E+08	9.83E+08
	CA1-S14-P3		1.13E+08	1.88E+08	1.39E+09	7.26E+08	1.17E+09
	CA2-S19-P1		7.79E+07	1.92E+08	7.49E+08	6.61E+08	8.64E+08
	CA2-S19-P2		9.45E+07	2.32E+08	1.26E+09	1.12E+09	1.46E+09
	CA2-S19-P3		7.58E+07	2.26E+08	2.07E+09	1.83E+09	2.38E+09
	CA2-S14-P1		1.06E+08	1.55E+08	1.22E+09	6.40E+08	1.03E+09
	CA2-S14-P2		1.29E+08	1.88E+08	1.90E+09	9.97E+08	1.61E+09
	CA2-S14-P3		1.03E+08	1.83E+08	2.81E+09	1.47E+09	2.37E+09
	CA2-S19-P1	CB	7.79E+07	7.54E+07	2.13E+09	Unlimited	6.24E+09
	CA2-S19-P2		9.45E+07	6.76E+07	2.15E+09		8.52E+09
	CA2-S19-P3		7.58E+07	4.68E+07	2.20E+09		1.23E+10
	CA2-S14-P1		1.06E+08	5.06E+07	3.00E+09		7.76E+09
	CA2-S14-P2		1.29E+08	4.83E+07	3.03E+09		9.98E+09
	CA2-S14-P3		1.03E+08	3.58E+07	3.07E+09		1.33E+10

Table S5.1 (continued) R_S and R_{liq} are calculated by experimental thermal conductivities

	Items	State	R_S	R_{liq}
CG	CA1-S19-P1	Wenzel	5.37E+05	3.08E+08
	CA1-S19-P2		5.37E+05	3.25E+08
	CA1-S19-P3		5.37E+05	3.43E+08
	CA1-S14-P1		7.32E+05	2.50E+08
	CA1-S14-P2		7.32E+05	2.63E+08
	CA1-S14-P3		7.32E+05	2.78E+08
	CA2-S19-P1		5.37E+05	3.04E+08
	CA2-S19-P2		5.37E+05	3.19E+08
	CA2-S19-P3		5.37E+05	3.33E+08
	CA2-S14-P1		7.32E+05	2.46E+08
	CA2-S14-P2		7.32E+05	2.58E+08
	CA2-S14-P3		7.32E+05	2.69E+08
	CA2-S19-P1	CB	5.37E+05	1.28E+08
	CA2-S19-P2		5.37E+05	1.04E+08
	CA2-S19-P3		5.37E+05	7.33E+07
	CA2-S14-P1		7.32E+05	8.49E+07
	CA2-S14-P2		7.32E+05	7.10E+07
	CA2-S14-P3		7.32E+05	5.26E+07
SPC/E	CA1-S19-P1	Wenzel	5.37E+05	3.08E+08
	CA1-S19-P2		5.37E+05	3.26E+08
	CA1-S19-P3		5.37E+05	3.41E+08
	CA1-S14-P1		7.32E+05	2.49E+08
	CA1-S14-P2		7.32E+05	2.64E+08
	CA1-S14-P3		7.32E+05	2.76E+08
	CA2-S19-P1		5.37E+05	3.02E+08
	CA2-S19-P2		5.37E+05	3.21E+08
	CA2-S19-P3		5.37E+05	3.28E+08
	CA2-S14-P1		7.32E+05	2.45E+08
	CA2-S14-P2		7.32E+05	2.60E+08
	CA2-S14-P3		7.32E+05	2.65E+08
	CA2-S19-P1	CB	5.37E+05	1.19E+08
	CA2-S19-P2		5.37E+05	9.34E+07
	CA2-S19-P3		5.37E+05	6.78E+07
	CA2-S14-P1		7.32E+05	7.99E+07
	CA2-S14-P2		7.32E+05	6.68E+07
	CA2-S14-P3		7.32E+05	5.19E+07

Figures S5.1 to S5.12 The detailed values in TCMs in Cu-water systems

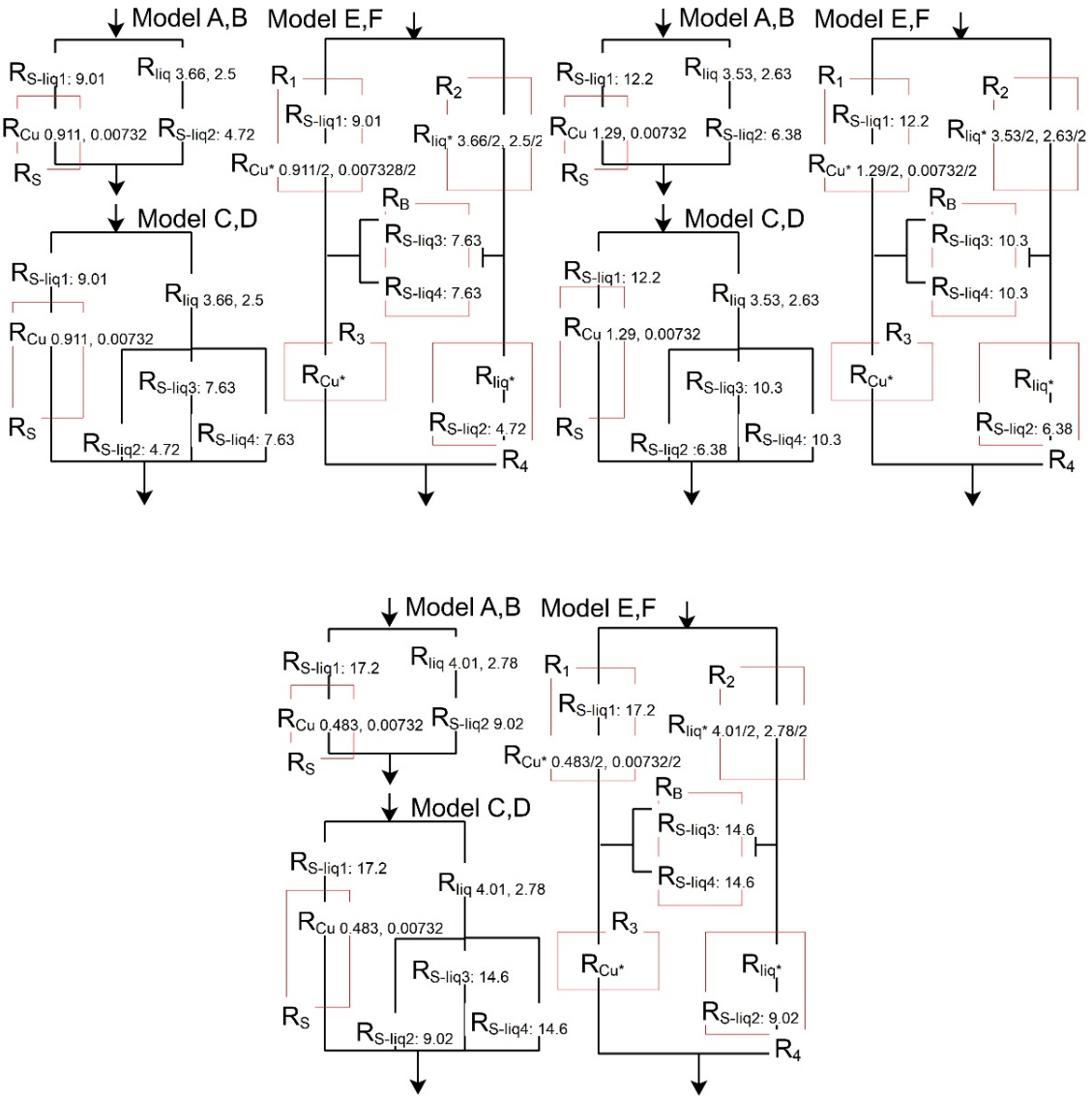

Figure S5.1 The local thermal resistances for the CG model in the case of the nanopillar width of S14 under the water pressure of P1(top-left), P2(top-right), and P3(bottom) in the Wenzel (CA1) state. All values were components of TCMs. The unit is 10^8 K/W.

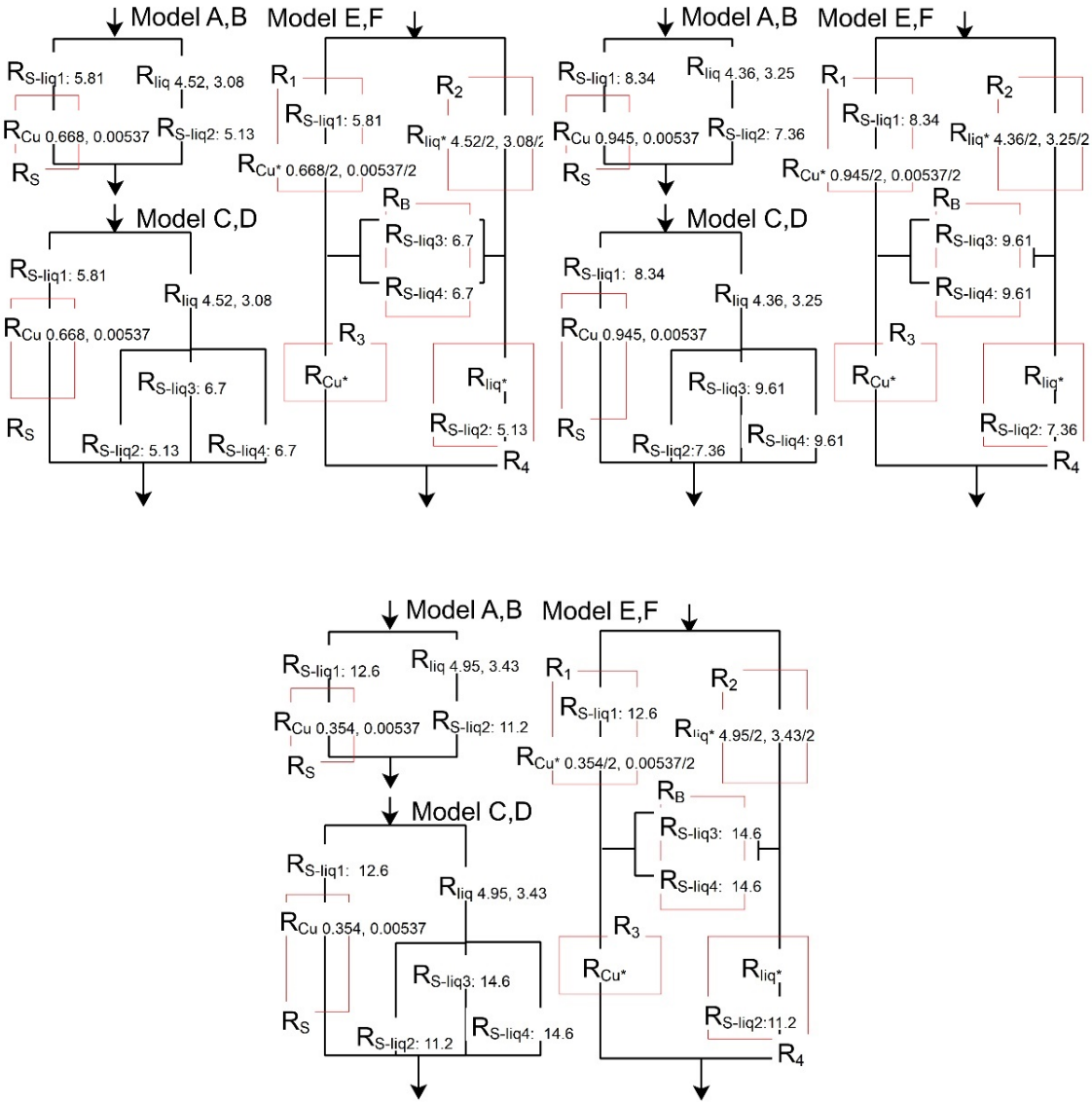

Figure S5.2 The local thermal resistances of model A to model F for the CG model in the case of the nanopillar width of S19 under the water pressure of P1(top-left), P2(top-right), and P3(bottom) in the Wenzel (CA1) state. All values were components of TCMs. The unit is 10^8 K/W.

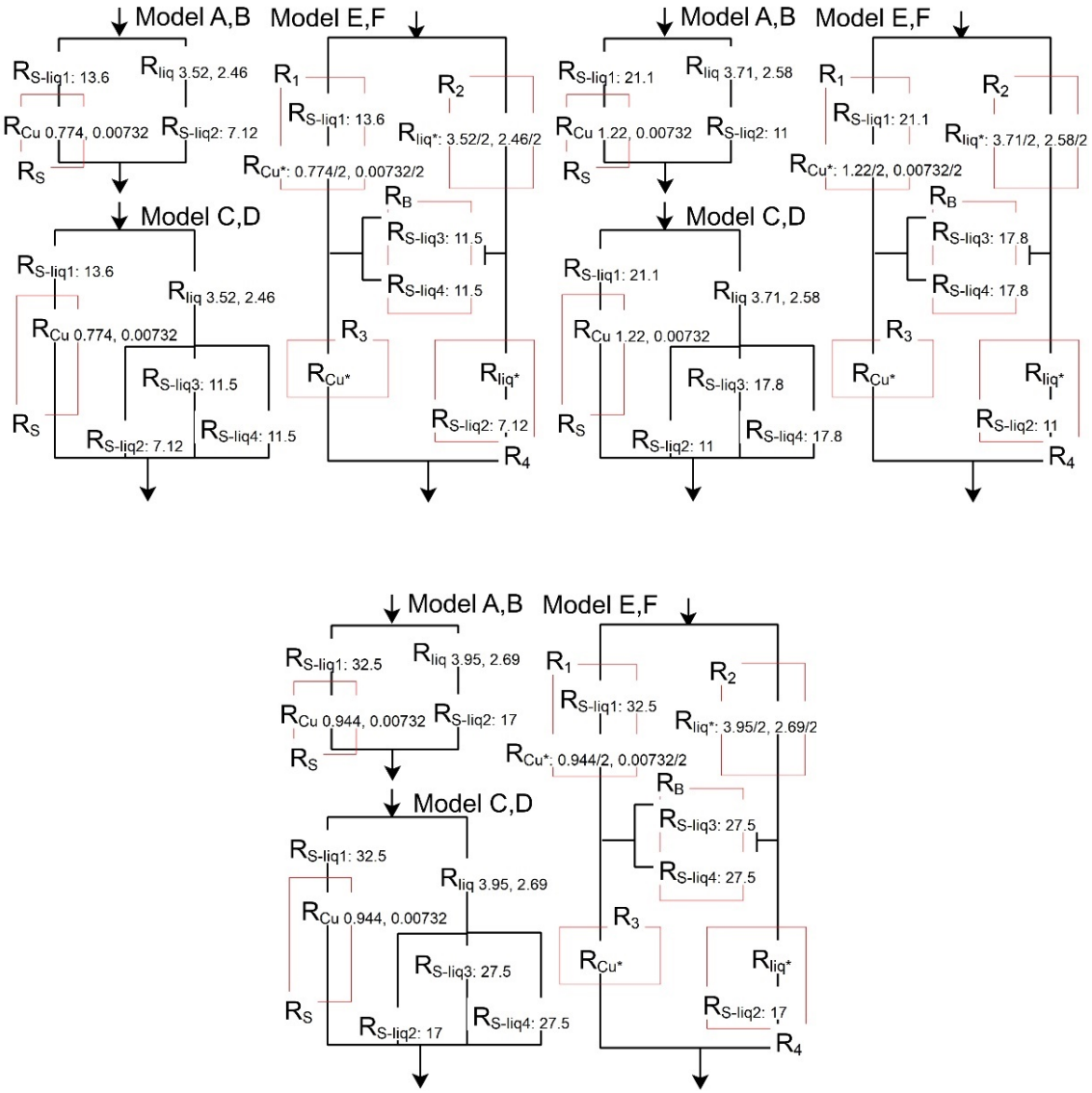

Figure S5.3 The local thermal resistances of model A to model F for the CG model in the case of the nanopillar width of S14 under the water pressure of P1(top-left), P2(top-right), and P3(bottom) in the Wenzel (CA2) state. All values were components of TCMs. The unit is 10^8 K/W.

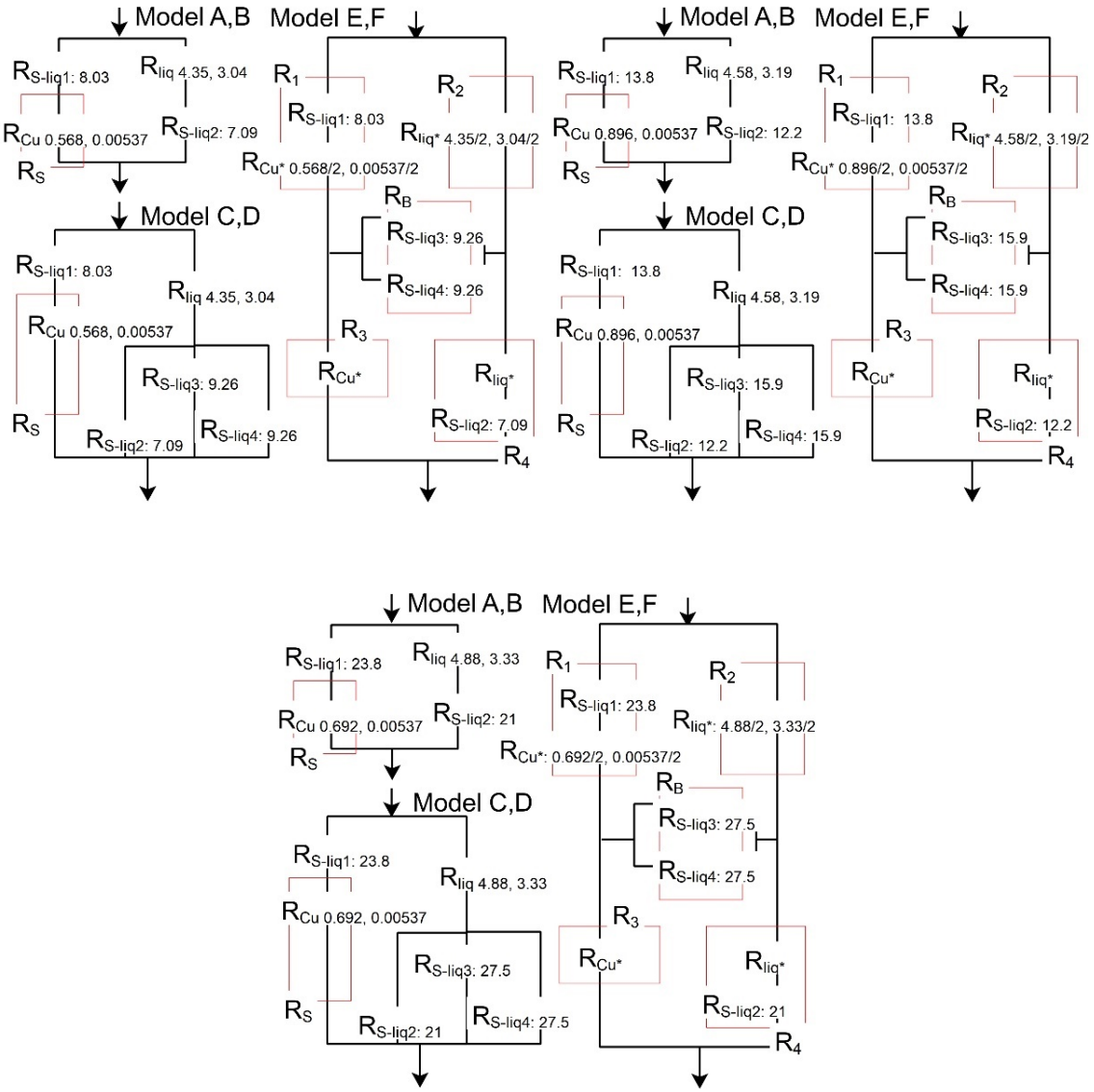

Figure S5.4 The local thermal resistances of model A to model F for the CG model in the case of the nanopillar width of S19 under the water pressure of P1(top-left), P2(top-right), and P3(bottom) in the Wenzel (CA2) state. All values were components of TCMs. The unit is 10^8 K/W.

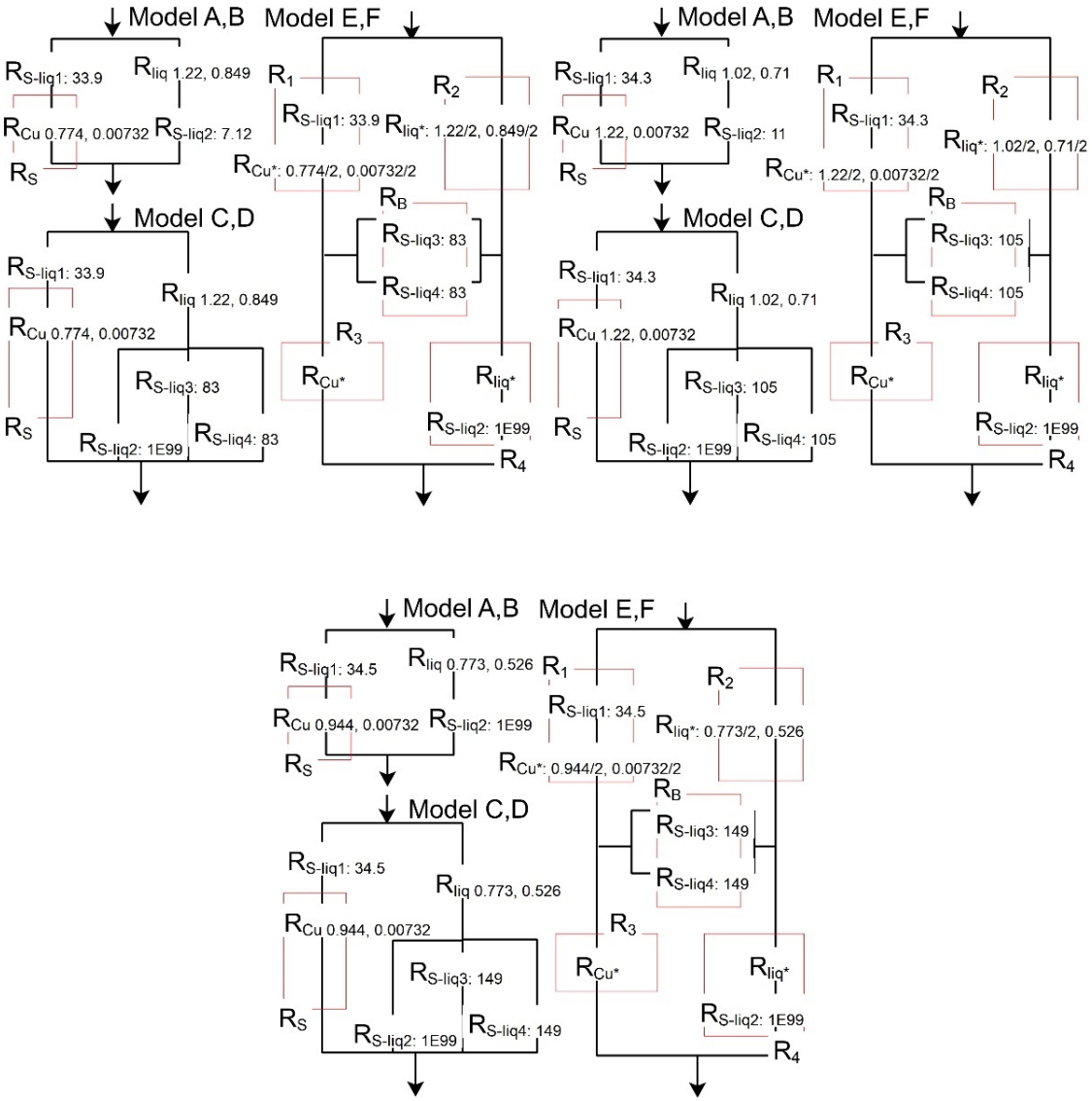

Figure S5.5 The local thermal resistances of model A to model F for the CG model in the case of the nanopillar width of S14 under the water pressure of P1(top-left), P2(top-right), and P3(bottom) in the CB state. All values were components of TCMs. The unit is 10^8 K/W.

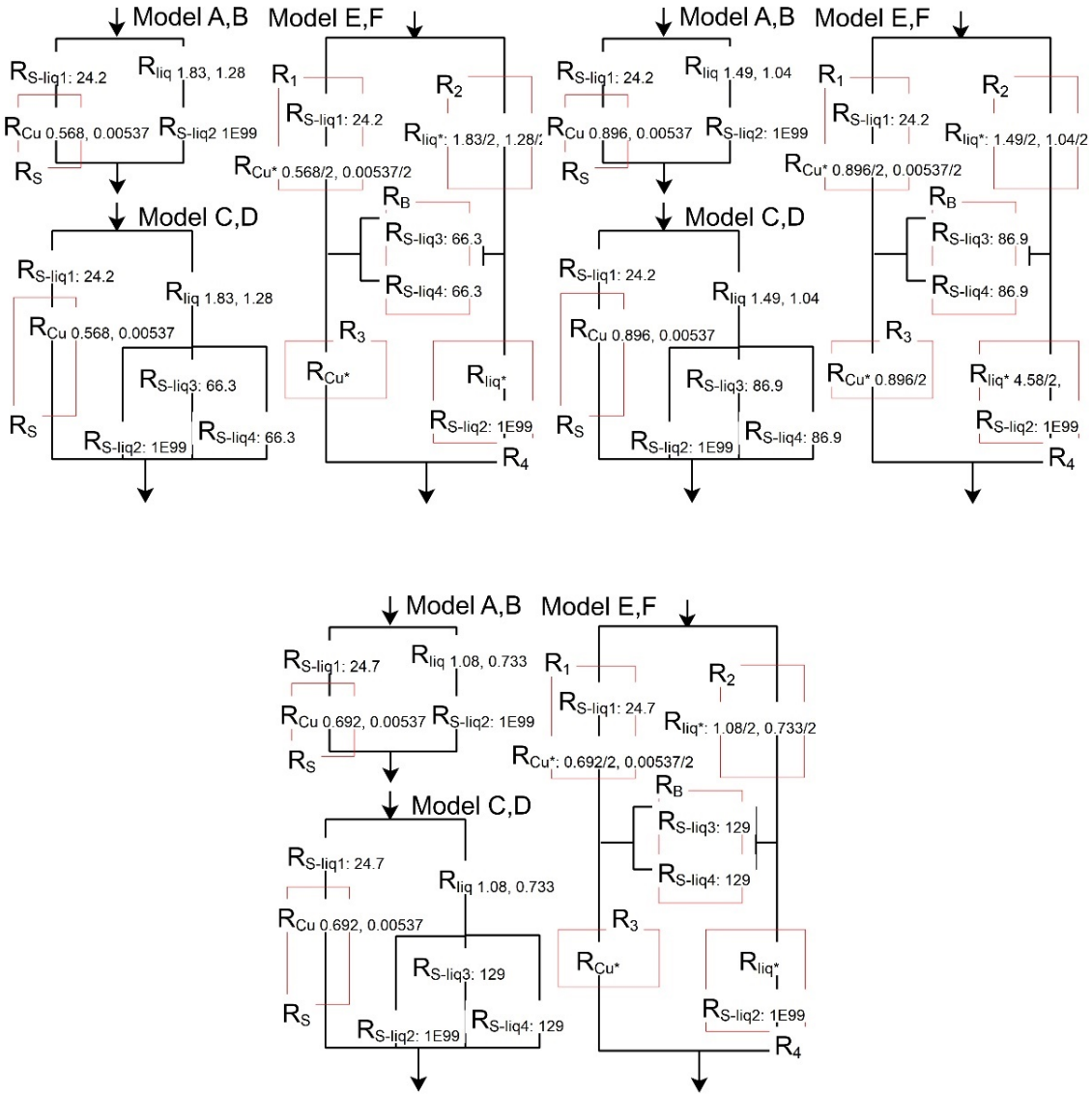

Figure S5.6 The local thermal resistances of model A to model F for the CG model in the case of the nanopillar width of S19 under the water pressure of P1(top-left), P2(top-right), and P3(bottom) in the CB state. All values were components of TCMs. The unit is 10^8 K/W.

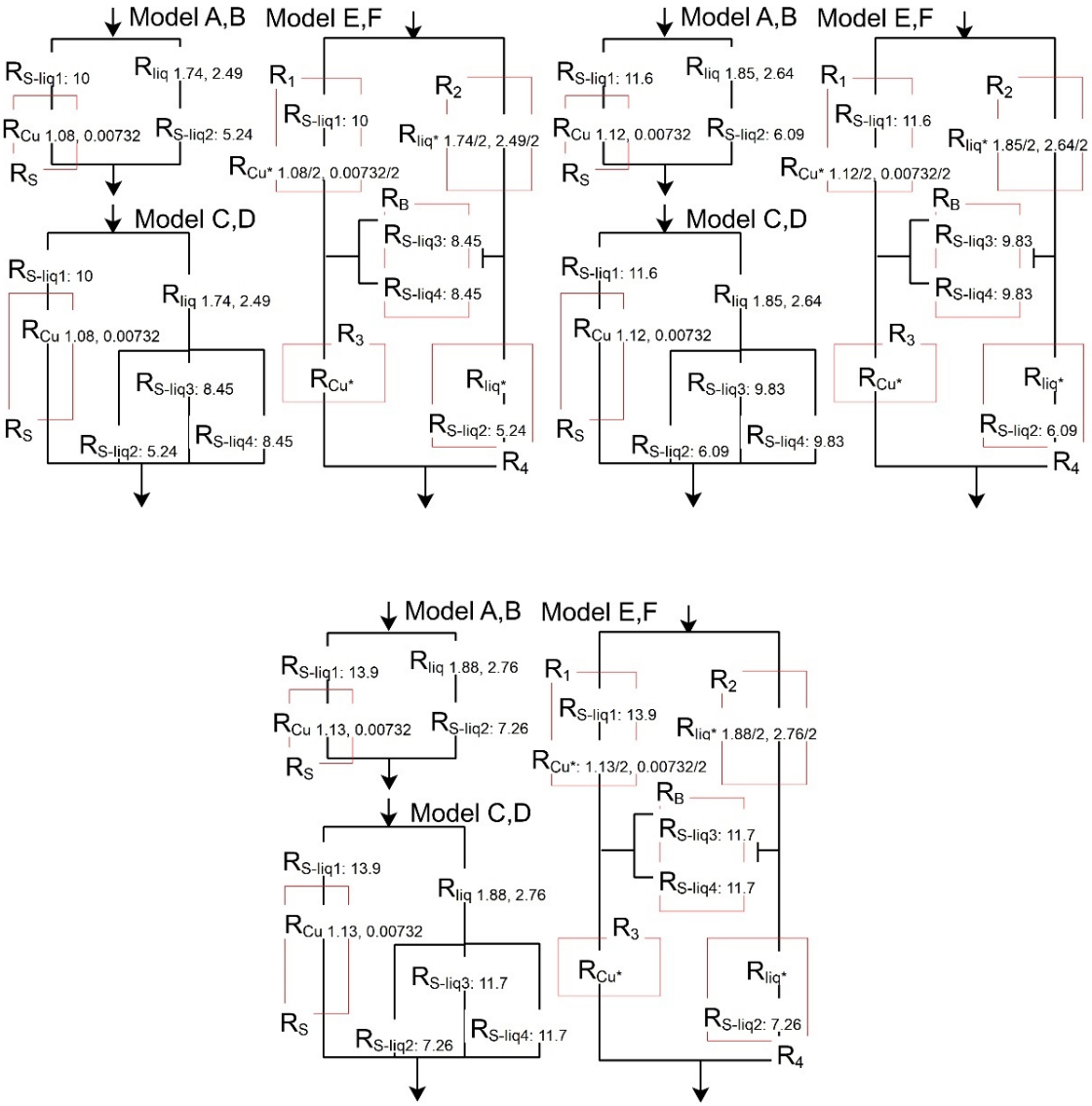

Figure S5.7 The local thermal resistances of model A to model F for the SPC/E model in the case of the nanopillar width of S14 under the water pressure of P1(top-left), P2(top-right), and P3(bottom) in the Wenzel (CA1) state. All values were components of TCMs. The unit is 10^8 K/W.

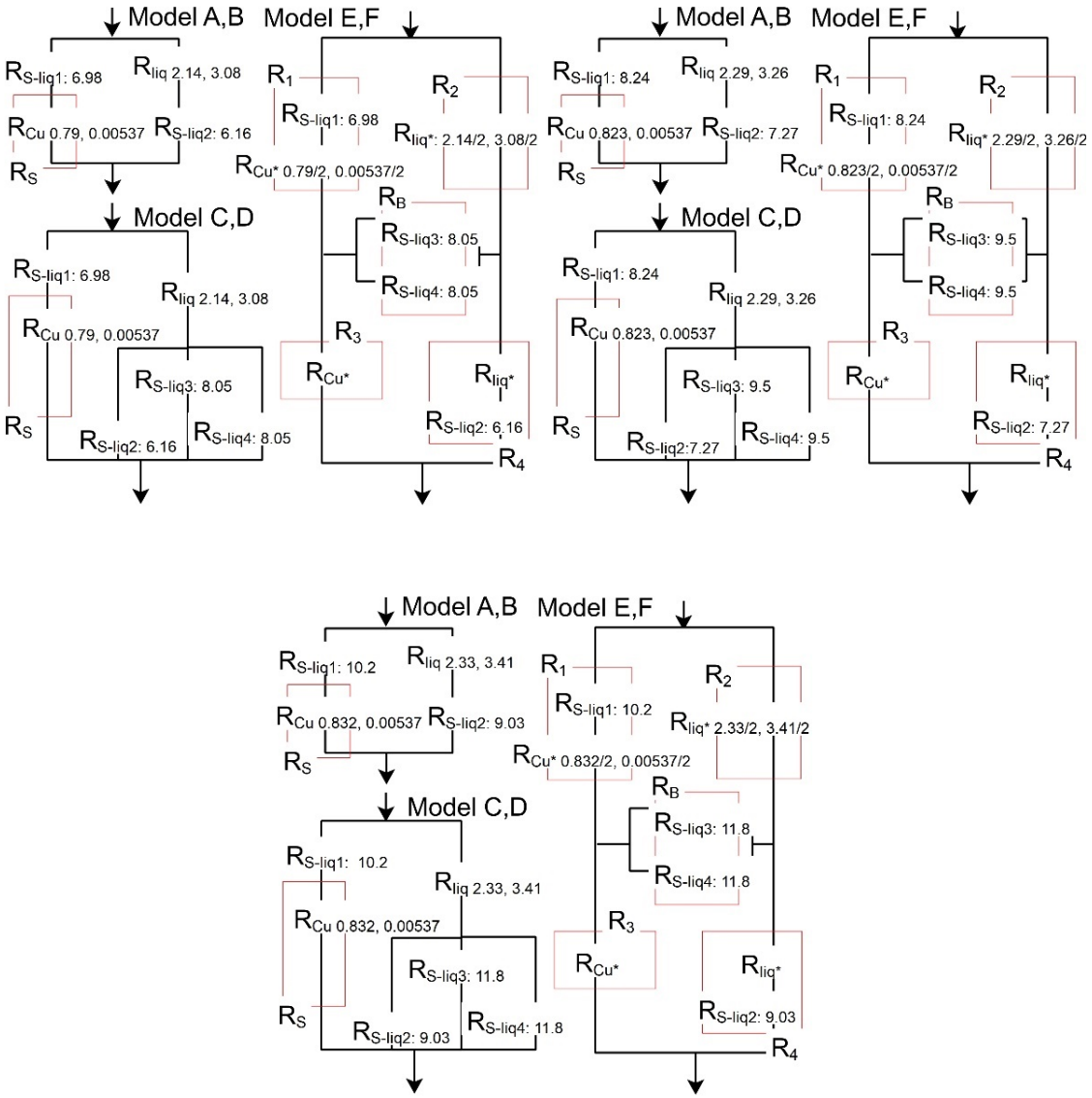

Figure S5.8 The local thermal resistances of model A to model F for the SPC/E model in the case of the nanopillar width of S19 under the water pressure of P1(top-left), P2(top-right), and P3(bottom) in the Wenzel (CA1) state. All values were components of TCMs. The unit is 10^8 K/W.

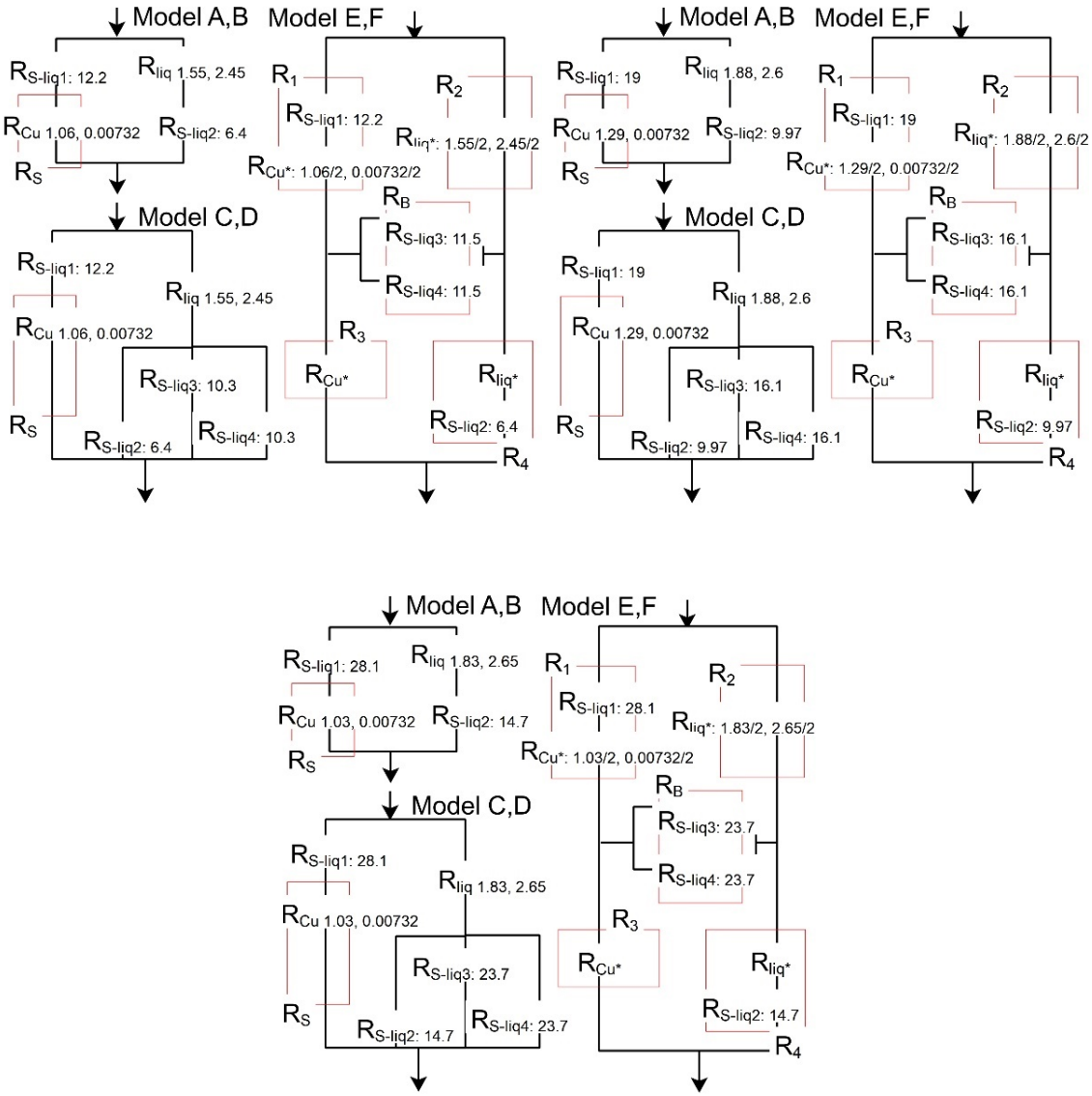

Figure S5.9 The local thermal resistances of model A to model F for the SPC/E model in the case of the nanopillar width of S14 under the water pressure of P1(top-left), P2(top-right), and P3(bottom) in the Wenzel (CA2) state. All values were components of TCMs. The unit is 10^8 K/W.

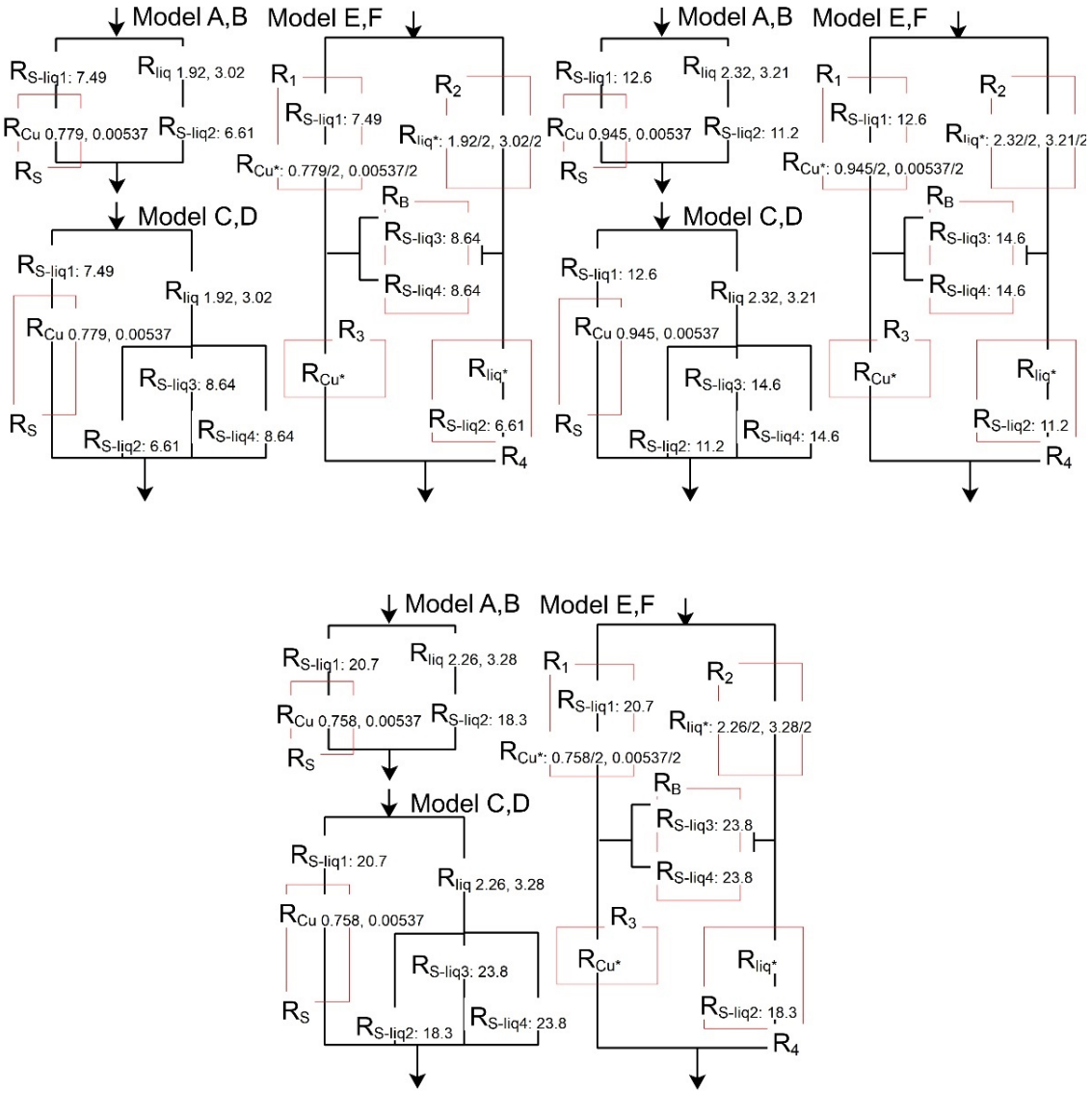

Figure S5.10 The local thermal resistances of model A to model F for the SPC/E model in the case of the nanopillar width of S19 under the water pressure of P1(top-left), P2(top-right), and P3(bottom) in the Wenzel (CA2) state. All values were components of TCMs. The unit is 10^8 K/W.

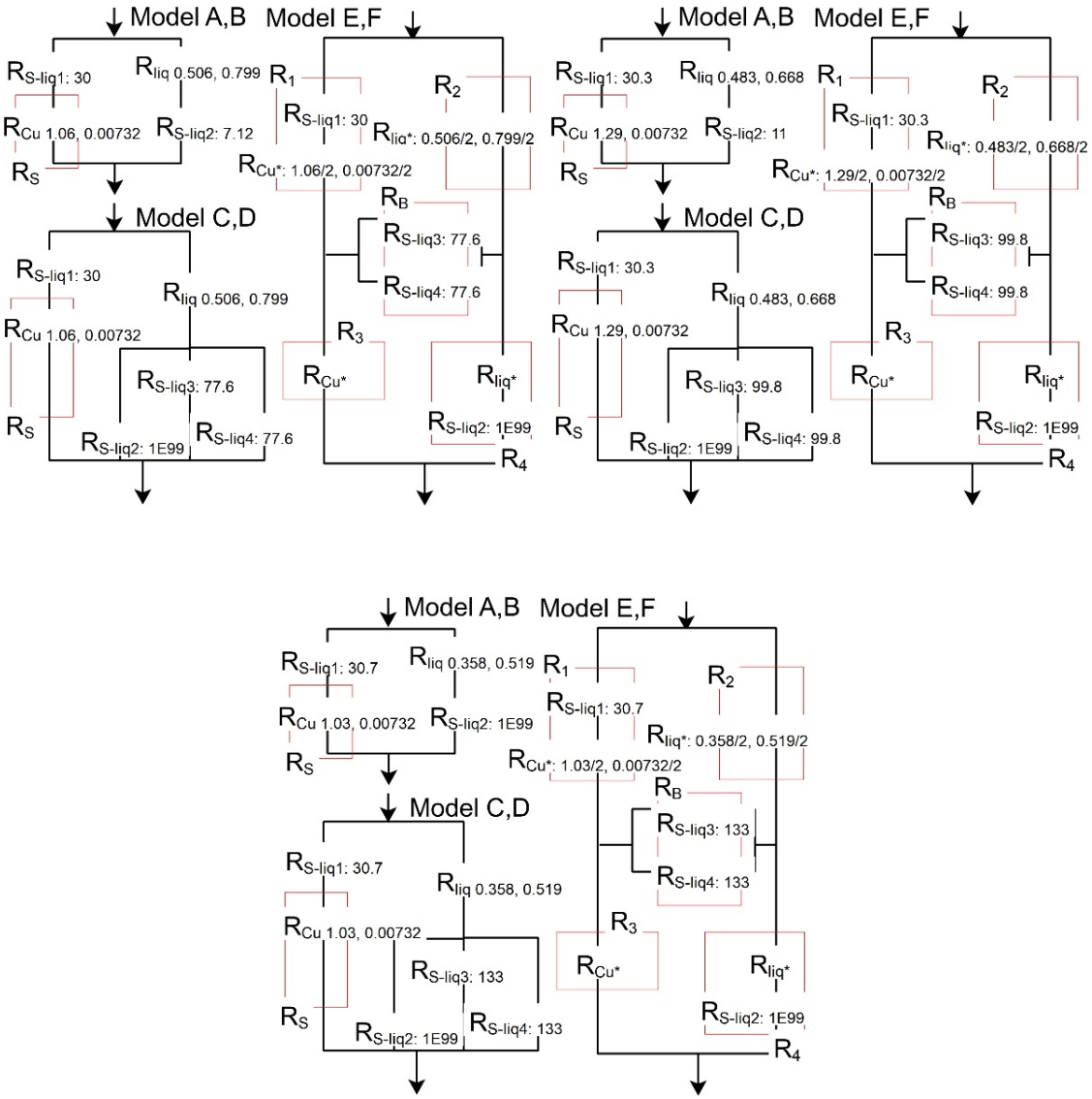

Figure S5.11 The local thermal resistances of model A to model F for the SPC/E model in the case of the nanopillar width of S14 under the water pressure of P1(top-left), P2(top-right), and P3(bottom) in the CB state. All values were components of TCMs. The unit is 10^8 K/W.

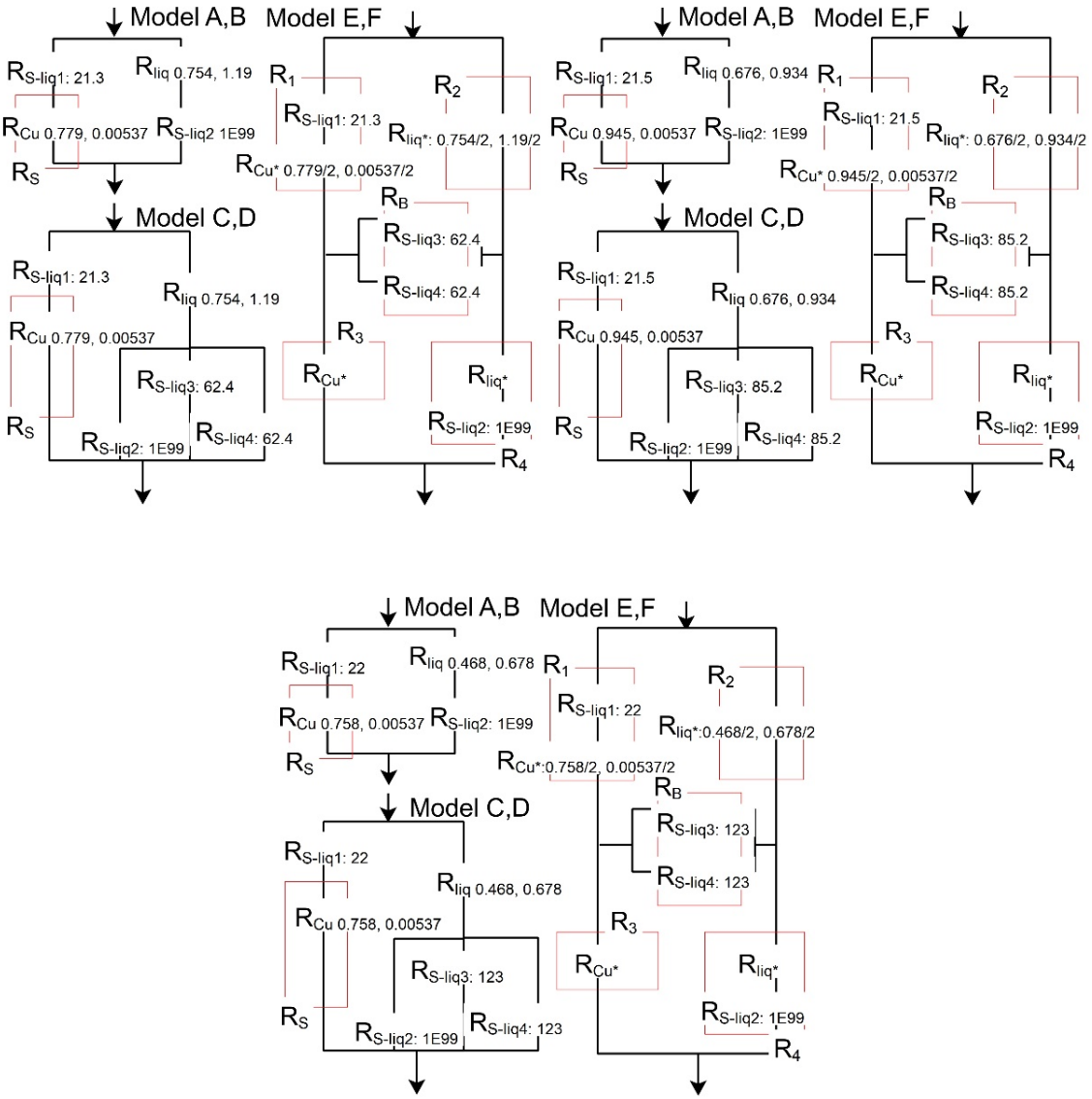

Figure S5.12 The local thermal resistances of model A to model F for the SPC/E model in the case of the nanopillar width of S19 under the water pressure of P1(top-left), P2(top-right), and P3(bottom) in the CB state. All values were components of TCMs. The unit is 10^8 K/W.

Figure S5.13 Calculation method of heat flow rate

The energy transfer between the solid surface atoms and water molecules was calculated by Eq. (S5.1). The $Q_{local\text{-}*}$ was the local rate of heat flow with the unit of the W. $\vec{F}_{ij}$ was the pairwise forces between water molecules and solid surface, $\vec{v}_i$ and $\vec{v}_j$ correspond to the velocities of solid surface atoms and water molecules, respectively. The term "sidewalls" was used to describe the energy transfer occurring in the nanopillar sidewalls,

which included half of the energy transfer observed in the corner-like regions, as illustrated in the red frames of Figure S5.13(b). The term "top" refers to the energy transfer occurring on the top nanopillar surface, which included half of the total energy transfer observed in the corner, as illustrated in the red frames of Figure S5.13(b).

$$Q_{local-*} = \frac{1}{2} \sum_{i \in liquid} \sum_{j \in solid} (\vec{F}_{ij} \cdot (\vec{v}_i - \vec{v}_j)) \; ; * \in \text{top, sidewalls, bottom} \tag{S5.1}$$

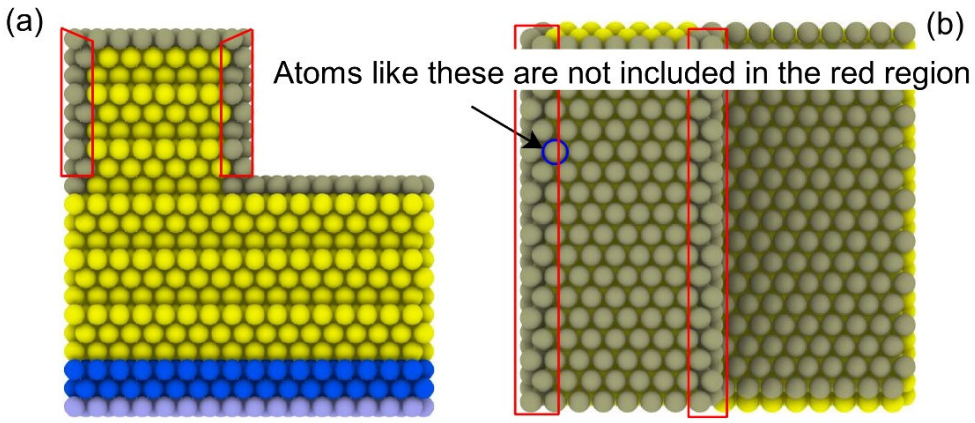

Figure S5.13 Calculation method of local heat flow rate for “top”, “sidewalls” and “bottom”. The definition of the "sidewalls" is indicated by the red frames that consist of (a) and (b). The grey atomic layer is just to highlight the surface atoms of the solid walls, including the "top", the "sidewalls" and the "bottom".

Equation (S5.2) was used to calculate the energy ratios, such as corresponding to Figures S5.14 to S5.16. $Q_{ratio-*}$ was the ratio of heat flow rate.

$$Q_{ratio-*} = \frac{Q_{local-*}}{Q_{local-top} + Q_{local-sidewalls} + Q_{local-bottom}} \tag{S5.2}$$

Figures S5.14 to S5.16 Energy transfer ratio between water and Cu

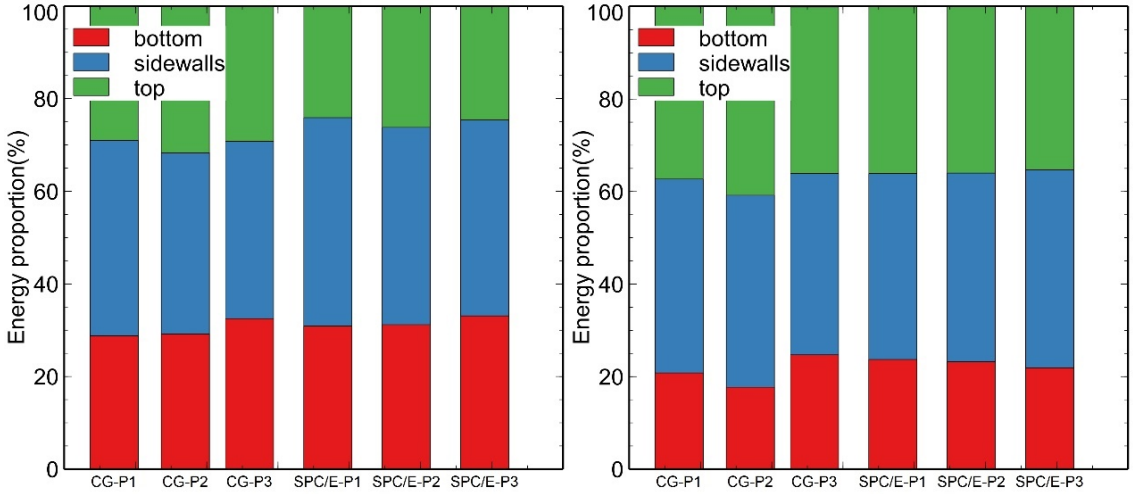

Figure S5.14 Energy transfer ratio between water and Cu calculated by MD simulations with nanopillar width of S19 (left) and S14 (right) in the CA1 cases. The "bottom", "sidewalls" and "top" refer to the energy transfer between water and the bottom of the groove, that between water and the nanopillar sidewalls, and that between water and the top nanopillar surface, respectively.

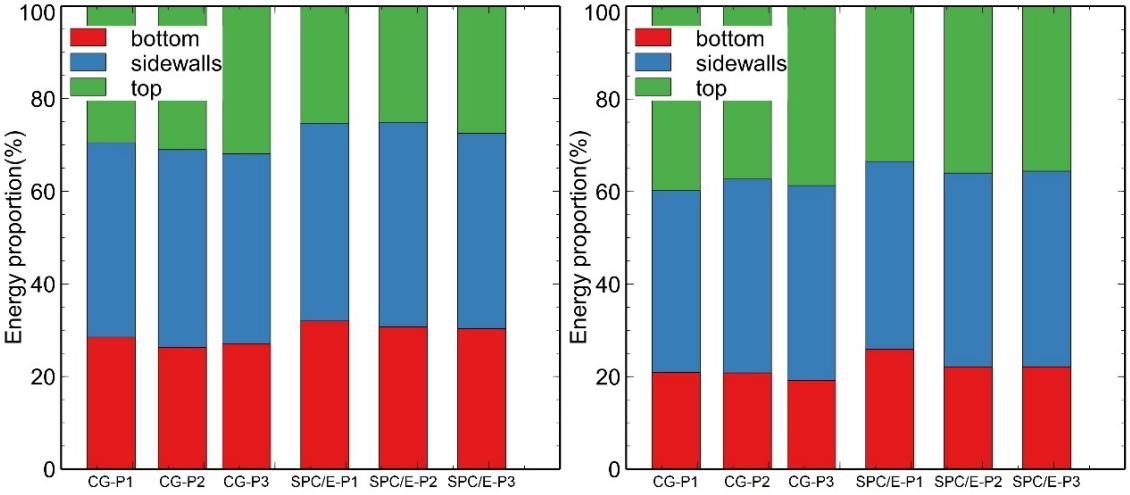

Figure S5.15 Energy transfer ratio between water and Cu calculated by MD simulations with nanopillar width of S19 (left) and S14 (right) in the Wenzel (CA2) state.

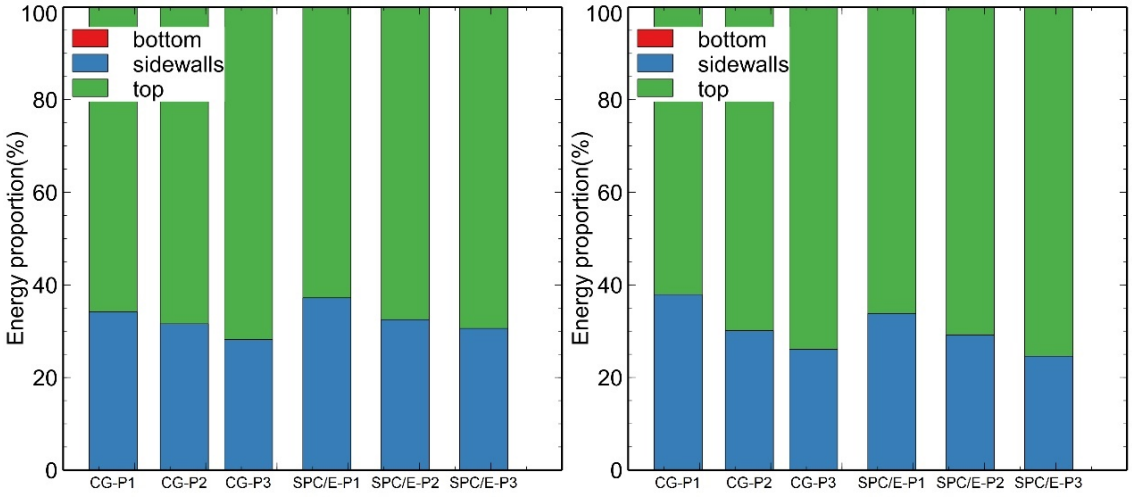

Figure S5.16 Energy transfer ratio between water and Cu calculated by MD simulations with nanopillar width of S19 (left) and S14 (right) in the CB (CA2) state.

Figures S5.17 to S5.22 2D temperature distribution in Cu-water systems

When calculating the 2D temperature of the SPC/E water molecules, one "resolved temperature" is calculated considering the temperature of a "completely" water molecule and the centroid of a "completely" water molecule. The centroid position is considered instead of the oxygen and hydrogen atomic positions.

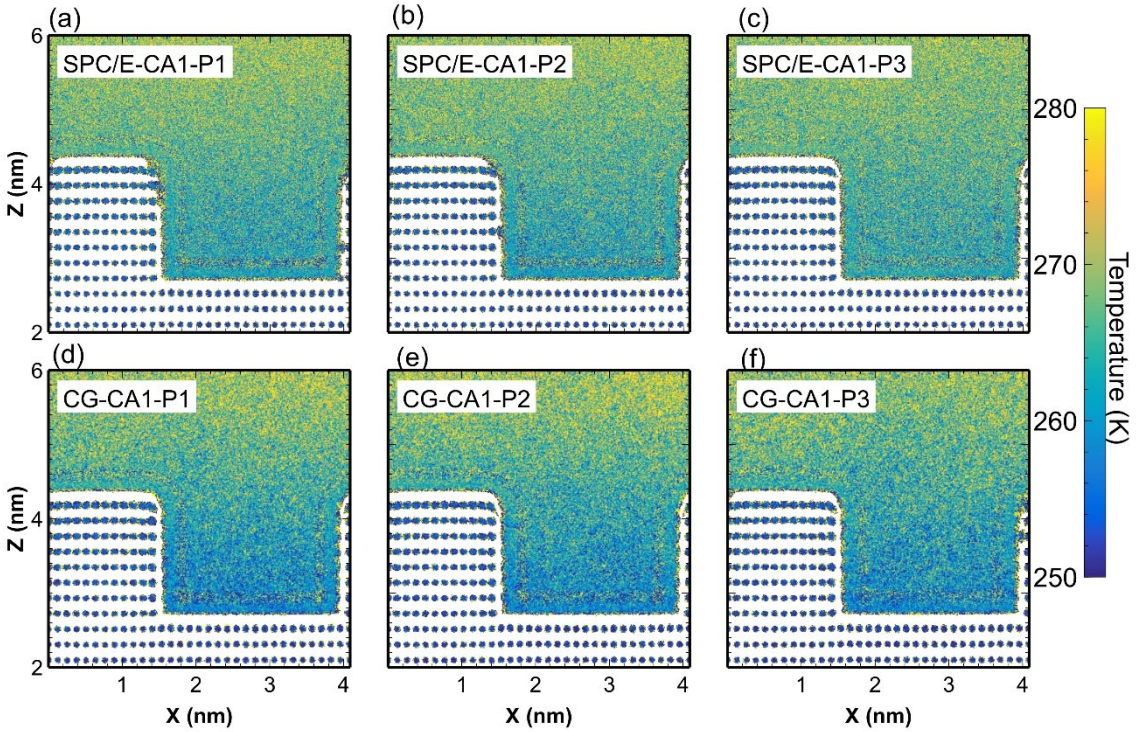

Figure S5.17 2D temperature distribution of the solids and water in the CA1 cases with the nanopillar width of S14. The unit of the scaler bar is K. (a) to (c) were related to the water pressure of P1 to P3 in the SPC/E model. (d) to (f) were related to the water pressure of P1 to P3 in the CG model.

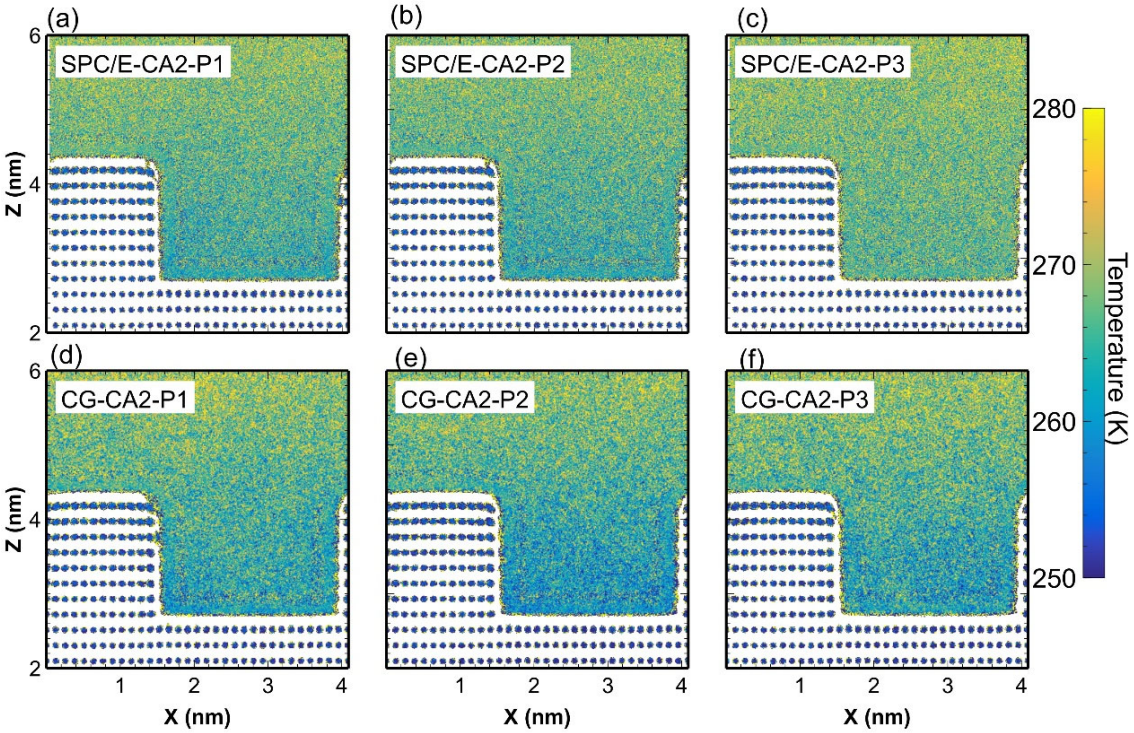

Figure S5.18 2D temperature distribution of the solids and water in the CA2 cases with the nanopillar width of S14.

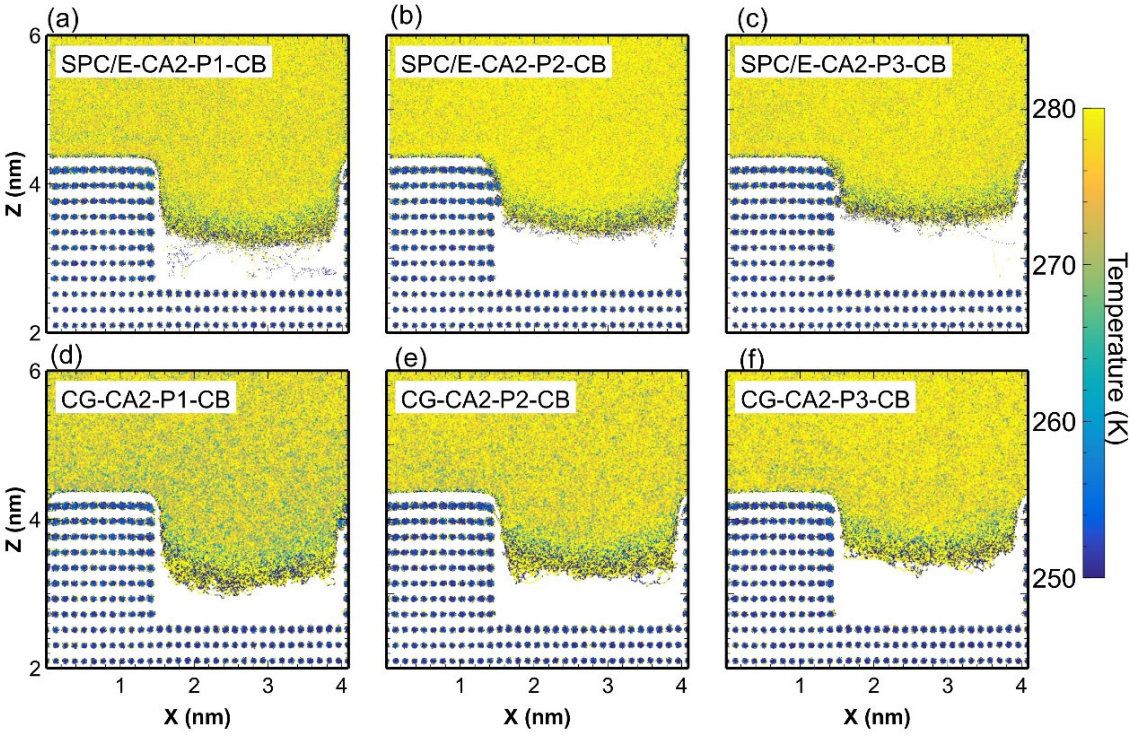

Figure S5.19 2D temperature distribution of the solids and water in the case of CB state with the nanopillar width of S14.

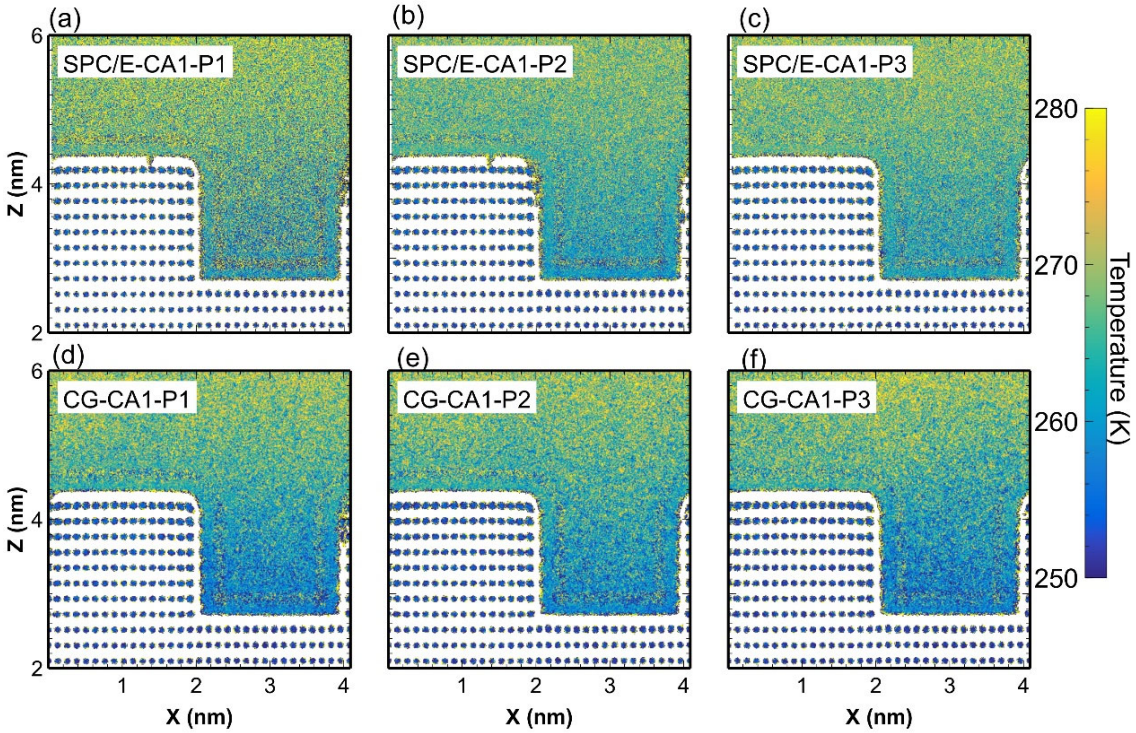

Figure S5.20 2D temperature distribution of the solids and water in the CA1 cases with the nanopillar width of S19.

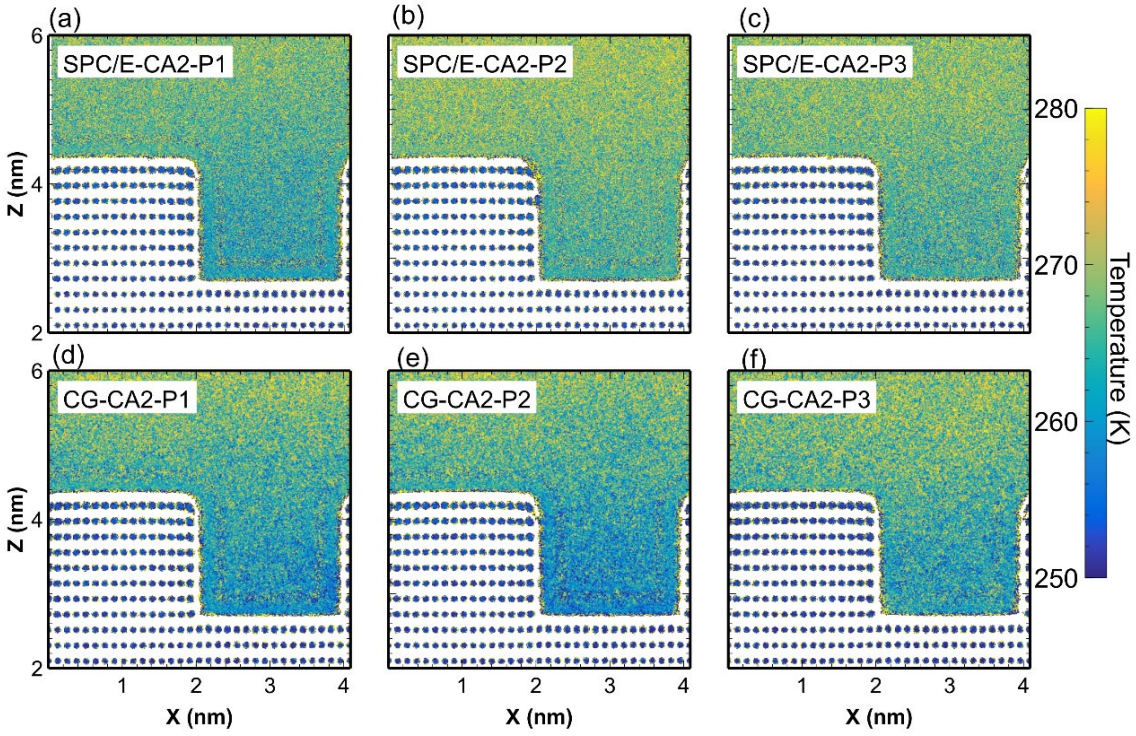

Figure S5.21 2D temperature distribution of the solids and water in the CA2 cases with the nanopillar width of S19.

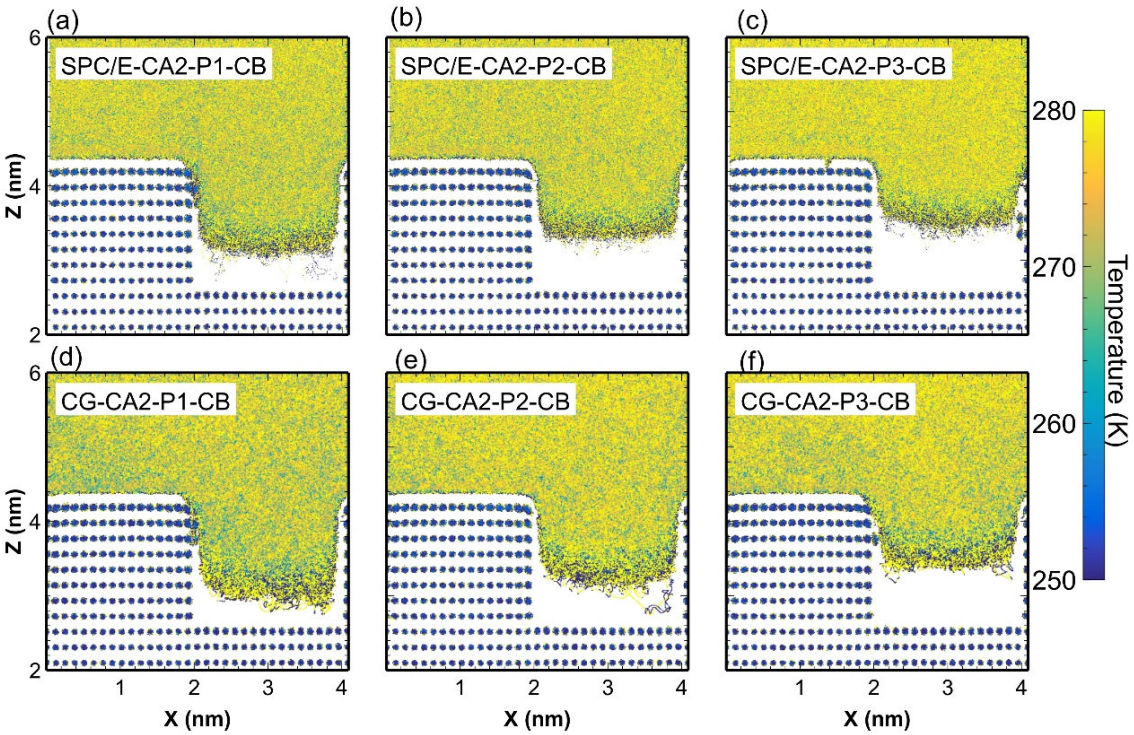

Figure S5.22 2D temperature distribution of the solids and water in the case of CB state with the nanopillar width of S19.

Figure S5.23 The energy transfer obtained by MD simulations and that calculated by TCMs in Cu-water systems

In Cu-water systems, the $Q_{MD\text{-}right}$ was the rate of heat flow in the right path of heat transfer calculated by MD simulations, as shown in Eq. (S5.3). The $Q_{MD\text{-}left}$ was the rate of heat flow in the left path calculated by MD simulations, as shown in Eq. (S5.4). The $Q_{local\text{-}sidewalls}$, $Q_{local\text{-}bottom}$, and $Q_{local\text{-}top}$ were calculated by Eq. (S5.1). The $Q_{Model\text{-}left}$ was the rate of heat flow based on the models A to D of the left path of heat transfer in TCM and calculated by Eq. (S5.5). The $Q_{Model\text{-}A,B\text{-}right}$ was the rate of heat flow based on the models A and B of the right path of heat transfer, which was calculated by Eq. (S5.6). The $Q_{Model\text{-}C,D\text{-}right}$ was the rate of heat flow based on the models C and D of the right path of heat transfer, as shown in Eq. (S5.7). The R_{eqm} in Eq. (S5.8) was a component in Eq. (S5.9) to Eq. (S5.11). For models E and F, the $Q_{Model\text{-}top}$, $Q_{Model\text{-}btm}$, and $Q_{Model\text{-}sidewalls}$ were the heat flow rate of the groove bottom surface, the nanopillar sidewalls, and the top nanopillar surface, respectively, which were calculated using Eq. (S5.9) to Eq. (S5.11) based on TCMs. The components of related equations were explained in Section 2.8.2.

$$Q_{MD-right} = Q_{local-sidewalls} + Q_{local-bottom} \quad \text{(S5.3)}$$

$$Q_{MD-left} = Q_{local-top} \quad \text{(S5.4)}$$

$$Q_{Model-left} = \Delta T_{th} \cdot (R_{S-liq1} + R_S)^{-1} \quad \text{(S5.5)}$$

$$Q_{Model-A,B-right} = \Delta T_{th} \cdot (R_{S-liq2} + R_{liq})^{-1} \quad \text{(S5.6)}$$

$$Q_{Model-C,D-right} = \Delta T_{th} \cdot ((R_{S-liq2}^{-1}+R_{S-liq3}^{-1}+R_{S-liq4}^{-1})^{-1} + R_{liq}) \quad \text{(S5.7)}$$

$$R_{eqm} = R_1R_2R_2 - R_1R_2R_4 - R_1R_3R_4 - R_1R_4R_B - R_2R_3R_4 - R_3R_4R_B \quad \text{(S5.8)}$$

$$Q_{Model-top} = (R_2R_2 - R_2R_3 - R_2R_4 - R_4R_B) \cdot \Delta T_{th} R_{eqm}^{-1} \quad \text{(S5.9)}$$

$$Q_{Model-btm} = (-R_1R_3 - R_1R_B + R_2^2 - R_2R_3 + R_2R_B - R_3R_B)\Delta T_{th} R_{eqm}^{-1} \quad \text{(S5.10)}$$

$$Q_{Model-sidewalls} = (R_1R_2 - R_1R_4 - R_2R_2 + R_2R_3) \cdot \Delta T_{th} R_{eqm}^{-1} \quad \text{(S5.11)}$$

To verify the basis of TCM in Cu-water systems, Figure S5.23 shows the rate of heat flow calculated by MD simulations and that derived by TCMs. The rate of heat flow derived by TCMs was calculated by Eq. (S5.5) and (S5.6) in models A and B, by Eq. (S5.5) and (S5.7) in models C and D, by Eq. (S5.9) to (S5.11) in models E and F. The dots correspond to the $Q_{Model-A,B-right}$ and $Q_{Model-C,D-right}$. The diamonds correspond to the $Q_{Model-left}$. The dots, diamonds, and squares in (e) and (f) correspond to the $Q_{Model-btm}$, $Q_{Model-top}$, and $Q_{Model-sidewalls}$, respectively.

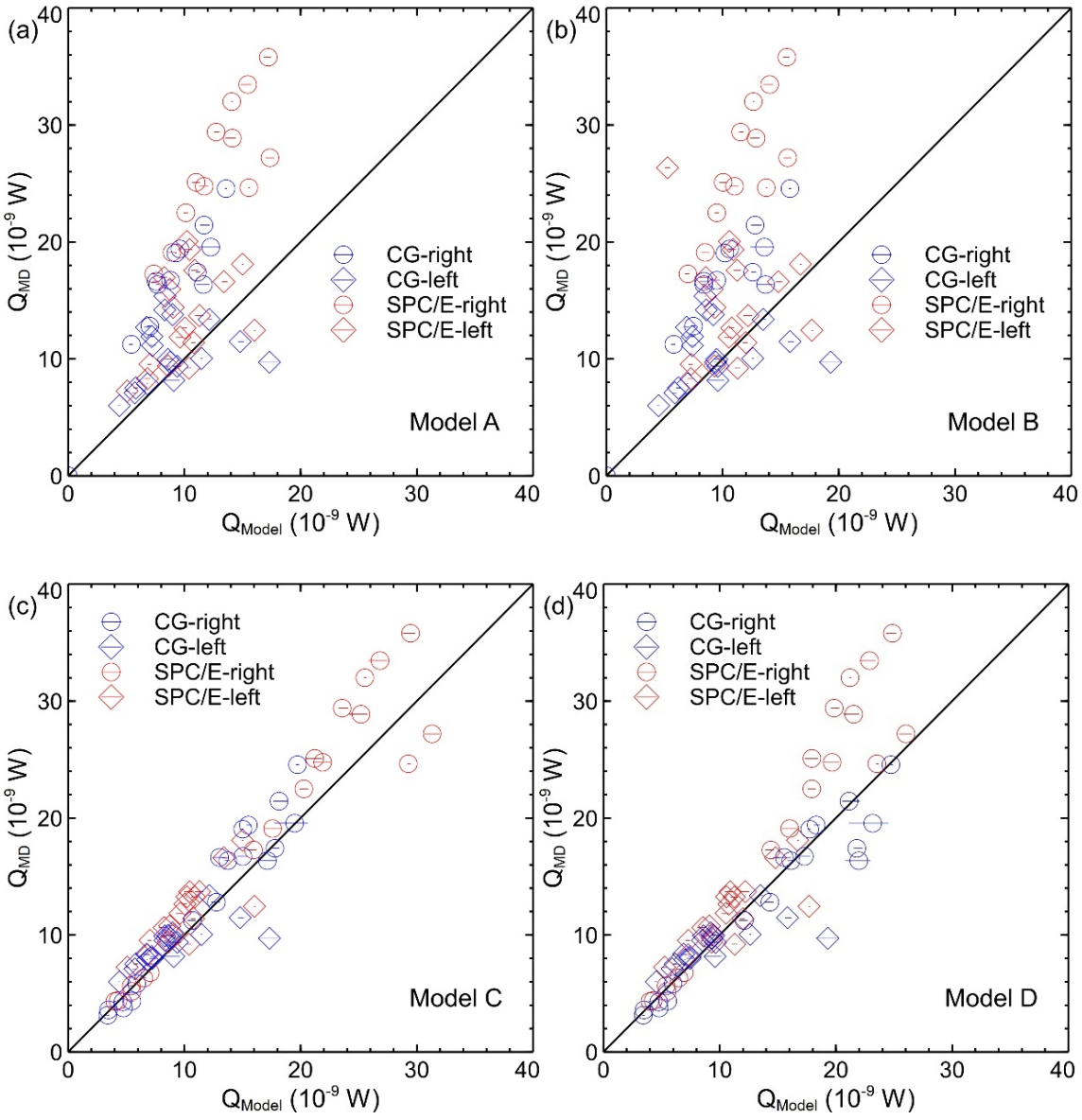

Figure S5.23 The energy transfer obtained by MD and that calculated by TCMs in Cu-water systems. The dots correspond to the right path of the TCMs. The diamonds correspond to the left path of the TCMs.

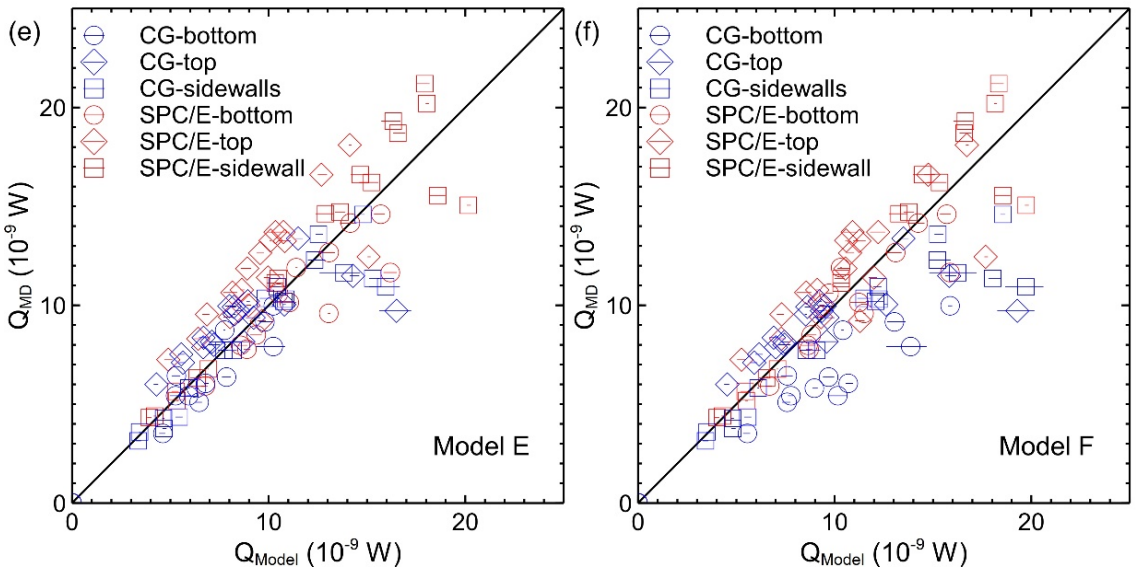

Figure S5.23 (continued) The energy transfer obtained by MD simulations and that calculated by TCMs in Cu-water systems. The dots, diamonds, and squares correspond to the bottom, top, and sidewalls of the TCMs in (e) and (f).

Appendix Chapter 6

Figures S6.1 to S6.2 Relationship between the water pressure and R_{flat} on flat surfaces in Cu-graphene-water systems

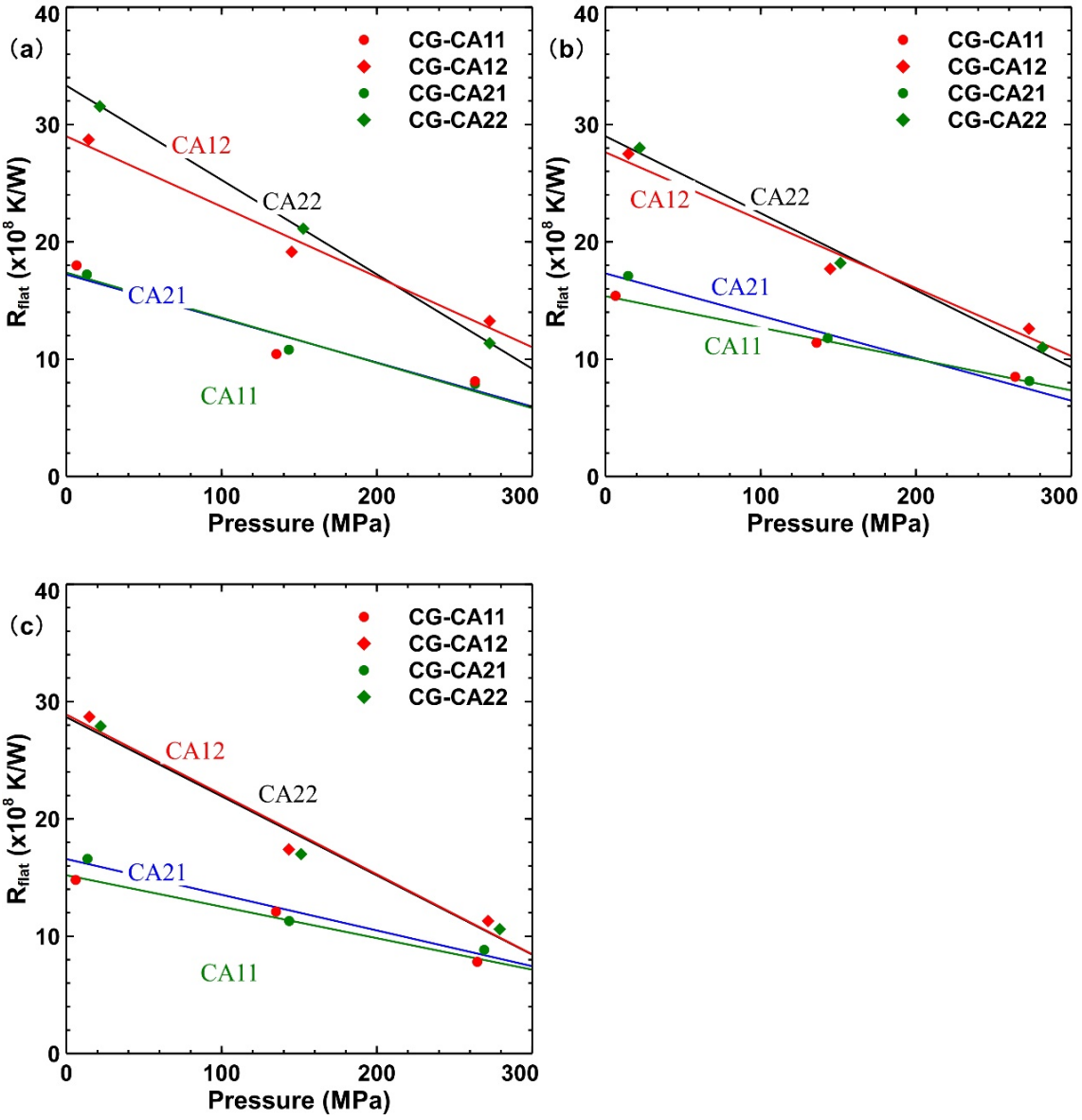

Figure S6.1 Relationship between the CG water pressure and thermal resistances (R_{flat}) on flat surfaces in Cu-graphene-water systems. An approximate line was used to describe the relationship between R and water pressure. The green and red lines were referred to as the fitting lines between water pressure and R_{flat}. (a), (b), and (c) correspond to the cases SV0.0, SV2.1, and SV2.8, respectively. The coefficients of green, blue, black, and red fitting functions (y=aa·x+bb) in (a), (b), and (c) are shown in Table S6.0.

Table S6.0 The coefficients of green, blue, black, and red fitting functions (y=aa·x+bb).

Lines	Defect surfaces	aa	bb	CoD
CG-green	SV0.0	-0.03849	17.38	0.92
CG-red		-0.05988	28.99	0.98
CG-blue		-0.03614	17.13	0.96
CG-black		-0.07741	33.12	0.99
SPC/E-green		-0.0393	16.8	0.97
SPC/E-red		-0.07193	31.98	0.96
SPC/E-blue		-0.02943	15.72	0.99
SPC/E-black		-0.08415	33.94	0.99
CG-green	SV2.1	-0.02676	15.37	0.99
CG-red		-0.05786	27.63	0.97
CG-blue		-0.03614	17.31	0.99
CG-black		-0.0656	29	0.99
SPC/E-green		-0.02876	14.78	0.99
SPC/E-red		-0.07777	30.45	0.99
SPC/E-blue		-0.02492	14.6	0.94
SPC/E-black		-0.0601	29.94	0.97
CG-green	SV2.8	-0.02683	15.2	0.98
CG-red		-0.06807	28.89	0.97
CG-blue		-0.03043	16.58	0.96
CG-black		-0.06744	28.67	0.98
SPC/E-green		-0.02902	14.48	0.99
SPC/E-red		-0.06366	27.13	0.93
SPC/E-blue		-0.0357	16.24	0.95
SPC/E-black		-0.07153	29.22	0.99

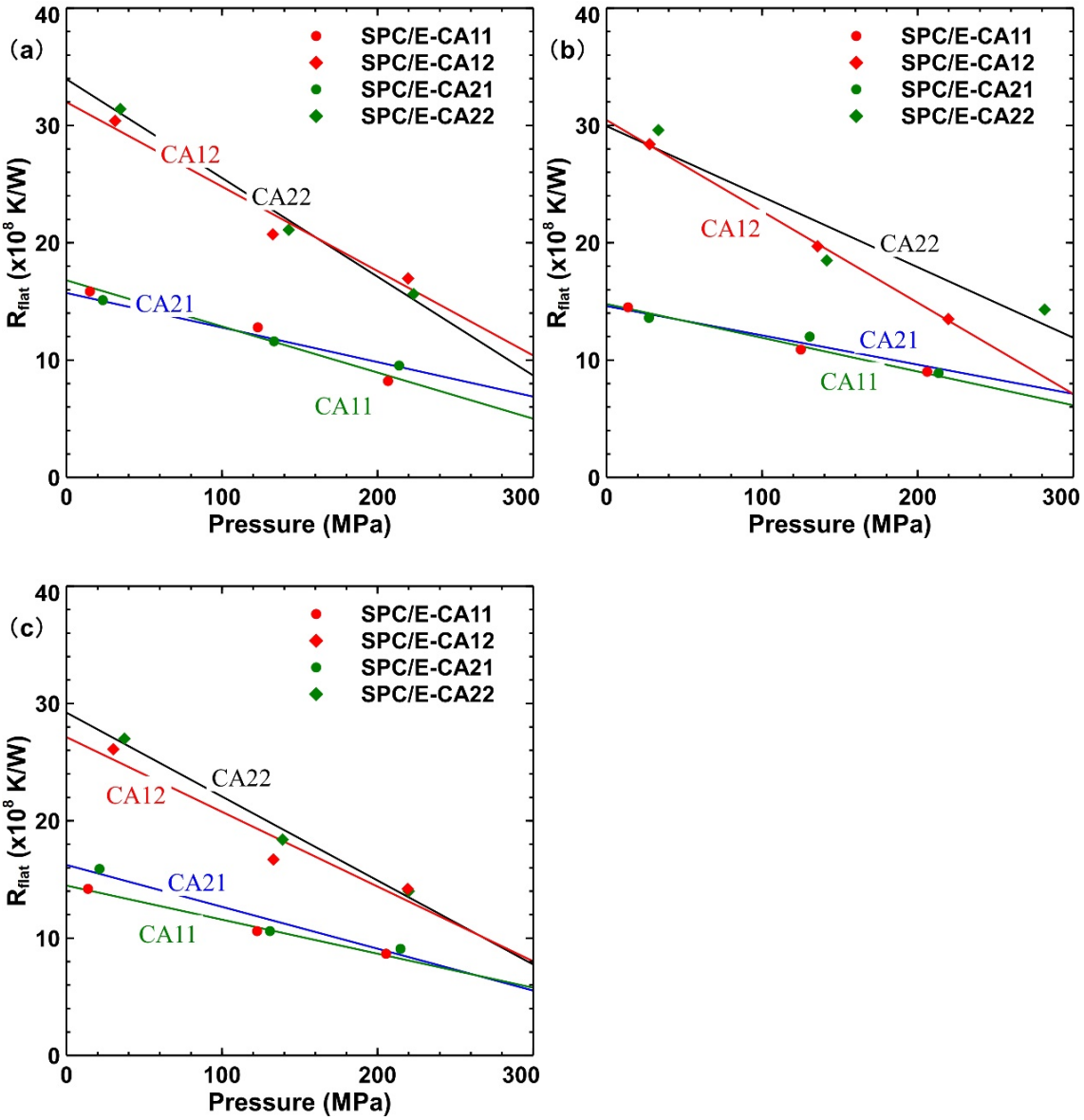

Figure S6.2 Relationship between SPC/E-water pressure and thermal resistances (R_{flat}) on flat surfaces in Cu-graphene-water systems. An approximate line was used to describe the relationship between R and water pressure. The coefficients of green, blue, black, and red fitting functions (y=aa·x+bb) in (a), (b), and (c) are shown in Table S6.0.

Table S6.1 The detailed R of the CG models on nanostructure surfaces in Cu-graphene-water systems under a correction of contact region thickness

The $R_{S\text{-}liq3,4}$ was referred to as $R_{S\text{-}liq3}$ and $R_{S\text{-}liq4}$. $R_{S\text{-}liq5,6}$ was referred to as $R_{S\text{-}liq6}$ and $R_{S\text{-}liq6}$. The R_S, R_{liq}, $R_{S\text{-}liq1}$, $R_{S\text{-}liq2}$, $R_{S\text{-}liq3}$, $R_{S\text{-}liq4}$, $R_{S\text{-}liq5}$, and $R_{S\text{-}liq6}$ have the same meanings in Section 2.8.3. "Unlimited" means the values were very high, such as 1E+99. All R unit is K/W. R_{Cu} and $R_{liq\text{-}MD}$ are calculated by the thermal conductivities of MD simulations. R_{Cu} for all cases is 5.20×10^5 K/W calculated by the experimental thermal conductivities.

Items	states	R_{Cu}	R_{liq}-MD	R_{liq}-Exp	$R_{liq1}+R_S$	$R_{S\text{-}liq2}$	$R_{S\text{-}liq3,4}$	$R_{S\text{-}liq5,6}$
CA11-SV0.0		4.90E+07	5.83E+08	3.51E+08	4.40E+09	1.12E+09	1.51E+09	2.28E+10
CA11-SV2.1		7.12E+07	4.96E+08	3.47E+08	3.82E+09	1.12E+09	1.51E+09	2.01E+10
CA11-SV2.8	P3	7.33E+07	5.28E+08	3.51E+08	3.80E+09	1.12E+09	1.51E+09	1.99E+10
CA12-SV0.0	Wenzel	6.76E+07	5.02E+08	3.41E+08	7.14E+09	1.11E+09	1.50E+09	3.76E+10
CA12-SV2.1		6.70E+07	5.22E+08	3.46E+08	6.13E+09	1.11E+09	1.50E+09	3.58E+10
CA12-SV2.8		9.27E+07	4.97E+08	3.41E+08	6.49E+09	1.11E+09	1.50E+09	3.74E+10
CA21-SV0.0		2.41E+07	1.78E+08	1.28E+08	4.12E+09		1.43E+10	2.13E+10
CA21-SV2.1		4.96E+07	1.68E+08	1.22E+08	3.90E+09		1.53E+10	2.15E+10
CA21-SV2.8	CB	2.59E+07	1.99E+08	1.27E+08	3.67E+09		1.46E+10	2.08E+10
CA22-SV0.0	N2	3.03E+07	1.85E+08	1.24E+08	6.99E+09		1.43E+10	4.04E+10
CA22-SV2.1		5.94E+07	1.98E+08	1.28E+08	6.11E+09		1.34E+10	3.55E+10
CA22-SV2.8		9.20E+07	1.59E+08	1.26E+08	6.36E+09		1.37E+10	3.50E+10
CA21-SV0.0		2.41E+07	1.78E+08	1.81E+08	4.07E+09	Unlimited	7.78E+09	2.10E+10
CA21-SV2.1		4.96E+07	1.75E+08	1.77E+08	3.89E+09		7.86E+09	2.14E+10
CA21-SV2.8	CB	2.59E+07	2.01E+08	1.80E+08	3.65E+09		7.86E+09	2.07E+10
CA22-SV0.0	N1	3.03E+07	1.85E+08	1.87E+08	6.99E+09		7.19E+09	4.03E+10
CA22-SV2.1		5.94E+07	1.90E+08	1.84E+08	6.14E+09		7.28E+09	3.58E+10
CA22-SV2.8		9.20E+07	1.55E+08	1.82E+08	6.36E+09		7.23E+09	3.50E+10
CA11-SV0.0		4.06E+07	4.59E+08	3.14E+08	3.48E+09	7.78E+08	1.05E+09	1.65E+10
CA11-SV2.1		3.73E+07	4.56E+08	3.14E+08	2.93E+09	7.80E+08	1.05E+09	1.58E+10
CA11-SV2.8	P2	4.33E+07	4.32E+08	3.15E+08	2.84E+09	7.77E+08	1.05E+09	1.55E+10
CA12-SV0.0	Wenzel	5.51E+07	4.57E+08	3.12E+08	5.40E+09	7.69E+08	1.04E+09	2.79E+10
CA12-SV2.1		6.15E+07	4.42E+08	3.08E+08	4.83E+09	7.67E+08	1.04E+09	2.64E+10
CA12-SV2.8		5.81E+07	4.70E+08	3.13E+08	4.86E+09	7.64E+08	1.03E+09	2.63E+10
CA11-SV0.0		3.95E+07	4.04E+08	2.95E+08	2.64E+09	4.80E+08	6.48E+08	1.10E+10
CA11-SV2.1		4.21E+07	4.17E+08	2.95E+08	2.51E+09	4.83E+08	6.52E+08	1.20E+10
CA11-SV2.8	P1	5.84E+07	4.13E+08	2.96E+08	2.45E+09	4.80E+08	6.48E+08	1.17E+10
CA12-SV0.0	Wenzel	3.53E+07	4.38E+08	2.93E+08	3.93E+09	4.69E+08	6.33E+08	1.94E+10
CA12-SV2.1		5.73E+07	3.81E+08	2.94E+08	3.59E+09	4.71E+08	6.36E+08	1.83E+10
CA12-SV2.8		3.48E+07	3.60E+08	2.95E+08	3.39E+09	4.71E+08	6.36E+08	1.68E+10

Table S6.2 The detailed R of the SPC/E models on nanostructure surfaces in Cu-graphene-water systems under a correction of contact region thickness

The $R_{S\text{-}liq3,4}$ was referred to as $R_{S\text{-}liq3}$ and $R_{S\text{-}liq4}$. $R_{S\text{-}liq5,6}$ was referred to as $R_{S\text{-}liq6}$ and $R_{S\text{-}liq6}$. The R_S, R_{liq}, $R_{S\text{-}liq1}$, $R_{S\text{-}liq2}$, $R_{S\text{-}liq3}$, $R_{S\text{-}liq4}$, $R_{S\text{-}liq5}$, and $R_{S\text{-}liq6}$ have the same meanings in Section 2.8.3. "Unlimited" means the values were very high, such as 1E+99. All R unit is K/W. $R_{Cu\text{-}MD}$ and $R_{liq\text{-}MD}$ are calculated by the thermal conductivities of MD simulations. R_{Cu} for all cases is 5.20×10^5 K/W calculated by the experimental thermal conductivities.

Items	states	R_{Cu}-MD	R_{liq}-MD	R_{liq}-Exp	$R_{S\text{-}liq1}+R_S$	$R_{S\text{-}liq2}$	$R_{S\text{-}liq3,4}$	$R_{S\text{-}liq5,6}$
CA11-SV0.0	P3 Wenzel	4.99E+07	2.67E+08	3.40E+08	4.52E+09	8.94E+08	1.21E+09	2.15E+10
CA11-SV2.1		4.93E+07	2.45E+08	3.42E+08	3.84E+09	8.90E+08	1.20E+09	1.89E+10
CA11-SV2.8		4.56E+07	2.74E+08	3.44E+08	3.89E+09	8.92E+08	1.20E+09	1.86E+10
CA12-SV0.0		3.80E+07	2.46E+08	3.30E+08	8.00E+09	8.91E+08	1.20E+09	4.07E+10
CA12-SV2.1		4.67E+07	2.25E+08	3.33E+08	7.22E+09	8.84E+08	1.19E+09	3.82E+10
CA12-SV2.8		4.08E+07	2.39E+08	3.31E+08	6.40E+09	8.86E+08	1.20E+09	3.42E+10
CA21-SV0.0	CB N2	5.30E+07	1.33E+08	1.78E+08	4.35E+09	Unlimited	6.81E+09	1.95E+10
CA21-SV2.1		5.09E+07	1.23E+08	1.74E+08	3.87E+09		6.79E+09	1.82E+10
CA21-SV2.8		5.39E+07	1.17E+08	1.79E+08	3.61E+09		6.77E+09	1.98E+10
CA22-SV0.0		4.75E+07	1.53E+08	1.85E+08	8.11E+09		6.19E+09	4.05E+10
CA22-SV2.1		3.49E+07	1.15E+08	1.85E+08	6.63E+09		6.20E+09	3.65E+10
CA22-SV2.8		5.08E+07	1.33E+08	1.83E+08	6.25E+09		6.23E+09	3.52E+10
CA21-SV0.0	CB N1	5.30E+07	1.33E+08	1.16E+08	4.35E+09		1.48E+10	1.97E+10
CA21-SV2.1		5.09E+07	1.21E+08	1.12E+08	3.89E+09		1.47E+10	1.83E+10
CA21-SV2.8		5.39E+07	1.18E+08	1.17E+08	3.68E+09		1.49E+10	2.03E+10
CA22-SV0.0		4.75E+07	1.53E+08	1.21E+08	8.13E+09		1.26E+10	4.07E+10
CA22-SV2.1		3.49E+07	1.15E+08	1.21E+08	6.64E+09		1.26E+10	3.66E+10
CA22-SV2.8		5.08E+07	1.33E+08	1.17E+08	6.22E+09		1.32E+10	3.50E+10
CA11-SV0.0	P2 Wenzel	3.64E+07	2.42E+08	3.14E+08	3.57E+09	7.82E+08	1.06E+09	1.71E+10
CA11-SV2.1		4.41E+07	2.45E+08	3.14E+08	3.41E+09	7.82E+08	1.06E+09	1.58E+10
CA11-SV2.8		6.28E+07	2.15E+08	3.16E+08	3.22E+09	7.83E+08	1.06E+09	1.54E+10
CA12-SV0.0		7.31E+07	2.05E+08	3.14E+08	6.33E+09	7.81E+08	1.05E+09	3.26E+10
CA12-SV2.1		2.38E+07	2.62E+08	3.09E+08	5.59E+09	7.78E+08	1.05E+09	2.97E+10
CA12-SV2.8		6.64E+07	2.34E+08	3.13E+08	5.35E+09	7.78E+08	1.05E+09	2.73E+10
CA11-SV0.0	P1 Wenzel	3.73E+07	2.23E+08	3.02E+08	2.68E+09	6.02E+08	8.13E+08	9.81E+09
CA11-SV2.1		6.20E+07	2.04E+08	3.02E+08	2.41E+09	6.06E+08	8.18E+08	1.06E+10
CA11-SV2.8		6.19E+07	2.03E+08	3.02E+08	2.28E+09	6.00E+08	8.11E+08	9.92E+09
CA12-SV0.0		8.02E+07	2.01E+08	2.98E+08	3.84E+09	6.01E+08	8.11E+08	1.94E+10
CA12-SV2.1		9.51E+07	1.87E+08	2.99E+08	3.41E+09	5.99E+08	8.09E+08	1.55E+10
CA12-SV2.8		2.51E+07	2.36E+08	2.96E+08	3.30E+09	6.01E+08	8.11E+08	1.57E+10

The detailed values in TCMs in the Wenzel state on the composite surface for the CG model

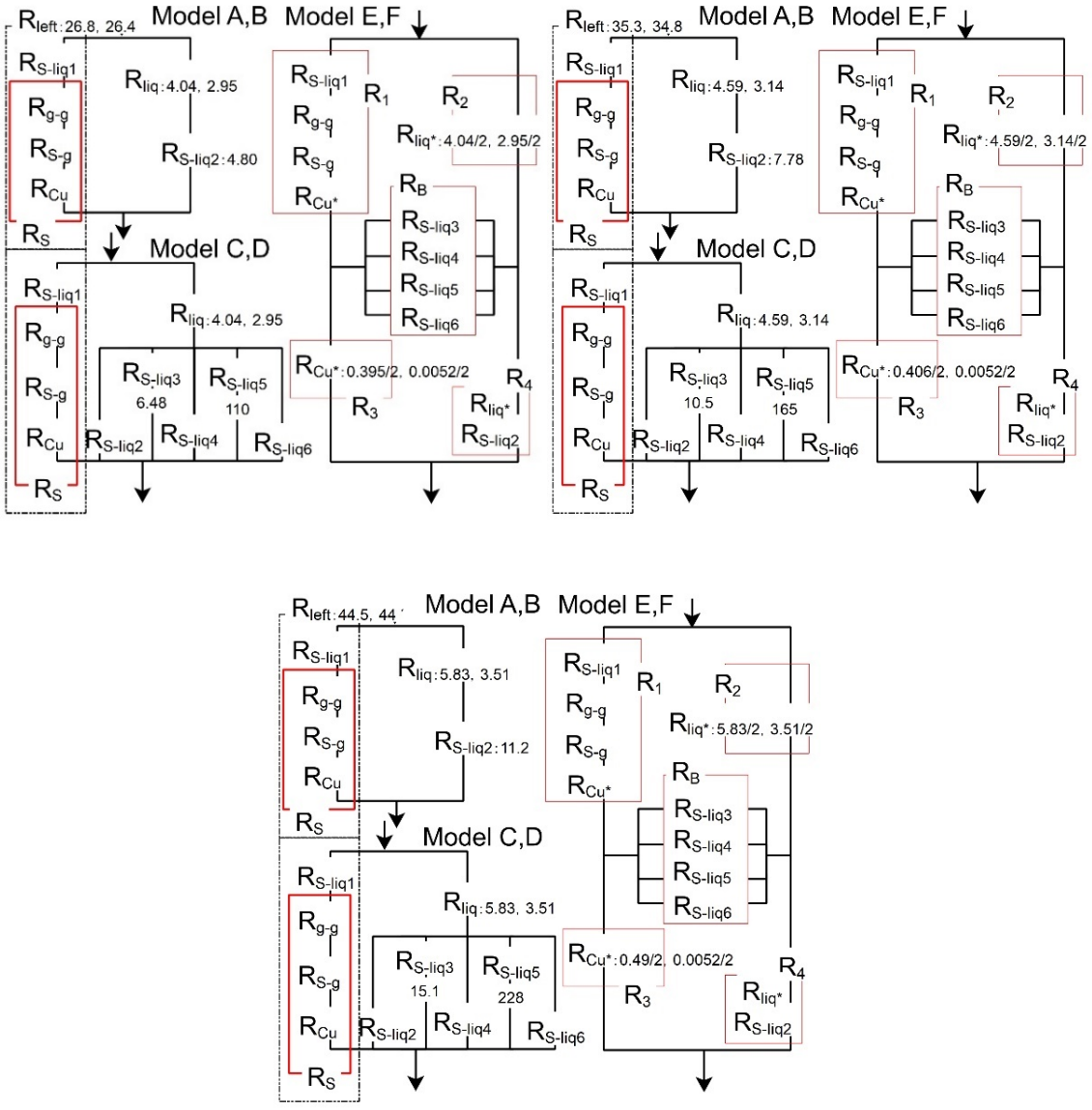

Figure S6.3 The local thermal resistances for the CG model in the Wenzel (CA11) state under the cases of pristine graphene (SV0.0). The top-left, top-right, and bottom of the figures correspond to the water pressure of P1, P2, and P3, respectively. All values were components of TCMs. The value unit is 10^8 K/W.

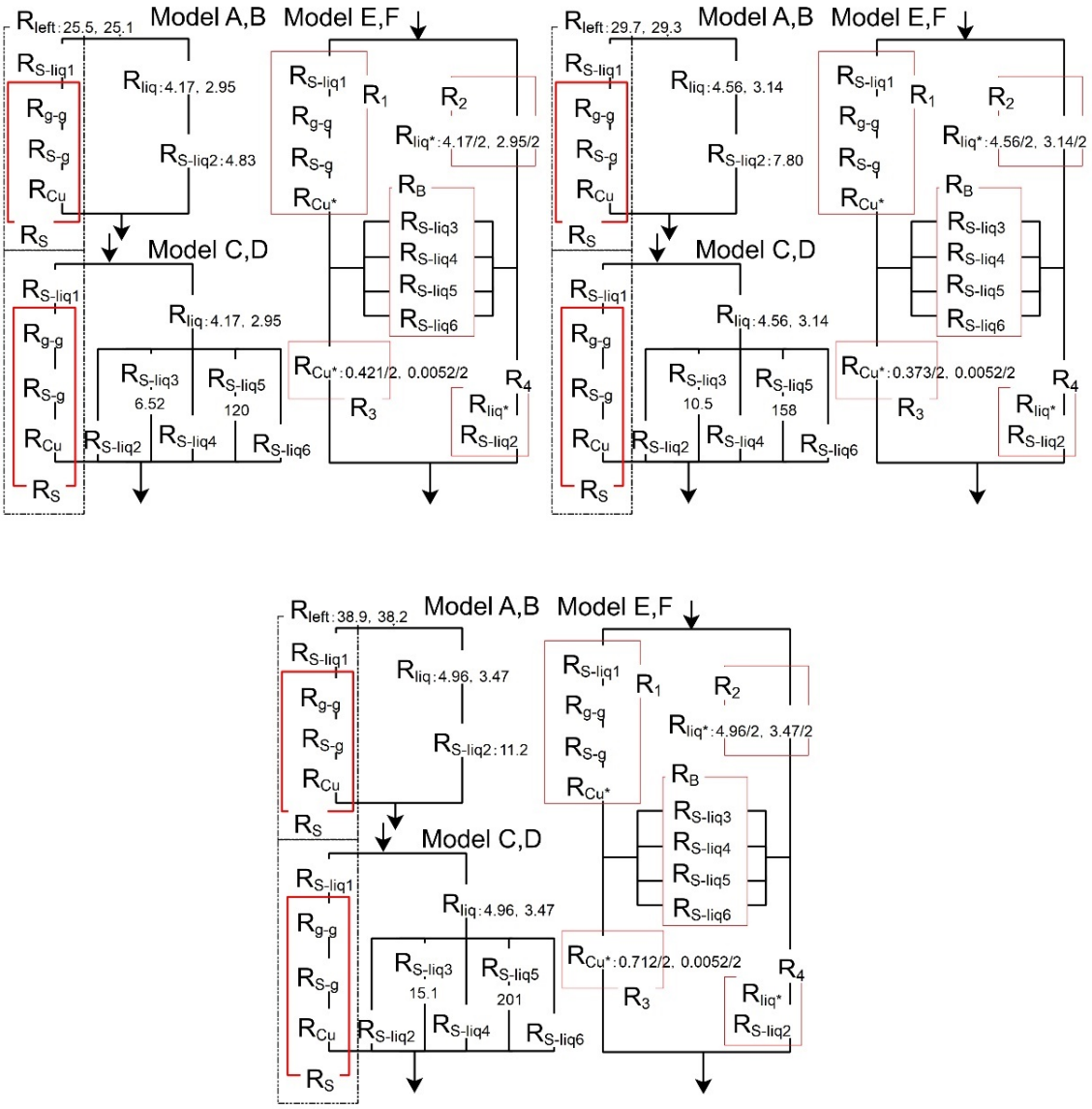

Figure S6.4 The local thermal resistances for the CG model in the Wenzel (CA11) state under the cases of pristine graphene (SV2.1). The top-left, top-right, and bottom of the figures correspond to the water pressure of P1, P2, and P3, respectively. All values were components of TCMs. The value unit is 10^8 K/W.

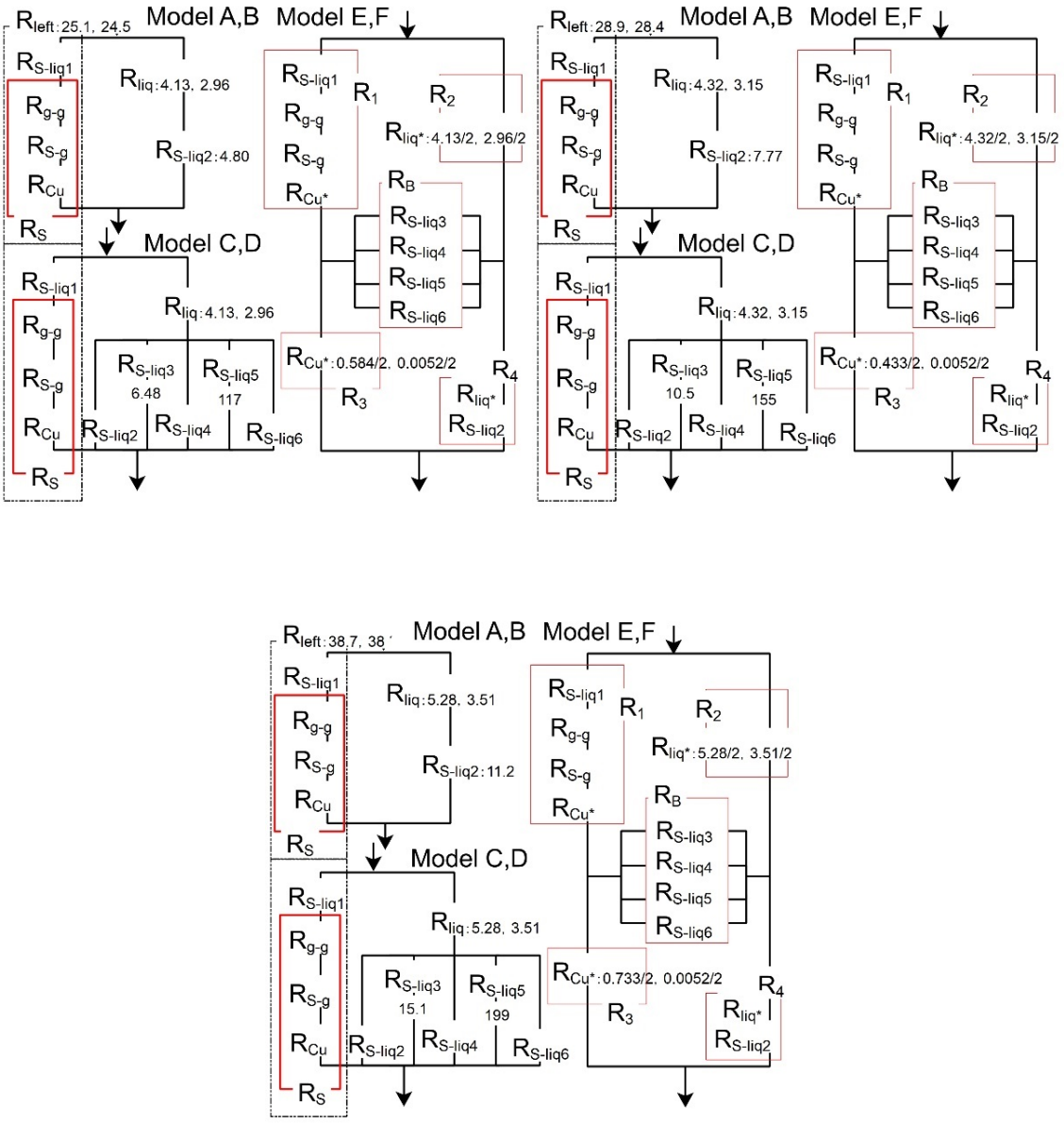

Figure S6.5 The local thermal resistances for the CG model in the Wenzel (CA11) state under the cases of pristine graphene (SV2.8). The top-left, top-right, and bottom of the figures correspond to the water pressure of P1, P2, and P3, respectively. All values were components of TCMs. The value unit is 10^8 K/W.

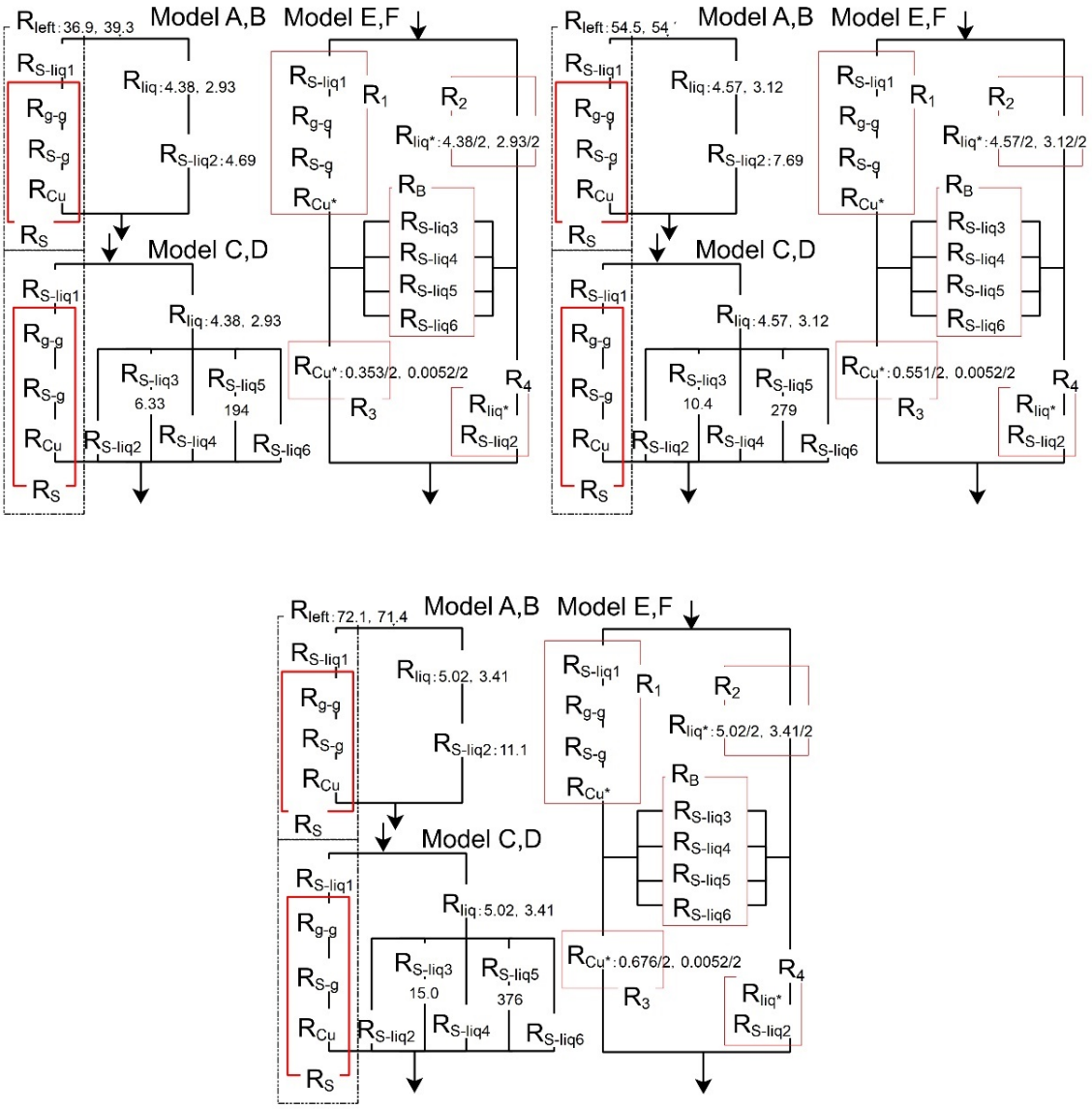

Figure S6.6 The local thermal resistances for the CG model in the Wenzel (CA12) state under the cases of pristine graphene (SV0.0). The top-left, top-right, and bottom of the figures correspond to the water pressure of P1, P2, and P3, respectively. All values were components of TCMs. The value unit is 10^8 K/W.

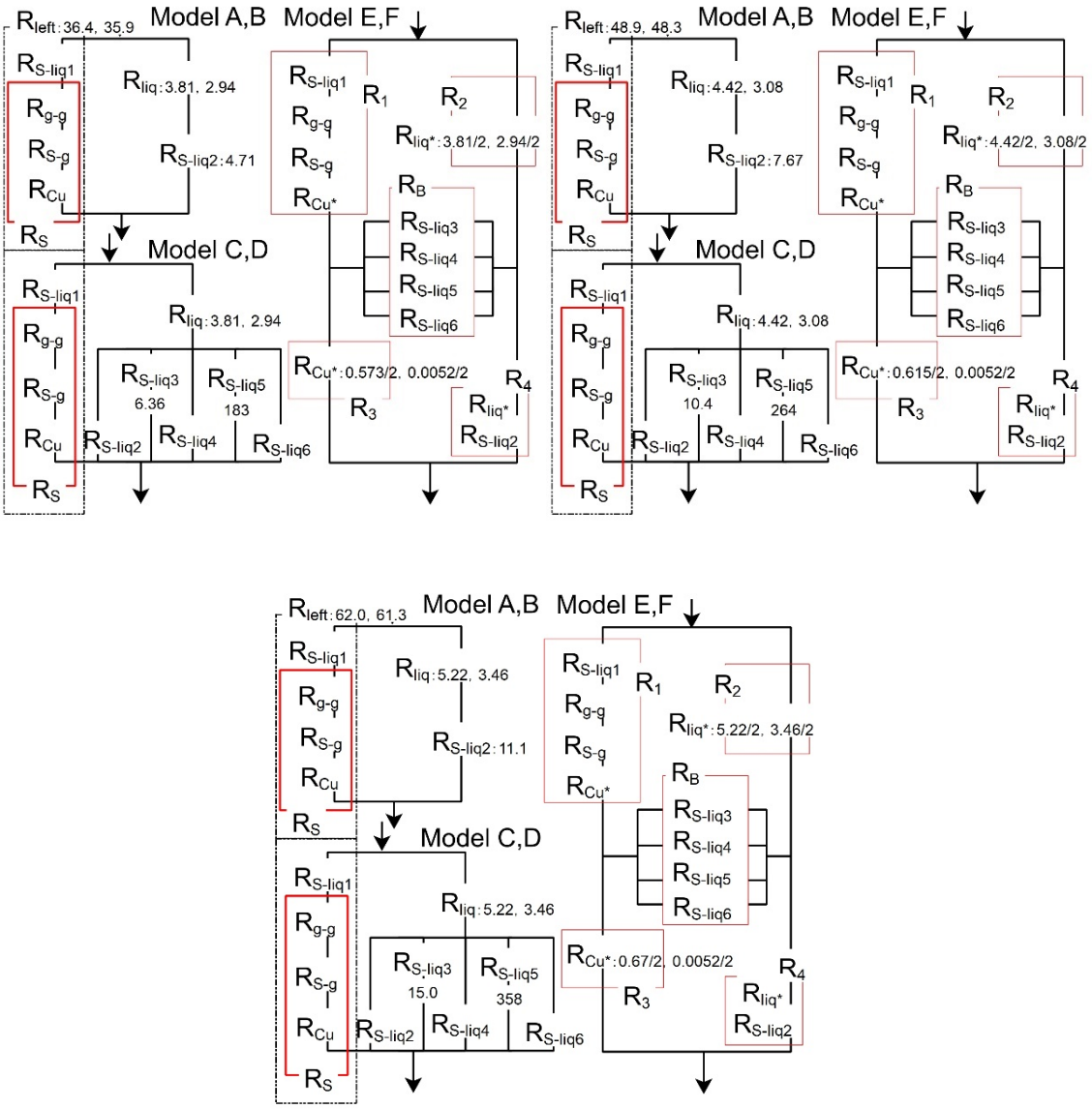

Figure S6.7 The local thermal resistances for the CG model in the Wenzel (CA12) state under the cases of pristine graphene (SV2.1). The top-left, top-right, and bottom of the figures correspond to the water pressure of P1, P2, and P3, respectively. All values were components of TCMs. The value unit is 10^8 K/W.

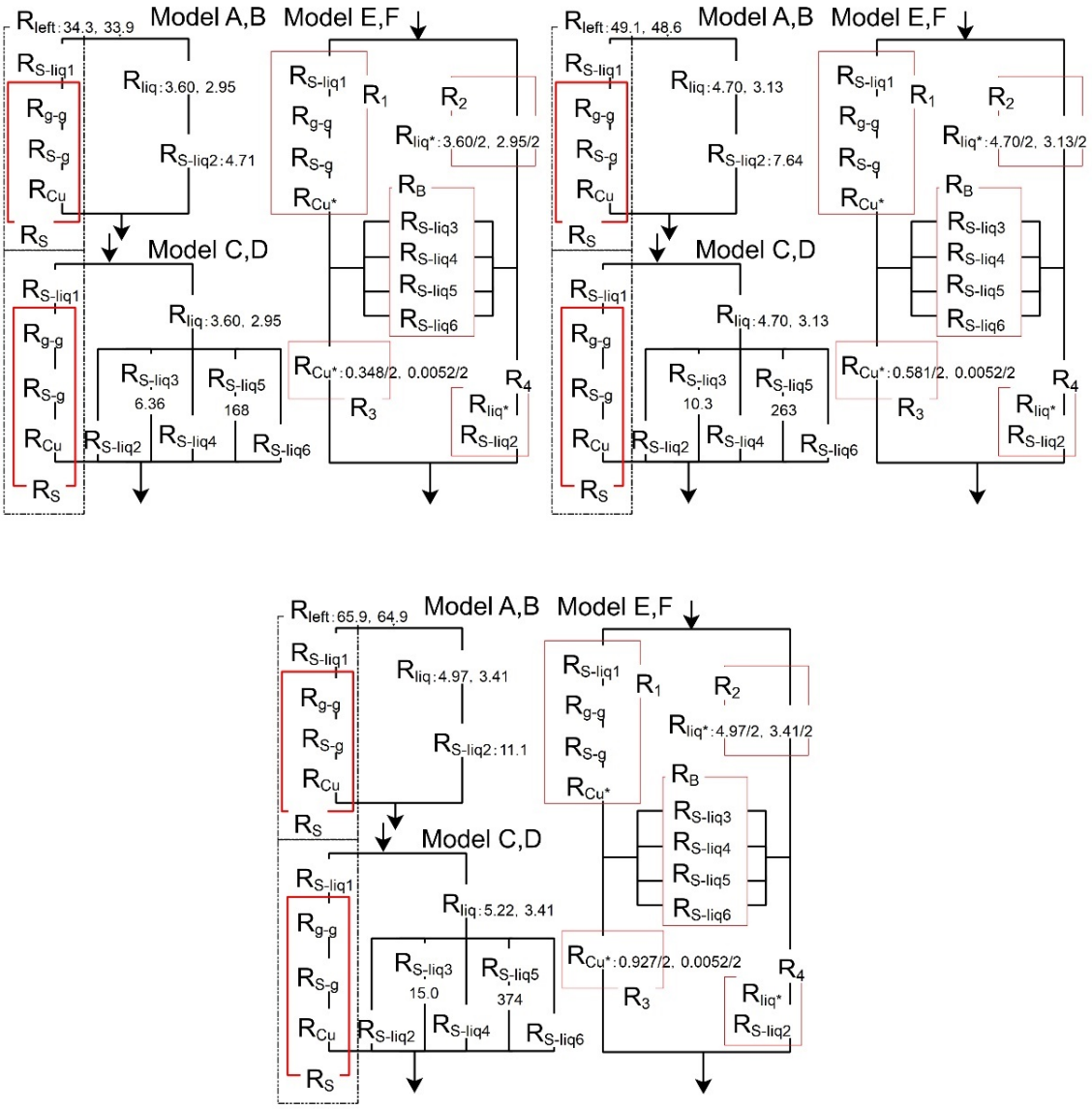

Figure S6.8 The local thermal resistances for the CG model in the Wenzel (CA12) state under the cases of pristine graphene (SV2.8). The top-left, top-right, and bottom of the figures correspond to the water pressure of P1, P2, and P3, respectively. All values were components of TCMs. The value unit is 10^8 K/W.

The detailed values in TCMs in the CB state on the composite surface for the CG model

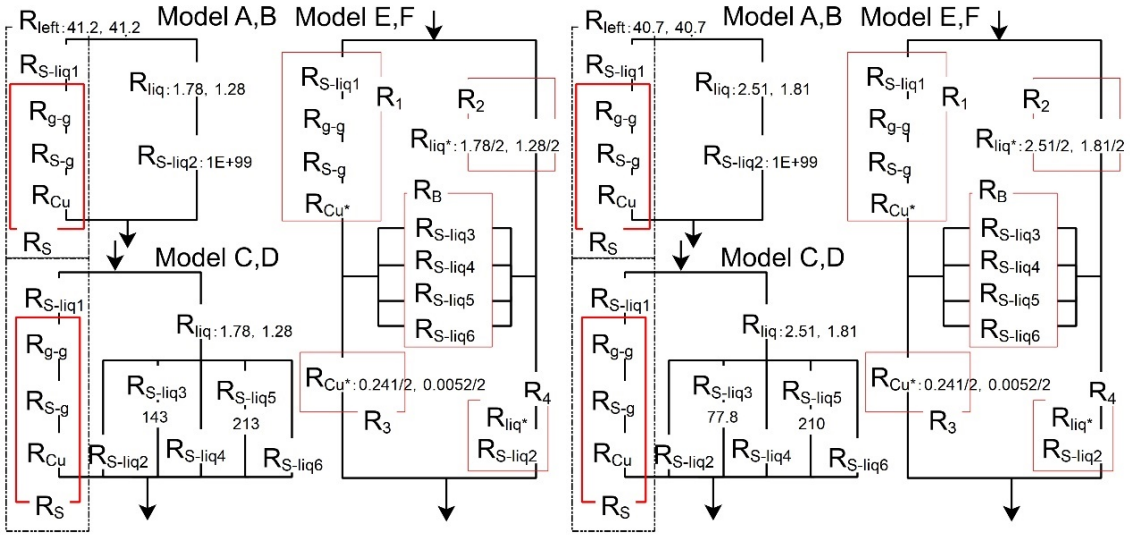

Figure S6.9 The local thermal resistances of model A to model F for the CG model in the CB (CA21) state under the cases of pristine graphene (SV0.0). The left and right figures correspond to the number of water molecules of N1 and N2, respectively. All values were components of TCMs.

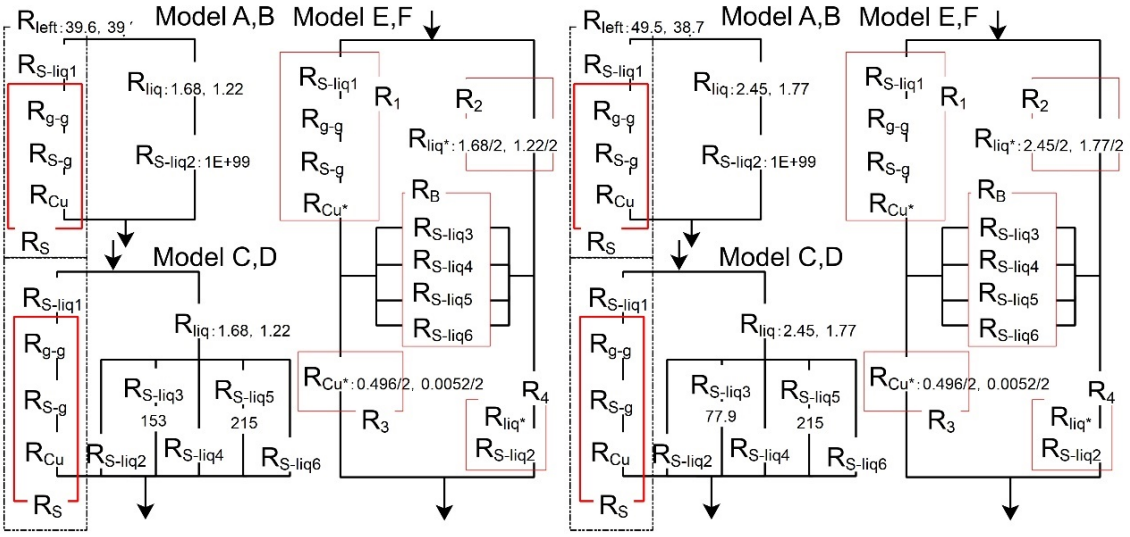

Figure S6.10 The local thermal resistances of model A to model F for the CG model in the CB (CA21) state under the cases of defective graphene (SV2.1). The left and right figures correspond to the number of water molecules of N1 and N2, respectively. All values were components of TCMs. The unit is 10^8 K/W.

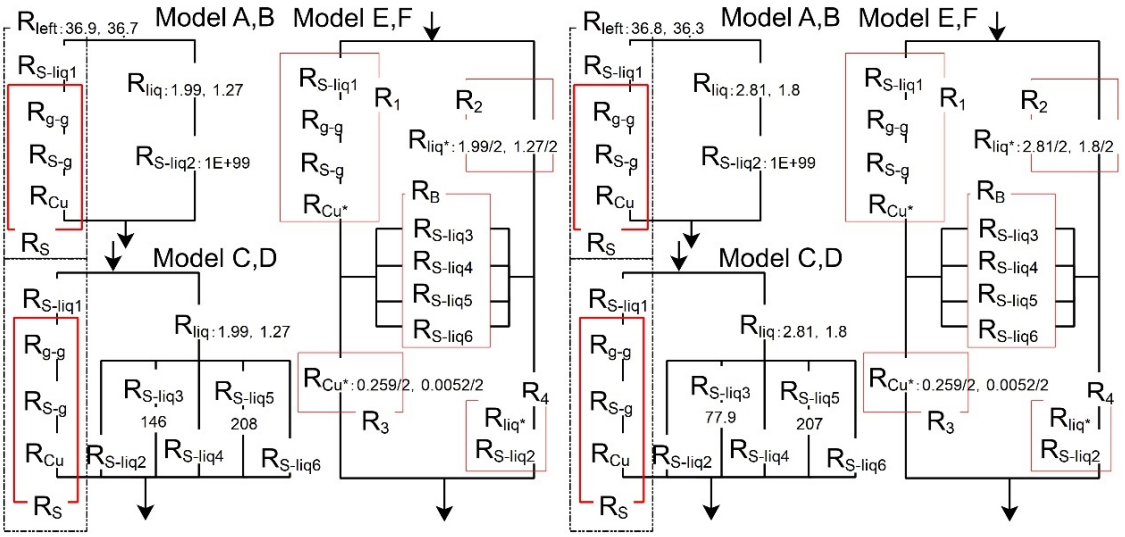

Figure S6.11 The local thermal resistances of model A to model F for the CG model in the CB (CA21) state under the cases of defective graphene (SV2.8). The left and right figures correspond to the number of water molecules of N1 and N2, respectively. All values were components of TCMs. The unit is 10^8 K/W.

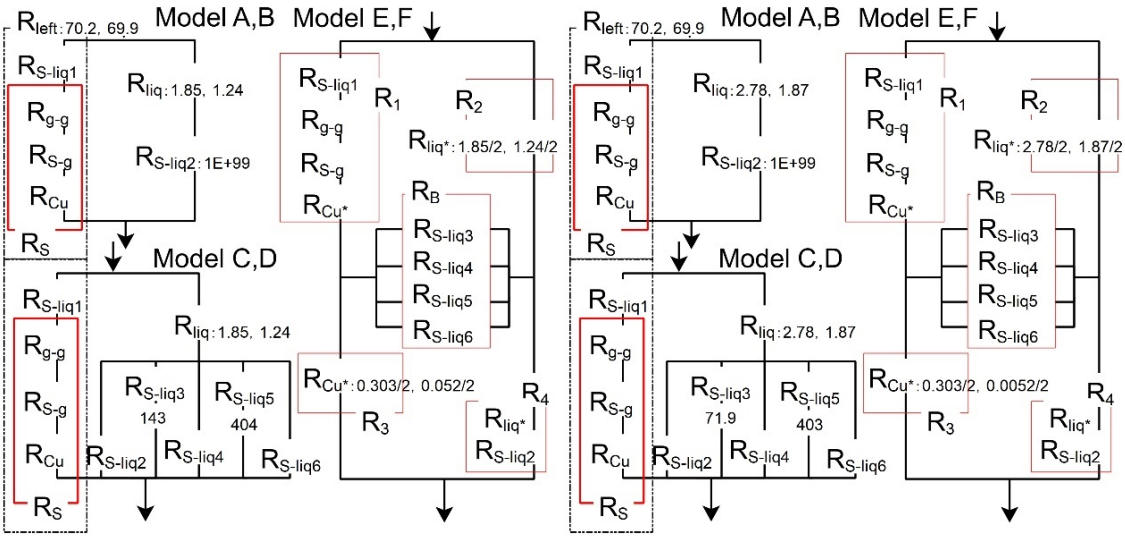

Figure S6.12 The local thermal resistances of model A to model F for the CG model in the CB (CA22) state under the cases of pristine graphene (SV0.0). The left and right figures correspond to the number of water molecules of N1 and N2, respectively. All values were components of TCMs. The unit is 10^8 K/W.

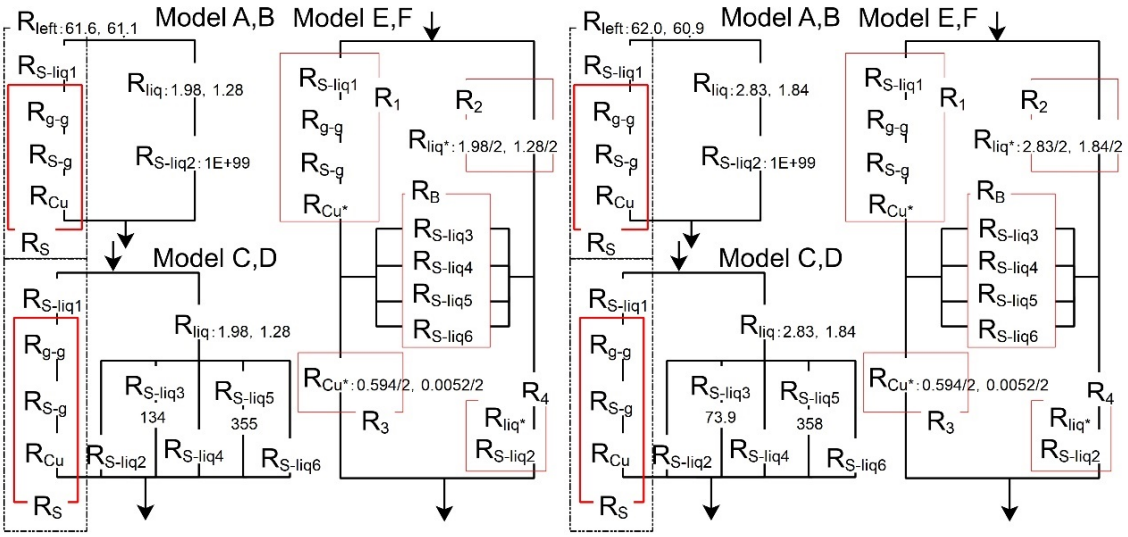

Figure S6.13 The local thermal resistances of model A to model F for the CG model in the CB (CA22) state under the cases of defective graphene (SV2.1). The left and right figures correspond to the number of water molecules of N1 and N2, respectively. All values were components of TCMs. The unit is 10^8 K/W.

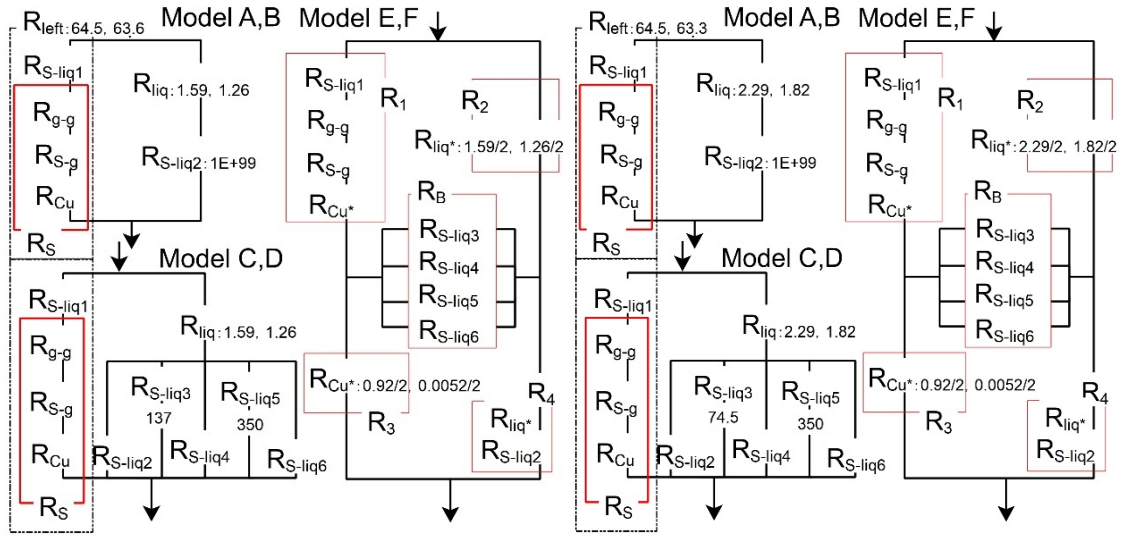

Figure S6.14 The local thermal resistances of model A to model F for the CG model in the CB (CA22) state under the cases of defective graphene (SV2.8). The left and right figures correspond to the number of water molecules of N1 and N2, respectively. All values were components of TCMs. The unit is 10^8 K/W.

The detailed values in TCMs in the Wenzel state on the composite surface for the SPC/E model

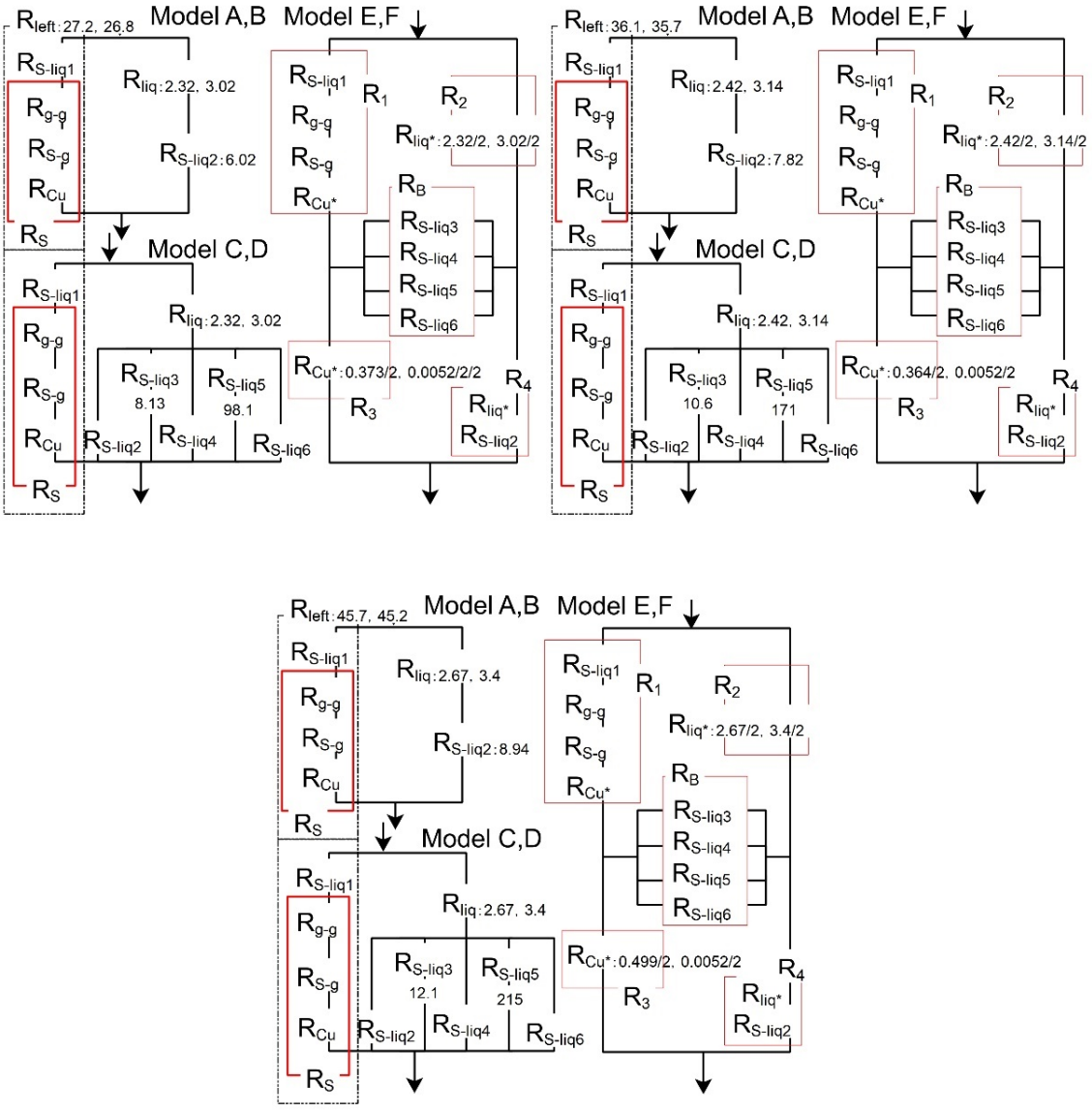

Figure S6.15 The local thermal resistances of model A to model F for the SPC/E model in the Wenzel (CA11) state under the cases of pristine graphene (SV0.0). The top-left, top-right, and bottom of the figures correspond to the water pressure of P1, P2, and P3, respectively. All values were components of TCMs. The unit is 10^8 K/W.

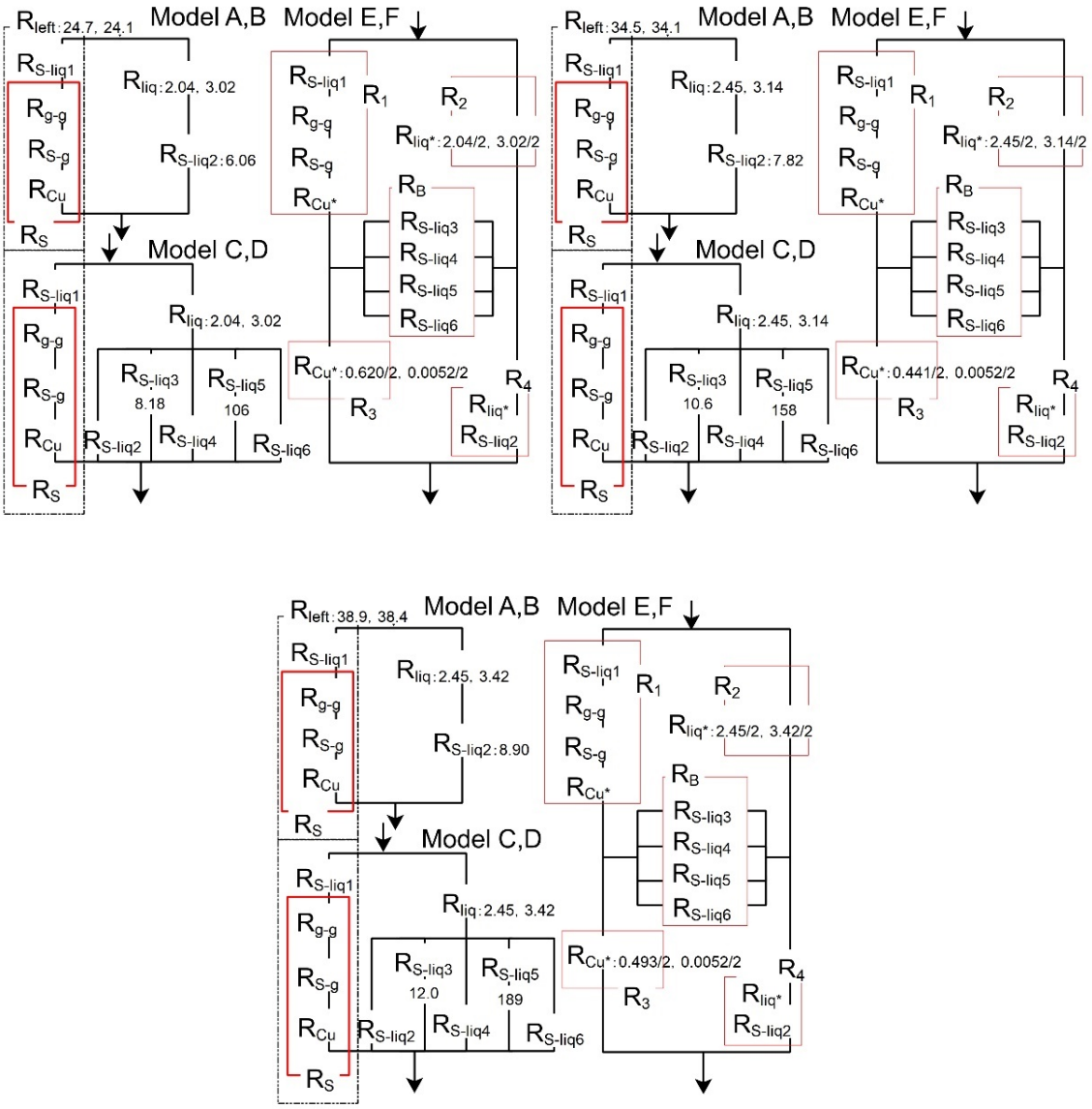

Figure S6.16 The local thermal resistances of model A to model F for the SPC/E model in the Wenzel (CA11) state under the cases of pristine graphene (SV2.1). The top-left, top-right, and bottom of the figures correspond to the water pressure of P1, P2, and P3, respectively. All values were components of TCMs. The unit is 10^8 K/W.

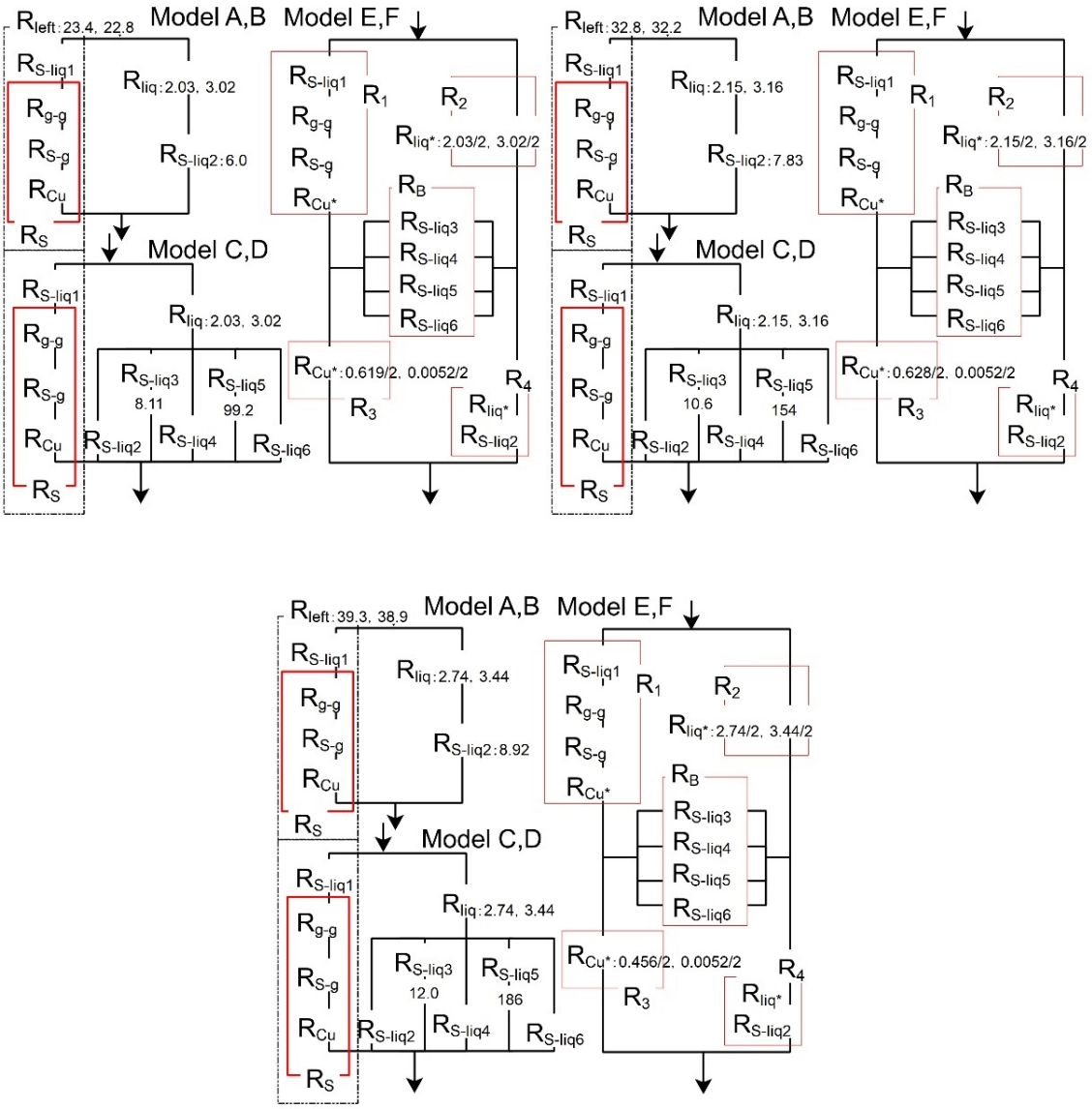

Figure S6.17 The local thermal resistances of model A to model F for the SPC/E model in the Wenzel (CA11) state under the cases of pristine graphene (SV2.8). The top-left, top-right, and bottom of the figures correspond to the water pressure of P1, P2, and P3, respectively. All values were components of TCMs. The unit is 10^8 K/W.

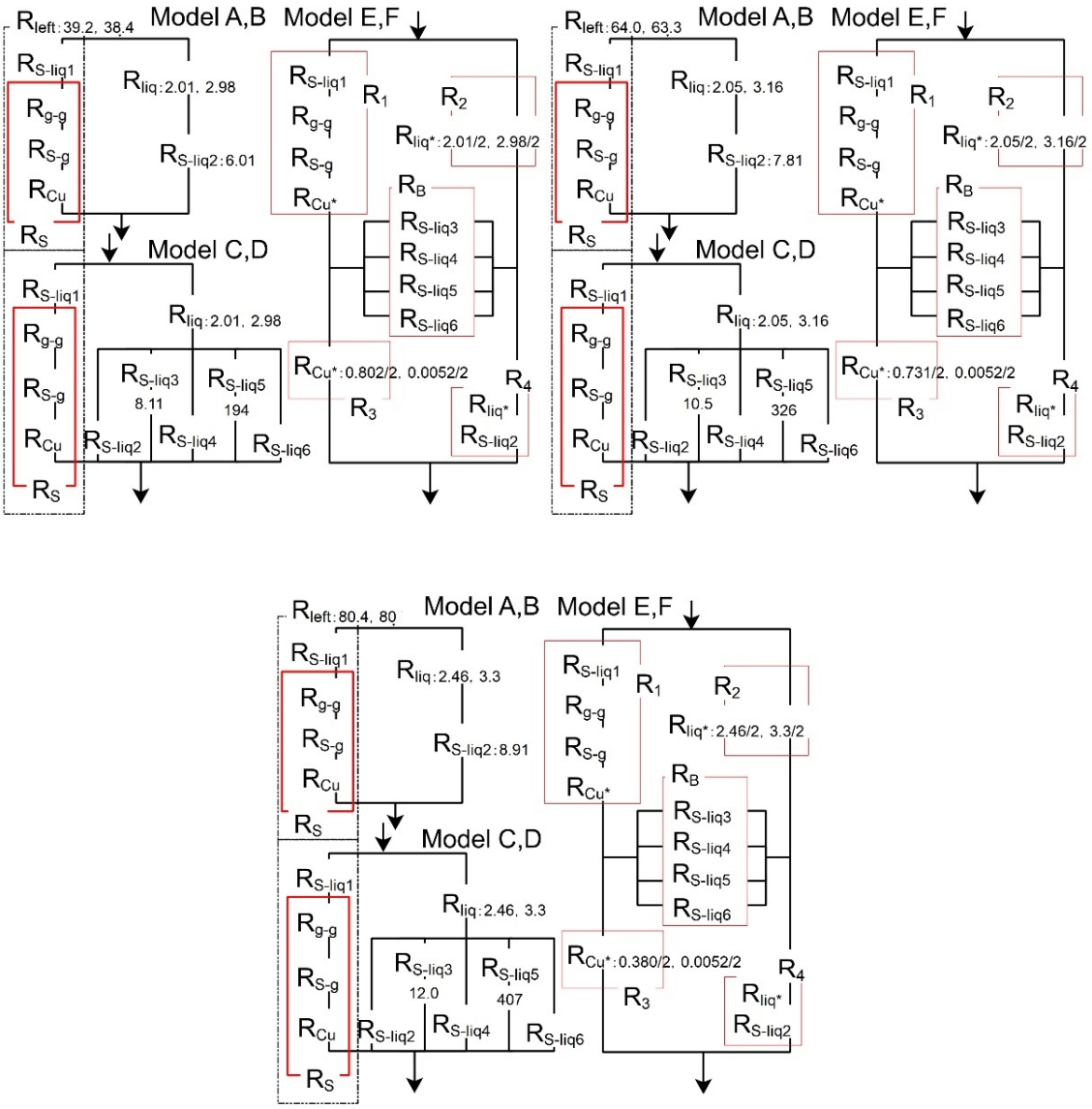

Figure S6.18 The local thermal resistances of model A to model F for the SPC/E model in the Wenzel (CA12) state under the cases of pristine graphene (SV0.0). The top-left, top-right, and bottom of the figures correspond to the water pressure of P1, P2, and P3, respectively. All values were components of TCMs. The unit is 10^8 K/W.

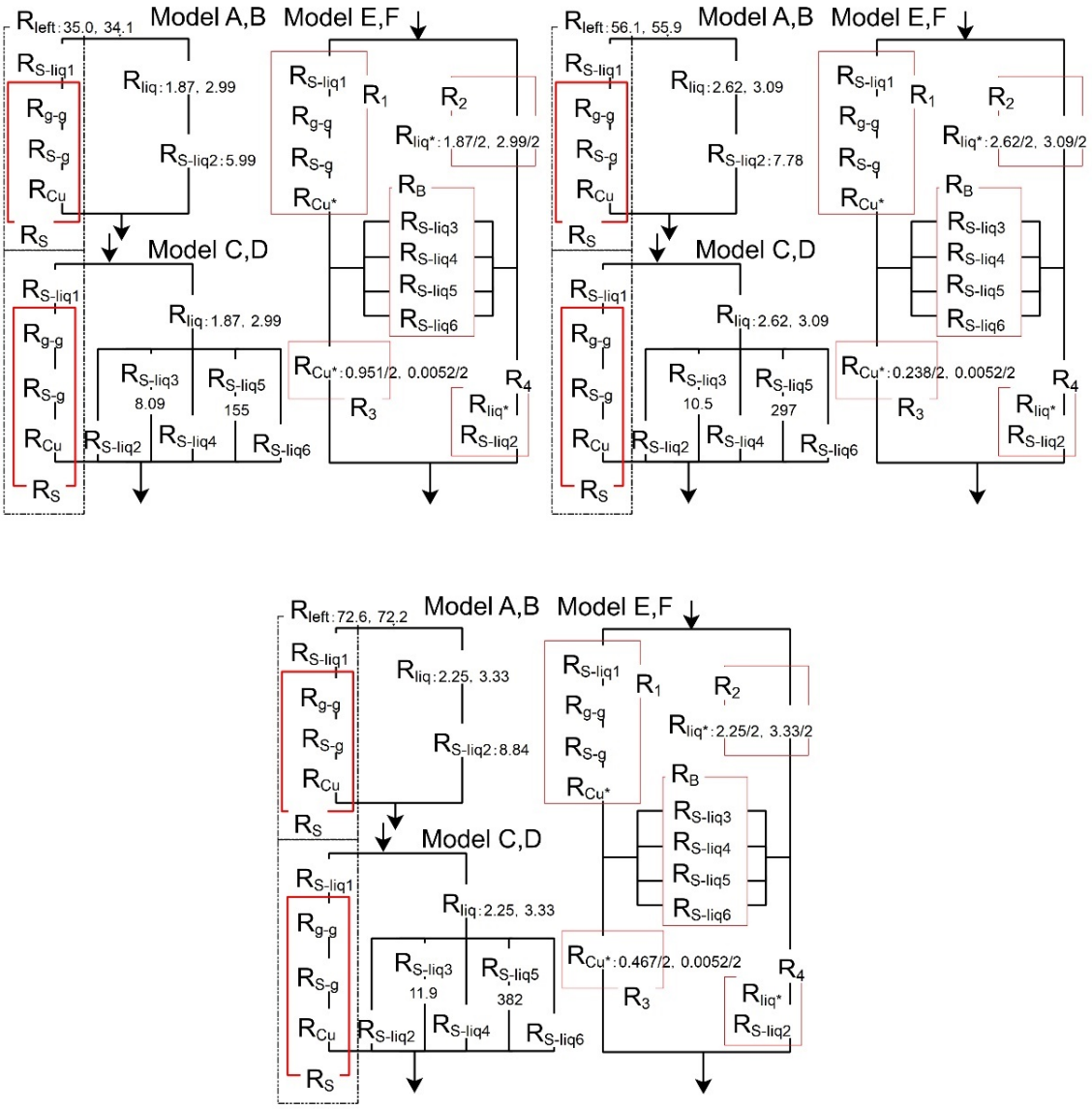

Figure S6.19 The local thermal resistances of model A to model F for the SPC/E model in the Wenzel (CA12) state under the cases of pristine graphene (SV2.1). The top-left, top-right, and bottom of the figures correspond to the water pressure of P1, P2, and P3, respectively. All values were components of TCMs. The unit is 10^8 K/W.

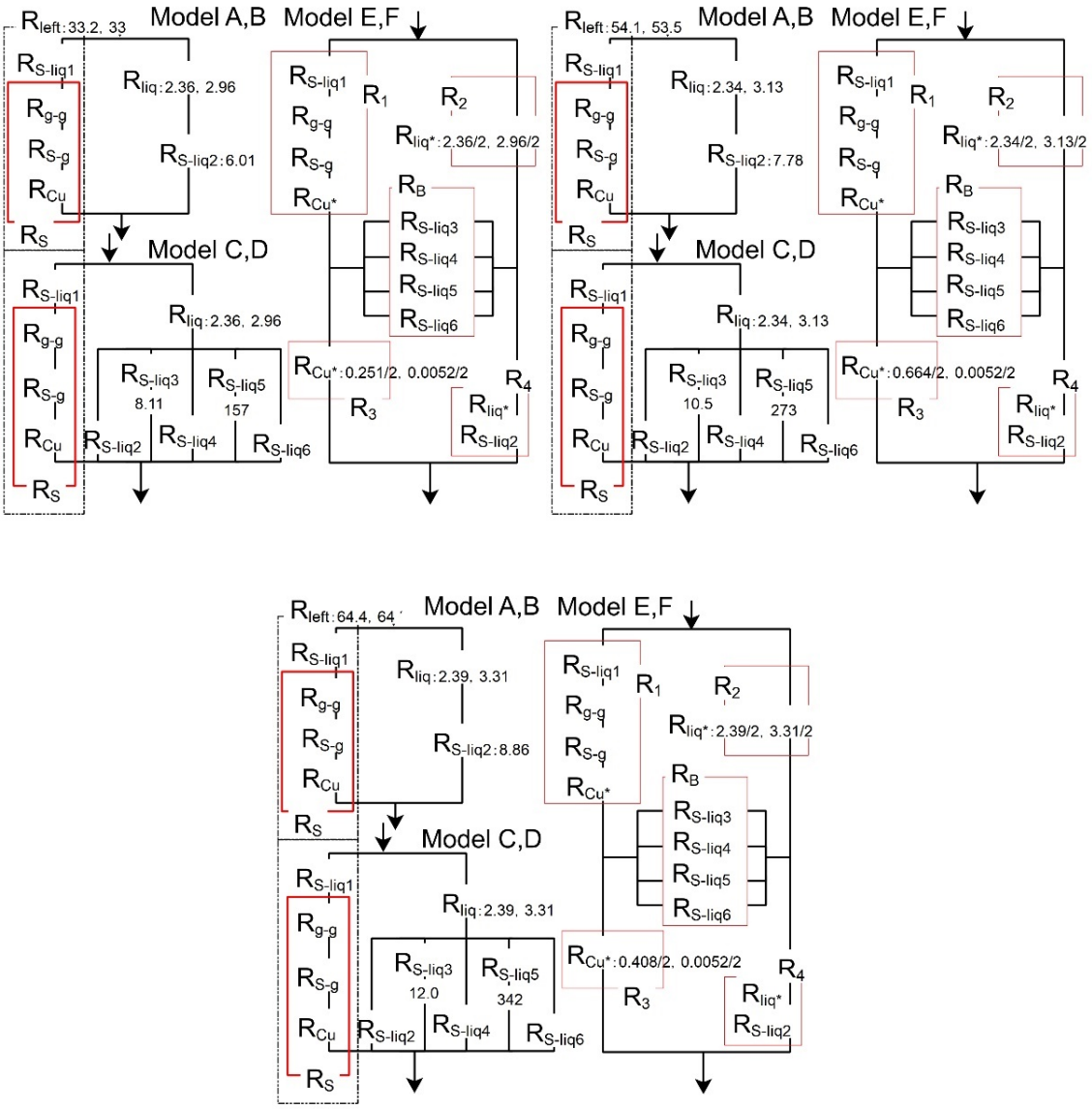

Figure S6.20 The local thermal resistances of model A to model F for the SPC/E model in the Wenzel (CA12) state under the cases of pristine graphene (SV2.8). The top-left, top-right, and bottom of the figures correspond to the water pressure of P1, P2, and P3, respectively. All values were components of TCMs. The unit is 10^8 K/W.

The detailed values in TCMs in Cu-graphene-SPC/E water systems in the CB state for the SPC/E model

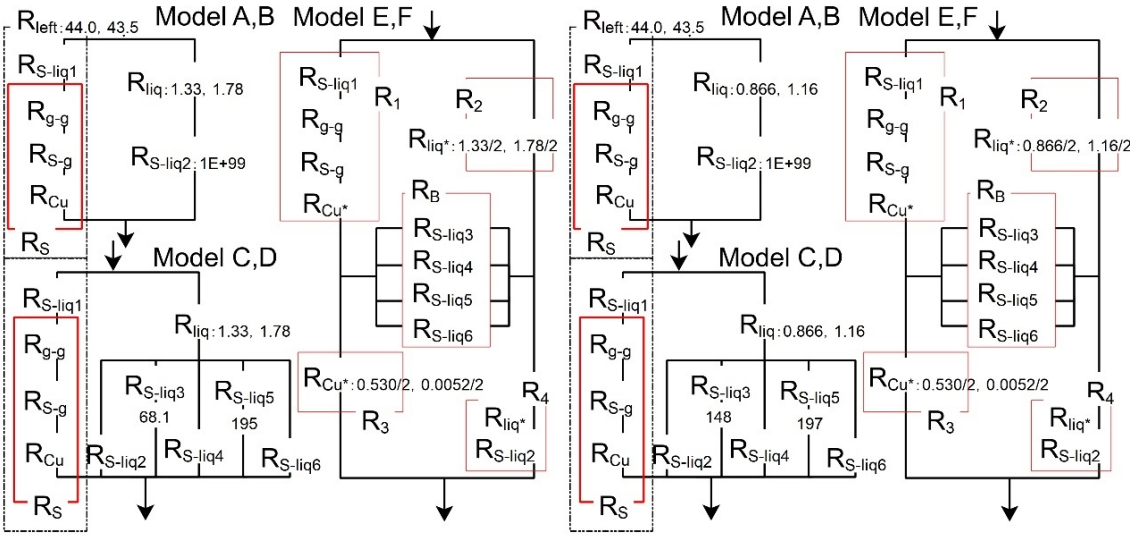

Figure S6.21 The local thermal resistances of model A to model F for the SPC/E model in the CB (CA21) state under the cases of pristine graphene (SV0.0). The left and right figures correspond to the number of water molecules of N1 and N2, respectively. All values were components of TCMs.

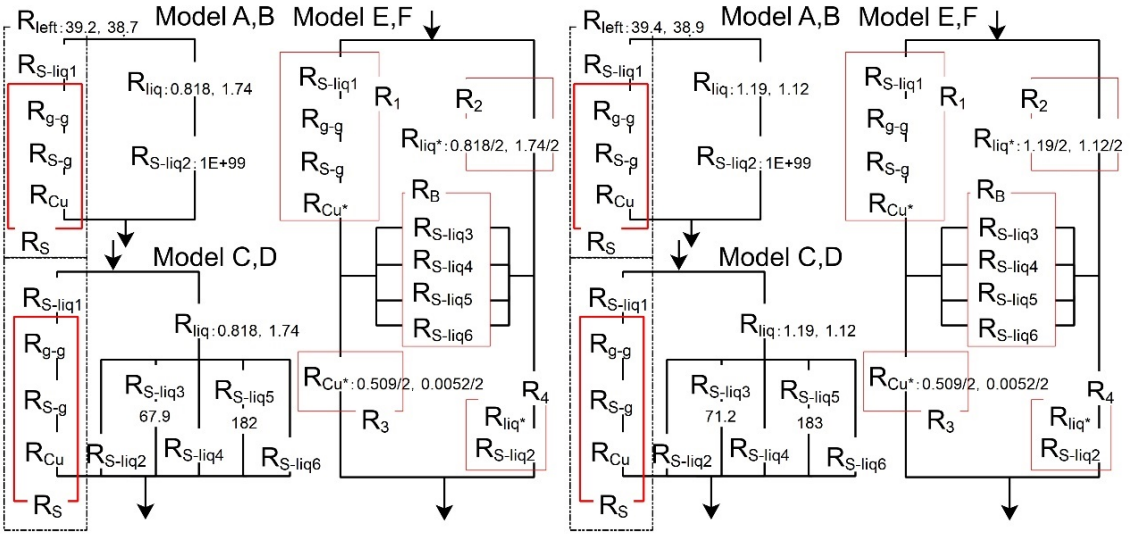

Figure S6.22 The local thermal resistances of model A to model F for the SPC/E model in the CB (CA21) state under the cases of defective graphene (SV2.1). The left and right figures correspond to the number of water molecules of N1 and N2, respectively. All values were components of TCMs. The unit is 10^8 K/W.

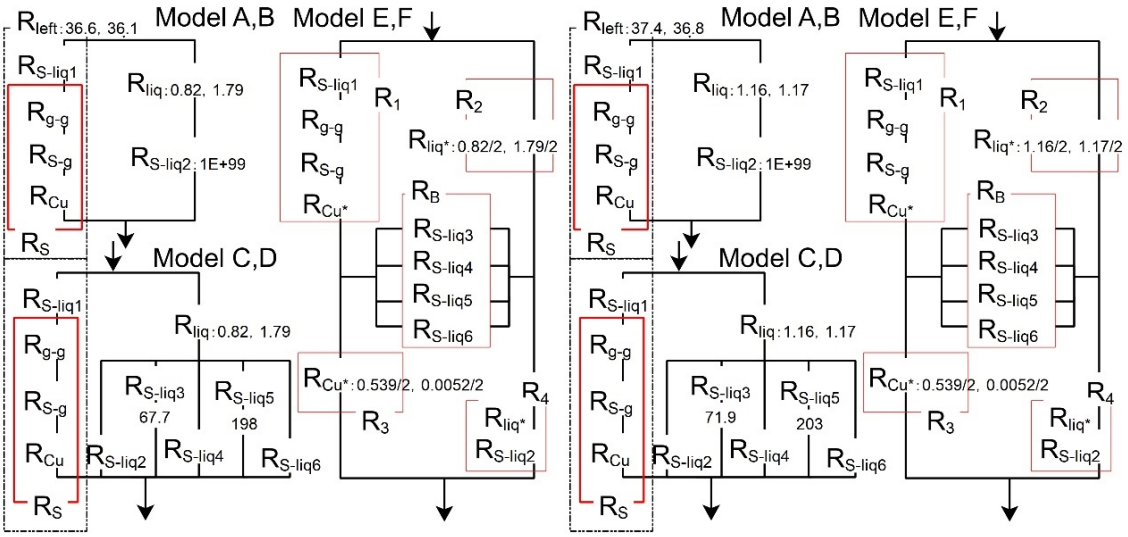

Figure S6.23 The local thermal resistances of model A to model F for the SPC/E model in the CB (CA21) state under the cases of defective graphene (SV2.8). The left and right figures correspond to the number of water molecules of N1 and N2, respectively. All values were components of TCMs.

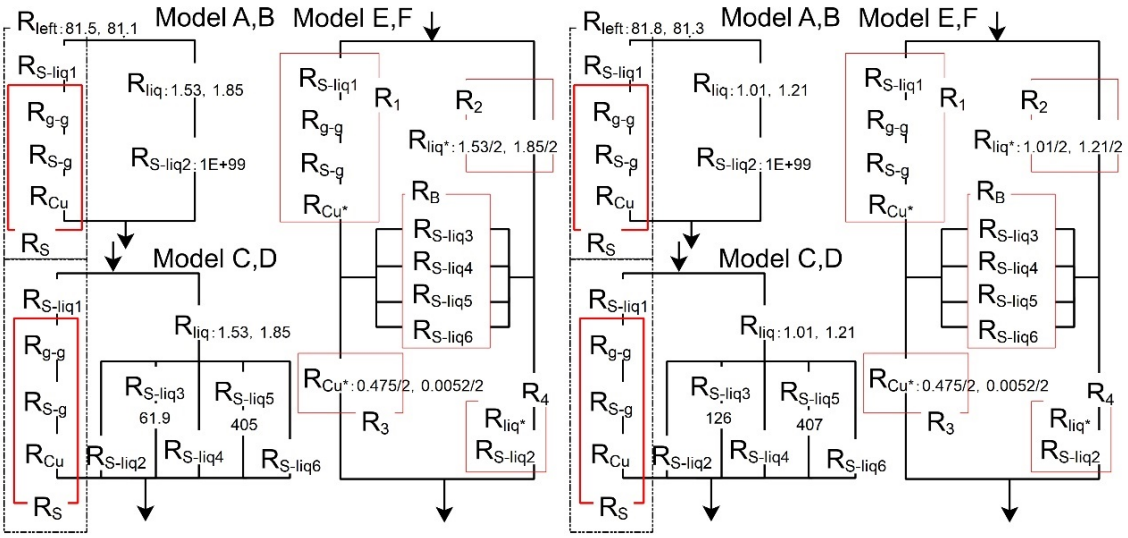

Figure S6.24 The local thermal resistances of model A to model F for the SPC/E model in the CB (CA22) state under the cases of pristine graphene (SV0.0). The left and right figures correspond to the number of water molecules of N1 and N2, respectively. All values were components of TCMs. The unit is 10^8 K/W.

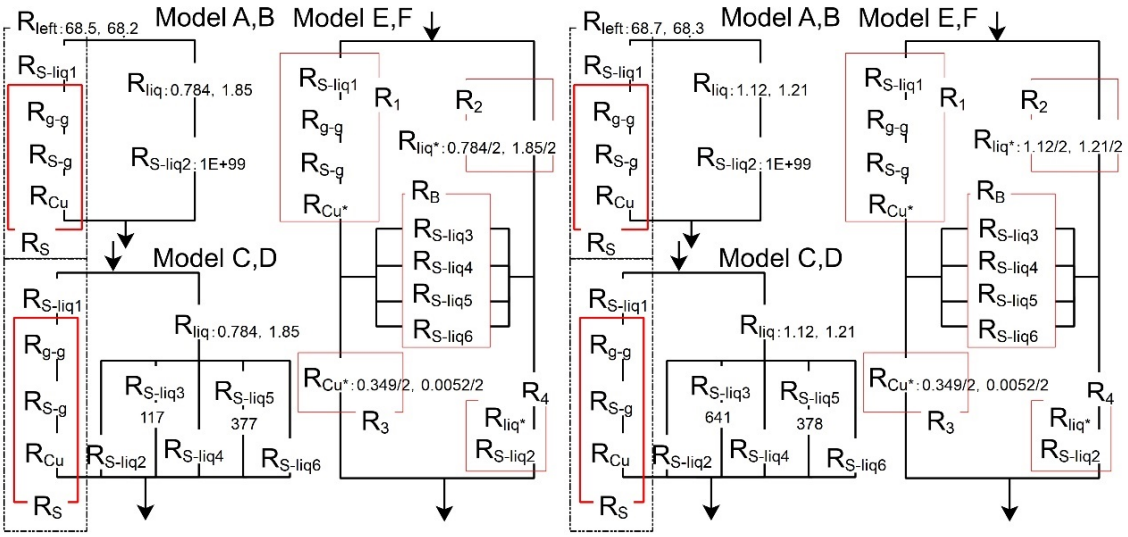

Figure S6.25 The local thermal resistances of model A to model F for the SPC/E model in the CB (CA22) state under the cases of defective graphene (SV2.1). The left and right figures correspond to the number of water molecules of N1 and N2, respectively. All values were components of TCMs. The unit is 10^8 K/W.

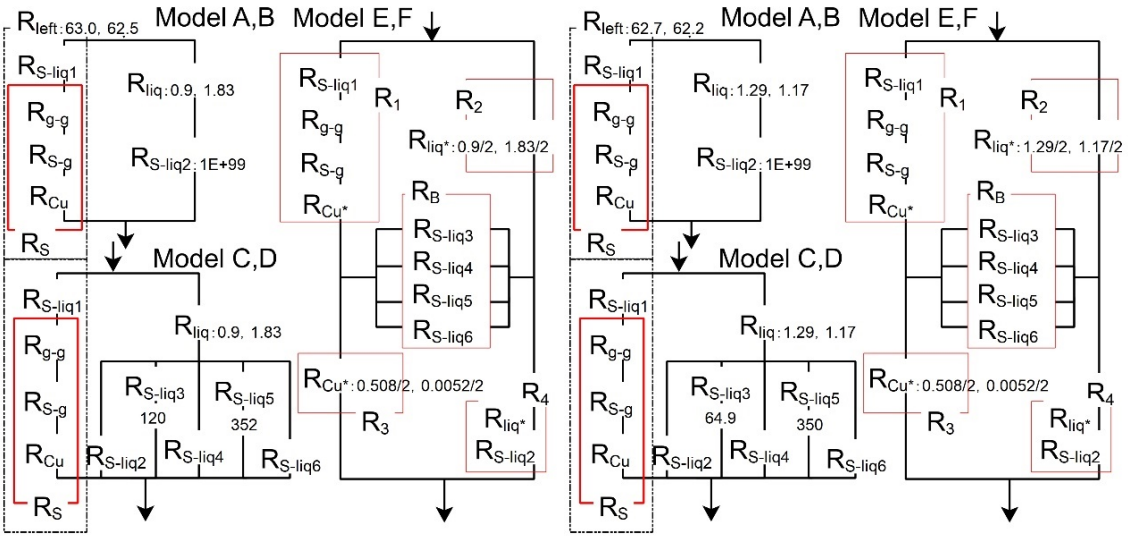

Figure S6.26 The local thermal resistances of model A to model F for the SPC/E model in the CB (CA22) state under the cases of defective graphene (SV2.8). The left and right figures correspond to the number of water molecules of N1 and N2, respectively. All values were components of TCMs. The unit is 10^8 K/W.

Figures S6.27 to S6.32 Energy transfer ratio between water and solid

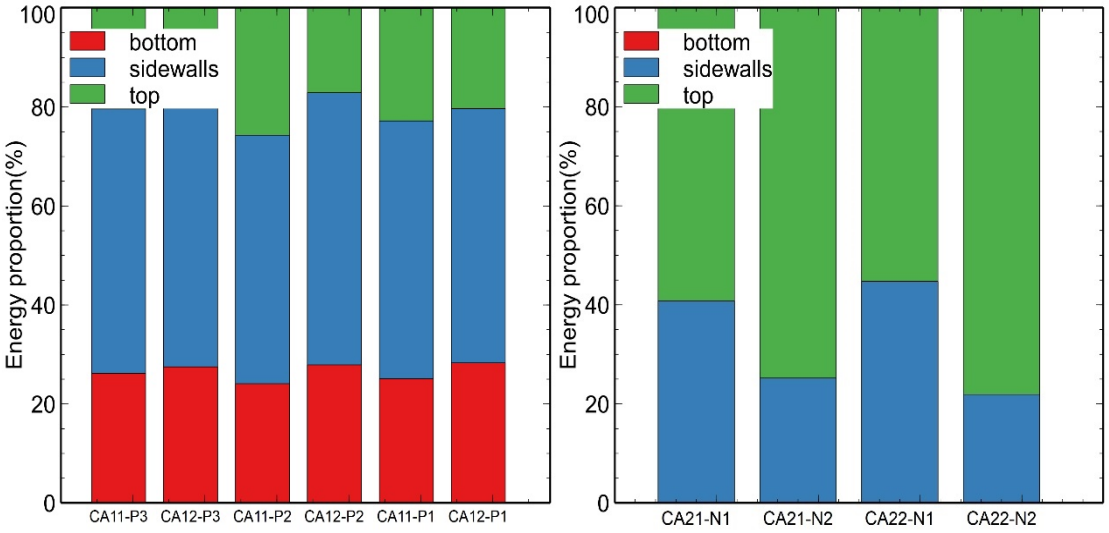

Figure S6.27 Energy transfer ratio between water of the CG model and Cu coated with pristine graphene (SV0.0) calculated by MD simulations in the Wenzel (left) and CB (right) states. The "bottom", "sidewalls" and "top" refer to the energy transfer between water and the groove bottom surface, that between water and the nanopillar sidewalls, and that between water and the graphene surface, respectively.

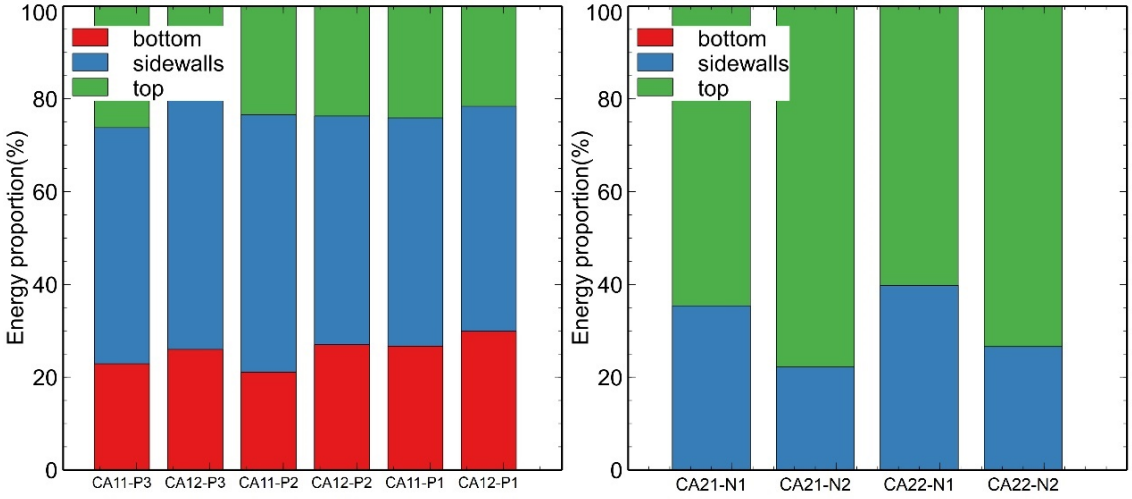

Figure S6.28 Energy transfer ratio between water of the CG model and Cu coated with defective graphene (SV2.1) calculated by MD simulations in the Wenzel (left) and CB (right) states.

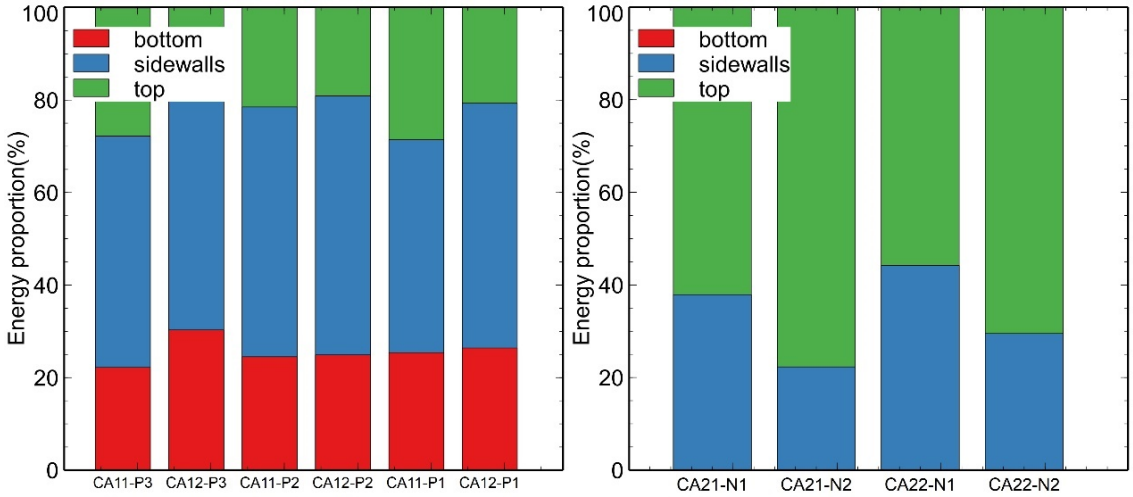

Figure S6.29 Energy transfer ratio between water of the CG model and Cu coated with the defective graphene (SV2.8) calculated by MD simulations in the Wenzel (left) and CB (right) states.

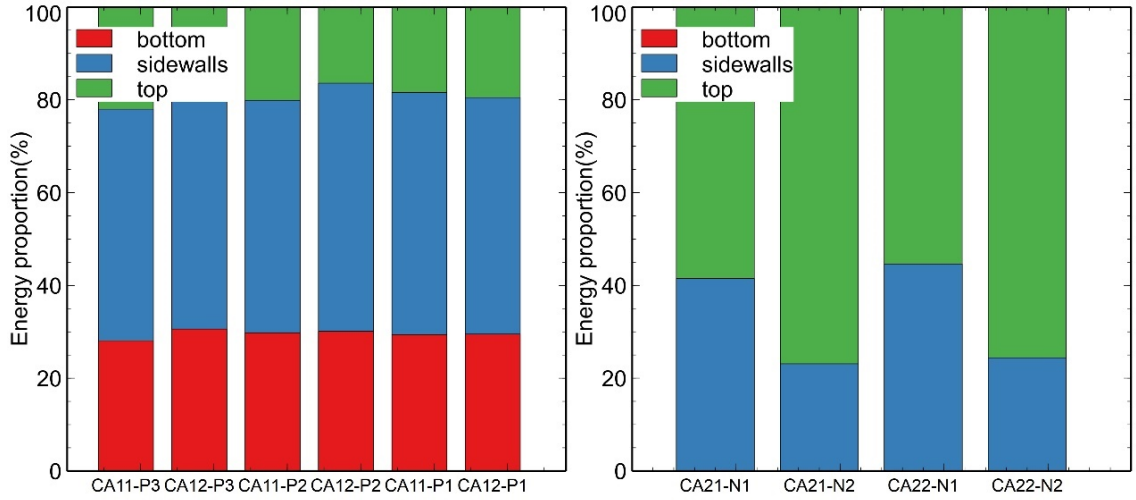

Figure S6.30 Energy transfer ratio between water of the SPC/E model and Cu coated with the pristine graphene (SV0.0) calculated by MD simulations in the Wenzel (left) and CB (right) states.

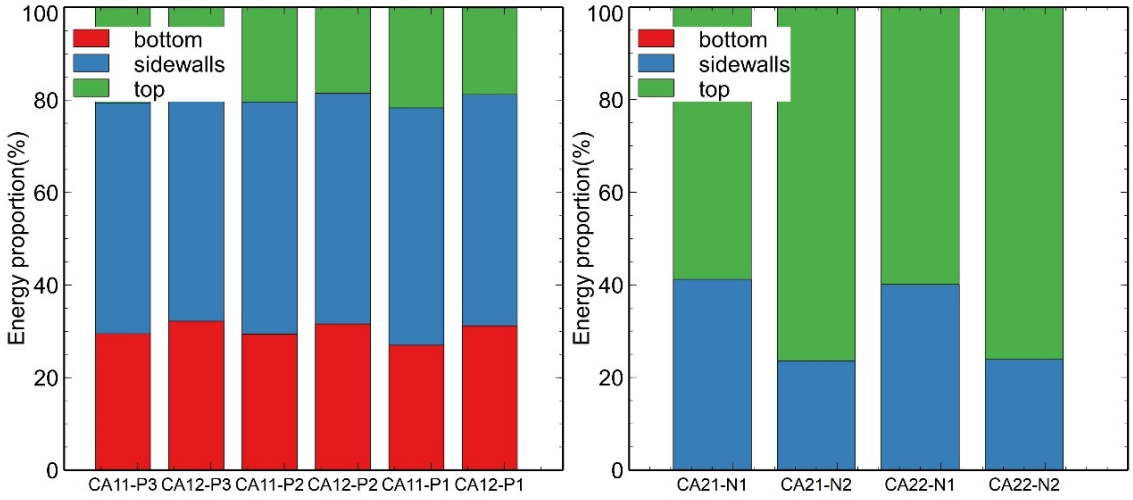

Figure S6.31 Energy transfer ratio between water of the SPC/E model and Cu coated with the defective graphene (SV2.1) calculated by MD simulations in the Wenzel (left) and CB (right) states.

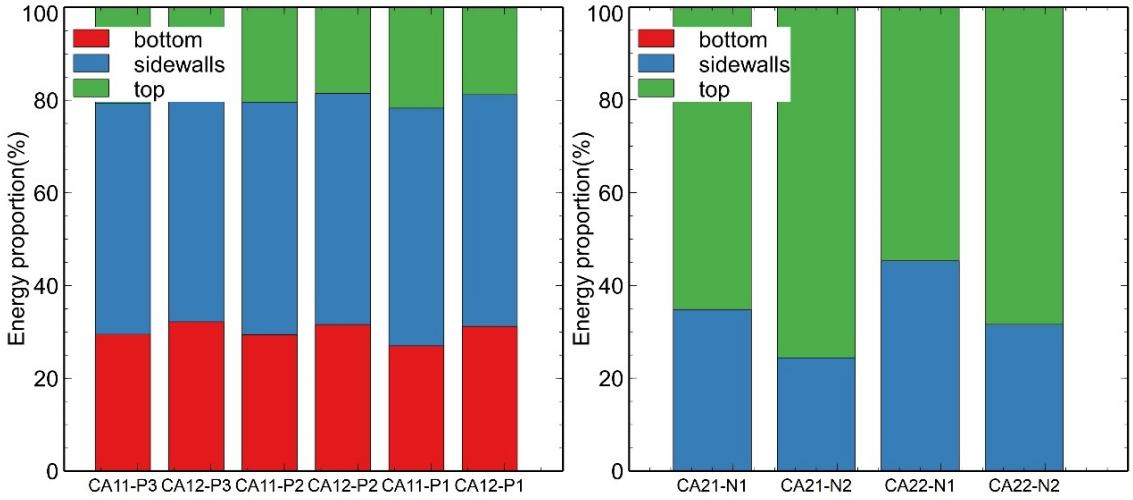

Figure S6.32 Energy transfer ratio between water of the SPC/E model and Cu coated with the defective graphene (SV2.8) calculated by MD simulations in the Wenzel (left) and CB (right) states.

Figures S6.33 to S6.40 2D temperature distribution in Cu-graphene-water systems

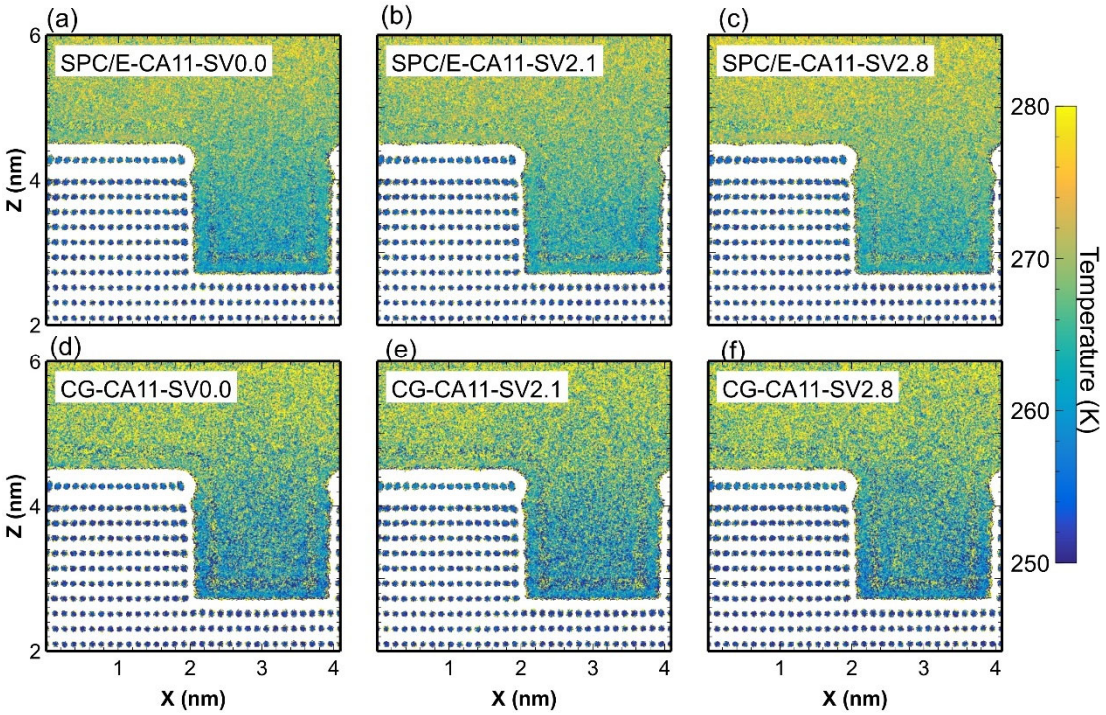

Figure S6.33 2D temperature distribution of the solids and water in the CA11 cases under the water pressure of P1.

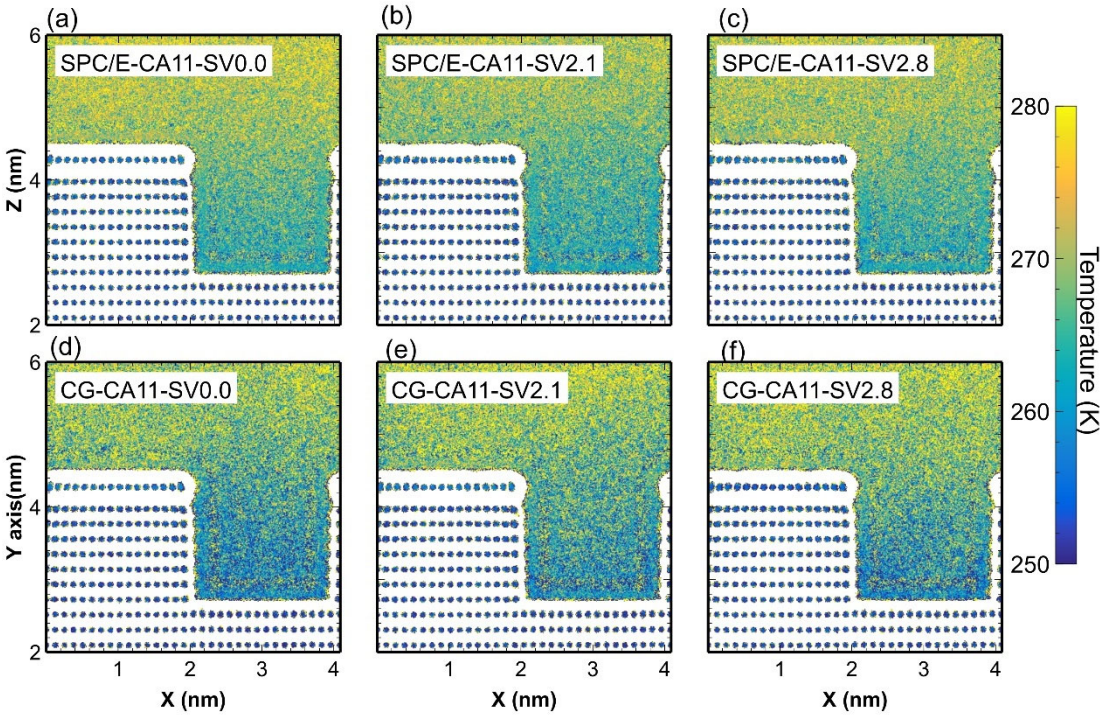

Figure S6.34 2D temperature distribution of the solids and water in the CA11 cases under the water pressure of P2.

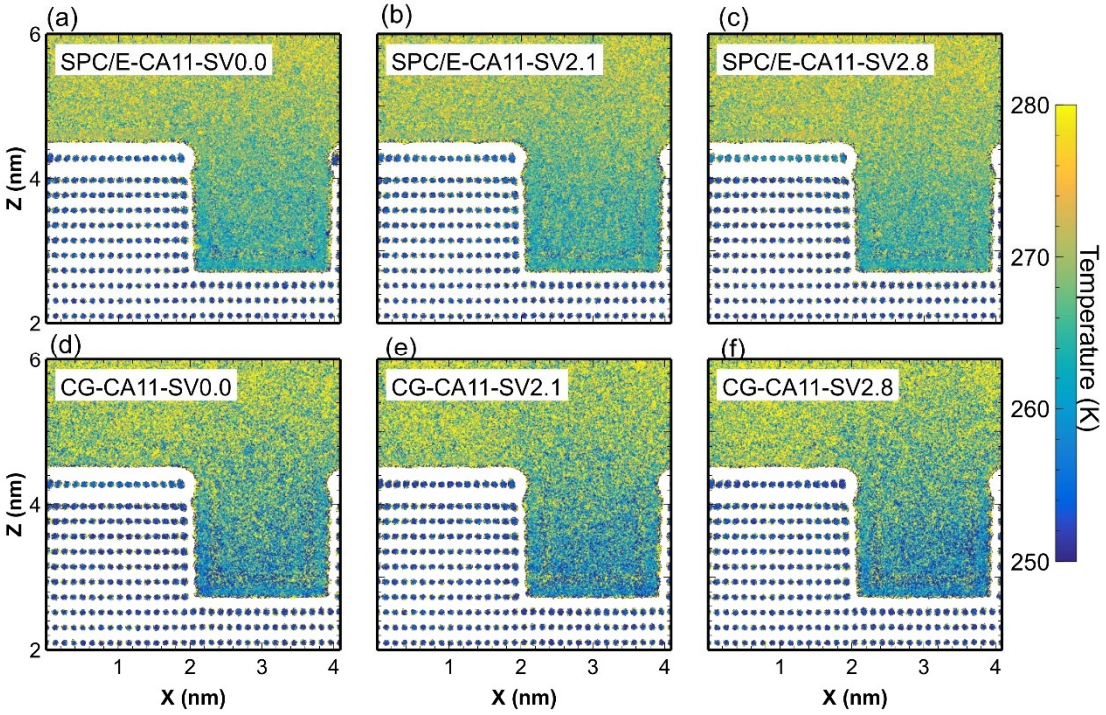

Figure S6.35 2D temperature distribution of the solids and water in the CA11 cases under the water pressure of P3.

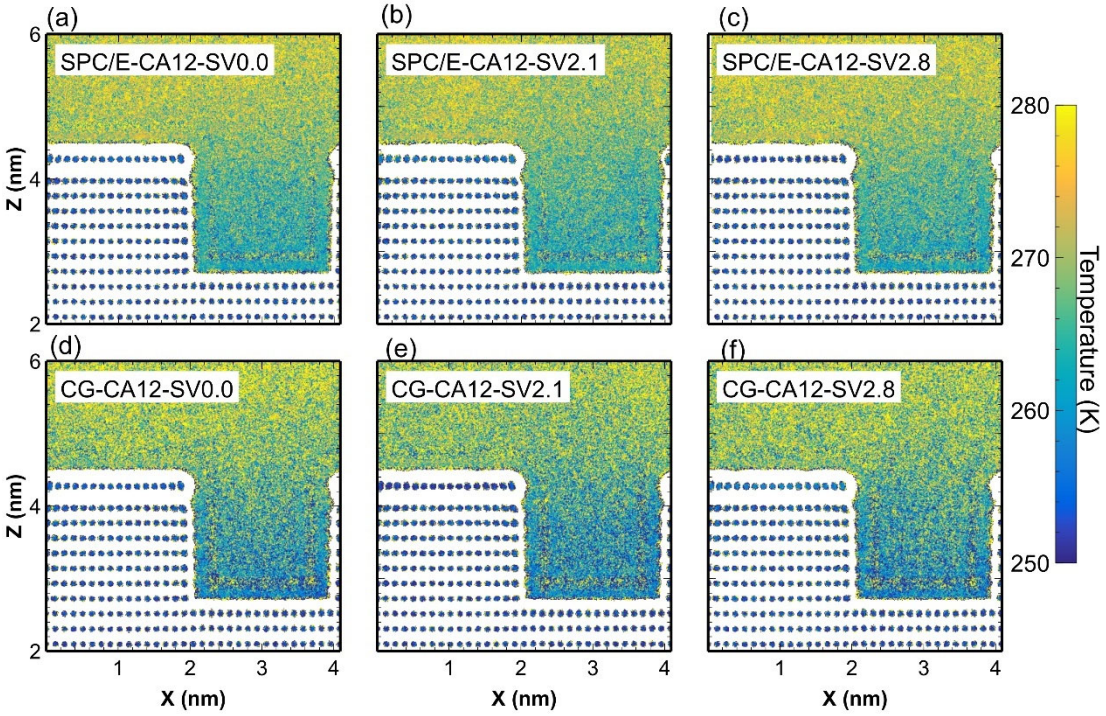

Figure S6.36 2D temperature distribution of the solids and water in the CA12 cases under the water pressure of P1.

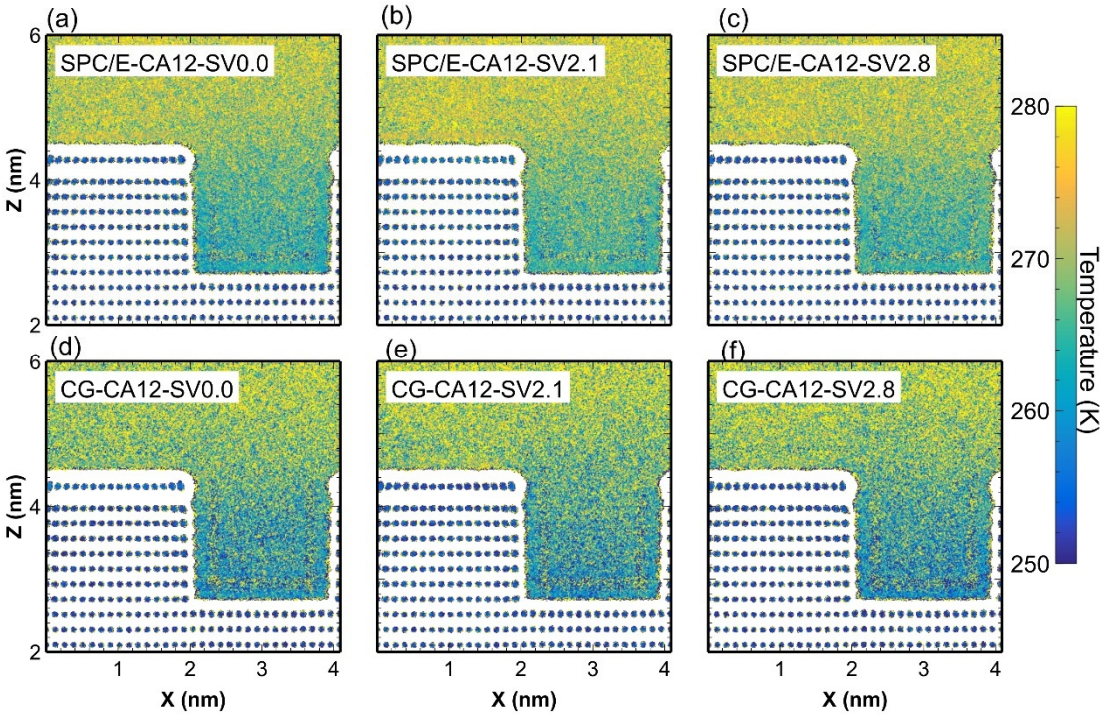

Figure S6.37 2D temperature distribution of the solids and water in the CA12 cases under the water pressure of P2.

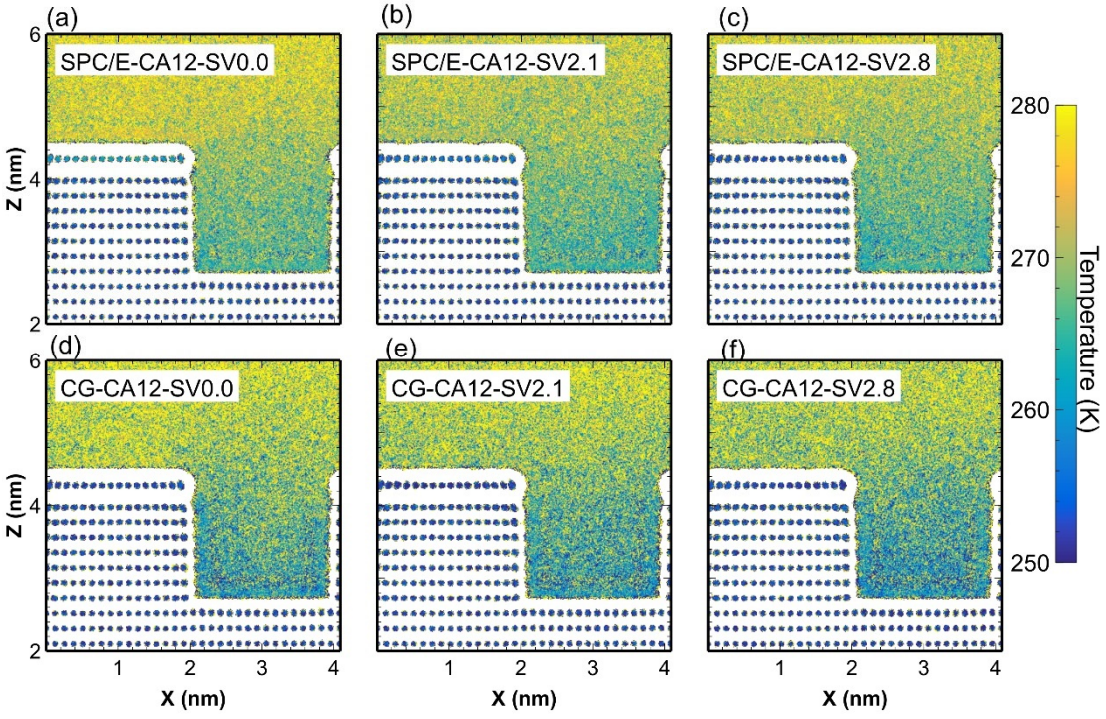

Figure S6.38 2D temperature distribution of the solids and water in the CA12 cases under the water pressure of P3.

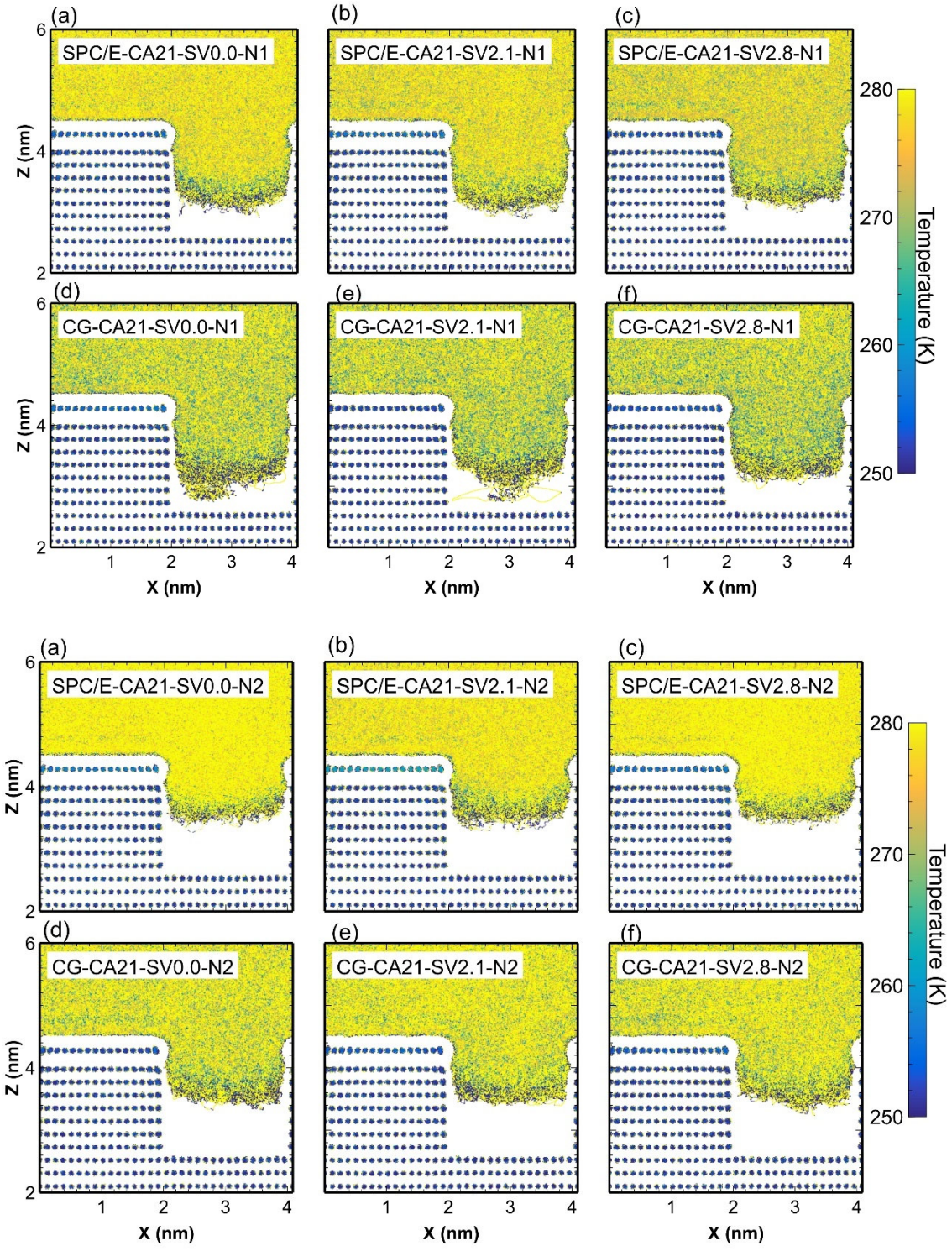

Figure S6.39 2D temperature distribution of the solids and water in the CA21 cases under the water pressure of N1(top) and N2(bottom).

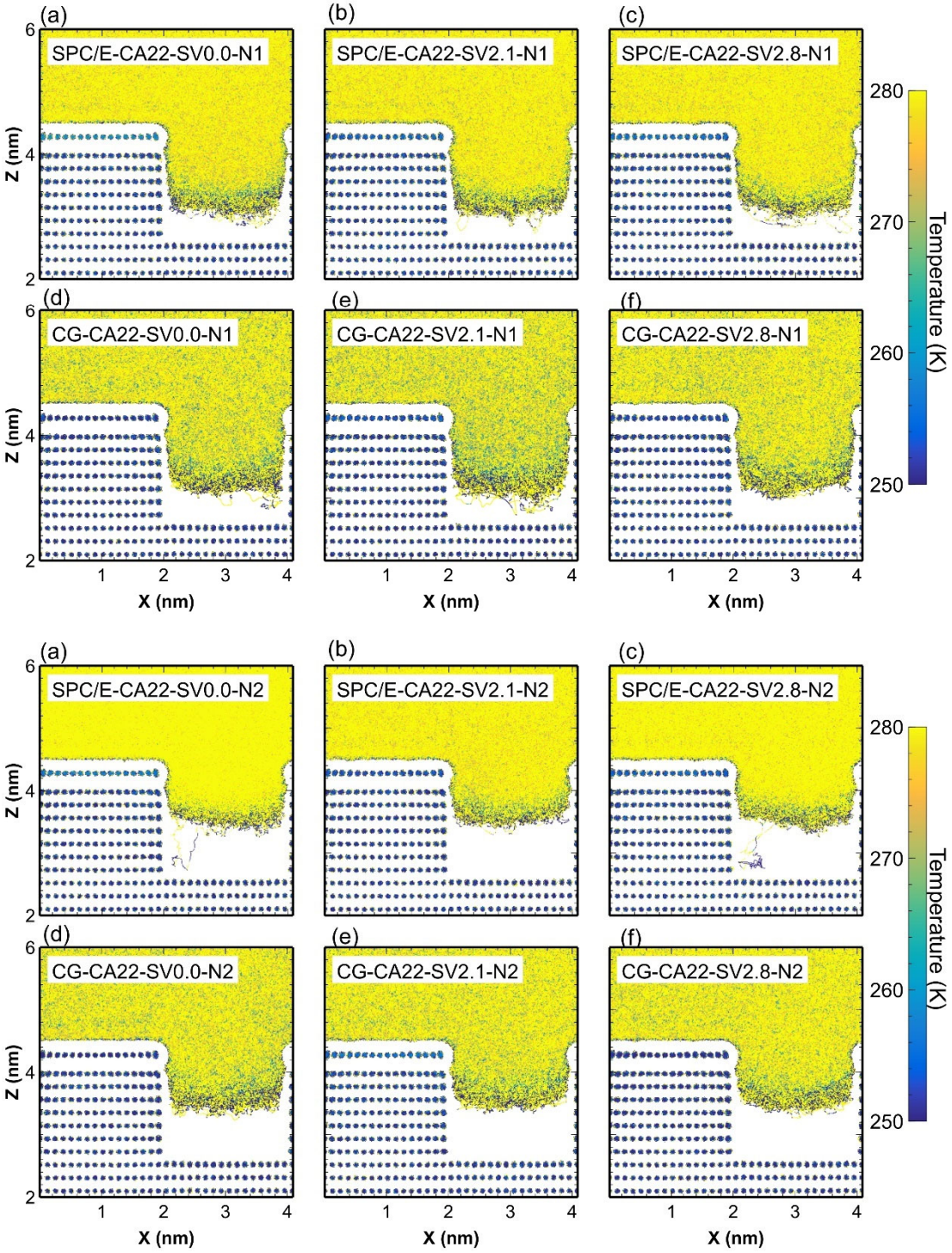

Figure S6.40 2D temperature distribution of the solids and water in the CA22 cases under the water pressure of N1(top) and N2(bottom).

Figure S6.41 The energy transfer obtained by MD simulations and that calculated by TCMs in Cu-graphene-water systems

The $Q_{Model\text{-}A,B\text{-}right}$ for models A and B was calculated by Eq. (S5.6). The $Q_{Model\text{-}A,B\text{-}left}$ and $Q_{Model\text{-}C,D\text{-}left}$ were calculated by Eq. (S5.5). The $R_{Model\text{-}C,D\text{-}right\text{-}c}$ in Eq. (S6.1) was a component, as shown in Eq. (S6.2). $Q_{Model\text{-}C,D\text{-}right}$ for models C and D was calculated by Eq. (S6.2). For models E and F, the $Q_{Model\text{-}top}$, $Q_{Model\text{-}btm}$, and $Q_{Model\text{-}sidewalls}$ in Cu-graphene-water systems were the local heat flow rate of the groove bottom surface, the nanopillar sidewalls, and the top nanopillar surface, respectively, which were calculated using Eq. (S5.9) to Eq. (S5.11) based on TCMs. The components of related equations were explained in Section 2.8.3.

$$R_{Model-C,D-right-c} = (R_{S-liq2}^{-1}+R_{S-liq3}^{-1}+R_{S-liq4}^{-1}+R_{S-liq5}^{-1}+R_{S-liq6}^{-1})^{-1} \quad \text{(S6.1)}$$

$$Q_{Model-C,D-right} = \Delta T_{th}(R_{Model-C,D-right-c} + R_{liq}) \quad \text{(S6.2)}$$

To verify the basis of TCM in the Cu-graphene-water system, Figure S6.41 shows the rate of heat flow calculated by MD simulations and that derived by TCMs. The dots correspond to the $Q_{Model\text{-}A,B\text{-}right}$ and $Q_{Model\text{-}C,D\text{-}right}$. The diamonds correspond to the $Q_{Model\text{-}left}$. The dots, diamonds, and squares in (e) and (f) correspond to the $Q_{Model\text{-}btm}$, $Q_{Model\text{-}top}$, and $Q_{Model\text{-}sidewalls}$, respectively.

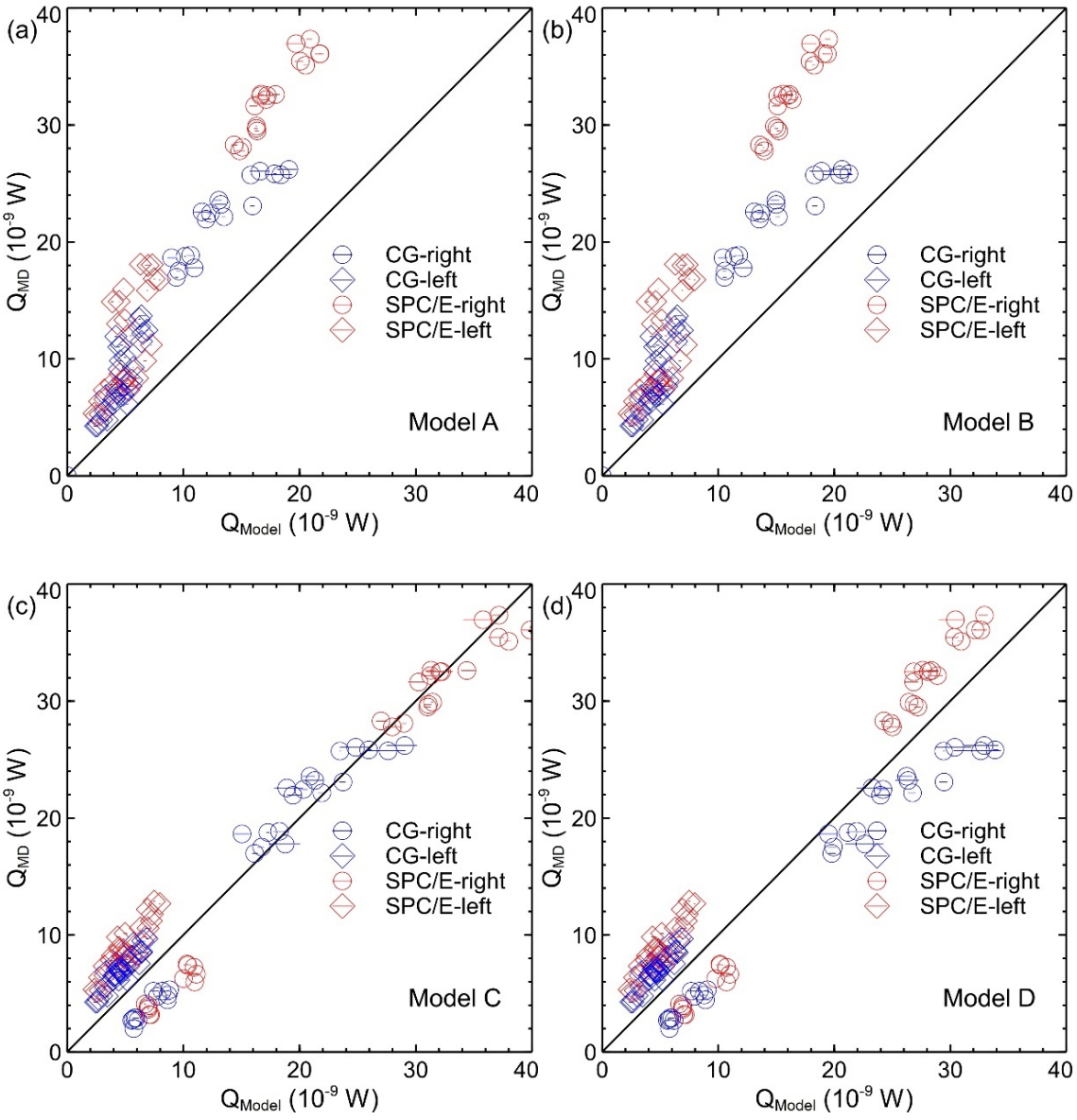

Figure S6.41 The energy transfer obtained by MD simulations and that calculated by TCMs in Cu-graphene-water systems. The dots correspond to the right path of the TCMs. The diamonds correspond to the left path of the TCMs.

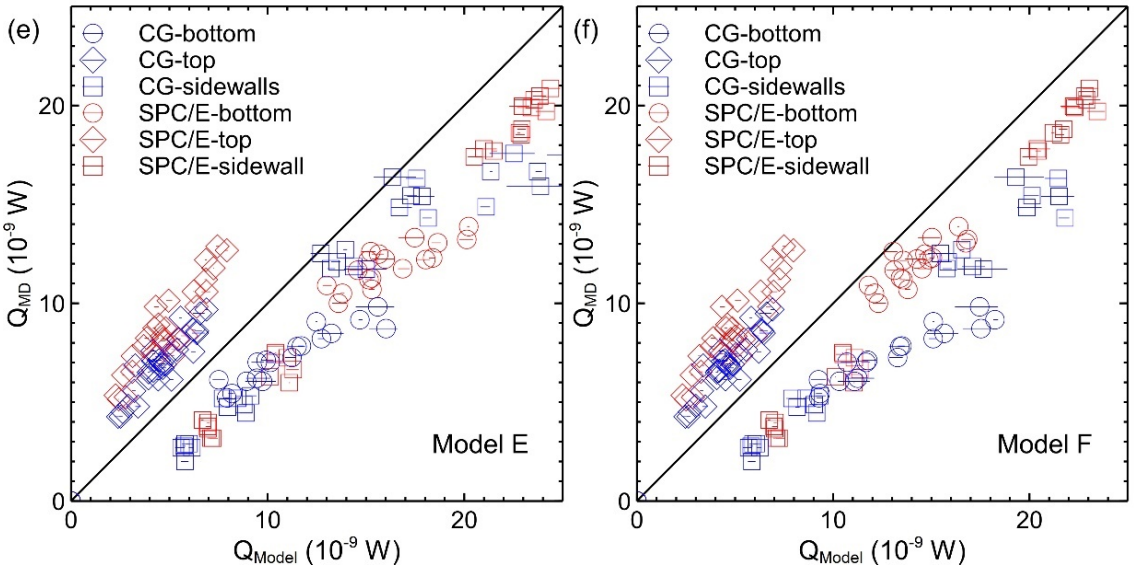

Figure S6.41 (continued) The energy transfer obtained by MD simulations and that calculated by TCMs in Cu-graphene-water systems. The dots, diamonds, and squares correspond to the bottom, top, and sidewalls of the TCMs in (e) and (f).